Monte Carlo Treatment Planning for Advanced Radiotherapy

Cronholm, Rickard; F. Behrens, Claus; Helt-Hansen, Jakob; E. Andersen, Claus

Publication date:
2012

Document Version
Publisher's PDF, also known as Version of record

DTU Nutech
Center for Nuclear Technologies

RICKARD O. OTTOSSON

DOCTORAL DISSERTATION

MONTE CARLO TREATMENT PLANNING FOR ADVANCED RADIOTHERAPY

COMMISSIONING, WORKFLOW AND APPLICATIONS FOR IMRT AND VMAT

SUPERVISORS:

CLAUS E. ANDERSEN

CLAUS F. BEHRENS

JAKOB HELT–HANSEN

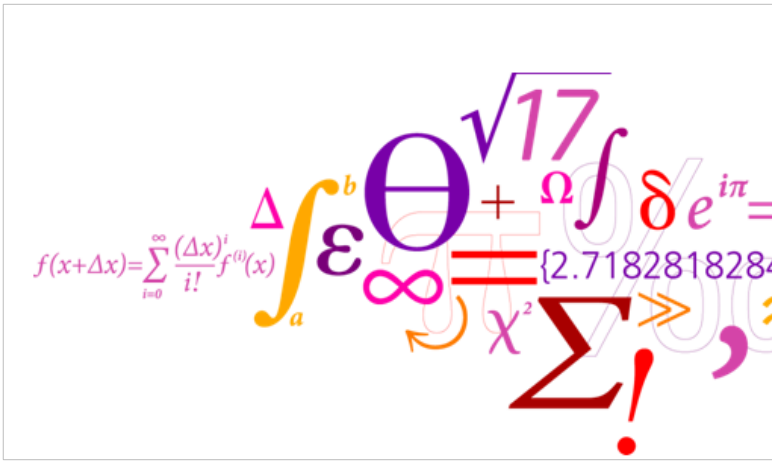

DTU Nutech

Center for Nuclear Technologies

Rickard O. Ottosson: *Monte Carlo Treatment Planning for Advanced Radiotherapy*, Commissioning, workflow and applications for IMRT and VMAT, © March 2012

ABSTRACT

This Ph.d. project describes the development of a workflow for Monte Carlo Treatment Planning for clinical radiotherapy plans. The workflow may be utilized to perform an independent dose verification of treatment plans. Modern radiotherapy treatment delivery is often conducted by dynamically modulating the intensity of the field during the irradiation. The workflow described has the potential to fully model the dynamic delivery, including gantry rotation during irradiation, of modern radiotherapy.

Three corner stones of Monte Carlo Treatment Planning are identified: Building, commissioning and validation of a Monte Carlo model of a medical linear accelerator (i), converting a CT scan of a patient to a Monte Carlo compliant phantom (ii) and translating the treatment plan parameters (including beam energy, angles of incidence, collimator settings etc) to a Monte Carlo input file (iii).

A protocol for commissioning of a Monte Carlo model of a medical linear accelerator, ensuring agreement with measurements within 1% for a range of situations, is presented. The resulting Monte Carlo model was validated against measurements for a wider range of situations, including small field output factors, and agreement with measurements within 1–2% was found. Although the protocol was applied to a specific accelerator type it can be applied to any medical linear accelerator with similair design.

A new algorithm for converting CT scan of a patient to a Monte Carlo compliant phantom is presented. It is more sophisticated than previous algorithms since it uses delineations of structures in order to include and/or exclude certain media in various anatomical regions. This method has the potential to reduce anatomically irrelevant media assignment.

In house MATLAB scripts translating the treatment plan parameters to Monte Carlo input files were written. The scripts are tested and validated for modern treatment delivery including multi leaf collimator movement and gantry rotation during irradiation.

Moreover, a workflow binding the elements together and thus enabling Monte Carlo Treatment Planning is presented.

Comparison between dose distribution for clinical treatment plans generated by a commercial Treatment Planning System and by the implemented Monte Carlo Treatment Planning workflow were conducted. Good agreement was generally found, but for regions involving large density gradients differences of 6% were observed.

DANSK SAMMENFATNING

Dette Ph.d.-projekt beskriver udviklingen af en arbejdsproces for Monte Carlo beregning af kliniske strålebehandlingsplaner. Arbejdsprocessen kan anvendes til at udføre en uafhængig dosis kontrol af behandlingsplaner. Moderne strålebehandling leveres ofte ved at dynamisk modulere intensiteten af feltet under bestrålingen. Den beskrevne arbejdsproces har potentiale til fuldt at modellere den dynamiske levering, inklusive rotation af stålehovedet under bestråling.

Tre hjørnestenene i Monte Carlo beregning er identificeret: Konstruktion, kommissionering og validering af en Monte Carlo model af en medicinsk lineær accelerator (i), konvertering af en CT–scanning af en patient til et Monte Carlo kompatibel phantom (ii) og oversætte af behandlingsplanens parametre (herunder stråleenergi, indfaldsvinkler, kollimator indstillinger osv.) til en Monte Carlo inputfil (iii).

En protokol for kommissionering af en Monte Carlo model af en medicinsk lineær accelerator, der sikrer overensstemmelse med målinger indenfor 1% for en række situationer, er præsenteret. Den resulterende Monte Carlo model blev valideret mod målinger for en bredere række af situationer, herunder output faktorer for små felter, og overensstemmelse med målinger inden for 1 til 2% blev fundet. Selv om protokollen blev anvendt til en specifik accelerator type, kan den anvendes på enhver medicinsk lineær accelerator med lignende design.

En ny algoritme for at konvertere en CT–scanning af en patient til et Monte Carlo kompatibel fantom blev præsenteret. Den er mere sofistikeret end tidligere algoritmer, da den bruger afgrænsning af strukturer med henblik på at inkludere og/eller udelukke visse materialer i forskellige anatomiske regioner. Denne metode har potentialet til at reducere anatomisk irrelevant materiale tildeling.

MATLAB scripts til oversætte af behandlingsplan parametre til Monte Carlo inputfiler blev kreeret. De scripts blev testet og valideret for moderne strålebehandlings levering, herunder multi blad kollimator bevægelse og gantry rotation under bestråling.

Desuden er en arbejdsproces der binder elementerne sammen og dermed gøre det muligt at udføre Monte Carlo beregninger præsenteret.

Sammenligning mellem dosisfordeling for klinisk behandling planer genereret af et kommercielt planlægningssystem og af det præsenterede Monte Carlo beregnings proces er udført. God overensstemmelse blev generelt fundet, men for regioner, der involverer store densitetsgradienter blev forskelle omkring 6% observeret.

Feeling gratitude and not expressing it
is like wrapping a present and not giving it.
— WILLIAM ARTHUR WARD

ACKNOWLEDGMENTS

I would like to thank all people who have helped and inspired me during my doctoral study.

This dissertation would not have been possible without the guidance from my supervisors, whom I would like to direct special thanks to; Dr. Claus E. Andersen for his invaluable input and endless string of solutions to the issues I have encountered, Dr. Claus F. Behrens for always motivating me in times of despair, Dr. Jakob Helt–Hansen for all his hands–on aid and all three of them for being great personalities in general and always managing to take time out of their busy schedules.

I am grateful for having had the privilege to draw knowledge from all my friends and colleagues at the Division of Radiophysics at the Copenhagen University Hospital, Herlev as well as the Radiation Research Department at Risø National Laboratory for Sustainable Energy.

The discussions I have had with Prof. I. Antoniu Popescu, British Columbia Cancer Agency, has not only led to a deeper understanding of the subjects, but has been a constant source of inspiration and, at times, entertainment.

The swift and pin–point–accurate MCSIM–advises, based on my equivocal problem descriptions, given by Dr. Jinsheng Li, Fox Chase Cancer Center, have all been greatly appreciated and useful.

Assistance during tedious measurement sessions given by Dr. Anders Ravnsborg Beierholm, DTU Center for Nuclear Technologies, whom also have conducted some of the measurements included in the thesis on his own.

My deepest gratitude goes to all of the 47 dual core nodes in the computer cluster at the Division of Radiophysics at the Copenhagen University Hospital, Herlev. Without their speed and reliability this study would not have been finished in time. I am heartbroken for those nodes that were not able to withstand my use and abuse over the last years. The aid an assistance provided by Dr. Kenneth Geisshirt on Linux and queue systems also merits special mention.

Last but certainly not least, the love and support shown by all my friends and family has been a vital contributing factor to me enduring this period of time; this dissertation simply had not been possible without them. I am forever indebted to my wife, Nathalie Blinkowska

Cronholm, for listening to my monologues on variance reduction techniques, statistics etc. and for putting up with me spending time with my laptop during many, many, many evenings, weekends and holidays.

CONTENTS

ACRONYMS

3DCRT 3D Conformal RadioTherapy

AAPM American Association of Physicists in Medicine

AAA Analytical Anisotropical Algorithm

BSF BackScatter correction Factor

BQI Beam Quality Index

CAX Central AXis

CPE Charged Particle Equilibrium

CTV Clinical Target Volume

CM Component Module

CERR Computational Environment for Radiotherapy Research

CT Computer assisted Tomography

DICOM Digital Imaging and Communications in Medicine

DBS Directional Bremsstrahlung Splitting

DTA Distance To Agreement

DVH Dose Volume Hisotgram

DVO Dose Volume Objective

ECUT Electron CUT-off energy

EPR Electron Paramagnetic Resonance

EPL Equivalent Path Length

EUD Equivalent Uniform Dose

FWHM Full Width Half Maximum

GTV Gross Tumor Volume

IMRT Intensity Modulated RadioTherapy

ICRU International Commission on Radiation Units and Measurements

SI International System of Units

IC Ionization Chamber

linac linear accelerator

LiF Lithium Formate monohydrate

MRI Magnetic Resonance Imaging

MV Mega Voltage

MU Monitor Unit

MC Monte Carlo

MCTP Monte Carlo Treatment Planning

MLC Multi Leaf Collimator

NTCP Normal Tissue Complication Probability

OBI On–Board Imaging

OAR Organ At Risk

PBC Pencil Beam Convolution algorithm

PDD Percentage Depth Dose curve

PCUT Photon CUT-off energy

PGO Plan Geometry Optimization

PTV Planning Target Volume

PET Positron Emission Tomography

QA Quality Assurance

ROF Relative Output Factor

SAD Source to Axis Distance

SSD Source to Surface Distance

SPR Stopping Power Ratio

TLD Thermo Luminescent Dosimeter

TMR Tissue Maximum Ratio

TERMA Total Energy Released in MAtter

TPS Treatment Planning System

TCP Tumor Control Probability

UBS Uniform Bremsstrahlung Splitting

VOI Volume Of Interest

VMAT Volumetric Modulated Arc Therapy

DISSERTATATION OBJECTIVES AND OUTLINE

Radiotherapy is regulated by the mutually contradicting objectives of delivering a high and uniform dose to the target volumes while sparing any surrounding healthy tissue. Thus it is integral that the absorbed dose can be accurately predicted. A decrease in dose to the target may lead to a severe decrease in Tumor Control Probability (TCP). Meanwhile, an excessive dose to the healthy tissue might lead to drastically increased Normal Tissue Complication Probability (NTCP). Due to the high dependence on dose of the TCP and NTCP curves and the small therapeutic window, even small deviations in dose may have serious consequences (see Figure 1).

International Commission on Radiation Units and Measurements (ICRU) recommends a dosimetrical accuracy, with respect to the planned dose, within 5% for the entire treatment chain [International Commission on Radiation Units and Measurements, 1976], which includes uncertainty of dose calculation, set upp errors, intra fraction movement etc. In order to acheive this limit it is estimated that the dose accuracy must be within 3% [Fraass et al., 2003].

Currently, commercially available treatment planning systems for high energy photon external beam, radiotherapy apply analytical approximations in the calculation of the delivered dose to the patient. Such approximations might lead to errors in the calculated dose. The are largest in regions of the body with considerable changes in mass density; e.g. in the chest where there is a large density difference between lung and other tissues and in the head and neck region where air cavities are present.

Monte Carlo (MC) methods have the potential to accurately calculate dose in heteregoneous geometries as it relies on precisely determined interaction cross sections and do not inherently employ any approximations. The major factors limiting the obtainable accuracy using an MC dose calculation engine are:

- how accurately the linear accelerator (linac) is modelled,
- statistical uncertainty due to the stochastic process of MC simulation,
- how accurately the dose scoring geometry can be modelled,
- uncertainties in the cross section database, and
- uncertainties in the modeling of the particle transport.

Implementation of a MC treatment planning work flow is not a plug and play task, but requires efforts in numerous areas. A virtual model

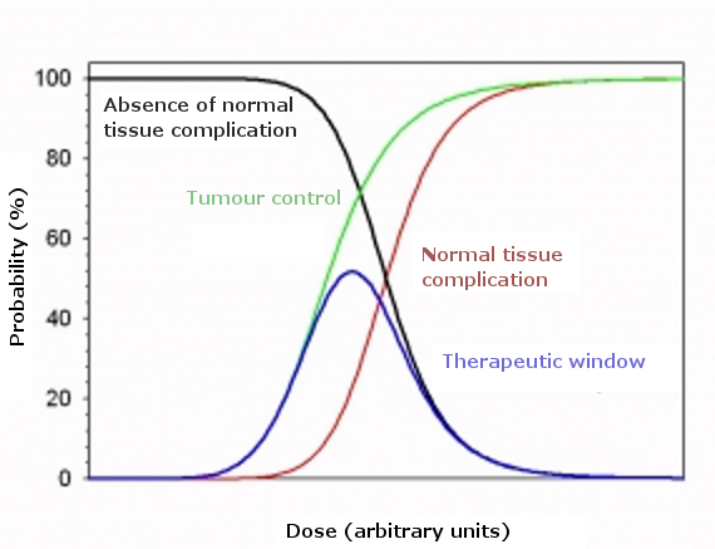

Figure 1: A schematic illustration of the dose dependence of TCP (green) and NTCP (red). As the goal of radiotherapy is to achieve a high TCP while a limited NTCP the absorbed dose should be in the region with the maximum TCP for acceptable NTCP. This region is called the therapeutic window (blue).

of a linear accelerater must be built and verified against measured doses for a range of situations. The geometry in which dose is to be calculated, this may be a homogenous phantom or a highly heterogeneous patient geometry, must be accurately represented in terms of interaction cross sections. Furthermore, means of realizing treatment planning parameters, such as gantry angle, jaws and Multi Leaf Collimator (MLC) positions etc. in the simulation must be designed and validated.

Although the particle transport in Monte Carlo codes is highly accurate, it is important to remember that the MC–linac output is commissioned using free parameters fitted to dosimetrical measurements. MC simulations report statistical uncertainty only. Adding uncertainty due to fitted parameters will be a step towards the full image of the uncertainty associated with MC simulation of medical linacs.

A properly commissioned MC system may be used to perform full MC dose calculation, to a high level of accuracy, in patient geometry as well as to study highly specific dosimetrical properties that are impractical or even impossible to measure physically.

Recently developed treatment delivery techniques (e.g. Intensity Modulated RadioTherapy (IMRT) and Volumetric Modulated Arc Therapy (VMAT)) consist of beam segments under which cavity theory, and thereby currently available dosimetry protocols, does not hold true. No valid protocol for dose measurements of such segments has been established and the uncertainty on dose in such segments, and thereby in treatments applying them, is unknown and might be large.

MC dose calculation can be utilized for situations where experimental measurements are impractical. For any given situation it is possible to assign an ideal detector in MC. Correction factors for experimental measurements can also be derived using MC.

The overall objectives of this Ph.D. project were to address the following topics using accurate Monte Carlo calculation procedures of radiation transport.

1. Develop and implement a work flow enabling Monte Carlo Treatment Planning for conventional as well as advanced radiotherapy. Benchmark results obtained with the conventional treatment planning system against high–accuracy Monte Carlo calculations for all types of treatment plans.

2. Benchmark commercial dose calculation engines against Monte Carlo for sites containing heterogeneous geometries, which are most susceptible to errors introduced by the approximation based dose–calculation algorithms used by the treatment planning systems of today (e.g. lung and head&neck).

3. Investigate the usability of alanine/EPR dosimetry in advanced radiotherapy beams and give recommendation based on issues related to energy dependence, dose gradients and perturbation.

4. Determine the influence of fitted parameters on the resulting fluence produced by the Monte Carlo–model of the linear accelerator.

The scope of this thesis is limited to consider high energy photon radiation only. Moreover, measurements as well as Monte Carlo simulations are conducted using Varian 2300 iX linacs or Monte Carlo models thereof. The thesis is structures as follows:

Chapter 1 deals with the theoretical aspects of dosimetry in radiotherapy and specifically addresses issues regarding dosimetry under situations where reference conditions are not applicable.

Chapter 2 serves as a short introduction to Monte Carlo techniques in radiotherapy. The main features of the different MC codes used throughout this dissertation are also discussed.

Chapter 3 accounts for the commissioning and verification of the virtual Monte Carlo model of the linac in question. The free parameters, mean energy and radial distribution of the impinging electrons are determined through fitting simulated profiles and output factors to the corresponding measurements. Furthermore, the considerations made on the modeled electron fluence incident on the linac target are discussed and motivated.

Chapter 4 regards the conversion of patient Computer assisted Tomography (CT) data to density and tissue composition, which are the information needed in order to perform Monte Carlo simulation using the codes encompassed in this thesis. A new algorithm for the conversion of CT data to a MC compliant phantom is presented in section 4.4. It uses delineations of structures in order to include and/or exclude certain media in various anatomical regions. This method has the potential to reduce anatomically irrelevant media assignment.

Chapter 5 highlights the most important issues to consider when translating the parameters of a DICOM treatment plan file to a EGS4/EGSnrc compliant input file and covers the steps necessary to calibrate the virtual MC model to report absolute dose as oppose to dose per particle incident on the linac target. Simulated field size dependent monitor chamber BackScatter correction Factors (BSFs) are compared to measurement and it is confirmed that the use of directional bremsstrahlung splitting does not compromise simulation of backscatter correction factors.

Chapter 6 summarizes the Monte Carlo Treatment Planning (MCTP) work flow developed in this study. In essence, it serves as a cookbook on how to go from a treatment plan in a Treatment Planning System (TPS) to full Monte Carlo dose calculation, converting the resulting dose distribution to absolute dose (Gy) and rewriting the structure of the EGS4/EGSnrc outputted dose file to a DICOM RP file.

Chapter 7 holds comparisons between dose distributions obtained through analytical calculations, by means of a treatment planning system, and through Monte Carlo simulations. Moreover, the influence of the fitted MC model parameters on the dose distribution of advanced radiotherapy treatment plans is discussed.

Chapter 8 investigates the need of additional correction factors for alanine/EPR dosimetry under non reference conditions by means of MC simulations.

Chapter 9 studies the potential use of an alanine/EPR based dosimetry system for determining small field ROFs by means of comparing measurements to Monte Carlo simulations.

Appendix A is a paper published in Physics in Medicine and Biology. The choice between low and high energy photon energy for Intensity Modulated RadioTherapy treatment of non–small lung cell cancer is investigated using Pareto front analysis. The included dose calculation algorithms are the Pencil Beam Convolution algorithm, the Analytical Anisotropical Algorithm and Monte Carlo.

Appendix B is a paper published in Physics in Medicine and Biology. A new algorithm, using delineation of structures in order to include and/or exclude certain media in various anatomical regions, for the conversion of CT data to a MC compliant phantom is presented and tested for a number of clinical cases.

Appendix C is a paper published in Physics in Medicine and Biology. A dosimetry system based on fiber–coupled organic scintillators is presented. It has the potential to conduct point measurements of absorbed dose in radiotherapy beams involving high spatial and temporal dose gradients. The system is tested against Monte Carlo simulations for Percentage Depth Dose curve and Relative Output Factor for square fields down to 0.6×0.6 cm^2 size.

Appendix D is a paper submitted for publication in Radiation Measurements. The need for additional correction factors for alanine dosimetry in small field photon beams is investigated using MC.

Appendix E is an unpublished study in which the Monte Carlo simulation of palliative IMRT lung treatment is compared to dose calculated by Pencil Beam Convolution algorithm and Analytical Anisotropical Algorithm for low (e.g. 6Mega Voltage (MV)) and high (e.g. 15MV) photon beams.

1 INTRODUCTION

The field of radiotherapy has evolved greatly over the years. Some of the milestones are the construction of the medical linac, the CT imaging and the introduction of IMRT. An integral part of the evolution of external beam radiotherapy has been the rapid development and increased availability of computers.

The objective of radiotherapy is to kill cancerous tissue, while minimizing the short and long term effects of surrounding healthy tissue. Ionizing radiation induce unrepairable DNA damage to tissue by causing single and double–strand breaks which leads to cell death if the damage is beyond repair. Thus, the goal of radiotherapy is to deliver high doses of ionizing radiation to cancerous tissue, while low doses to surrounding healthy tissue. These objectives are naturally mutually contradicting, which leads to radiotherapy being a trade off between the two objectives.

The absorbed dose is defined as the absorbed energy deposited by the ionizing radiation in a medium per mass unit, i.e J/kg. The International System of Units (SI) derived unit for absorbed dose is gray (Gy) after the British physicist Louis Harold Gray (1905–1965).

Radiotherapy can be classified as internal or external depending on weather the source of radiation is situated inside or outside of the patient during treatment, respectively. External radiotherapy can furthermore be divided according to the primary delivery particle type (e.g. photon, electron, positron etc.). This dissertatation encompass only external beam radiotherapy using high energy X–rays and for simplicity this is what will be referred to whenever radiotherapy is discussed, unless otherwise specifically stated.

1.1 THE LINAC

In medical linacs (Figure 2) electrons, generated from a filament (the electron gun) are accelerated to a given potential, using an RF–field. Once accelerated, the electrons are directed onto the target using a bending magnet, which also functions as an energy filter. For high energy X–rays the electron beam is incident on a high–Z target in which the electrons undergo interaction resulting in a divergent bremsstrahlung photon beam. The photons emitted from the target are referred to as the primary radiation.

A number of additional components, each with a specific purpose, are encompassed in the treatment head and each of them generate scattered, or secondary, radiation. The largest source of secondary

Figure 2: One of the Varian Clinac 2300 iX linacs located at the Copenhagen University Hospital, Herlev.

radiation is the field flattening filter [Jaffray et al., 1993], which is introduced in order to ensure uniform radiation intensity distribution.

Two independent transmission ionization chambers are mounted below the flattening filter as a dose monitoring system.

The shape of the photon beam emitted form the treatment head can be defined using a beam limiting aperture. A fixed primary collimator is located close to the bremsstrahlung target, while movable secondary collimating jaws are located further down the beam direction. These jaws are made of a material with high atomic number, usually tungsten, which blocks transmission of radiation through them. In addition to the secondary jaws a set of opposing MLC banks (Figure 3) are mounted on modern linacs. An MLC bank consists of a number of parallel collimating leafs, with a typical width of 2.5 to 5 mm each. The leafs may be positioned independently of each other and can thus be utilized to produce irregular field shapes that can be conformed to a desired target. The design of the MLCs leads to inter– and intra–leaf leakage and are therefore commonly used in conjunction with the collimating jaws.

1.1.1 *Calibration*

It is the upper transmission ionization chambers (the monitor chambers), located in the linac treatment head, that are responsible for terminating the beam when the requested dose has been delivered. The monitor chamber is located above the beam collimating devices and is therefore relatively[1] insensitive to changes in field size and is

1 Depending on the design of the linac a small field size dependent back scatter contribution to the monitor chamber dose may be observed.

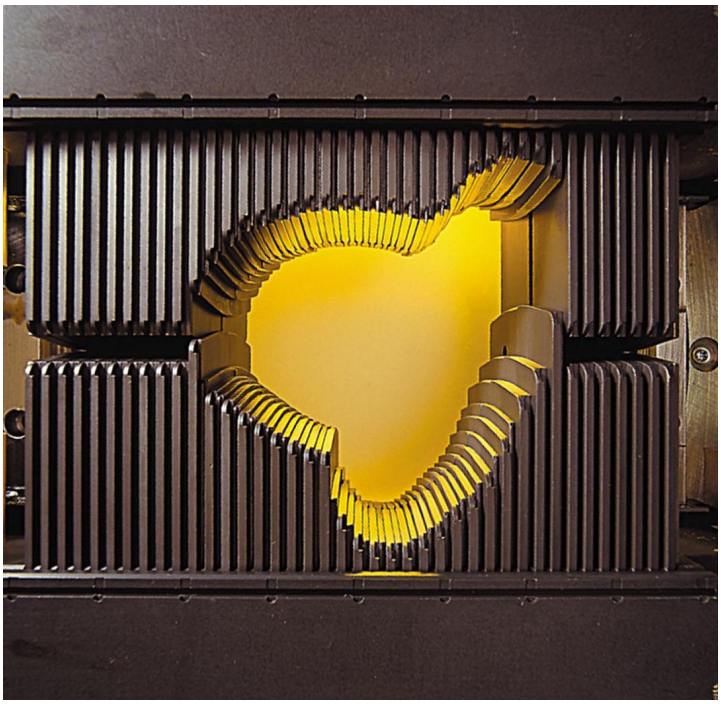

Figure 3: The MLC used in the Varian Clinac 2300 iX linacs located at the Copenhagen University Hospital, Herlev. The two opposing banks are located above each other. The individual leaf can be positioned independently of each other.

blind to the actual patient or phantom geometry. Therefore an additional unit of dose has been established, namely Monitor Unit (MU). In order to relate the signal from the monitor chamber to a physical dose in the treatment geometry it is necessary to calibrate the linac. The calibration is typically conducted so that the delivery of 100 MU for a 10×10 cm^2 field, delivered with a Source to Surface Distance (SSD) of 100 cm corresponds to 1 Gy at the maximum dose along the central axis, d_{max}, in a homogeneous water phantom [Almond et al., 1999; Andreo et al., 2000].

1.2 TREATMENT DELIVERY

The treatment mode can be categorized depending which features that are being employed during the beam delivery. Each treatment delivery mode has its benefits and drawbacks and ultimately the choice of delivery mode is determined by the characteristics of the region that is to be treated. The treatment delivery modes encompassed by this dissertatation are outlined in chronological order in the following text.

1.2.1 *3D Conformal Radiotherapy*

Before the introduction of computers in radiotherapy, the delivered dose was calculated by hand using simple methods. With the introduction of computers, the dose could be calculated on a 3D rendered volume of the patient, typically a CT scan.

Prior to the introduction of MLCs, treatment fields were defined using the secondary collimator alone. This limited the shape of the treatment field to square geometries seriously compromising the conformity of the treatment field. Field specific molded lead blocks were at times used to achieve increased conformity. The drawback of lead blocks is that they need to be manually positioned before delivering the treatment field and removed after. This drawback was eliminated with the introduction of the MLCs as they can be positioned automatically.

1.2.2 *Intensity Modulated Radiotherapy*

IMRT is a treatment modality in which MLC leaves are used to modulate the intensity of the radiation. This can be achieved either by dynamically moving the MLC during the beam delivery (dynamic IMRT) or by dividing the treatment field into a number of static segments each with a different MLC collimation and delivering the radiation when the MLC are positioned in accordance with one of the segments (step and shoot IMRT). The advantage of IMRT over 3D Conformal RadioTherapy (3DCRT) is the possibility of higher dose conformity to the target, while still sparing proximal healthy tissue.

The inherent drawback of IMRT over 3DCRT is an increased complexity. Stricter demands are required on the precision of the MLC as they are used to shape the dose region throughout the field rather than along the edges of the field. A non–flat lateral dose profiles requires a Quality Assurance (QA) system in which the dose is measured using a high spatial resolution.

1.2.3 *Volumetric Modulated Arc therapy*

VMAT is a recent sophistication of IMRT. The implementation of VMAT on Varian linacs is called RapidArc (developed by Varian Medical Systems Inc., USA). As for IMRT the target conformity is achieved by modulating the intensity of the radiation. The most apparent difference between VMAT and IMRT is that the entire linac gantry is rotated during delivery in addition to the dynamically moving MLC jaws. Moreover the rotational speed of the gantry and the dose rate may be varied continuously during the beam delivery.

The target conformity and dose sparing of healthy tissue of VMAT is comparable to that of IMRT, but since the treatment can be delivered

faster it generally requires less MUs [Otto, 2008]. Compared to IMRT a VMAT delivery is more complex and poses higher demands on precision of the gantry angle as well as the dose rate. The QA of VMAT is more demanding as it requires a non–angular dependent detector or a reliable method to correct for the dependence.

An apparent drawback of increased complexity of treatment delivery is that the resulting dose distribution is less intuitive.

1.3 TREATMENT PLANNING

The treatment planning process is conducted using a dedicated software – a Treatment Planning System. Patients scheduled for radiotherapy are commonly diagnosed using a three dimensional imaging modality (e.g. CT, Magnetic Resonance Imaging (MRI) or Positron Emission Tomography (PET)–CT). Once diagnosed the Clinical Target Volume (CTV), or volumes if multiple, is delineated on the image data set. Margins are added to the CTV in order to account for uncertainties of the delineated volume and the setup procedure as well as for movement of the CTV during treatment. The CTV with margins applied is called the Planning Target Volume (PTV). The prescribed dose to the target volume, ordinated by a radiation oncologist, will depend on the type of diagnosis. Population based dose response curves for tumor cells as well as for healthy tissue have been derived and allow for translation of an expected radiological effect to a measurable physical dose. Ideally, a high and uniform dose would be delivered to the target, while not irradiating the surrounding healthy tissue at all. The PTV and important Organ At Risk (OAR), each with its own dose constraints, are delineated on the image data set. The objective of treatment planning procedure is to ensure delivery of the ordinated dose to the PTV, while not exceeding the constraints of the OARs. Due to the characteristics of the interaction of high energy photons with matter those objectives are often mutually contradicting. Therefore radiation therapy is often a balance between target coverage and OAR sparing. The prescribed target dose is often delivered using multiple angles of incidence as an act to limit the dose to OARs. Moreover, the prescribed dose is often delivered in multiple fractions. This procedure makes use of the feature that healthy cells exhibit a higher repair rate than malignant cells.

The treatment planning approach will inevitably depend on the treatment delivery mode. For static delivery modes (i.e. 3DCRT) a technique called forward planning is employed, while a technique called inverse planning is utilized for dynamic delivery modes (i.e. IMRT and VMAT).

1.3.1 *Forward Planning*

For 3DCRT an forward planning approach is utilized. The procedure starts by defining a number of beams each with its individual set of parameters, such as x–ray energy, gantry, collimator and couch angle, MU as well as collimator and MLC settings. The planning procedure is a trial and error process in which beams are added, removed or have their parameters altered. The forward planning process is determined to be completed once a satisfactory treatment plan has been achieved.

1.3.2 *Inverse Planning*

For treatment modalities where the delivered fluence is intensity modulated an inverse planning approach is utilized. Initially the procedure resembles the forward planning process as a number of beams (or arcs) each with a set x–ray energy, gantry (start and end angle for VMAT), collimator and couch angle as well as collimator settings are defined. For inverse treatment planning the modulated fluence is determined using an optimization process. At the start of the optimization process Dose Volume Objectives (DVOs) each with a weight factor, related to the importance of fulfilling the objective, are assigned to important structures (e.g. CTV, PTV, OAR etc.) in accordance with the dose prescription. An iterative optimization process is conducted in order to achieve a dose distribution in accordance with the specified objectives. The optimization is terminated when a satisfactory treatment plan has been achieved. The optimized fluence is converted to deliverable fluence by taking the MLC movement (and gantry rotation in the case of VMAT) into account.

1.3.3 *Dose Calculation*

In order to predict the dose distribution in the patient delivered in a given treatment plan, analytical dose calculation algorithms have been developed. The dose calculation process in a TPS needs to be accurate, but it is also required to be fast as not to be a bottle neck in the patient flow of a radiotherapy clinic. This has lead to the development of a number of approximation based commercially available dose calculation algorithms.

1.3.3.1 *Commercial Dose Calculation Algorithms*

Throughout this study the Varian Eclipse (Varian Medical Systems Inc., USA) TPS was used for treatment planning. Two different dose calculation algorithms were however used; the Pencil Beam Convolution algorithm (PBC) and the Analytical Anisotropical Algorithm (AAA). The two algorithms share many commonalities, but are distinct in

certain aspects. The following text aims at describing the general procedure of a dose calculation algorithm but will also describe the differences between the two algorithms and outline their respective approximations.

The dose distribution can be divided into four main components [Ahnesjö and Aspardakis, 1999]; dose due to

a) primary particles,

b) secondary (scattered) particles originating from the treatment head (head scatter),

c) secondary (scattered) particles originating from the patient or phantom geometry (phantom scatter), and

d) dose due to contaminating electrons.

The primary and phantom scatter components contribute the most to the dose and originate from photons that have not interacted before reaching the patient. Dose due to head scatter and contaminating electrons stem from photons that have undergone interaction in the treatment head prior to being incident on the patient or – i.e. secondary particles. The interaction processes might lead to electrons with energy high enough to reach the patient (d) or to photons scattered in the treatment head reaching the patient (b). Head scattered photons (b) might reach large depths in the dose scoring geometry, whilst the charged particles only have range of a few centimeters.

Commercial dose calculation algorithms are based on dose kernels. Considering a dose scoring region, divided into voxels, the dose distribution from a single point kernel will yield a dose distribution governed by the photon interactions in a given voxel. The total dose distribution of the dose scoring region is the summation of the photon interactions from all point kernels, thus photon interactions occurring in all voxels are accounted for. This process is usually referred to as kernel superposition.

Most current algorithms use kernels that are calculated in a homogeneous medium (water). The dose computed by commercial algorithm are based on two main parameters: the Total Energy Released in MAtter (TERMA) by primary photons and a pattern for the dose deposition about the interaction point of a primary photon (the kernel) [Papanikolaou et al., 2004]. The point kernels are typically integrated over the z–axis, thus resulting in pencil kernels. In order to accurately compute the dose distribution a number of factors needs to be considered:

- The dose scoring volume is not infinite, which means that special surface effects need to be accounted for.
- The patient (or phantom) geometry may differ in atomic composition and density from water, which the kernels were calculated

for, requiring a scaling of the kernels. Moreover, the geometry may be heterogeneous requiring a complex density correction.

- The kernels are computed under the assumption of charged particle equilibrium, which may not be fulfilled near tissue interfaces or at field edges.
- The divergence of the beam is not accounted for in the kernels, which will have implications in the penumbra regions.
- The beam hardening effect is not accounted for in the computation of the kernels, and must be corrected for in the dose calculation.
- The treatment fields are not identical to the fields for which the TPS was commissioned. This introduces an uncertainty in the characterization of the beam.

These issues are handled differently by the dose calculation algorithms encompassed in this study. The approaches of each algorithm is outlined in the following paragraphs.

THE PENCIL BEAM CONVOLUTION ALGORITHM

The PBC consists of two steps; i: the beam reconstruction model and ii: the patient model.

In the beam reconstruction model the dose is calculated for homogeneous water and is based on convolution of pencil beam kernels that have been estimated from a measured data set used to describe the accelerator. Beam modifiers are accounted for by modulating the intensity of the fluence. The beam exiting the treatment head is described by a field intensity function. The value of the field intensity function has the value 1 if the pencil beam did not transverse any beam modifier, 0 if either of the collimating jaws where encountered and a value between 0 and 1 if an MLC was traversed. The attenuation of the MLC is based on measured data.

In the patient model, the depth–dose is calculated through convolution of the field intensity function with a 2D pencil beam scatter kernel. The convolution, evaluated using fast Fourier transformation, is performed at five standard depths only and followed by an interpolation along the fanlines of the beam for the remaining voxels in the dose grid. Moreover, the convolution is conducted under the assumption that the geometry consists of homogeneous water and that the kernel is spatially invariant. Thus, neglecting the effect of the off–axis softening of the beam energy due to the shape of the flattening filter [Ahnesjö and Aspardakis, 1999].

The heterogeneity of the patient or phantom geometry is handled by a modified Batho inhomogeneity correction method [Wong and

Purdy, 1990]. A correction factor is computed for each voxel, taking the electron density of the medium from the CT–scan and tabulated Tissue Maximum Ratio (TMR) data for the beam energy into consideration. Only density variations along the fan lines of the beam are considered, this results in density correction not being applied for positions located laterally from the calculation point. The dose matrix computed in a homogenous water geometry is multiplied by the correction factor–matrix. Furthermore, the modified Batho is invalid for scattered radiation and assumes that all interactions are Compton interactions. This is particularly an issue for higher energy, where Compton interactions become less predominant, as the relative scatter contribution will be overestimated.

THE ANALYTICAL ANISOTROPIC ALGORITHM

The AAA is a pencil beam superposition algorithm, while still using convolution in some situations. The algorithm consists of two steps i: the source model, where the delivered beam is described using a multiple–source model and ii: the patient model where the dose deposition in the patient (or the phantom) is computed.

The source model divides the radiation into three different sources [van Esch et al., 2006]:

PRIMARY SOURCE relates to the primary photons. The primary source is assumed to be a point located at the focal point of the linac target.

EXTRA–FOCAL SOURCE models the photons scattered in the flattening filter, the primary collimator and the collimating jaws.

ELECTRON CONTAMINATION SOURCE considers the electrons originating from the photon interactions occurring in the linac head.

The energy spectrum resulting from each of the sources is computed using Monte Carlo.

The primary photon source is modeled with three fundamental physical parameters: The unattenuated initial photon energy spectra, which is precalculated with MC methods. The mean radial energy, to take into account the beam hardening effect from the flattening filter, how the mean energy of the photon beam decreases with increase distance from the beams central axis. The radial intensity profile takes into account the variation of the photon fluence below the flattening filter across the treatment field.

The extra–focal photon source is modeled as a virtual source with a finite width located at the bottom plane of the flattening filter. This second source is closer to the isocenter and by that produces a broader beam than the primary photon source. It is calculated from the primary fluence. This results in empirically based mean energy and relative

intensity of the extra–focal photon spectrum. The off–axis variation in the spectrum is not modeled.

The electron contamination source models charged particles originating from interactions in the flattening filter, monitor ionization chambers, collimators and air. If accessories, such as MLCs, are employed a large fraction of the contaminating electrons will be observed and the accessory itself will be treated as a source of contaminating electrons. This is modeled with a depth dependent curve that describes laterally integrated electron contamination dose at different depth. Parameters used to characterize the MLC are measurements of the leaf transmission and the effective dosimetric opening between mechanically closed leaf pairs (the dosimetric leaf gap), where the latter parameter takes the effects of the rounded leaf tip into consideration.

In the patient model a diverging coordinate system is defined in order to account for the divergence of the beam. Each voxel is attributed an electron density, which is determined using information of the CT data set. The beam is split into narrow beams (beamlets) with geometrical cross–sections corresponding to the resolution of the dose calculation grid. The resulting dose distribution in the geometry is calculated by superpositioning the dose from primary and secondary photons as well as contaminating electrons for each beamlet.

The pencil beam kernels are computed using MC in a homogeneous water geometry and composed by monoenergetic kernels weighted according to the derived energy spectrum of the treatment beam. The energy deposition from the primary and the extra–focal sources is separated into a depth direction (along the fanline) and a lateral (perpendicular to the fanline) component. In the heterogeneity correction, the depth and lateral components are scaled independently using the inverse relative electron density. This implies that the dose geometry is considered to be made of water with a varying density distribution.

The fluence of the contaminating electrons is modeled as a convolution of the primary fluence and a Gaussian distribution. The dose due to the contaminating electrons is calculated as the convolution of this fluence with a second Gaussian distribution, which is multiplied by a depth dependent function.

The final energy distribution is the accumulated energy distribution of all sources. The energy distribution is converted to a dose distribution by division by the relative electron density distribution.

1.3.3.2 *Monte Carlo dose calculation*

In addition to the analytical dose calculation algorithms, used in current clinical routine, Monte Carlo methods can be applied. MC is based on repeated random sampling using probability distributions. Due to the stochastic nature of interaction of radiation with matter, which can be well described by probability distributions, it is very well

suited for MC simulations. MC applications in radiotherapy in general and for dose calculation in specific is further discussed in Chapter 2.

1.3.4 *The DICOM standard*

Digital Imaging and Communications in Medicine (DICOM) is an international standard for medical digital images and the information related to them. The different components in the radiotherapy treatment chain (e.g. CT, TPS and the linac) all communicate through DICOM files. Moreover, all the information required at any given step of the treatment process can be obtained in the DICOM files.

A DICOM file always contains a header, where all information (imaging parameters, time stamp, patient ID and name etc.) is stored in a standardized structure. If applicable the DICOM file will also contain a 2D or 3D matrix of the element the DICOM file is describing. For this dissertatation there are four classes of DICOM files that are of interest.

CT During a CT scanning a DICOM file is created for each slice. The 2D matrix containing the pixel values are encompassed in the DICOM file along with information related to the scanning procedure, such as scanning modality, the name of the scanner, scanning potential, slice location, slice width etc.

STRUCTURE The information about the delineated structures are stored in a separate DICOM file, which is linked to the CT data set it was delineated on. Each structure is attributed with a name, type of structure and an array of points describing the delineation in the CT data set coordinates.

PLAN The information related to the treatment plan is stored in a separate DICOM file which is linked to the CT data set used during the treatment planning process. The fractionation scheme of the treatment plan along with characteristics of each beam is contained in the DICOM plan file. Moreover, for dynamical delivery modes, each beam is divided into a number of static control points each with settings for the dynamical components and a cumulative MU index, which effectively sets a time scale for the treatment delivery. The control points are utilized as a check point scheme during the treatment delivery. For an IMRT plan the linac control software checks that the actual MLC settings correspond to that of the i^{th} control point when the cumulative MU index of the i^{th} control point has been delivered.

DOSE The 3D dose matrix is stored in a separate DICOM file that also contains information on the coordinates of the dose grid, which typically is more sparse than the CT grid. The file is linked to the DICOM file of the treatment plan it is calculated for.

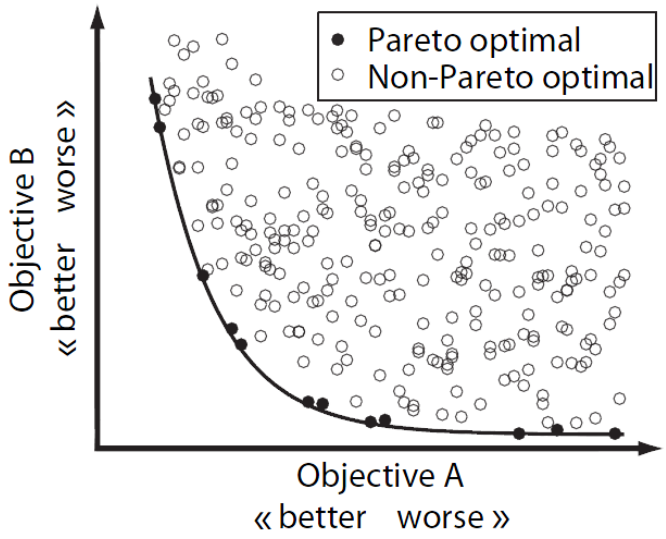

Figure 4: A schematic sketch, illustrating the Pareto concept. For two mutually contradicting objectives, A and B, an endless number of solutions exist. The solutions where one of the objectives can not be improved without detoriating the other are Pareto optimal. All Pareto optimal solutions lie on the Pareto front (represented by the solid line) and are dominating the non-Pareto optimal solutions.

1.3.5 *Pareto Front Comparison*

Even though a treatment plan has been approved for treatment there is no guarantee that it is the optimal plan since the number of possible combinations of parameters is virtually endless. A solution to a problem with mutually contradicting objectives is said to be Pareto optimal when it is not possible to improve one objective without deteriorating at least one of the other. A Pareto front is constituted by the Pareto optimal solutions (Figure 4). The Pareto concept applies well to the inverse planning process, which involves inherently contradictory objectives, high and uniform target dose on one hand, and sparing of surrounding tissue and nearby OAR on the other.

Thieke et al. [2007] demonstrated the usefulness of creating a database of Pareto optimal solutions for interactive treatment plan selection on a case to case basis. Craft and Bortfeld [2008] concluded that $N+1$ treatment plans (where N is the number of objectives) are sufficient to sample the Pareto front. By interpolation of the $N+1$ plans it is possible to construct a number of treatment plans that are close to being Pareto optimal. The treatment plan can then be selected by browsing the Pareto front.

The Pareto front concept can be useful when comparing classes of plans in addition to single plan–to–plan comparisons. Consider the situation where two treatment strategies with different energies or gantry angles are discussed. If a single plan is constructed for each strategy

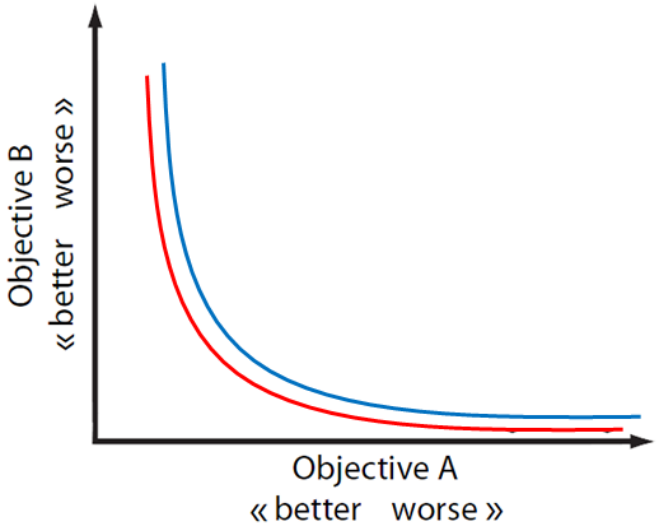

Figure 5: A schematic sketch illustrating the Pareto fronts of two competing strategies (red and blue). As seen the Pareto front representing the red strategy is consistently better in terms of both objectives and is thus superior to the blue strategy.

the comparison will be rather inconclusive. The respective plans may not be optimal or representative for the strategy. By sampling the Pareto front for each strategy the comparison can be conducted using the entire Pareto front. If the Pareto front representing either strategy is consistently more optimal than the other (see Figure 5), clearly that strategy is favorable.

In clinical situations multiple target structures and numerous OARs are usually considered. Thus Pareto surfaces, rather than Pareto fronts needs to be considered.

1.4 DOSIMETRY

The general goal in dosimetry is to determine the absorbed point–dose in a medium, D_{med}, in the absence of the detector. The absorbed dose in a medium, D_{med}, is related to the photon energy fluence in the medium, $h\nu\Phi_{med}$, by

$$D_{med} \overset{CPE}{=} h\nu\Phi_{med} \left(\frac{\mu_{en}}{\rho}\right)_{med} \tag{1.1}$$

where $h\nu$ is the photon energy and (μ_{en}/ρ) is the mass–energy absorption coefficient of the medium in question. It should be stressed that equation 1.1 is valid only under Charged Particle Equilibrium (CPE) conditions.

Correspondingly, D_{med} may be related to the charged particle fluence in the medium by

$$D_{med} \overset{\delta\text{–eq}}{=} \Phi^{e^-}_{med} \left(\frac{S_{col}}{\rho} \right)_{med} \tag{1.2}$$

where (S_{col}/ρ) is the unrestricted electron mass collision stopping power of the medium in question. Equation 1.2 is valid only under δ–ray equilibrium (equilibrium in terms of secondary charged particles).

1.4.1 *Cavity Theory*

Excellent texts on the fundamentals of cavity theory have been published on multiple occasions. Section 1.4.1 covers the basics needed in later sections of this dissertatation. A much more extensive review, written by Nahum, of the field can be found in chapter 3 of [Rogers and Cygler, 2009].

The goal of any dosimetric exercise is to determine the absorbed point–dose in a medium, D_{med}, in the absence of the detector. The set up can be thought of as a homogeneous medium to which we introduce a detector of a different medium. For historical reason we shall call the detector a cavity, although the theory presented holds true also for non–cavity–like media. *Cavity theory* gives us an expression that relates the dose to the detector to that of the undisturbed system.

$$f(Q) = \left(\frac{D_{med}}{D_{det}} \right)_Q \tag{1.3}$$

for the radiation quality Q.

In two special cases it is possible to derive exact expressions for f(Q): (i) for large photon detectors in a photon field where there is CPE and assuming that the perturbation inferred by the detector is negligible and (ii) for Bragg–Gray cavities.

1.4.1.1 *Large photon detectors*

In order for a detector to be able to be treated as a large photon detector the photon attenuation within the detector must be negligible and the dimension of the sensitive material of the detector must be large in comparison to the ranges of the secondary electrons, so that CPE is established within the detector. With these conditions fulfilled the dose at a point can be calculated through

$$D_{med} \overset{CPE}{=} \Psi_{med} \left(\frac{\mu_{en}}{\rho} \right)_{med} \tag{1.4}$$

where Ψ_{med} is the energy fluence at the point of interest. Equation 1.4 applies analogously to a the situation where a detector is placed

at the point of interest. Providing that the introduction of a detector infers negligible changes on Ψ_{med}, f(Q) is given by

$$f(Q) = \frac{D_{med}}{\overline{D}_{det}} = \left(\frac{\overline{\mu_{en}}}{\rho}\right)^{med}_{det} \tag{1.5}$$

where the bar over D_{det} indicates that we are considering the average signal to a finite size detector with its effective point of measurement at the point of interest. As we in RT are concerned with a bremsstrahlung spectrum as oppose to monoenergetic beams, equation 1.5 is written as

$$\left(\frac{\overline{\mu_{en}}}{\rho}\right)^{med}_{det} = \frac{\int_0^{E_{max}} E_{h\nu} \frac{d\Phi_{med}}{dE} \left(\frac{\mu_{en}(E)}{\rho}\right)_{med} dE}{\int_0^{E_{max}} E_{h\nu} \frac{d\Phi_{med}}{dE} \left(\frac{\mu_{en}(E)}{\rho}\right)_{det} dE} \tag{1.6}$$

where $(d\Phi_{med}/dE)$ is the energy differential photon fluence.

1.4.1.2 *Bragg–Gray Cavity Detectors*

A detector may be considered as a Bragg–Gray cavity if the following two prerequisites are fulfilled:

- The cavity must not disturb the charged particle fluence (including its distribution in energy) existing in the medium in absence of the cavity.
- The absorbed dose in the cavity is deposited entirely by the charged particle crossing it.

The first prerequisite can be fulfilled in two ways: (i) when the interaction properties of the detector and the medium are identical for the radiation quality, Q, in question or (ii) if the cavity is small compared to the electron ranges. In the case of MV photon beams, as used in radiotherapy, this is only fulfilled for gas filled detectors, i.e. ionization chambers.

The ratio of dose to the undisturbed medium and dose to the detector may be written as

$$\frac{D_{med}}{\overline{D}_{gas}} = \frac{\Phi^{e^-}_{med} (S_{col}/\rho)_{med}}{\Phi^{e^-}_{gas} (S_{col}/\rho)_{gas}} \tag{1.7}$$

Given that the detector is a Bragg–Gray cavity, the electron fluencies are identical and the dose ration, f(Q) then becomes

$$\frac{D_{med}}{\overline{D}_{gas}} = \left(\frac{\overline{S_{col}}}{\rho}\right)^{med}_{gas} \tag{1.8}$$

which is known as the mass (collision) Stopping Power Ratio (SPR). Just as for photons, the general case is a fluence spectrum as oppose

to monoenergetic electrons. Therefore the SPR must be evaluated as an integral over the electron fluence spectrum, this corresponds to rewriting equation 1.8 as

$$\left(\frac{\overline{S_{col}}}{\rho}\right)_{gas}^{med} \overset{\delta\text{--eq}}{=} \frac{\int_0^{E_{max}} \left(\Phi_E^{e^-}\right)_{med} (S_{col}(E)/\rho)_{med}\, dE}{\int_0^{E_{max}} \left(\Phi_E^{e^-}\right)_{med} (S_{col}(E)/\rho)_{gas}\, dE} \tag{1.9}$$

The electron fluence considered in equation 1.9 must be that of primary electrons only, as all other generations of charged particles, δ–rays, are accounted for in the collision stopping power.

Equation 1.9 is only valid under δ–ray equilibrium. In short, one can assume that δ–ray equilibrium only can exist if the mean excitation energies of the detector material and the medium are identical or very close.

A modification of the Bragg–Gray theory was published by Spencer and Attix [1955], in which identical electron fluencies only is required in the range [Δ,$E_m ax$] but not below. The formalism consider all generations of charged particles entering the cavity and is considers weather the incoming particle has enough energy to cross the cavity or not. Only incoming electrons with energy larger than a cutoff energy Δ, derived from the size of the cavity and the charged particle range, are considered and energy losses less than Δ are assumed to remain in the medium they are generated. With this equation 1.9 may be written as

$$\left(\frac{\overline{L_\Delta}}{\rho}\right)_{gas}^{med} = \frac{\int_\Delta^{E_{max}} \left(\Phi_E^{tot}\right)_{med} [L_\Delta(E)/\rho]_{med}\, dE}{\int_\Delta^{E_{max}} \left(\Phi_E^{tot}\right)_{med} [L_\Delta(E)/\rho]_{gas}\, dE} \tag{1.10}$$

where $[L_\Delta/\rho]$ is the restricted SPR. It should be noted that the lower limit of the integrals is Δ as oppose to o in equation 1.9. The interpretation of this is that energy depositions between o and Δ are left unaccounted for. This is rectified by including a "track end" term: $\Phi_E^{tot}(\Delta)\,[S_{col}(\Delta)/\rho]\,\Delta$. The absorbed point–dose in a medium, f(Q), can then be written as

$$\left(\frac{\overline{L_\Delta}}{\rho}\right)_{gas}^{med} = \frac{\int_\Delta^{E_{max}} \left(\Phi_E^{tot}\right)_{med} [L_\Delta(E)/\rho]_{med}\, dE + \Phi_E^{tot}(\Delta)\,[S_{col}(\Delta)/\rho]_{med}\,\Delta}{\int_\Delta^{E_{max}} \left(\Phi_E^{tot}\right)_{med} [L_\Delta(E)/\rho]_{gas}\, dE + \Phi_E^{tot}(\Delta)\,[S_{col}(\Delta)/\rho]_{gas}\,\Delta} \tag{1.11}$$

1.4.1.3 *General Cavity Theory*

For cases where the detector size can be treated as neither as large nor small compared to the range of electrons no exact expression for

f(Q) can be derived. If neither small nor large, the detector size may be thought of as intermediate. Hence, a weighted average between the two exact expressions may be used as an approximation. The "General cavity theory" was suggested by Burlin [1966], therefore detectors that fall into this category can be referred to as *Burlin Cavities*. The approximate expression for f(Q) may then be written as [Attix, 1986]

$$\frac{\overline{D_{det}}}{D_{med}} = d\left(\frac{\overline{L_\Delta}}{\rho}\right)_{med}^{det} + (1-d)\left(\frac{\overline{\mu_{en}}}{\rho}\right)_{med}^{det} \tag{1.12}$$

where d is a weighting factor whose value depends on the size of the detector compared to the range of electrons as well as the radiation quality.

In the case of megavoltage photon beams all solid–state detectors are classified as Burlin detectors. As oppose to using analytical expressions to solve f(Q) for Burlin detectors Monte Carlo techniques can readily be applied [Rogers, 2006].

1.4.2 *Detectors*

There are numerous types of detectors, each with specific benefits and intended situations of usage. A number of requirements needs to be considered when choosing a detector type.

STABILITY The measurement result from a detector should be highly reproducible, preferably over a high dose range as well as over a long period of time.

DOSE LINEARITY The response of the detector should ideally be linear over a the dose range of interest.

DOSE RATE INDEPENDENCE As the dose rate of a linac can be varied, the detector should be insensitive to changes in dose rate.

ENERGY RESPONSE As dose generally is measured as dose–to–water, the ideal detector should be totally water equivalent. A water equivalent detector would not suffer from variations in stopping power ratios or mass energy absorption coefficient ratios with energy variation. Moreover the signal should be proportional to the absorbed dose regardless of energy. Many solid–state detectors are susceptible to ionization density effects, dose–rate effects etc.

SPATIAL RESOLUTION The detector should have a spatial resolution high enough to resolve gradients in the dose distribution. However, reduction of detector volume inevitably leads to a reduction of signal–to–noise ratio and in increased uncertainty.

ORIENTATION The response of the detector should ideally not be affected by the influence angle of the radiation. This is of particular importance when considering VMAT, where the linac gantry rotates about the detector during measurements.

PERTURBATION Unless the detector consists of water it will perturb the photon fluence. This is particularly important for small fields where the detector volume becomes relatively large compared to the field size. Apart from the detector itself, cables will also perturb the photon fluence.

The types of detectors utilized in this study will here be briefly described.

1.4.2.1 *Air Filled Ion Chambers*

The air filled ionization chamber, commonly simply referred to as an ionization chamber, has been the back bone of radiotherapy dosimetry since its introduction. An Ionization Chamber (IC) typically consists of an air-filled cavity and a central electrode, and is connected to an electrometer via a coaxial cable. The air in the sensitive volume of the detector is ionized by the incident radiation. The central electrode collects the generated ions, which produces a measurable current. The ionization current, which is measured using an electrometer, is proportional to the dose absorbed in the chamber volume.

The sensitive volume of an ionization chamber is typically too large to resolve high dose gradients. Moreover, the signal–to–noise ratio is low in comparison with other detector types. Since the active material in the detector is air, the detector is highly energy dependent, but precise correction factors are available.

The estimated relative uncertainty on measured dose to water at reference conditions, using an ionization chamber, is approximately 1.5% [Andreo et al., 2000].

1.4.2.2 *Diodes*

Diodes are an alternative to ionization chambers in many situations. The diodes are doped semiconductors, in which ionization leads to electron–hole pairs which induces a measurable current in the p–n junction of the sensitive volume. Diodes are more sensitive than ionization chambers and typically have higher spatial resolution. However, the sensitivity of diodes depend on temperature, dose rate and irradiation angle, and therefore corresponding correction factors must be applied. Moreover, diodes are highly energy dependent and typically only calibrated to a single nominal beam energy and under CPE conditions. This may infer complications as the energy spectrum varies slightly with off–axis distance and substantially when CPE no longer is fulfilled.

1.4.2.3 *Alanine/EPR*

Alanine is an amino acid that produces free radicals when exposed to irradiation. The amount of free radicals is proportional to the absorbed dose and can be measured using Electron Paramagnetic Resonance (EPR) [Bradshaw et al., 1962; Regulla and Deffner, 1982]. Using a binder material, alanine can be pressed into dosimeter of any size and shape. Typically cylindrical pellets of (ø5×3 mm) are used. The alanine dosimeters are close to water equivalent and thus only slightly energy dependent. The non–destructive read out procedure and low fading are desirable characteristics of alanine dosimeters [Anton, 2005, 2006]. Moreover alanine dosimetry does not require any wires or cables and thus the only perturbation of the particle fluence is that of the detector.

The sensitivity of alanine is low and in order to achieve reasonable measurement precision the pellets must be irradiated to doses in the region of 10 Gy. The read out procedure of alanine by EPR spectroscopy is complex and requires dedicated equipment [Helt-Hansen et al., 2009]. Furthermore, alanine is hydrophobic which yields practical limitations in measurements in liquid water. Therefore alanine is more suitable for measurements in solid phantoms.

EPR dosimetry is not limited to using alanine. Lithium Formate monohydrate (LiF) is a particularly promising substance. Compared to alanine it exhibits higher sensitivity than alanine [Lund et al., 2003; Vestad et al., 2004] and equally limited energy dependence for clinical MV photon beams [Waldeland and Malinen, 2011]. LiF is however neither as well documented as alanine nor as easily available.

1.4.2.4 *Radiochromic film*

A Radiochromic film is a thin (≈300 µm) layer of plastic material with a radiosensitive dye material (the active layer is ≈30 µm thick). When exposed to radiation the radiosensitive layer undergoes a polymerization process that changes the optical density. The change in optical density is proportional to the absorbed dose for doses in the cGy to Gy range. The radiation–induced change in optical density is self–developing and is established a couple of hours post irradiation. The film is typically read out using a commercial flatbed scanner. Ferreira et al. [2009] found that the optimal scanning resolution for a Gafchromic EBT film (International Specialty Products, NJ, USA) was 75 dpi, which corresponds to a resolution of ≈0.35 mm. Thus, radiochromic film is a suitable detector alternative in situations where apparent dose gradients exist. Moreover, the plastic material of radiochromic film is considered near–tissue equivalent and is therefore only moderately energy dependent.

The accuracy of radiochromic film has been reported to lie within 2–3% [Devic et al., 2005; Mack et al., 2003; McLaughlin et al., 1994].

Hartmann et al. [2010] reported that due to manufactoring inhomogeneities the uncertainty may increase to 8.7% for Gafchromic EBT2 film.

2 MONTE CARLO METHODS IN RADIOTHERAPY

A Monte Carlo method consists of representing the solution of a problem as a parameter of a hypothetical population, and using a random sequence of numbers to construct a sample of the population, from which statistical estimates of the parameter can be obtained.

— JOHN H. HALTON *Halton [1970]*

The above quote is one of many definitions of Monte Carlo methods. The interpretation of the definition is that MC is an analytical technique in which a large number of simulations are run using random quantities for uncertain variables and looking at the distribution of results to infer which values are most likely. With this it is easy to see that MC applies well to particle transport, where interaction cross sections can be parameterized. Thus, MC is a useful method for dose calculation in radiotherapy. In fact, it is the most accurate method available [Andreo, 1991; Chetty et al., 2007; Reynaert et al., 2007; Rogers et al., 1995].

Numerous MC codes for particle transport in matter have been developed and a variety are used for Monte Carlo simulations of radiotherapy. The MC codes discussed in this work can be divided into two classes: general purpose codes and MC dose engines for MCTP.

2.1 GENERAL PURPOSE MONTE CARLO CODES

The general purpose Monte Carlo codes commonly used in radiotherapy include EGSnrc, EGS4, GEANT4, PENELOPE and MCNP. The particle transport is conducted in similar fashion for all of the codes. Consider a particle obtained from a source, the characteristics of the primary particle and how it is generated is not of concern at this point, with a certain energy and direction. A random number is drawn in order to determine a distance to the next particle interaction, which will depend on the type of particle, its energy and the medium in which the particle is located. The particle is transported along its direction for a distance determined by the random number drawn. A new random number is drawn in order to determine the type of interaction the particle should undergo using a cross section database. The type of interaction will again depend on the type of particle, its energy and the medium in which the interaction takes place. Depending on the type of interaction, the particle may change its direction and/or energy, moreover new particles may be generated as a consequence of

the interaction. This is again determined by drawing random numbers and using a cross section data base. This process is repeated until the primary particle either reaches a predetermined cut–off energy (see Section 2.3) or leaves the boundaries of the system. The process is then conducted for all secondary particles, which in turn may give rise to additional particles, created along its path. A new primary particle is subsequently drawn from the source and the same procedure is repeated.

The mean free path of MV photons in a tissue–like medium is on the order of decimeters, thus relatively few photon interactions occur within a typical simulation geometry. Therefore it is reasonable to treat each photon and interaction individually.

For charged particles, however, as a slowing–down process of a single electron can encompass hundreds of thousands of interactions. To treat each interaction individually would be extremely time consuming and is not a reasonable approach. A condensed history technique [Berger, 1993] is utilized, in which a large number of interactions are condensed and considered in a single electron step. This is a feasible approximation since the majority of the charged particle interactions result in small energy losses and minor directional changes. The energy losses, directional and positional changes of the electron are sampled from multiple scatter distributions.

The energy deposition events are kept track of over the course of the simulation and converted to absorbed dose by dividing the accumulated deposited energy in all defined regions with their respective masses.

The general purpose MC codes of choice for this study were EGS4 (electron gamma shower) [Nelson et al., 1985] and EGSnrc [Kawrakow and Rogers, 2012] (developed by the Canadian national research council, hence the nrc). As indicated by the names they simulate particle transport of electrons (and positrons) and photons, but disregards other particles such as neutrons and protons. EGSnrc may be considered as a continued development of EGS4 and as such the two systems share many properties. The major new features of EGSnrc in terms of particle transport properties include a new electron transport algorithm, EXACT, in which electrons are transported in single elastic scattering mode when they are within a user–defined distance from a region boundary [Kawrakow, 2000*a*]. The EGSnrc system has been benchmarked against EGS4 for a range of situations relevant to radiotherapy. Although the results are generally in agreement, the small differences found are attributed to the improvements made to EGSnrc in general and the multiple scattering theory [Walters et al., 2012].

2.2 SPECIFIC PURPOSE MONTE CARLO CODES

In addition to the general purpose MC codes, user codes dedicated to addressing specific situations have been developed. This section discusses the specific purpose MC codes used throughout this study. Commonly for all of the specific purpose MC codes are that they have been developed as add–ons to a general purpose MC codes. In short this means that the particle transport is handled by the general purpose MC code, and that the specific purpose MC codes is used an "interface" in which the geometry and parameters necessary for the particle transport are defined.

2.2.1 *BEAMnrc*

BEAMnrc is an add–on to EGSnrc, which handles the actual particle transport. BEAMnrc was developed as a user code intended to simulate a medical linear accelerator. A number of Component Modules (CMs), each intended to model a specific component in a medical linear accelerator (i.e. flattening filter, monitor chamber etc.), are available. A model of the linear accelerator is constructed by stacking CMs along the beam direction. The input file consists of a text file in which the geometrical properties of each CM is defined along with a number of parameters defining the primary particle source, the scoring plane, particle transport parameters and variance reduction parameters (see Section 2.3).

A number of different source routines are available, each with its own characteristics and required input parameters. Throughout this study two different source routines are used in BEAMnrc. The characteristics and input parameters of these source routines are described below.

SOURCE 19 models an elliptical beam with Gaussian distributions, with user–defined Full Width Half Maximum (FWHM), in X and Y. The type of particles[1] incident on the first CM and their energy needs to be defined in the input file. The particles may be monoenergetic or defined by an energy spectrum. Furthermore, the direction of the incident particles is defined by a set of parameters and an optional angular spread about the Z–axis (the beam direction) may be defined.

SOURCE 21 utilizes a phase space file as a source. The required source parameters include a path to the phase space file in question, the charge of the particles to be considered and which CM, in the simulation geometry, the particles are incident on.

1 electrons, photons or positrons

At each user–defined scoring plane, which can be located at the bottom of any CM, a phase space file may be generated as a result of the simulation. Coarsely described, a phase space file is a list of the particles crossing the scoring plane and their characteristics[2]. The characteristics recorded in the phase space file are particle charge, position (X and Y) in the scoring plane, direction and the particle weight. The transport history of the particle is also recorded, which allows the code to calculate the dose contribution from user defined region.

A file (.egslst) listing a summary of the simulation parameters, warning messages if any, dose and fluence results of the simulation. Furthermore the dose and deposited energy in all user defined dose scoring zones are listed.

2.2.2 *DOSXYZnrc*

The MC user code DOSXYZnrc simulates dose in a Cartesian voxalized geometry (e.g. a phantom or a patient). The input file consists of a text file in which the particle source, the geometry and variance reduction parameters are defined. The geometry may be defined implicitly in the input file or explicitly by pointing to a predefined phantom file. Each voxel is assigned a density and medium. The actual particle transport is handled by EGSnrc.

A number of different source routines are available, each with its own characteristics and required input parameters. The characteristics and input parameters of the source routines used in this study are described below.

SOURCE 2 utilizes a full phase space file as a particle source. The required parameters include a path to the phase space file, which types of particle that are to be considered, the location of the iso center, the distance between the iso center and the scoring plane and angles defining the direction of incidence on the geometry.

SOURCE 9 refers to a BEAMnrc simulation which is runs concurrently with the DOSXYZnrc simulation. An analogy to source 2 can be made as the particles are sampled from the scoring plane of the BEAMnrc simulation. With this the need for intermediate phase space files is eliminated. The required input parameters of source 9 are consistent with those of source 2, but with a path to a BEAMnrc simulation rather than a phase space file.

SOURCE 20 uses a phase space source as input but allows for continuously variation of the incident angles. This is realized by

2 The IAEA phase-space database for external beam radiotherapy (url: http://www-nds.iaea.org/phsp/phsp.htmlx) features downloadable phase space files for various linacs.

listing a number of settings, each with its own parameters of the location of the iso center, the distance between the iso center and the scoring plane and angles defining the direction of incidence on the geometry. Each setting is attributed with an acummulated index, ranging from 0 to 1. For each incident particle a random number, between 0 and 1, is drawn and used to decide the source parameters. Moreover, an external MC code simulating the MLC may be encompassed in the DOSXYZnrc simulation.

SOURCE 21 is related to source 20 analogously to the relation between source 9 and source 2. This means that the treatment head may be simulated concurrently using BEAMnrc with the incidence parameters changing during the simulation as for source 20.

The main output of a DOSXYZnrc simulation is a 3ddose file, which lists the dose and the relative statistical uncertainty for each voxel defined in the simulation geometry. For the sources discussed, the dose is given in Gy per incident particle[3]. For the full BEAMnrc simulation source (i.e. sources 9 and 21), doses are normalized by the number of primary histories incident in the BEAMnrc simulation. Since the BEAMnrc simulation is being run concurrently with DOSXYZnrc, the exact number of primary histories is known. For phase space sources (i.e. source 2 and 20) the quantity is estimated [Rogers et al., 2009]. The statistical uncertainty is estimated using a history by history method [Walters et al., 2002] in which the uncertainty of the dose is estimated by grouping all energy depositions originating from the same primary particle rather than using the variance of individual events. The method takes the latent variance of a phase space file into account, which means that the uncertainty introduced by statistical variations in the phase space file itself is accounted for.

2.2.3 *DOSRZnrc*

DOSRZnrc is another EGSnrc–based user code developed to score dose in an user–defined geometry. It differs from DOSXYZnrc in that the geometry is cylindrical, where each element is defined by a thickness, an inner and an outer radius. As in DOSXYZnrc each element is assigned a density and a medium. A number of different source routines are available each with its own characteristics and required input parameters. The characteristics and input parameters of the source routines used in this study are described below.

SOURCE 0 describes a parallel beam incident on the top of the described geometry. The required parameters are the particle type and energy (this may be an energy distribution or mono en-

3 This refers to the primary particles in the BEAMnrc simulation

Table 1: The energy deposition categories of SPRRZnrc

Category	Description
α	Energy deposition events from electrons for a step with the energy entirely above Δ (a cutoff energy below which energy losses are assumed to remain in the medium they are generated).
β	Events formed by electrons and photons which are created with their energy initially below the cut off energies of the simulation.
δ	The energy deposition events in which a particle (electrons and photons) starts with its energy greater than cut off energy of the simulation and ends with an energy below.
γ	The energy deposition events in which an electron starts a step with its energy greater than Δ and ends with an energy below Δ.

ergetic) as well as the radius and the direction of the parallel beam.

SOURCE 22 utilizes a full phase space file as a particle source and is analogous to source 2 of DOSXYZnrc.

The resulting dose and uncertainty estimation are computed using the same procedures as for DOSXYZnrc. For source 0, however, the dose is normalized to the incident particle fluence as no phase space is used.

2.2.4 *SPRRZnrc*

The EGSnrc–based user code SPRRZnrc was developed in order to simulate Spencer–Attix restricted mass collision stopping–power ratios. The simulation is conducted for a cylindrical geometry, which is defined just as for DOSRZnrc. The SPR are computed by scoring the dose deposited in the medium and the cavity, see Section 1.4.1 and Equation 1.11, but for a simulation in which the cavity is filled with the transport medium rather than the detector medium. The energy deposition in the detector medium is then computed by multiplying the energy deposited in the transport medium, at the location of the cavity, with stopping power ratios. Whether restricted or unrestricted stopping power ratios and at what energy they are considered depends on the type of energy deposition events. SPRRZnrc divides the energy deposition events into four categories; α, β, δ and γ each described in Table 1.

For the α events, restricted stopping powers at the mid point energy of the particle step are used. The β particles are not considered in the SPR computation as they would deposit their energy locally regardless

of medium and thus cancel in the computation of ratios. For the δ events, which are not β events, the unrestricted stopping powers at Δ, the cutoff energy below which energy losses are assumed to remain in the medium they are generated (see Section 1.4.1) are used. The γ event are divided into two components. The component with energy above Δ are treated as an α event, while the part of the energy deposited below Δ is treated as it were an δ event. The stopping power ratios are then computed as the ratio of accumulated dose to the cavity voxel occupied by the transport medium and the estimated dose to the detector medium.

2.2.5 *particle Dmlc*

The particle Dmlc is a stand alone MC user code intended for fast, while still accurate, simulation of MLCs [Keall et al., 2001; Siebers et al., 2002]. Incident particles are read from a phase space file, this is typically a simulation of the part of the linac head located above the MLC, transported through the MLC and written to a phase space file below the MLC.

The particle transportation through the MLC is simplified. The MLC is divided into a number of regions along the beam direction. The weight of the particles are modified by considering the amount of material the particle transverses when being transported through a region. Electrons encountering any MLC material are assumed to be absorbed, while for photons attenuation and Compton scattering (first generation only) is considered.

Although the particle transportation is simplified and includes approximations, the geometry of the MLC is accurately modeled, which results in the method accounting for the intraleaf thickness variations, interleaf leakage, MLC leaf end effects and tongue and groove.

The method has been benchmarked against measurements for MLC apertures with high modulation [Siebers et al., 2002].

2.2.6 *MCSIM*

MCSIM is a MC user code developed for radiotherapy treatment verification studies and dose calculation. MCSIM is in many ways similar to DOSXYZnrc in that it calculates dose to a Cartesian voxalized geometry in which each element is assigned a density and a medium. The particle transport of MCSIM is handled by EGS4, which is one of the distinct differences between MCSIM and DOSXYZnrc. Another distinct difference is that beam modifiers, such as collimators and MLC, are included in the patient simulation. Full particle transport is performed for the collimating jaws, whereas the MLCs are simulated by modifying the particle weights using an intensity distribution derived

from an MLC sequence file [Pawlicki and Ma, 2001]. The intensity maps are generated by accumulating the MUs for all unblocked areas and a transmission fraction of the MUs for blocked areas. The fraction is determined by taking a set of parameters for MLC inter– and intra–leaf transmission, which are defined in the input file, into account. The transmission factor for areas wich are blocked by the jaw collimators is set to zero. In this approach, beam hardening due to attenuation of low energy photons in the MLC, and scatter from the MLC leafs are ignored. Moreover, the MLC geometry is simplified and each leaf is approximated by a rectangular slab, which effectively means that MLC leaf end effects and tongue and groove are not considered.

2.3 VARIANCE REDUCTION TECHNIQUES

Simulation of particle transport in matter requires a large number of computations and is therefore time consuming. In order to reduce the time, while not compromising statistical accuracy, numerous variance reduction techniques have been implemented. The following text is limited to discussing only the variance reduction techniques explicitly employed throughout this study. Some of the variance reduction techniques may not be applicable to all MC user codes.

Cutoff energy

The energy below which particles transport is terminated is called the cutoff energy. Any particles falling below that energy deposits all of its remaining energy locally. Different cutoff energies may be attributed to photons and electrons and to different regions of the simulation geometry. The cutoff energy for electrons highly influences the simulation time, since electrons undergo many interactions with small energy losses. The general rule of thumb is to choose the Electron CUT-off energy (ECUT) corresponding to less than a third of the range[4] of the smallest dimension in the scoring geometry. The Photon CUT-off energy (PCUT) does not influence the simulation time to the same degree, therefore a low value, typically 10 keV, may be chosen for photons.

Range Rejection

An efficient variance reduction technique for charged particles is range rejection. An energy, ECUTRR, which charged particles needs to exceed in order to be able to leave the current region is defined. Different values for ECUTRR may be chosen for each region. The range

4 The continuous slowing down approximation range is typically used since it is easily calculated while still a very close approximation to the average path length traveled by a charged particle.

corresponding to ECUTRR is determined using restricted stopping power ratios and, thus, correspond to the the longest possible range. Range rejection is available for BEAMnrc only.

Bremsstrahlung Splitting

Bremsstrahlung splitting may be conducted for photons in BEAMnrc. Two different types of splittings are used; Uniform Bremsstrahlung Splitting (UBS) and Directional Bremsstrahlung Splitting (DBS).

UBS

When an electron undergoes a bremsstrahlung event, instead of producing only one photon, NBRSPL (the splitting number) photons are generated each with a weight of $\frac{1}{\text{NBRSPL}}$ times the weight of the electron. The characteristics of the each photon, energy and direction, are sampled individually. The energy of the electron, however, is determined by one of the bremsstrahlung interactions. This means that the energy is not conserved for a given bremsstrahlung event, but for a large number of histories the energy is conserved on average. This approach is implemented in order to preserve the effect of energy straggling.

DBS

Just as for UBS, bremsstrahlung events generate NBRSPL photons each with a weight of $\frac{1}{\text{NBRSPL}}$ times the weight of the electron. For DBS, photons aimed inside a user defined splitting field (which is defined at radius at a given plane, typically the iso center plane) are continued while photons aimed outside the splitting field undergo Russian Roulette with a "survival threshold" of $\frac{1}{\text{NBRSPL}}$. The weight of the surviving photons are multiplied by NBRSPL. The photons surviving the Russian Roulette are called fat photons. Should a fat photon undergo a Compton event generating a charged particle, it is considered a fat charged particle.

While employing DBS only a limited number of charged particle reach the scoring plane. This is due to all Compton interactions undergoing Russian Roulette, with a survival ratio of $\frac{1}{\text{NBRSPL}}$ and playing Russian Roulette on "non–fat" photons before they are allowed to undergo pair production, Compton events or photoelectric effect. Thus charged particles reaching the scoring plane will be fat charged particles, unless they are are generated just above the splitting field.

In order to improve on the charged particle statistics, a splitting plane for charged particles may be defined inside a given CM. When crossing the defined plane, all fat charged particles are split NBRSPL times (and their weights are multiplied by $\frac{1}{\text{NBRSPL}}$). A "Russian Roulette plane" is placed above the charged particle splitting plane. Below this Russian Roulette plane the DBS characteristics are relaxed:

Electrons generated through "non–fat" photons undergoing Compton interaction are no longer subjected to Russian Roulette. "Non–fat" photons undergo pair production, photoelectric and Compton events without Russian Roulette. Moreover, fat photons pair production and photoelectric effect interactions result in the generation of 2×NBRSPL and NBRSPL non–fat charged particles, respectively.

Photon and electron splitting

Photon splitting may be employed in DOSXYZnrc and in MCSIM. Each photon incident on the scoring geometry is split `n_split` times and given a wight of $\frac{1}{\texttt{n\_split}}$ times the weight of the original photon. The mean free path to the next iteration is determined individually for each split photon. At the following interaction site each secondary photon undergo Russian Roulette, with a survival ratio of $\frac{1}{\texttt{n\_split}}$ and the survivors having their wight multiplied by `n_split`. Charged particles generated through interactions are allowed to survive, but have their wight reduced by a factor of `n_split`. Should the charged particles undergo bremsstrahlung or annihilation events the generated photons undergo Russian Roulette (with a survival ratio of $\frac{1}{\texttt{n\_split}}$). The surviving photons have their wight increased by `n_split`. Thus, the photons have a weight equal to the incident photon and are subjected to photon splitting again.

A phase space file of a linac consists of relatively few electrons compared to photons. When employing photon splitting, the contaminating electrons will be few but have a high weight factor, compared to the split photons. This might lead to the dose in the build up region being too highly influenced by the electrons. In order to compensate for this the particle splitting may be conducted for the charged particles as well. It is recommended to employ the same splitting factor for electrons, e_split as for photons [Rogers et al., 2009].

Howfarless

When simulating homogeneous geometries in DOSXYZnrc, a variance reduction technique called howfarless may be employed. If so, only the outer boundary of the geometry is considered when calculating the distance along the particle trajectory to the next region boundary and the perpendicular distance to the nearest region boundary respectively. Charged particle trajectories are approximated by two straight line steps joined at a hinge point. It is imperative to disengage howfarless for simulation of heterogeneous geometries.

3

COMMISSIONING OF THE MONTE CARLO LINAC MODEL

In order to ensure that a Monte Carlo linac model accurately predicts dose in any given circumstance it must be calibrated and validated for a range of critical situations. The process of calibration and validating is what here is referred to as commissioning. This purpose of this chapter is to describe the commissioning of a Varian 2300iX linear accelerator at Copenhagen University Hospital, Herlev but the process could in principle be applied to any linac. The underlaying issue with commissioning of an MC model of a linac is that the exact geometry generally is not known and impracticle to measure directly. Moreover, the characteristics of the electrons impinging on the linac target are also unknown.

The first issue encountered is how to define what to verify. Chetty et al. [2007] states that a MC dose calculation engine will benefit from a verification procedure similar to a conventional TPS. Chetty et al. [2007] therefore recommend that the commissioning procedure should follow the guidelines, with regards to the dose calculation, presented in the American Association of Physicists in Medicine (AAPM) TG–53 report [Fraass et al., 1998]. A verification scheme covering the range of clinical usage is advised. Specifically, comparison with measurements should be conducted for open (square, rectangular and asymmetrical) as well as blocked fields (wedge and MLC). Comparisons should be conducted along the Central AXis (CAX) as well as in the transverse plane. Moreover, relative as well as absolute agreement with measurements should be investigated.

For an MC model, the initial step is however to build the geometry. A linac vendor will typically provide details on the main component of the linac treatment head. There is no practical way to experimentally determine the validity of these details and therefore they are considered as ground truth. An initial estimate of the parameters of the particle impinging on the linac target may or may not be provided by the vendor. The commissioning procedure is then reduced to finding a set of parameters of the impinging particles that results in dose distributions agreeing with measured dose distributions, within a given accuracy. This raises the question of what parameters that should be tweaked, how they influence the resulting dose distribution and most importantly, how to determine their values.

There are many studies devoted to the commissioning/verification MC linac models and many different strategies are suggested in the literature [Bush et al., 2009; Chibani et al., 2011; De Smedt et al., 2005;

Deng et al., 2000; Ding, 2002, 2003; Fix et al., 2001; Hartmann Siantar et al., 2001; Künzler et al., 2009; Lewis et al., 1999; Libby et al., 1999; Lovelock et al., 1995; Ma and Jiang, 1999; Ma et al., 1999; Mesbahi et al., 2005; Mohan et al., 1985; Rogers et al., 1995; Schach von Wittenau et al., 1999; Sempau et al., 2001; Sheikh-Baghei and Rogers, 2002; Sheikh-Bagheri et al., 2000; Siebers et al., 1999; Verhaegen and Seuntjens, 2003]. The common denominator of all studies is that a measurable quantity is compared to the simulated one. The initial guess on, for example, mean impinging electron energy and focal spot size is tweaked until agreement, within an acceptance criteria, is found. The agreement is typically quantified using a statistical measure (e.g. γ–analysis or χ^2–test). Typically the fit is made by tuning the mean energy and the spatial distribution of the electrons impinging on the target. Some studies also include the angular spread of the electrons (e.g. [Bush et al., 2009; Chibani et al., 2011]) and the target density [Keall et al., 2003].

A review of existing relevant literature is initially presented below and followed by a sensitivity analysis of the characteristics of the electrons impinging on the linac target. A protocol for calibration of an MC model representing a Varian 2300iX linear accelerator, but in principle applicable to any linac type, is presented, using the BEAMnrc [Rogers et al., 2009] MC code. Finally, the validity of the calibrated model is verified over a wide range of situations.

3.1 REVIEW OF LITERATURE

Keall et al. [2003] describe the commissioning process of a Varian 21EX accelerator (Varian Oncology Systems, Palo Alto, CA, USA) in which a number of assumptions on the initial electron fluence are made. The following section revisits and revises the assumptions made by Keall et al. [2003].

The distribution of the electrons impinging on the bremsstrahlung target, Ψ, can be described by a five dimensional function

$$\Psi(E, x, y, \theta, \phi), \tag{3.1}$$

where E is the kinetic energy, x and y are the lateral positions and θ and ϕ are the polar and azimuthal angles, respectively.

As will be outlined in the following sections consensus is not found in the literature as to what simulations type are best suited to determine the values of the mean energy, spread in energy, spatial distribution and mean angular divergence of the electrons impinging on the linac target. This might be due to differences between linac types and models.

3.1.1 *The spread of the electrons about the mean energy*

Tanabe and Hamm [1985] found an energy spread of 3% FWHM for a Varian Clinac 1800 for both 6 and 18 MV modes. The sensitivity to the energy distribution of the impinging electrons were studied by Sheikh-Baghei and Rogers [2002] for a Siemes KD linac, which has a nominal energy spread FWHM of 14%. They found no statistical significant impact on off–axis factors when varying the FWHM of the energy distribution between 0 and 20%. This is explained by multiple scattering effects and Bremssstrahlung angular distribution for electrons with energy above mean are compensated by those below and thus resulting in photon distribtution similar to the corresponding monoenergetic spectrum. The Percentage Depth Dose curve (PDD) on the other hand showed small dependence on energy distribution, especially for large depths. This is explained by the nonlinear variation of attenuation and scattering with energy. For the 18 MV mode, a suggested distribution was Lorentzian, with a sharper fall of past the peak, rather than a Gaussian. This was modelled by joining two Gaussian distributions with FWHM of 14% and 3% for the low and high end, respectively. Simulated off–axis factors[1]), at 15 cm, showed a 2% deviation for the assymetrical distribution compared to the symmertrical 14% FWHM.

3.1.2 *Divergence of the impinging electrons*

Karzmark et al. [1993] state that the acceptance value for the initial electron energy should be 1–5 mradians (corresponding to 0.06–0.3 degrees). This angle is very close to 0 and it may be tempting to assume non diverging beam based on this alone. Sheikh-Baghei and Rogers [2002] investigated the impact on off–axis factors due to beam divergence for a Siemens KD linac and found no difference on off–axis factors for a divergence of 0.5°. Moreover PDD were insensitive to a divergence as large as 5°. Studies by [Chibani et al., 2011; Ding, 2002; McEwen et al., 2011; Tonkopi et al., 2005] indicate that angular divergence increase the amount of scattered radiation and thereby the contaminating (scattered) radiation impinging on the phantom surface. This primarily affects the dose in the build–up region [Ding, 2002]. The need to include angular distribution seems to be more important for high energy modes [Chibani et al., 2011; Tonkopi et al., 2005]. Chibani et al. [2011] found agreement between simulated PDDs and lateral profiles for the 15 MV mode of a Varian 21EX using an angular divergence of 0.6°, while a 1.15° divergence was reported for the 25 MV mode of an Elekta Precise linac by Tonkopi et al. [2005]. Both of these findings far exceeds the acceptance values stated by Karzmark

1 The off–axis factor is defined as the ratio of the dose at a point located at a distance from the central axis to that on the central axis.

et al. [1993]. The need to use such a large angular divergence may be due to discrepancies between the specifications by the vendor and the real linac. Errors in the vendor specified data have been pointed out (e.g. Chibani [2004]) and later on been confirmed by the vendor. It is not unlikely that other inaccuracies that will affect the exit fluence in general and the fluence due to scattered radiation in particular exists. Moreover, high energy modes would be more susceptible to such inaccuracies since the scattered radiation generated will have higher energies and thus longer ranges. A pragmatic approach is employed in Tonkopi et al. [2005], where the angular divergence was included only when a match could not be found by varying the incident electron energy and spot size alone. Moreover, Sheikh-Baghei and Rogers [2002] ignored the divergence of the electron beam based on the fact that no reliable estimate is supplied by the vendors.

3.1.3 *The spatial distribution of impinging electron source*

Jaffray et al. [1993] measured the size and shape of the focal spot of various linacs. In short it was conducted by restricting the source, as viewed from the detector, to small strips by a collimating slit. The signal produced in the detector will then correspond to the integrated x–ray emission spectrum over the slit. Measurement were conducted for various locations and angles. The size and shape of the focal spot was then reconstructed using CT reconstruction techniques. A Gaussian distribution was found for all linacs studied. Karzmark et al. [1993] also report that the electron beam impinging on the target has Gaussian shape. Jaffray et al. [1993] found that the FWHM of the bremsstrahlung focal spot of a Varian 2100C was between 1.2 and 1.4 mm for the 6 MV mode and between 0.9 and 1.6 mm for the 18 MV mode. The Varian 2300iX linac design is similar to that of Varian 2100C and therefore the results can be expected to be similar. At the very least the focal spot can be expected to be Gaussian as this was found for all linacs studied. A recent study by Bush et al. [2009] found that a Gaussian spot size with an extra focal halo present resulted in better agreement between measured and MC simulated 18 MV 40×40 cm^2 lateral profiles for a Varian 21EX. However, no supporting measurements of the focal spot shape were presented. Moreover, the current version of EGS/BEAM does not allow the use of such a source.

3.1.4 *The symmetry of the spacial distribution*

The final assumption made by Keall et al. [2003], and the only one to be revised in this study, was that the focal spot size was rotational symmetric about the z–axis. Jaffray et al. [1993] showed the spot size was elliptical rather than circular on almost all occasions. Moreover

Scott et al. [2009] found that an elliptical electron spot size[2] yielded better agreement on penumbra widths for small fields. The degree of ellipticity is rather small and the symmetry of the spacial distribution can to first order approximated circular.

Outcome of the assumptions

The parameters to be considered for tweaking are thus the mean energy, spread in energy, spatial distribution and mean angular divergence of the electrons impinging on the linac target.

3.1.5 *Sensitivity to characteristics of the impinging electrons*

Verhaegen and Seuntjens [2003] published a concept for commissioning of external photon beams for radiotherapy where simulated PDDs and lateral dose profiles are to be compared with measurements. The general idea of the protocol is that PDDs can be commissioned by tweaking the mean impinging electron energy, that lateral profiles can be commissioned by tweaking the focal spot size FWHM. The underlying hypothesis is that this can be done independently, such that simulated PDDs are unaffected by changes in focal spot size FWHM and that lateral profiles are unaffected by changes in mean impinging electron energy. An iterative commissioning process as described in figure 6 was suggested.

Several studies have pointed out that PDDs are rather insensitive to changes in mean energies [Keall et al., 2003; Libby et al., 1999; Lovelock et al., 1995; Pena et al., 2004]. Pena et al. [2004] demonstrated that for a change of mean energy of 0.5 MeV to result in two well separated depth dose curves, for a Siemens PRIMUS linacs, the relative, statistical, uncertainty of the simulations needed to be 0.3–0.4%.

Sheikh-Baghei and Rogers [2002] showed that in–air off-axis factors are sensitive both to mean energy and focal spot size. In–air off–axis factors require measurements that are generally not part of the standard data set generated during commissioning of a linac. Furthermore, they are costly, in terms of CPU time, to simulate as they ideally require separate simulations for each data point. Keall et al. [2003] and Pena et al. [2004] suggested the use of wide–field lateral–profiles instead as they also show sensitivity to both to mean energy and focal spot size and typically are contained in a standard linac commissioning data set. Comparison should be done at as a shallow depth as possible as phantom scatter becomes increasingly more important with depth and reducing the sensitivity to the electron beam

2 It is important to distinguish between the focal spot of the electrons impinging on the target and that of the bremsstrahlung photons emitted from the target – the one typically discussed in MC is the focal spot of the electrons impinging on the target.

parameters [Sheikh-Baghei and Rogers, 2002]. However, comparison should be conducted for depths below d_{max}, since dosimetry in the build up region is associated with large uncertainties.

3.2 SENSITIVITY ANALYSIS

In this work MC simulations were conducted in order to study the influence of the mean energy, spread in energy and spatial distribution of the electrons impinging on the linac target for a Varian 2300 iX, which is the linac model to be commissioned in this study (a detailed description of the model is presented in Section 3.3).

Figure 7 show MC simulated PDDs of a 10×10 cm^2 field for the Varian 2300iX linac modelled in this study[3]. The mean energy was varied from 5.60 MeV to 6.20 MeV in steps of 0.10 MeV and the spot size FWHM was 0.075 cm. The number of histories were chosen so that the relative uncertainty was at most 0.5% between d_{max} and 30 cm depth along the CAX. The depth dose curves were normalized at 10 cm using a forth degree polynomial fit between 5 and 15 cm [Pena

3 DOSXYZnrc was used for phantom simulation with a voxel size of 0.5×0.5×0.2 cm^3. Simulation properties were ECUT = 521 keV, PCUT = 10 keV, nsplit = 25, esplit = 25 and howfarless turned on. The treatment head was simulated using source 9 in DOSXYZnrc. Simulation properties were ECUT = 700 keV, PCUT = 10 keV, direction bremsstrahlung splitting was used (FS = 10, SSD = 100), NBRSPL was set to 1000, with the splitting plane for electrons (ZPLANE_DBS) defined as the bottom of the flattening filter and russian roulette conducted for electron at a plane 0.20 cm above the bottom of the flattening filter.

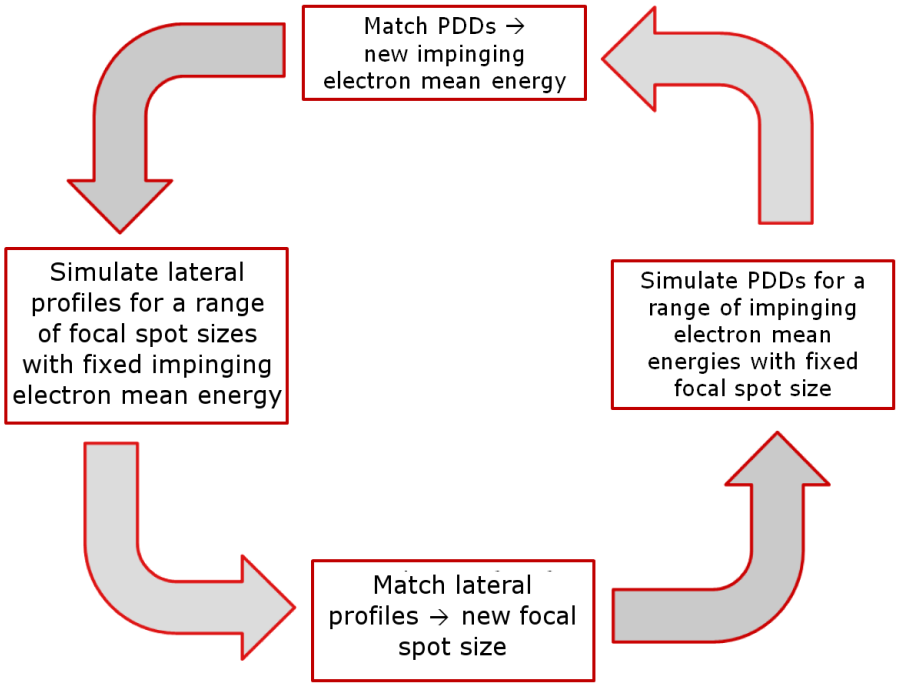

Figure 6: Schematic sketch of the iterative commissioning process.

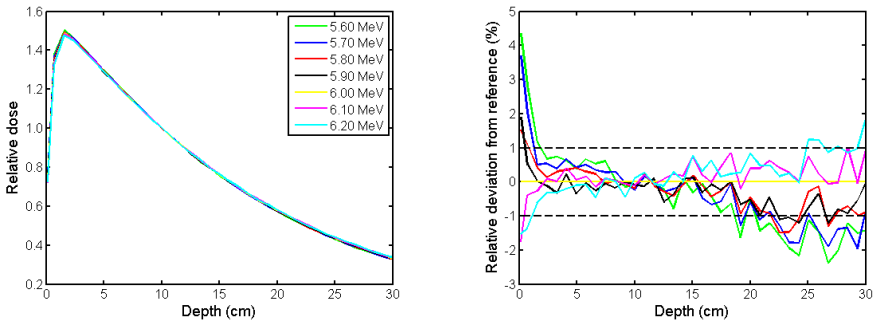

Figure 7: 10×10 cm^2 PDD along CAX for MC simulation of a range of mean energies (left) and local deviation from the reference energy (right). Also shown is the ±1% deviation level (dashed black). The nominal photon beam nominal energy, 6.00 MeV, was chosen as the reference.

et al., 2004]. The electron energy corresponding to the nominal energy of the photon beam, i.e. 6.00 MeV, was chosed as the reference energy. Local deviation from the reference energy was generally within 1% beyond d_{max} for the mean energy range [5.80,6.20] MeV. Considering the statistical uncerntainty of the simulated data it was not possible to distinct between PDDs differing by less than 0.30 MeV. This is slightly better than reported by [Pena et al., 2004], but still showing that PDDs are insensitive to small changes in mean energy.

In order to study the influence of spot size on wide–field lateral–profiles MC simulations[4] were conducted for 20×20 and 40×40 cm^2 fields with a mean energy of 6.0 MeV and for (circular) spot sizes with FWHM 0.10, 0.20 and 0.30 cm (figure 8–9). The central value (spot FWHM = 0.20 cm) was taken as the reference and local relative deviation were calculated through: $(X_i - X_i^{ref})/X_i^{ref} \times 100$. Uncertainties of the ratio were computed using error propagation. The result showed that the larger fields were more susceptible to changes in spot size and that a variation of 0.10 cm FWHM results in profiles differing by 10% near the field edges. Similair results were found when making the same comparison at 10 cm depth (not shown).

4 DOSXYZnrc was used for phantom simulation with a voxel size of 0.25×0.25×0.5 cm^3. Simulation properties were ECUT = 761 keV, PCUT = 10 keV, nsplit = 25, esplit = 25 and howfarless turned on. The treatment head was simulated using source 9 in DOSXYZnrc. Simulation properties were ECUT = 700 keV, PCUT = 10 keV, direction bremsstrahlung splitting was used (FS = 20 and 40 cm for the 20×20 and 40×40 cm^2 fields respectively at SSD = 100), NBRSPL was set to 1000, with the splitting plane for electrons (ZPLANE_DBS) defined as the bottom of the flattening filter and russian roulette conducted for electron at a plane 0.20 cm above the bottom of the flattening filter.

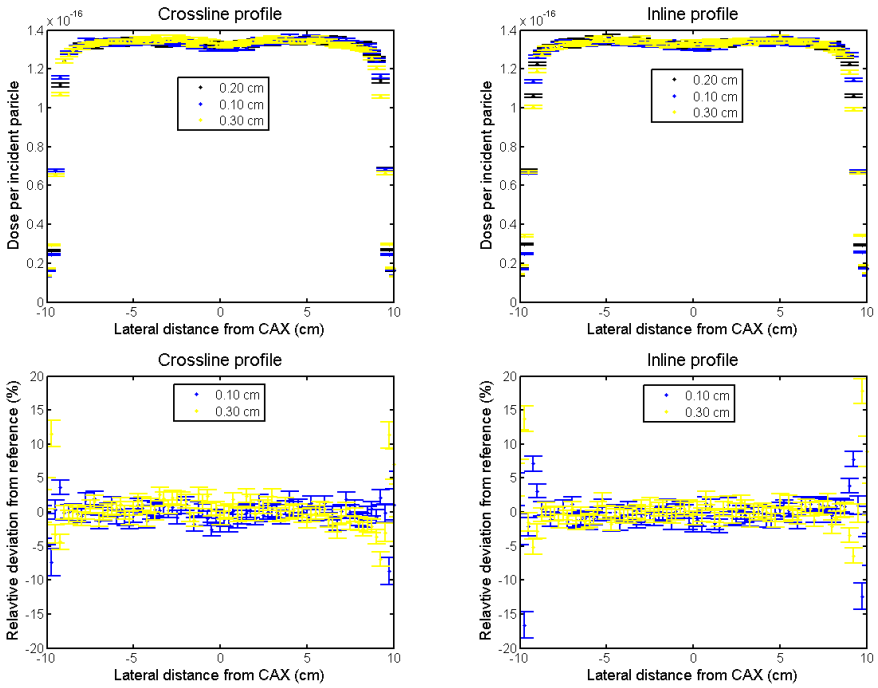

Figure 8: 20×20 cm^2 field, at 5 cm depth, for a varying spot size (top) and local deviation from reference (spot FWHM = 0.20 cm) simulation (bottom) for crossline (left) and inline (right) lateral profiles.

In order to study the influence of mean energy on wide–field lateral–profiles MC simulations[5] were conducted for 40×40 cm^2 fields with a spot size FWHM of 0.175 cm and mean energies 5.70, 5.85 and 6.00 MeV (figure 10). The central value (mean energy = 5.85 MeV) was taken as the reference and local relative deviation were calculated through: $(X_i - X_i^{ref})/X_i^{ref} \times 100$. Uncertainties of the ratio were computed using error propagation. The profiles were normalized to the same value as the reference at CAX before computing local deviation. The results show that a 0.15 MeV change in mean energy produced differences on the order of 4% near the field edges for the decreased energy, whereas no difference was observed for the increase of energy. The comparison was conducted for simulations with statistical uncertainty of 0.8% and it is likely that improving on this would lead to more distinct separation between the profiles as an, insignificant, trend was observed on the relative deviation in case of the increase in energy.

5 DOSXYZnrc was used for phantom simulation with a voxel size of 0.25×0.25×0.5 cm^3. Simulation properties were ECUT = 761 keV, PCUT = 10 keV, nsplit = 25, esplit = 25 and howfarless turned on. The treatment head was simulated using source 9 in DOSXYZnrc. Simulation properties were ECUT = 761 keV, PCUT = 10 keV, direction bremsstrahlung splitting was used (FS = 40 cm at SSD = 100), NBRSPL was set to 1000, with the splitting plane for electrons (ZPLANE_DBS) defined as the bottom of the flattening filter and russian roulette conducted for electron at a plane 0.20 cm above the bottom of the flattening filter.

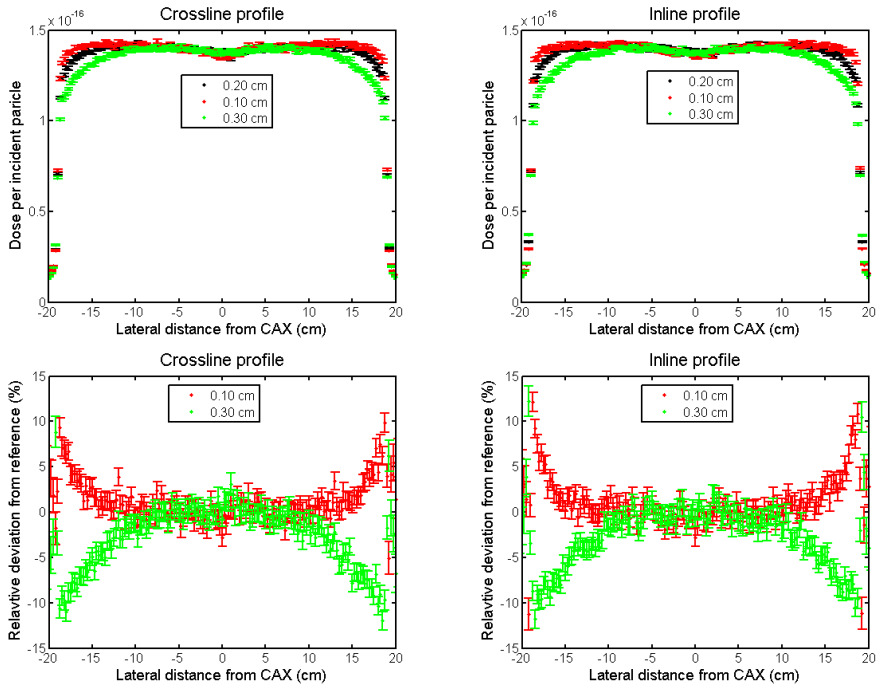

Figure 9: 40×40 cm^2 field, at 5 cm depth, for a varying spot size (top) and local deviation from reference (spot FWHM = 0.20 cm) simulation (bottom) for crossline (left) and inline (right) lateral profiles.

With this, it should be clear that 40×40 cm^2 profiles are more sensitive to changes in mean energy than PDDs. Similair results were found when making the same comparison at 10 cm depth (not shown).

The effect of the angular divergence of the beam on 10×10 cm^2 field PDDs as well as 40×40 cm^2 field lateral profiles were investigated. Simulations[6] were conducted, at SSD = 90 cm, for a fixed mean energy (15.5 MeV) and spot size FWHM (0.15 cm – cylindrical) while the angular divergence was 0.0°, 0.5° and 1.0°. The 10×10 cm^2 field PDDs were normalized at 10 cm using a forth degree polynomial fit between 5 and 15 cm, whereas no normalization was conducted for the 40×40 cm^2 field lateral profiles. The PDDs and residuals (taking $\theta = 0.0°$ as reference) are shown, without uncertainties, in figure 11. From the residuals it can be concluded that the difference is limited to the build up region. The increase in build up–dose with increased

6 DOSXYZnrc was used for phantom simulation with a voxel size of 2.0×2.0×0.25 cm^3 for the 10×10 cm^2 field PDDs and 0.25×0.25×0.5 cm^3 for the 40×40 cm^2 field lateral profiles. Simulation properties were ECUT = 761 keV, PCUT = 10 keV, nsplit = 25, esplit = 25 and howfarless turned on. The treatment head was simulated using source 9 in DOSXYZnrc. Simulation properties were ECUT = 700 keV, PCUT = 10 keV, direction bremsstrahlung splitting was used with FS = 10 and 40 cm (for the 10×10 cm^2 fields and 40×40 cm^2 fields, respectively) at SSD = 100, NBRSPL was set to 1000, with the splitting plane for electrons (ZPLANE_DBS) defined as the bottom of the flattening filter and russian roulette conducted for electron at a plane 0.20 cm above the bottom of the flattening filter.

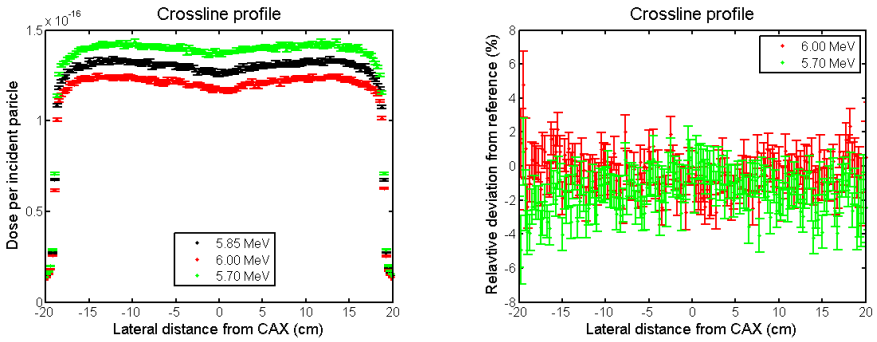

Figure 10: 40×40 cm^2 field, at 5 cm depth, for a varying mean energy (left) and local deviation from reference (mean energy = 5.85 MeV) simulation (right) for crossline profiles. The profiles were normalized to the same value as the reference at CAX before computing local deviation.

angular divergence is likely to be due to the increased amount of contaminant electrons (as described in section 3.1.2). The results are in contradiction with Chibani et al. [2011], who reported a 1.5% difference at 30 cm depth for a 10×10 cm^2 field PDD of a Varian 2300C/D linac. The sensitivity of the 10×10 cm^2 field PDDs shows agreement with the results of Sheikh-Baghei and Rogers [2002]. Inline and crossline profiles, at 3 cm depth and SSD = 90 cm, are shown for the 40×40 cm^2 fields in figure 12. For the residuals (lower panel in figure 12) the local devation from the simualtion with $\theta = 0.0°$ was computed through: $(X_i - X_i^{ref})/X_i^{ref} \times 100$. Uncertanties of the ratio were computed using error propagation. A local difference of ≈3% and 10% is observed for $\theta = 0.5°$ and $\theta = 1.0°$, respectively along the CAX. The difference is however confined to the central part (approximately in the [-5;5] cm range) of the profiles, making it possible to distinguish between the impact of varying the spot size, which predominantly is present on the distal parts of the lateral profiles (see e.g. figure 9).

In order to investigate the impact of the spread in energy of the electrons impinging on the linac target, 10×10 cm^2 cm field CAX–PDD and off–axis factors, for a 40×40 cm^2 cm field, were simulated for three different spectra with mean energy 6.0 MeV: i) a monoenergetic spectrum, ii) a Gaussian distribution about 6.0 MeV with 3% FWHM and iii) a Gaussian distribution with 1.5% FWHM on the lower end and a sharp cut off at 6.0 MeV (figure 13). The latter was to account for the fact that the energy distribution presented by Tanabe and Hamm [1985], for a Varian Clinac 1800, showed a sharper fall of on the high end.

No difference between the three different energy spectra was noted on the PDD beyond the build–up region Figure 14. Furthermore no substantial differences, as compared to influence of mean energy

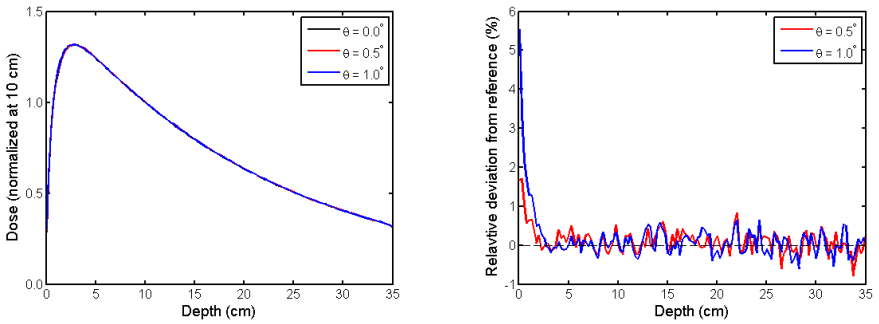

Figure 11: **Left:** Simulated 10×10 cm^2 field PDDs with mean energy 15.5 MeV, (cylindrical) spot size FWHM 0.15 cm and an angular divergence of 0.0° (black), 0.5° (red) and 1.0° (blue). The PDDs were normalized at 10 cm depth using a forth degree polynomial fit in the [5;15] cm region. Local statistical uncertainty was 0.2–0.3%. **Right:** Local relative deviation from the reference simulation ($\theta = 0.0°$ selected as reference) for angular divergence of 0.5° (red) and 1.0° (blue). A line corresponding to perfect agreeement is also shown in the figure (dashed black).

and/or spot size changes, were noted on the off–axis factors. A Gaussian spread with a 3% FWHM was assumed for this study.

The use of a 40×40 cm^2 field for commissioning does however pose a possible problem. The maximum field size that the Varian Millennium 120 leaf MLC can define is 40×40 cm^2 and thus the MLC may influence the dose distribution. However, the properties of the MLC are not given in full detail by the vendor and merits a separate commissioning where density, distance from the source and dimensions of the individual leafs are determined. A cyclic dependence between the MLC properties and those of the impinging electron source (mean energy and spatial distribution) may not be neglected without further investigation. Simulations[7] of 6MV 40×40 cm^2 fields were conducted with MLC parameters as derived by Heath and Seuntjens [2003] (hereafter referred to as with MLC) and with MLC parameters where the leafs were further contracted and with over exaggerated leaf widths so that the MLC defined a 45×45 cm^2 field (hereafter referred to as without MLC). As shown previously, the wide–field profiles are highly sensitive to changes in spot size, therefore the simulations were conducted for a number of different spot sizes (0.100, 0.250 and

7 DOSXYZnrc was used for phantom simulation with a voxel size of $0.25\times0.25\times0.5$ cm^3. Simulation properties were ECUT = 761 keV, PCUT = 10 keV, nsplit = 25, esplit = 25 and howfarless turned on. The treatment head was simulated using source 9 in DOSXYZnrc. Simulation properties were ECUT = 761 keV, PCUT = 10 keV, direction bremsstrahlung splitting was used (FS = 40 cm at SSD = 100), NBRSPL was set to 1000, with the splitting plane for electrons (ZPLANE_DBS) defined as the bottom of the flattening filter and russian roulette conducted for electron at a plane 0.20 cm above the bottom of the flattening filter.

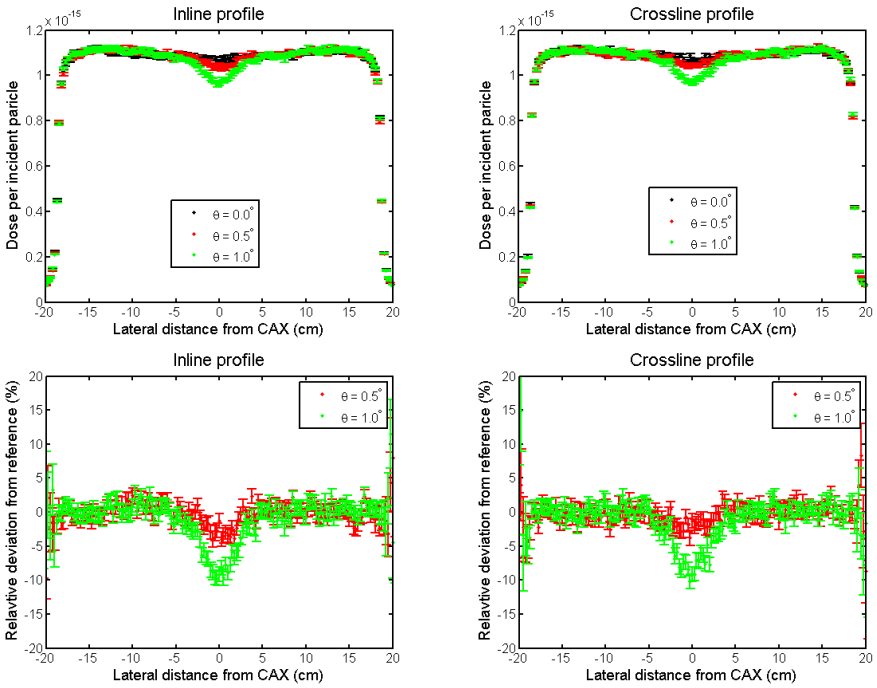

Figure 12: **Upper panel:** Simulated 40×40 cm^2 field profiles, at 3 cm depth, with mean energy 15.5 MeV, (cylindrical) spot size FWHM 0.15 cm and an angular divergence of 0.0° (black), 0.5° (red) and 1.0° (green). No normalization of the data was conducted. **Lower panel:** Local relative deviation from the reference simulation ($\theta = 0.0°$ selected as reference) for angular divergence of 0.5° (red) and 1.0° (green).

0.325 cm) while the mean energy was kept constant at 6.0 MeV. Local relative deviation, between simulations with and without MLC, were calculated through: $(X_i - X_i^{ref})/X_i^{ref} \times 100$. Uncertainties of the ratio were computed using error propagation. The profiles were normalized to the same value as the reference at CAX before computing local deviation. No difference were observed between simulations with and without the MLC (figure 15), hence the general commissioning can safely be conducted without a properly commissioned MLC, which in turn can be conducted once satisfactory agreement has been obtained for open fields.

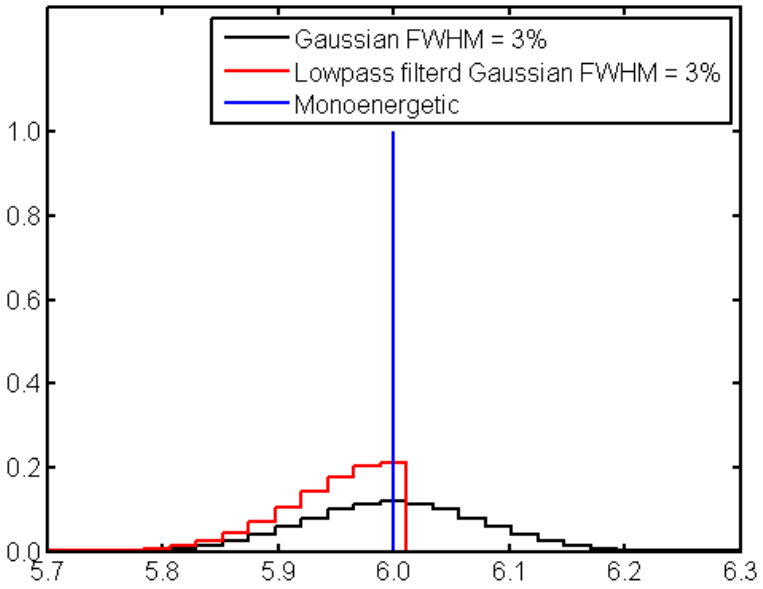

Figure 13: The three energy spectra used: a monoenergetic spectrum (blue), a Gaussian distribution with 3% FWHM (black) and a Gaussian distribution with 1.5% FWHM on the lower end with a sharp cut off at 6.0 MeV (red).

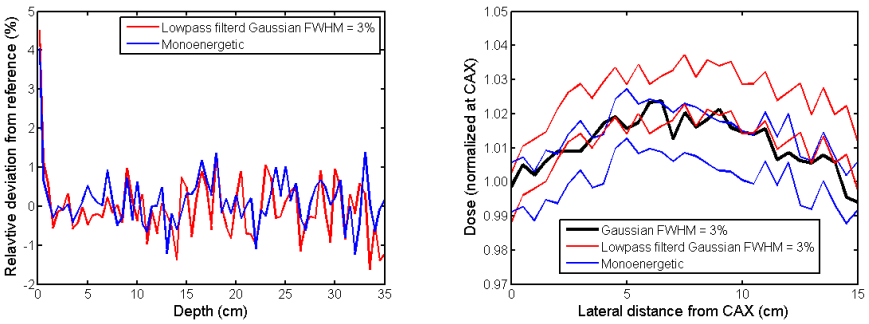

Figure 14: **Left:** Local relative difference in dose along CAX for 40×40 cm^2 fields simulated the Gaussian distribution with 1.5% FWHM on the lower end with a sharp cut off at 6.0 MeV (red) and the monoenergetic spectrum (blue) compared to the 3% FWHM Gaussian distribution (black). The local combined statistical uncertainty is on the order of 1%. **Right:** Lateral profiles for 40×40 cm^2 fields simulated with the monoenergetic spectrum (blue), a Gaussian distribution with 3% FWHM (black) and a Gaussian distribution with 1.5% FWHM on the lower end with a sharp cut off at 6.0 MeV (red).

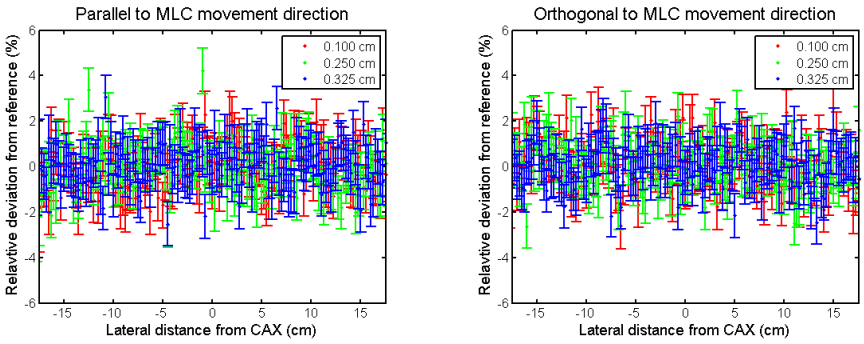

Figure 15: Local dose difference for MC simulations of a 6MV 40×40 cm^2 field with and without (reference) the MLC included. Lateral profiles are scored parallel (left) and orthogonal (right) to the MLC direction of movement for three different (Gaussian shaped) spot sizes with FWHM 0.100 (red), 0.250 (green) and 0.325 cm (blue) respectively and at 5 cm depth in a homogenous water phantom.

3.3 SUGGESTED PROTOCOL FOR CALIBRATION

The following section describes the calibration of an MC model of a Varian 2300iX linear accelerator at Copenhagen University Hospital, Herlev. The commissioning is conducted for two high energy photon modes: 6MV and 15MV.

The first step in the calibration process is to build the representation of the physical linac — the MC model. In this study, the model was based on drawings supplied by the vendor [Varian Medical Systems, 1999; Varian Oncology Systems, 2008]. A model was built using EGSnrc and BEAMnrc. The different CM of BEAMnrc can readily be used as building blocks, where the specific geometrical and physical properties of each module can be specified independently of each other. Table 2 lists the included components and the CM used to model them and a schematic illustration of the 6MV treatment head geometry is shown in Figure 16.

Measurements used for the calibration were all conducted during the commissioning of the physical linac. The advantage of this is obviously that no, time consuming, dedicated measurements were required. The measurements conducted are listed in Sjöström et al. [2009]. All measurements were conducted in a Blue Phantom (IBA Dosimetry AB, Uppsala, Sweden) $48\times48\times48$ cm^3 water tank ($\pm$ 0.1 mm position accuracy) and the data acquisition was controlled by the OmniPro Accept v.6.5A (IBA Dosimetry AB, Uppsala, Sweden) software. Depth dose curves were measured using a Wellhöfer/IBA CC13 (IBA Dosimetry AB, Uppsala, Sweden) Ionization Chamber (0.13 cm^3 active volume) while lateral profiles were measured using a Scanditronix/IBA PFD^{3G} (IBA Dosimetry AB, Uppsala, Sweden) Si–photon diode. The shielded diodes produce reliable readings under

Table 2: List of linac components and the corresponding CM used to model them

Linac component	EGSnrc CM
Target and backing	SLABS
Primary collimator	CONS3R
Vacuum window	CONESTAK
Flattening filter	FLATFILT
Monitor chamber	CHAMBER
Light mirror	MIRROR
Secondary movable collimators	JAWS/SYNCJAWS*
MLC	DYNVMLC
Exit window	SLABS

*Used exclusively in VMAT simulations utilizing DOSXYZnrc source 20/21.

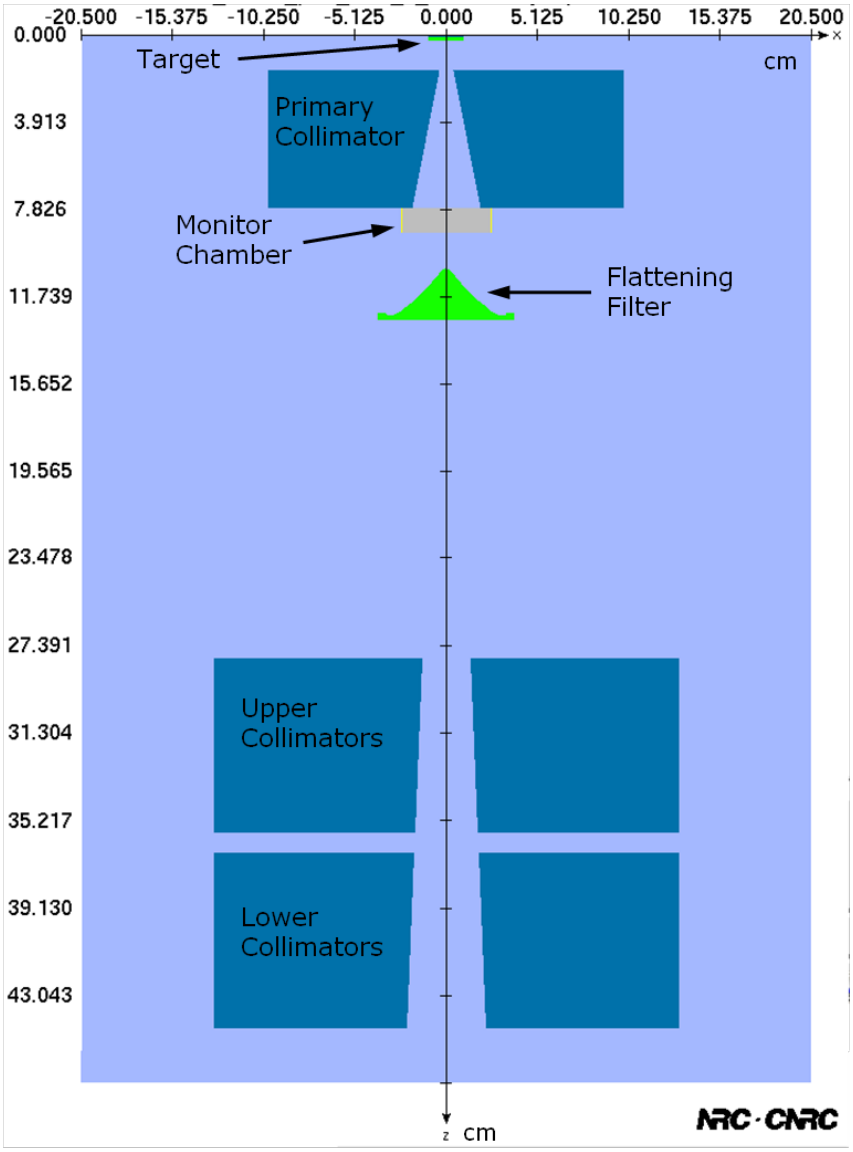

Figure 16: Schematic illustration of the 6MV MC model geometry. The upper collimating jaws are shown rotated 90°. The figure was produced using BEAMnrc.

requirement of lateral CPE condition only. This requirement is not fulfilled near the edges of the lateral profiles. In order to account for that, comparisons are made up to off-axis distances of $X - 3$ cm and $X - 5$ cm for 6MV and 15MV, respectively. Within this range lateral CPE will exist. All measurements are assumed to have negligible uncertainties in the comparisons.

The protocol suggested in this study is based on matching simulated dose distributions to measurements of PDDs, lateral profiles as well as Relative Output Factors (ROFs). Agreement between simulated and measured PDDs and lateral profiles is enough if single field relative comparisons with experimental data is of interest alone. In order to

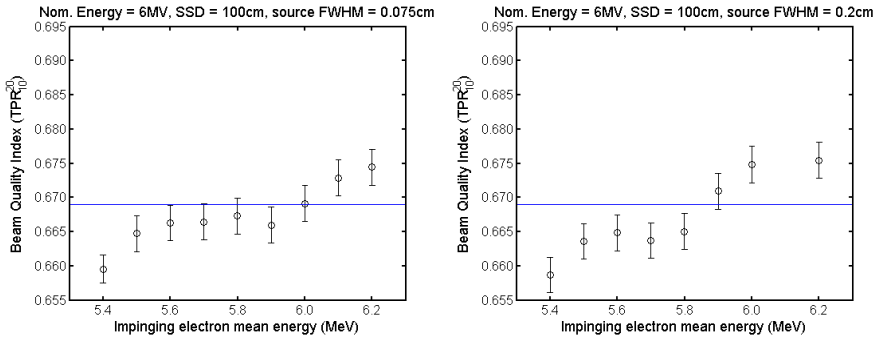

Figure 17: Simulated 6MV beam quality index as a function of impinging electron mean energy for initial electron beam radial FWHM 0.075 cm (left) and 0.20 cm (right). The blue line corresponds to measured TPR^{20}_{10}, while black circles represent simulated values. The error bars corresponds to the combined statistical uncertainties of the simulations.

utilize MC to calculate dose distributions generated by multiple fields of different shapes and sizes, which is commonly used in radiotherapy, it is also vital that agreement is found between simulated and measured ROFs.

As an initial step a range of possible mean impinging electron energies were selected by comparison between measured and simulated TPR^{20}_{10}, calculated from $10 \times 10 cm^2$ field with SSD = 100 cm, as described in Andreo et al. [2000], using the empirical expression established by Followill et al. [1998]: $TPR^{20}_{10} = 1.2661 PDD^{20}_{10} - 0.0595$. MC simulations[8] were conducted for both the small and large initial focal spot size guess (figure 17). The range of energies resulting in simulated Beam Quality Index (BQI) (for either spot size) in agreement, within the statistical uncertainty, with measurments were selected. The selected energies were [5.6;6.0] and [14.75;16.25] MeV for 6MV and 15MV, respectively.

8 DOSXYZnrc was used for phantom simulation with a voxel size of $0.5 \times 0.5 \times 0.2$ cm^3. The number of histories were chosen so that the statistical uncertainty along the CAX was 0.2–0.3% at 5–15 cm depth. Simulation properties were ECUT = 521 keV, PCUT = 10 keV, nsplit = 25, esplit = 25 and howfarless turned on. The treatment head was simulated using source 9 in DOSXYZnrc. Simulation properties were ECUT = 700 keV, PCUT = 10 keV, direction bremsstrahlung splitting was used (FS = 10, SSD = 100), NBRSPL was set to 1000, with the splitting plane for electrons (ZPLANE_DBS) defined as the bottom of the flattening filter and russian roulette conducted for electron at a plane 0.20 cm above the bottom of the flattening filter.

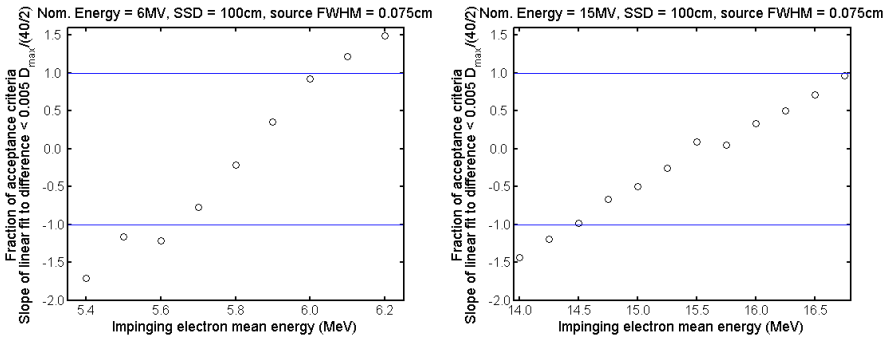

Figure 18: Slope of ratio between simulated and measured PDDs compared to the acceptance criteria $0.005D_{max}/(40/2)$ as a function of impinging electron mean energy for 6MV (left) and 15MV (right). Energies within [-1,1] was selected of further calibration. The selection criteria, ± 1.0, is also shown in the figure (solid blue line).

10×10 cm² CAX PDDs

PDDs were simulated[9] for 10×10 cm² fields with varying impinging electron mean energy while keeping the focal spot sizes constant at 0.075 cm. The depth dose curves were normalized at 10 cm using a forth degree polynomial fit between 5 and 15 cm [Pena et al., 2004]. As oppose to other commissioning protocols, (e.g. Verhaegen and Seuntjens [2003]) where the mean energy best fitting the measurements is selected for further calibration, a range of energies are selected. The acceptance criteria were based on the criteria specified by Keall et al. [2003] where the slope of a linear fit to the ratio between the measured and simulated curve is computed. A ratio of <0.5% was sought over (0,40) cm depth. In order to fulfill this criteria, the slope of the ratio needs to be less than $0.005D_{max}/(40/2)$. The selected range of consideration was [5,25] cm, since it is well beyond the build–up region for both energies and thus not influenced by contaminating electrons while not extending to the bottom of the phantom where material producing back scatter radiation was omitted in the simulations. Energies where ratio of the slope of the linear fit, to the ratio between measured and simulated PDDs, and the acceptance criteria was <|1| were selected for further calibration (Figure 18). The selected energies were [5.7,6.0] and [14.5,16.75] MeV for 6MV and 15MV, respectively.

9 DOSXYZnrc was used for phantom simulation with a voxel size of 0.5×0.5×0.2 cm³. The number of histories were chosen so that the statistical uncertainty along the CAX was 0.2–0.3% at 5–15 cm depth. Simulation properties were ECUT = 521 keV, PCUT = 10 keV, nsplit = 25, esplit = 25 and howfarless turned on. The treatment head was simulated using source 9 in DOSXYZnrc. Simulation properties were ECUT = 700 keV, PCUT = 10 keV, direction bremsstrahlung splitting was used (FS = 10, SSD = 100), NBRSPL was set to 1000, with the splitting plane for electrons (ZPLANE_DBS) defined as the bottom of the flattening filter and russian roulette conducted for electron at a plane 0.20 cm above the bottom of the flattening filter.

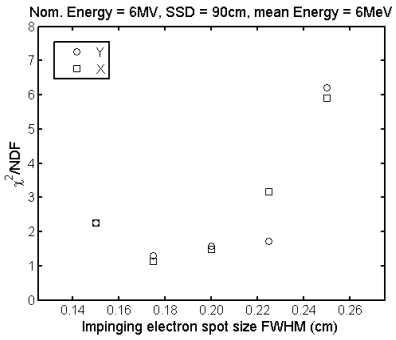

Figure 19: χ^2/NDF for 40×40 cm^2 lateral profiles as a function of radial focal spot size FWHM for impinging electron mean energies 6.0 MeV.

40×40 cm^2 lateral profiles

For each of the selected energies lateral 40×40 cm^2 fields were simulated[10] for a range of focal spot sizes, while keeping the impinging electron mean energy constant. The shallowest measured depth, beyond d_{max}, was used for comparison. The selected depths were 10 cm and 3 cm for 6MV and 15MV, respectively. The descission to compare at the shallowest depth of measurement was motivated by the fact that phantom scattering becomes increasingly important with depth. Thus, the sensitivity to the calibration parameters (e.g. spot size FWHM and angular divergence) will decrease with depth due to increased phantom scatter. The lateral profiles were normalized at CAX using a second degree polynomial fit to the inner most 4 cm of the profiles. χ^2/NDF were calculated, using equation Equation 3.2, and plotted as a function of radial focal spot size (Figure 19 shows χ^2/NDF as a function of spot size for a mean energy of 6.0 MeV).

$$\chi^2/\mathrm{NDF} = \sum_{i=1}^{N} \frac{(s_i - m_i)^2}{\sigma_i^2}/(N-1), \tag{3.2}$$

where s_i is the simulated dose at position i, m_i is the measured dose at position i and σ_i is the simulated uncertainty at position i. A visual inspection of the profiles were also conducted. Such a visual inspection is shown in Figure 20 for a impinging electron mean energy of 6.0 MeV and for a (circular) spot size FWHM ranging from 0.15 cm to 0.25

10 DOSXYZnrc was used for phantom simulation with a voxel size of 0.25×0.25×0.5 cm^3. The number of histories were chosen so that the statistical uncertainty along the CAX was 0.5–0.7% at 3–15 cm depth. Simulation properties were ECUT = 761 keV, PCUT = 10 keV, nsplit = 25, esplit = 25 and howfarless turned on. The treatment head was simulated using source 9 in DOSXYZnrc. Simulation properties were ECUT = 700 keV, PCUT = 10 keV, direction bremsstrahlung splitting was used (FS = 40, SSD = 100), NBRSPL was set to 1000, with the splitting plane for electrons (ZPLANE_DBS) defined as the bottom of the flattening filter and russian roulette conducted for electron at a plane 0.20 cm above the bottom of the flattening filter.

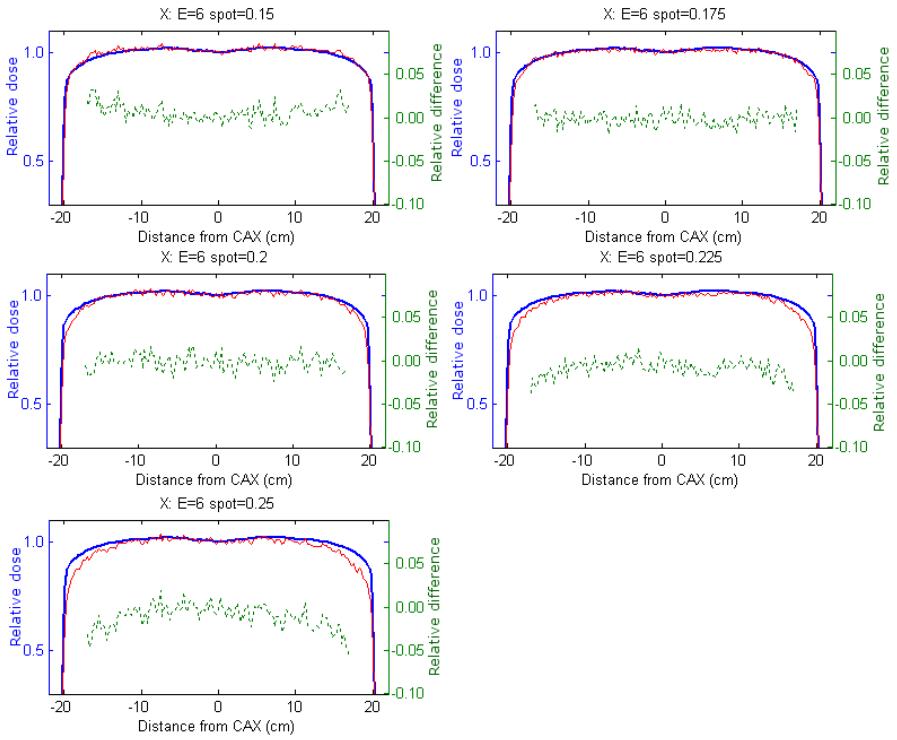

Figure 20: 6MV 40×40 cm^2 lateral profiles, along X–direction at 10 cm depth, for a number of radial focal spot size FWHM for an impinging electron mean energy of 6.0 MeV. The actual spot size FWHM is indicated in the title of each figure. The figures shows measured (blue) and simulated (red) profiles as well as relative difference (green) between them (taking the measurement as reference).

cm. It can clearly be seen that the horns of the profiles are decreased with increasing spot size FWHM.

If passing the visual inspection, the spot size FWHM yielding the minimum χ^2/NDF, for X– and Y–profiles individually, was selected for each energy. All energies selected for the 6MV mode passed the visual inspection and for each energy a set of spot size FWHMs was identified as best matching the measurements. The parameters selected for each energy is given in Table 3. For the 15MV mode, however, the visual inspection resulted in rejection of all parameter sets. This is illustrated by Figure 21, where the simulated profile undershoots, in comparison with the measurement for all spot size FWHMs, indicating that angular divergence needs to be considered.

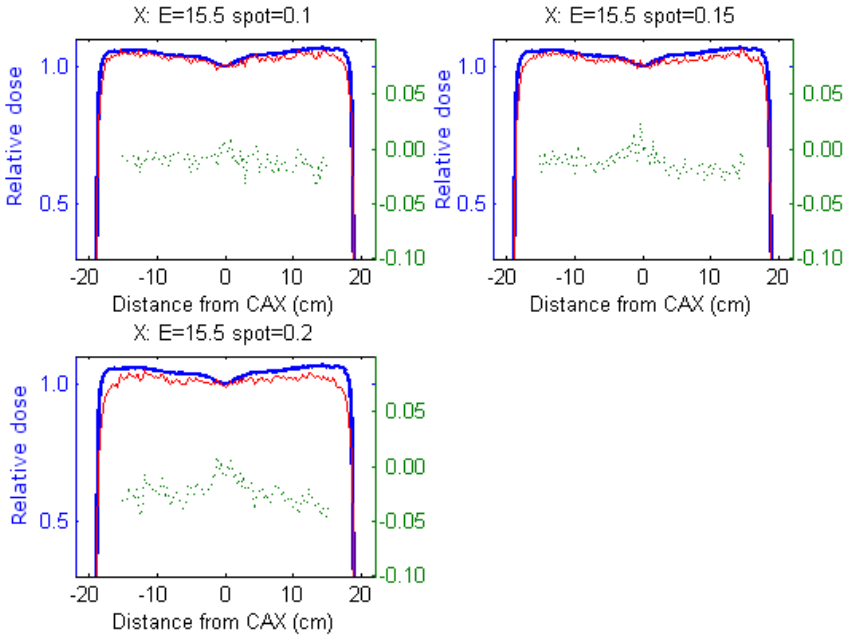

Figure 21: 15MV 40×40 cm^2 lateral profiles, along X–direction at 3 cm depth, for a number of radial focal spot size FWHM for an impinging electron mean energy of 15.5 MeV. The actual spot size FWHM is indicated in the title of each figure. The figures shows measured (blue) and simulated (red) profiles as well as relative difference (green) between them (taking the measurement as reference).

For each of the selected 15MV energies lateral 40×40 cm^2 fields were simulated[11] for a range of focal spot size FWHMs and mean angular divergencies, while keeping the impinging electron mean energy constant. With spot size FWHM and mean angular divergence as free parameters all energies selected for the 15MV mode passed the visual inspection as well and for each energy a compination of spot size FWHMs and angluar divergence was identified as best matching the measurements. The parameters selected for each energy is given in Table 3. 15MV 40×40 cm^2 lateral profiles, along X–direction at 3 cm depth, for a number of radial focal spot size FWHM for an impinging electron mean energy of 15.5 MeV and a mean angular divergence of 0.4° is shown in Figure 22. It can clearly be seen that the simulations coincided substantially better with the measurements when including

11 DOSXYZnrc was used for phantom simulation with a voxel size of 0.25×0.25×0.5 cm^3. The number of histories were chosen so that the statistical uncertainty along the CAX was 0.5–0.7% at 3–15 cm depth. Simulation properties were ECUT = 761 keV, PCUT = 10 keV, nsplit = 25, esplit = 25 and howfarless turned on. The treatment head was simulated using source 9 in DOSXYZnrc. Simulation properties were ECUT = 700 keV, PCUT = 10 keV, direction bremsstrahlung splitting was used (FS = 40, SSD = 100), NBRSPL was set to 1000, with the splitting plane for electrons (ZPLANE_DBS) defined as the bottom of the flattening filter and russian roulette conducted for electron at a plane 0.20 cm above the bottom of the flattening filter.

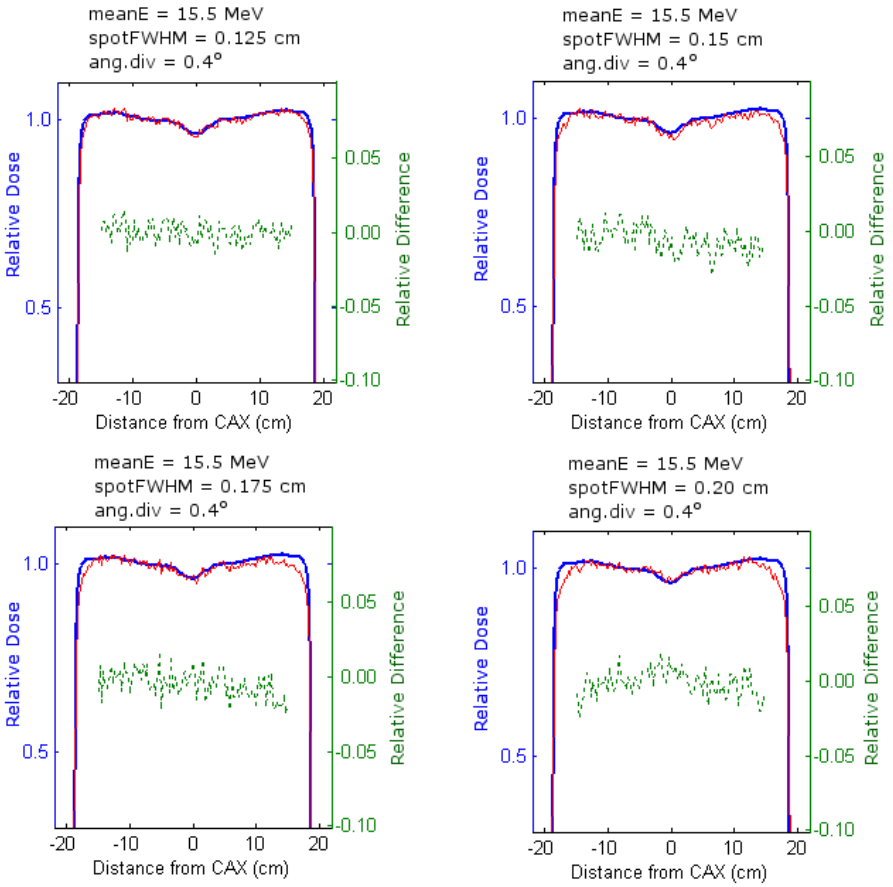

Figure 22: 15MV 40×40 cm^2 lateral profiles, along X–direction at 3 cm depth, for a number of radial focal spot size FWHM for an impinging electron mean energy of 15.5 MeV and a mean angular divergence of 0.4°. The actual spot size FWHM is indicated in the title of each figure. The figures shows measured (blue) and simulated (red) profiles as well as relative difference (green) between them (taking the measurement as reference).

angular divergence as a free parameter (cf. Figure 21 where the angluar divergece was set to 0°).

The χ^2/NDF test is intended for uncorrelated events, which may not be assumed when considering a lateral dose profile. Moreover, if a simulated lateral profile differs only from the corresponding measurement by statistical fluctuation the computed χ^2/NDF should precisely equal 1 and in any other situation the χ^2/NDF is expected to be >1. However, as the uncertainty in the measurements are neglected the total combined uncertainty is therefore underestimated, which might lead to a χ^2/NDF of <1. The set of parameters minimizing χ^2/NDF, regardless of its value, were selected as the optimal parameter set for each energy. A useful feature of the χ^2/NDF test is that it is possible to relate the computed values to uncertainties of the varied parameters. An increment of 1 on the χ^2/NDF, for a single varied parameter, corresponds to one standard deviation on that parameter [Berendsen,

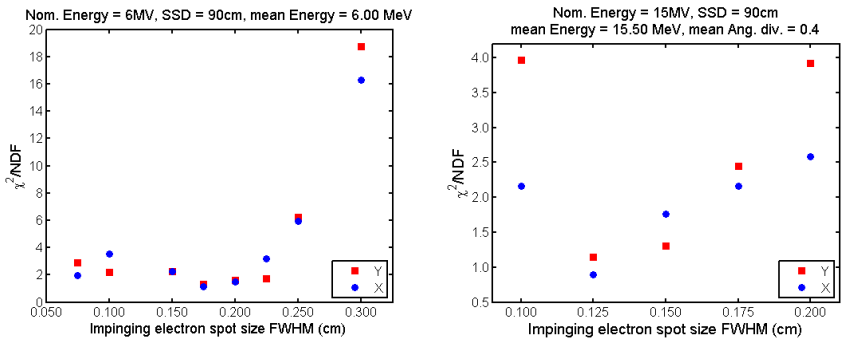

Figure 23: χ^2/NDF plots for a fixed mean energy (6.0 and 15.5 MeV) and mean angular divergence (0.0 and 0.4°) as a function of varying (circular) spot size FWHM for 6 (left) and 15MV (right) mode. Evaluation was conducted for a 40×40 cm^2 profile at 10 and 3 cm depth, respectively for the 6 and 15MV mode and for crossline (X) and inline (Y) profiles separately. A single (global) minima is identifiable for each data set.

2011; Hughes and Hase, 2010]. Put more clearly, the value minimizing the χ^2/NDF corresponds to the optimal value while one standard deviation of that parameter is the value resulting in min(χ^2/NDF)+1. This was used as an criteria such as only parameter sets resulting in min(χ^2/NDF)+1 (of the global min(χ^2/NDF) for 6MV and 15MV, respectively) were accepted for further calibration. χ^2/NDF for a fixed mean energy (6.0 and 15.5 MeV) and mean angular divergence (0.0 and 0.4°) as a function of varying (circular) spot size FWHM are shown in Figure 23. A single, global, minima is identifiable for each data set and about that minima the χ^2/NDF is monotonically increasing (except for the smallest spot size FWHM for the 6MV mode).

Relative Output Factors

Special attention must also be given to the agreement between measured and simulated ROF. IC measured ROFs (normalized to 10×10 cm^2) was measured using a Wellhöfer/IBA CC13 ion chamber, with a sensitive volume of 0.6 cm^3, in an otherwise homogenous water phantom, for a range of field sizes at a depth of 10 cm and with SSD

Table 3: Parameter sets resulting in local minima of χ^2/NDF, while still fulfilling the acceptance criteria for further calibration.

Name	Mean energy (MeV)	Spot size FWHM: X (cm)	Spot size FWHM: Y (cm)	Mean angular divergence (°)
		6MV		
6a	5.70	0.250	0.250	–
6b	5.80	0.250	0.225	–
6c	5.90	0.175	0.175	–
6d	6.00	0.175	0.175	–
		15MV		
15a	15.00	0.150	0.150	0.20
15b	15.25	0.125	0.150	0.30
15c	15.50	0.125	0.125	0.40

90 cm. MC simulations[12] were conducted in a homogenous water phantom were the dose to a voxel of 0.6 cm^3 at 10 cm depth, with SSD 90 cm, was scored for a range of field sizes (3×3, 5×5, 10×10, 15×15 and 20×20 cm^2). The ROFs were calculated as the ratio between the dose at a given field size and that of 10×10 cm^2. The simulated ROFs were multiplied by the corresponding measured back scatter correction factor in order to compensate for backscatter to the monitor chamber (see Section 5.1). The relative deviation between simulated and measured ROF (Figure 24) were computed through:

$$\left(\mathrm{ROF}_{\mathrm{MC}} - \mathrm{ROF}_{\mathrm{measured}}\right)/\mathrm{ROF}_{\mathrm{measured}} \times 100. \tag{3.3}$$

The parameter set resulting in the smallest summed absolute value of the relative difference was selected for further calibration. The parameter sets were 6d and 15b (The full parameter sets are given in Table 3) for 6MV and 15MV, respectively.

40×40 cm^2 lateral profiles revisited

Figure 9 illustrate that lateral profiles are sensitive to changes in spot size FWHM. Small changes in spot size FWHM on one of the axes

12 DOSXYZnrc was used for phantom simulation with a voxel size of 0.8434×0.8434×0.8434 cm^3. The number of histories were chosen so that the statistical uncertainty at 10 cm depth along the CAX was 0.5%. Simulation properties were ECUT = 521 keV, PCUT = 10 keV, nsplit = 25, esplit = 25 and howfarless turned on. The treatment head was simulated using source 9 in DOSXYZnrc. Simulation properties were ECUT = 700 keV, PCUT = 10 keV, direction bremsstrahlung splitting was used (FS was set equal to the length of the square field and SSD = 100), NBRSPL was set to 1000, with the splitting plane for electrons (ZPLANE_DBS) defined as the bottom of the flattening filter and russian roulette conducted for electron at a plane 0.20 cm above the bottom of the flattening filter.

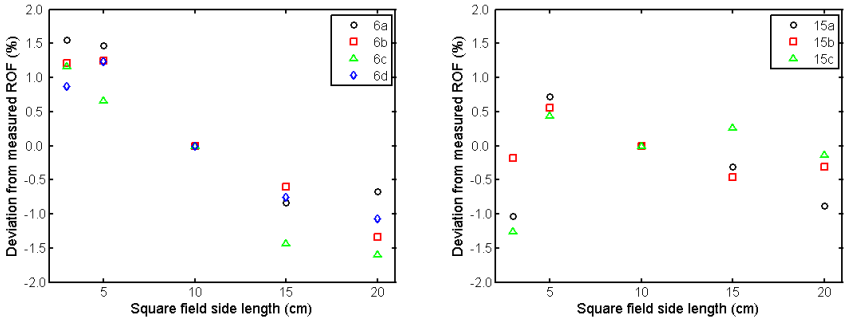

Figure 24: Relative deviation between simulated and measured ROF for 6MV (left) and 15MV (right). The full parameter sets are given in Table 3

affects the profile lined up with that axes, while the orthogonal profile is rather unaffected (Figure 25). Thus the X–and Y–spot size FWHM can be tuned individually. The selected parameter sets were fine tuned by varying the parameters individually, while keeping the others fixed. As small changes of mean energy is not detected on 40×40 cm^2 lateral profiles it was not further tuned. The remaining parameters were thus: spot size FWHM in X– and Y–direction as well as mean angular divergence (for 15MV mode only). The spot size FWHM in X–and Y–direction was varied independently of each other and thus allowing for an elliptical source. Simulations[13] were conducted for a resolution of 0.05 cm and 0.05° on spot size FWHM and mean angluar divergence, respectively. χ^2/NDF tests were conducted as previously and the parameter minimizing the χ^2/NDF was selected and used in the tuning process of the latter parameters. The order of the fine tuning process were: spot size FWHM in X–direction, spot size FWHM in Y–direction and mean angular divergence (for 15MV mode only).

An acceptance criteria similar to that for 10×10 cm^2 PDDs were posed such that the slope of a linear fit to the ratio between the measured and simulated curve was computed. A ratio <1.0% was sought over [0;20] cm lateral distance form the CAX. In order to fulfill this criteria, the slope of the ratio needs to be less than $0.01 D_{max}$ cm^{-1}. The selected range of consideration was [0;20-3 cm] and [0;20-5 cm] for 6MV and 15MV, respectively. Within this range, lateral CPE will exist, and the diode reading is reliable.

13 DOSXYZnrc was used for phantom simulation with a voxel size of 0.25×0.25×0.5 cm^3. The number of histories were chosen so that the statistical uncertainty along the CAX was 0.5–0.7% at 3–15 cm depth. Simulation properties were ECUT = 761 keV, PCUT = 10 keV, nsplit = 25, esplit = 25 and howfarless turned on. The treatment head was simulated using source 9 in DOSXYZnrc. Simulation properties were ECUT = 700 keV, PCUT = 10 keV, direction bremsstrahlung splitting was used (FS = 40, SSD = 100), NBRSPL was set to 1000, with the splitting plane for electrons (ZPLANE_DBS) defined as the bottom of the flattening filter and russian roulette conducted for electron at a plane 0.20 cm above the bottom of the flattening filter.

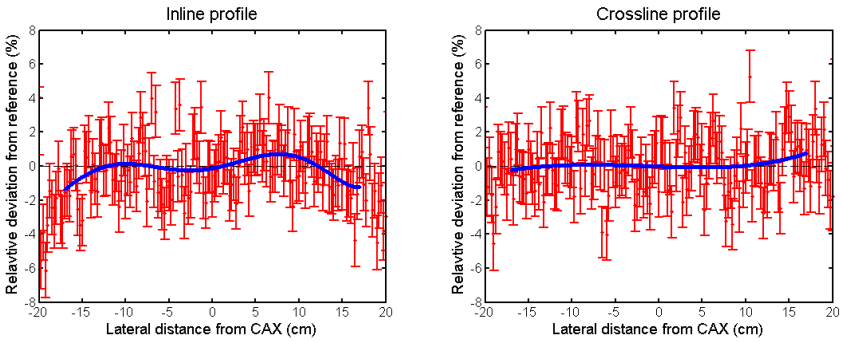

Figure 25: Local relative difference between 40×40 cm^2 lateral profiles with spot size FWHM set to 0.15 and 0.20 cm respectively (mean energy = 6.00 MeV, spot Size FWHM 0.175 in X–direction). Comparison was made at 10 cm depth. Included in the figure is a line representing identical profiles (dashed black) and a four degree polynomial fit to the results (blue). It can be seen that the inline profiles are affected in the entire range [-15; 15] cm and predominantly so with increasing distance from the CAX, while the crossline profile is affected only at the very edges of the range and to a smaller degree.

Table 4: Parameter sets producing best agreement with measurements, by means of χ^2/NDF test, after the final fine tuning of spot size FWHM (for X– and Y–direction separately) and mean angular divergence.

Nominal Energy (MV)	Mean energy (MeV)	Spot size FWHM: X (cm)	Spot size FWHM: Y (cm)	Mean angular divergence (°)
6	6.00	0.155	0.170	–
15	15.25	0.130	0.140	0.35

Agreement with measurement using the slope of difference/acceptance criteria were -0.2/0.6 for the 6MV model in X– and Y– direction, respectively and 0.4/0.1 for the 15MV model in X– and Y– direction, respectively and thus well within the criteria of <1.0% difference over [0;20] cm (a slope of difference/acceptance criteria <|1| correspondce to having met the criteria).

The parameter sets resulting in the best agreement with measurements are given in Table 4.

10×10 cm^2 CAX PDDs revisited

Following the fine tuning of the parameter set, the 10×10 cm^2 CAX PDDs were resimulated[14] in order to verify that the agreement with measurement had not been invalidated. Measured and simulated PDDs along CAX are shown in Figure 26. Most data points agree within ±0.5%. The scatter of the difference is larger with increasing depth due to the increased uncertainty of the individual voxels with depth. Agreeemnet with measurement using the slope of difference/acceptance criteria (as descirbed in section 3.3) were -0.4 and 0.5 for 6MV and 15MV, repsecitively and thus well within the crietria of <0.5% difference over (0,40) (a slope of difference/acceptance criteria <|1| correspondce to having met the criteria).

Relative Output Factors revisited

ROFs were resimulated[15] using the final pramtere set and compared to IC measurements. Simulated ROFs were multiplied by measured BSF to account for field size dependant monitor chamber backscatter. Measured and simulated ROFs as well as deviation between the two are shown in Figure 27. Measured and simualted ROFs agreed within the statistical uncertainty from the simulations. A trend is observed for the 6MV, where simulated ROFs for field sizes < 10×10 cm^2 are higher compared to measured and ROFs for field sizes > 10×10 cm^2 are lower. This is not seen for 15MV and might be due to the inclusion of mean angular divergence.

14 DOSXYZnrc was used for phantom simulation with a voxel size of 0.5×0.5×0.2 cm^3. The number of histories were chosen so that the statistical uncertainty along the CAX was 0.2–0.5% at 5–30 cm depth. Simulation properties were ECUT = 521 keV, PCUT = 10 keV, nsplit = 25, esplit = 25 and howfarless turned on. The treatment head was simulated using source 9 in DOSXYZnrc. Simulation properties were ECUT = 700 keV, PCUT = 10 keV, direction bremsstrahlung splitting was used (FS = 10, SSD = 100), NBRSPL was set to 1000, with the splitting plane for electrons (ZPLANE_DBS) defined as the bottom of the flattening filter and russian roulette conducted for electron at a plane 0.20 cm above the bottom of the flattening filter.

15 DOSXYZnrc was used for phantom simulation with a voxel size of 0.8434×0.8434×0.8434 cm^3. The number of histories were chosen so that the statistical uncertainty at 10 cm depth along the CAX was 0.5%. Simulation properties were ECUT = 521 keV, PCUT = 10 keV, nsplit = 25, esplit = 25 and howfarless turned on. The treatment head was simulated using source 9 in DOSXYZnrc. Simulation properties were ECUT = 700 keV, PCUT = 10 keV, direction bremsstrahlung splitting was used (FS was set equal to the length of the square field and SSD = 100), NBRSPL was set to 1000, with the splitting plane for electrons (ZPLANE_DBS) defined as the bottom of the flattening filter and russian roulette conducted for electron at a plane 0.20 cm above the bottom of the flattening filter.

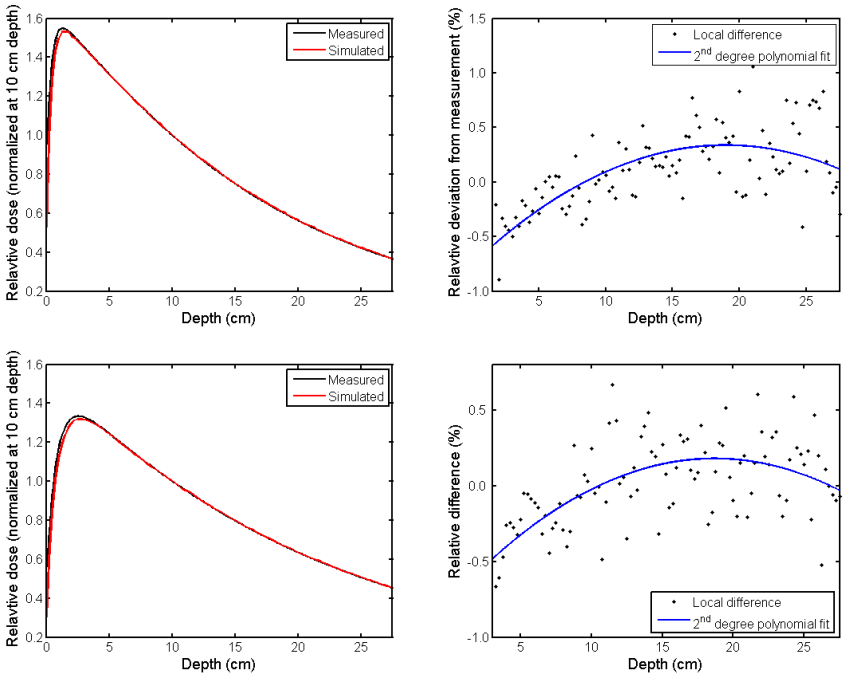

Figure 26: Simulated and measured 10×10 cm^2 PDDs for 6MV (top) and 15MV (bottom) for the final parameter set of the MC model (see Table 4). The left panel shows the PDDs while the right panel shows local relative difference (black) and a second order polynomial fit (in the range [1.5;27.5] cm and [3;27.5] for 6MV and 15MV, respectively) to the difference (blue).

3.4 THE MULTI LEAF COLLIMATOR

So far only open fields (fields collimated by the jaw collimators) have been considered. An important component for advanced radiotherapy, such as IMRT and VMAT, are the MLCs which are used as an additional collimation device. The Varian Millennium 120 leaf MLC has been hard coded in MCSIM (2.2.6), whereas it may be modelled in detail using the DYNVMLC [Heath and Seuntjens, 2003] CM in BEAMnrc. Moreover, DOSXYZnrc sources 20 and 21 [Lobo and Popescu, 2010] have the option to include an external MLC simulation (e.g. the particle dMLC transport described by Keall et al. [2001]; Siebers et al. [2002]).

Studies investigating the influence of MLC parameters on the MC dose distributions have been conducted by several groups (e.g. Belec et al. [2005]; Borges et al. [2012]; Fix et al. [2011]; González et al. [2011]; Heath and Seuntjens [2003]; Jang et al. [2006]; Kairn et al. [2010]; Keall et al. [2001]; Leal et al. [2004]; Li et al. [2010]; Pönisch et al. [2006]; Reynaert et al. [2005]; Siebers et al. [2002]; Tyagi et al. [2007]). In order to commission the MLC measurements of a 10×30 cm^2 field with fully closed MLC (at 10 cm from CAX) were conducted

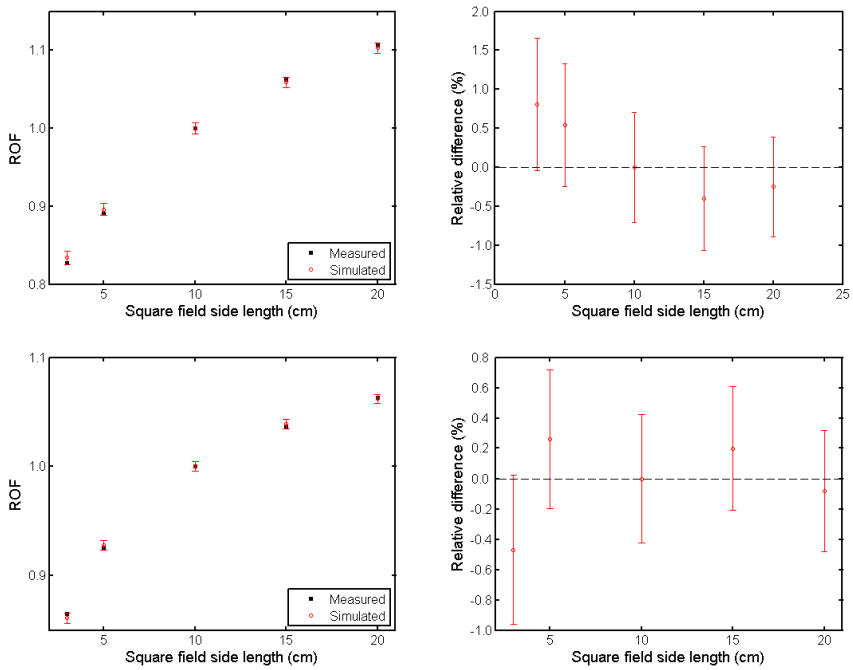

Figure 27: Simulated and measured ROFs for 6MV (top) and 15MV (bottom) for the final parameter set of the MC model (see Table 4). The left panel shows the ROFs while the right panel shows local relative difference (red). Included in the residual plots are also a line corresponding to perfect agreement (dashed black).

using GafChromic EBT film (International Specialty Products, NJ, USA) placed at 5 cm depth in a Gammex 457 solid water phantom (Gammex–RMI, Nottingham, UK) with an SSD of 95 cm and irradiated for 4000 MU. The film was read with a flatbed Epson (Seiko Epson Corporation, Nagano, Japan) 4990 scanner the day after irradiation (as to prevent any effect of post–exposure density growth). The scan was conducted at resolution of 72 dpi (0.35 mm per pixel) as recommended by Ferreira et al. [2009]. The optical density was converted to dose using a calibration curve obtained during the same measurement session.

MC simulation corresponding to the measurements were utilized in order to commission the MLC. The procedure differed between the two MC codes due to the inherent differences in the codes. The procedure is described below for each of the two MC codes in turn.

Commissioning of the hard coded MLC in MCSIM consists of fitting the two parameters MLC–transmission and MLC–leakage to measurements. The former parameters defines the fraction of radiation that passes through an MLC leaf while the latter corresponds excess radiation due to interleaf leakage Department of Radiation Oncology, Fox Chase Cancer Center [2008]. The commissioning process of the MLC in MCSIM is reduced to finding the combination of MLC transmission

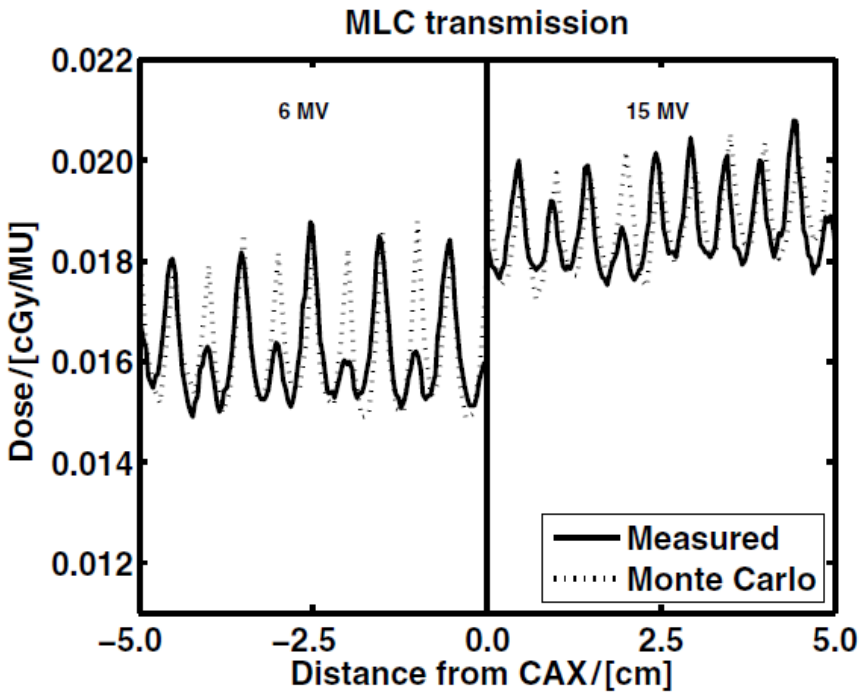

Figure 28: Lateral dose profiles for a 10×30 cm^2 field with a fully closed MLC. The film measurements illustrate a leaf pair effect (most distinguished for 6 MV) that was not reproduced by the MCSIM simulations.

and leakage that results in agreement with measurements. Specifically, simulations of a field with fully closed leaves was compared with film measurements. The field size was 10×30 cm^2 and all leaf pairs were fully closed 10 cm off CAX. Corresponding simulations were performed, using a voxel size of $2.0\times0.1\times0.5$ cm^3 for 9×10^9 histories with cut off energies of 521 keV (including rest mass) and 10 keV for electrons and photons, respectively. The only variance reduction technique switched on was IETRACK (electron track repeating). The parameters resulting in the best match to measurements (Figure 28) are given in Table 5. The parameters agree well with the findings reported by Galvin et al. [1993], where the reported transmission through the MLC, for 6MV and 15MV of a Varian 2100C linac, was approximately 2% and and additional 0.5% due to interleaf leakage. Klein et al. [1995] reported an MLC transmission of 1.5–2.0% for 6MV and 1.5–2.5% for 18MV for the same accelerator. The slightly increase in transmission with energy is concurrent with the findings of this study.

The drawings provided by the manufacturer [Varian Medical Systems, 1999; Varian Oncology Systems, 2008] holds detailed information on the MLC dimensions but not on the composition and density. The commissioning of the MLC as modelled in BEAMnrc using the DYNVMLC CM is therefore reduced to finding the composition and density resulting in agreement between measurements and simulations. The

Table 5: MLC transmission and leakage parameters for MCSIM

	MLC transmission	MLC leakage
6MV	0.015	0.022
15MV	0.017	0.025

composition used by Heath and Seuntjens [2003], a tungsten alloy consisting of 90% tungsten, 6% nickel, 2.5% copper and 1.5% iron, was used to model the MLC also in this study. Simulations[16], corresponding to the EBT film measurement, were then conducted with the density varyied between 17.0 and 18.8 g cm^{-3} in steps of 0.1 g cm^{-3}. The simulated dose was converted to absolute dose per MU by Equation 5.3 where the BSF was accounted for by means of I_{target} measurements. The density resulting in best agreemenet, by means of visual inspection, with measurements was selected. Figure 29 shows measured and simulated MLC transmission/leakage profiles for the 6MV mode. It can clearly be seen that an increased MLC density leads to a reduction in MLC transmission, as expected. The density resulting in the best agreemenet with measurements was 17.3 g cm^{-3}. The density is slightly lower than that found by Heath and Seuntjens [2003] (17.7 g cm^{-3}) but within what is recommended for MLCs by Boyer et al. [2001] (17.0 – 18.5 g cm^{-3}). The difference compared to Heath and Seuntjens [2003] may be due to differences in the actual MLC, in the drawings or in the implementations of the them. A transmission of 0.015 $cGyMU^{-1}$ is equivalent to a transmission of 1.5%, which is in agreement with the findings of Galvin et al. [1993] and Klein et al. [1995]. A transmission/leakage profile was simulated for 15MV using the same parameters (Figure 29). Satisfactory agreement with measurement was found at a slightly higher transmission rate as expected.

The same composition and density was used for the particle DMLC code but no dedicated commissioning simulation was conducted.

The inner 40 leaf pairs of the Varian Millennium 120 leaf MLC are arranged in an alternating pattern of two leaf types. This design results

16 A homogeneous Gammex solid water phantom with voxel sizes $2.0 \times 0.1 \times 0.25$ cm^3 with SSD = 95 cm was defined in DOSXYZnrc. The number of histories were chosen so that the statistical uncertainty at 5 cm depth was ≈1%. Simulation properties were ECUT = 521 keV, PCUT = 10 keV, nsplit = 25, esplit = 1 and howfarless turned on. The treatment head was simulated using source 9 in DOSXYZnrc. Simulation properties were ECUT = 700 keV, PCUT = 10 keV, direction bremsstrahlung splitting was used (FS = 30 cm and SSD = 100), NBRSPL was set to 1000, with the splitting plane for electrons (ZPLANE_DBS) defined as the bottom of the flattening filter and russian roulette conducted for electron at a plane 0.20 cm above the bottom of the flattening filter.

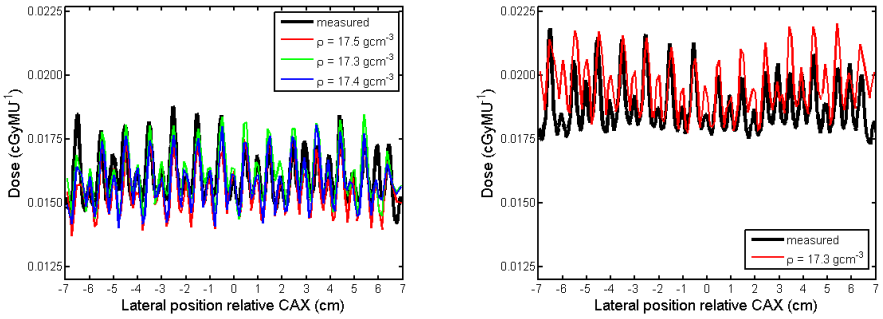

Figure 29: Measured (black) and simulated lateral dose profiles for a 10×30 cm^2 field with a fully closed MLC for 6MV (left) and 15MV (right). Some simulations have been excluded from the visualization as to increase readability of the figure.

in transmission and leakage profiles resembling a saw–blade pattern with alternating tooth heights Heath and Seuntjens [2003]; Siebers et al. [2002] as seen in the film measurements (Figure 28). The effect was most distinguished for 6 MV. Due to limitations in leaf shape modeling, the MCSIM simulations did not reproduce this pattern. However, the average leaf leakage effect agreed well between film measurements and simulations (Figure 28). The influence of this on dose distribution of clinical IMRT and VMAT plan is hard to estimate but assumed to be small and not considered further in this study. The MLC transmission/leakage profile simulated using DOSXYZnrc and DYNVMLC was able to reproduce the saw tooth pattern to a much higher degree (Figure 29).

3.5 VERIFICATION

In order to verify the accuracy of the MC model, simulation of a range of different situations were conducted and compared to measurements. The measurements were conducted as described on page 51. Additional measurements were conducted using Gafchromic EBT 2 film placed in a Gammex 457 solid water phantom ($30 \times 30 \times 30$ cm^2) and an in–house developed ME40 Scintillator Dosimetry System (DTU, Roskilde, Denmark). The ME40 system functions by connecting Burr–Brown ACF2101 switched integrator circuits [Mountford et al., 2008] to the SYNC BNC contact of the linac. The charge built up in a 100 pF capacitor is held, integrated, and read out before it is reset at the onset of the next synchronization pulse. The detector used was a 1 mm diameter, polystyrene–based scintillating fibers (BCF-60, Saint–Gobain Ceramics & Plastics Inc., France). The scintillating fibers were cut to a length of 1 mm and coupled to PMMA–based optical fibers (ESKA GH-4001P, Mitsubishi-Rayon Co.,Japan) of 1 mm core diameter, 2.2

mm outer jacket diameter and approximately 10 m length, terminated by an SMA connector. Before coupling, the exposed ends of the scintillator and the optical fiber were polished using aluminum oxide polishing paper of 5, 3, 1 and 0.3 µm grain size (Thorlabs Sweden AB, Göteborg, Sweden) and cleaned using water and pressurized air. The two components were aligned using a mechanical fixation mount and a stereo microscope, before making the coupling permanent using UV-curing, refractive index-matching glue (NOA68, Norland Products Inc., USA). Finally, a jacket of black epoxy cement (EPOTEK 320, EpoxyTechnology Inc., USA) was molded around the exposed junction to light–tighten the probe. The fiber cable was placed in a Gammex 457 solid water phantom (30×30×30 cm^3) with a groove, ensuring a snug fit for the scintillator probe, drilled in on of the slabs. That slab was placed at the desired measurement depth. In order to ensure positioning the scintillator was replaced with a lead piece of the same size. The beam isocenter was aligned with the lead piece using the positioning lasers as a first estimate. The actual position of the beam isocenter was relative to the lead marker was investigated by taking a portal image, using the linac On–Board Imaging (OBI) device. In case of an offset, the solid water phantom was carefully repositioned to correct for the offset. A second portal image was acquired in order to verify the positioning. If the lead piece still was not aligned with the beam isocenter, the procedure was reiterated until agreement.

MC simulations reproducing the measurements were conducted using the model parameters listed in Table 4.

PDD

Simulated[17] 6MV and 15MV CAX PDDs, for the field sizes 5×5, 10×10 and 20×20 cm^2, were compared to measurements using a Wellhöfer-/IBA CC13 (IBA Dosimetry AB, Uppsala, Sweden) Ionization Chamber (0.13 cm^3 active volume) (Figure 30–31). The PDDs were normalized at 10 cm depth, using a forth degree polynomial fit in the [5;15] cm region and multiplied by their respective, measured, ROF. The results demonstrate that agremment within 1% was achieved beyond d_{max} in all but a few voxels and within 2% the remaining voxels. An overrepsonce of the IC, compared to the MC simulation, was consistently noted in the build–up region. It is a well known fact that measurements using plane parallel [Velkley et al., 1975] as well as thimble–type

17 DOSXYZnrc was used for phantom simulation with a voxel size of 1.0×1.0×0.25 cm^3. The number of histories were chosen so that the statistical uncertainty along the CAX and beyond d_{max} was 0.3–0.6%. Simulation properties were ECUT = 700 keV, PCUT = 10 keV, nsplit = 25, esplit = 25 and howfarless turned on. The treatment head was simulated using source 9 in DOSXYZnrc. Simulation properties were ECUT = 521 keV (700 keV for the collimating jwas), PCUT = 10 keV, direction bremsstrahlung splitting was used (FS set equal to the side length of the square field, SSD = 100) and NBRSPL was set to 1000.

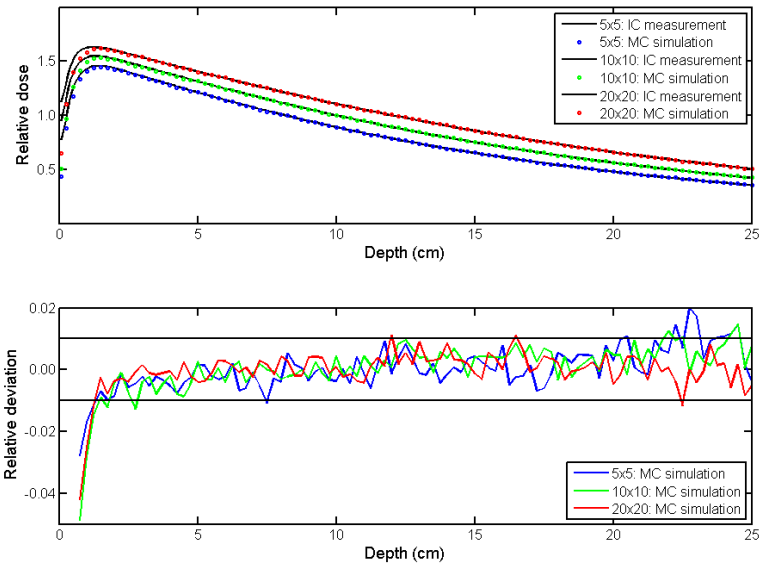

Figure 30: **Top:** Measured (solid line) and simulated (circles) 6MV PDD for 5×5 (blue), 10×10 (green) and 20×20 (red) cm^2. All curves were normalized at 10 cm depth, using a forth degree polynomial fit in the [5;15] cm range, and multiplied by the ROF of that field size. **Bottom:** relative deviation between MC simulated and measured 6MV PDDs for 5×5 (blue), 10×10 (green) and 20×20 (red) cm^2.

ion chambers [Zhu, 2010] leads to a substantial overestimation of the dose in the build–up region unless dedicated corrections are made. In fact, the suggested correction for thimble ion chamber measurement of an effective point of measurment shift of $0.6 \times r_{detector}$ [Almond et al., 1999; Andreo et al., 2000] might be inaccurate [Kawrakow, 2006; Tessier and Kawrakow, 2010]. The agreement for depths shallower than d_{max} should therefore not be considered in Figure 30–31.

In order to further investigate the validity of the MC model in the build up region measurements were conducted for a 10×10 cm^2 field impinging on a homogenous PMMA phantom described in Behrens [2006]. A Capintec PS–033 plane–parallel ionization chamber (Capintec, Inc. , New York, USA) was used to measure dose in steps of 1 mm from 0 mm to 31 mm depth. The plane–parallel chamber will over respond in the the build up region due to secondary electrons scattered from the walls of the chamber [Velkley et al., 1975]. Gerbi and Khan [1990] reported a correction method for the chamber in question by comparison with measurements conducted with an extrapolation chamber. For a given beam quality the correction the detector reading can be corrected through:

$$P'(d) = P(d) - \xi(d) \qquad (3.4)$$
$$\xi(d) = \xi(0) e^{-\alpha(d/d_{max})}$$

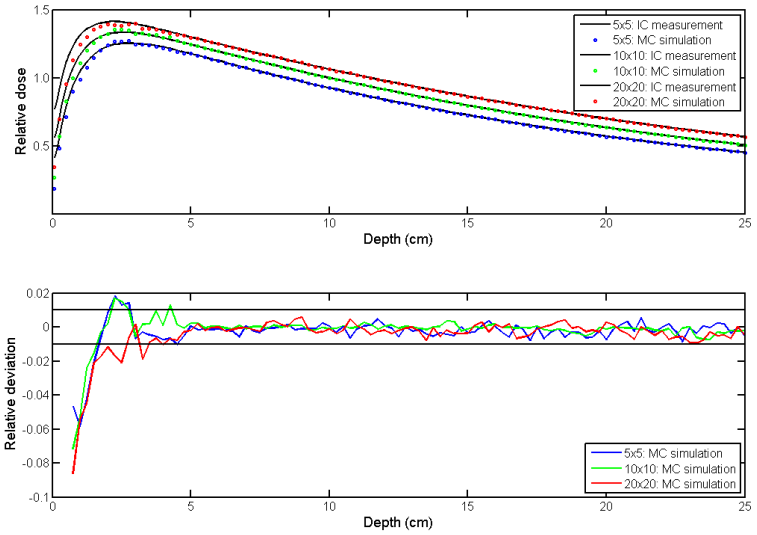

Figure 31: **Top:** Measured (solid line) and simulated (circles) 15MV PDD for 5×5 (blue), 10×10 (green) and 20×20 (red) cm^2. All curves were normalized at 10 cm depth, using a forth degree polynomial fit in the [5;15] cm range, and multiplied by the ROF of that field size. **Bottom:** relative deviation between MC simulated and measured 15MV PDDs for 5×5 (blue), 10×10 (green) and 20×20 (red) cm^2.

where $P'(d)$ and $P(d)$ are the corrected and uncorrected measurements, respectively, and the latter must be normalized to 100% at d_{max}, $\xi(d)$ is the over response at depth d. Gerbi and Khan [1990] proposed to use $\alpha = 5.5$ and $\xi(0) = 4.4$ for the Capintec PS–033 plane–parallel ionization chamber. This correction method was applied to the measurements.

Measurements were also conducted using the ME40 system in the same geometry. Simulations were conducted using the EGSnrc user code DOSrz[18] where dose to PMMA was scored. The dose was normalized to the maximum dose for each curve independently.

The comparison between MC and measurements are shown in Figure 32. Deviation of ≈10% are noted at the very surface, but already at 5 mm depth the deviation is < 2% between MC and any of the measurement systems. The deviation is within 1% for nearly all, and well within 2% for all, of the depths beoynd 6 and 10 mm for 6 MV and 15 MV, respectively.

18 A PMMA phantom of 30 cm depth and an outer radius of 15 cm was used. The central region had a radius of 0.24 cm and the slab thickness was 0.25 cm. The number of histories were selected so that the uncertainty along the CAX was ≈0.7% in the [0,5] cm depth range. Cut off energies were set to 521 keV (including rest mass) and 10 keV for electrons and photons, repsectively. The treatment had was simulated using source 23 (full treatment head simulation) and simulation properties were ECUT = 521 keV (700 keV for the collimating jwas), PCUT = 10 keV, direction bremsstrahlung splitting was used (FS = 10, SSD = 100) and NBRSPL was set to 1000.

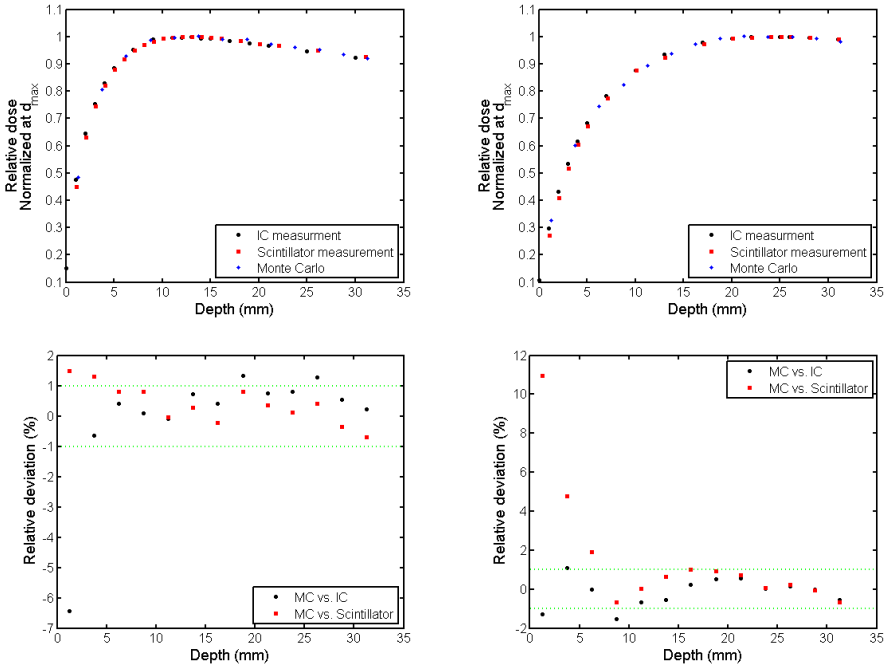

Figure 32: **Top panel**: 10×10 cm^2 field CAX PDD in a PMMA phantom measured with a Capintec PS–033 ionization chamber (black), the ME40 Scintillator system (red) and MC simulated (blue) for 6 MV (left) and 15 MV (right), respectively. **Bottom panel**: Relative local deviation between MC and IC measurements (black) and MC and scintillator measurements (red) for 6 MV (left) and 15 MV (right), respectively. Shown in the figure are also lines corresponding to ±1% deviation (green).

Lateral profiles

Simulated[19] lateral profiles field sizes the following field sizes: 5×5, 10×10 and 20×20 cm^2 were selected for verifaction. Comparisons were conducted with diode, Scanditronix/IBA PFD^{3G} (IBA Dosimetry AB, Uppsala, Sweden) Si–photon diode, measurements.

Agreement between MC simulation and diode measurements was generally within 1% in the regions where CPE exists. Figure 33–40

19 DOSXYZnrc was used for phantom simulation with a voxel size of 0.25×0.25×0.5 and 0.1×0.1×0.5 cm^3. The number of histories were chosen so that the statistical uncertainty along the CAX was 0.5–0.7% at 5–20 cm depth. Simulation properties were ECUT = 521 keV, PCUT = 10 keV, nsplit = 25, esplit = 25 and howfarless turned on. The treatment head was simulated using source 9 in DOSXYZnrc. Simulation properties were ECUT = 700 keV, PCUT = 10 keV, direction bremsstrahlung splitting was used (FS set equal to the side length of the square field at SSD = 100), NBRSPL was set to 1000, with the splitting plane for electrons (ZPLANE_DBS) defined as the bottom of the flattening filter and russian roulette conducted for electron at a plane 0.20 cm above the bottom of the flattening filter.

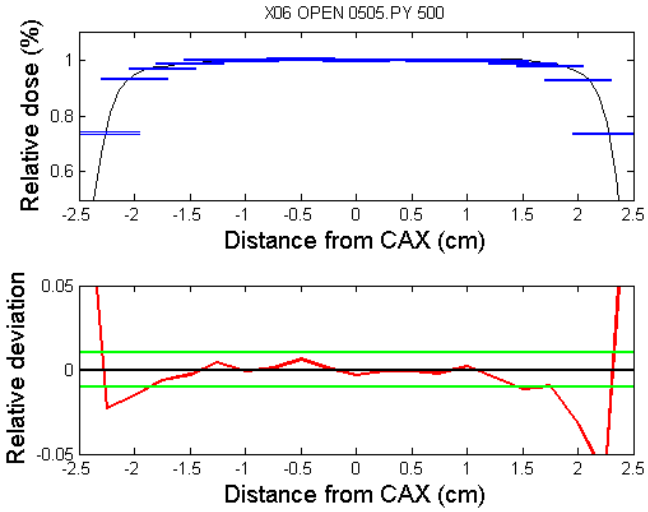

Figure 33: **Top:** Measured (black) and simulated (blue) lateral crossline profile for 6MV, field size = 5×5 cm^2 and at 5 cm depth. Both curves were normalized at the central axis, using a second degree polynomial fit in the inner [-1.25;1.25] cm region. The errorbars on the MC simulated dose correspond to the statistical uncertainty (as calculated by EGSnrc). **Bottom:** relative deviation between the MC simulated and measured profile (red). Lines representing ideal agreement (black) as well as ±1% (green) are also shown.

show measured and simulated profiels as well as residuals for a number of field sizes and depths.

ROF

ROFs were measured for field sizes ranging from 10×10 cm^2 to 0.6×0.6 cm^2, using the ME40 Scintillator Dosimetry System, and simulated[20]. The combined uncertainty of the simulatied and measured ROFs was ≈1% for a given field size. Agreement between measurements and simulations were found, within the given relative combined uncertainty, for all field sizes except the smallest where the deviation was 1.5% (Figure 41). It should be noted that effect of positioning errors increases with decreasing field size and was estimated to be 6% for a 1 mm displacement for the 0.6×0.6 cm^2 field [Beierholm et al., 2011]. The field size was not verified specifically for the measurements.

20 A phantom mimicking the measurement situation was built in DOSXYZnrc (see Figure 42). The number of histories were chosen so that the statistical uncertainty to the scintillator crystal was ≈0.5%. Simulation properties were ECUT = 521 keV, PCUT = 10 keV, nsplit = 25, esplit = 25 and howfarless turned on. The treatment head was simulated using source 9 in DOSXYZnrc. Simulation properties were ECUT = 700 keV, PCUT = 10 keV, direction bremsstrahlung splitting was used (FS set equal to the side length of the square field for field sizes ⩾ 5×5 cm^2 and to 5 cm for field sizes < 5×5 cm^2, SSD = 100

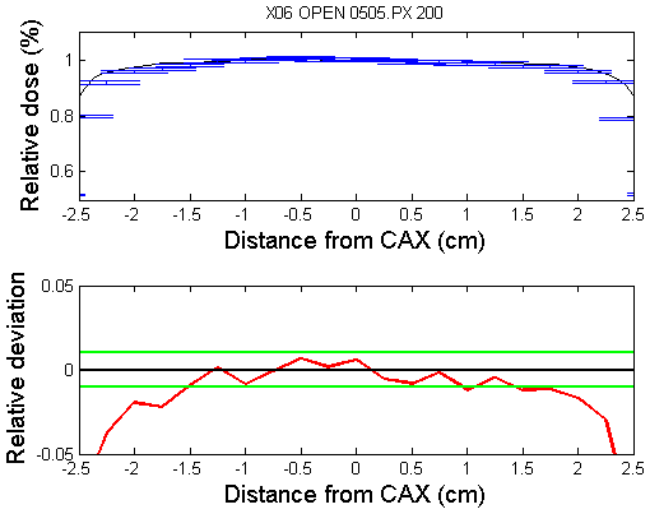

Figure 34: **Top:** Measured (black) and simulated (blue) lateral inline profile for 6MV, field size = 5×5 cm^2 and at 20 cm depth. Both curves were normalized at the central axis, using a second degree polynomial fit in the inner [-1.25;1.25] cm region. The errorbars on the MC simulated dose correspond to the statistical uncertainty (as calculated by EGSnrc). **Bottom:** relative deviation between the MC simulated and measured profile (red). Lines representing ideal agreement (black) as well as ±1% (green) are also shown.

SUMMARY ON THE COMMISSIONING

Previous studies state that the parameters necessary to tweak during calibration of the MC model are the mean energy, spatial distribution and mean angular divergence of the electrons impinging on the linac target. Consensus is not found on what situations to compared simulations to measurements for in order to determine the values of said parameters.

A sensitivity analysis was conducted and it was found that PDDs are somewhat sensitive to changes on the mean energy, but in principle insensitive to the other parameters of interest. Wide–field lateral profiles are on the other hand sensitive to all of the three parameters (i.e. the mean energy, spatial distribution and mean angular divergence of the impinging electrons) and in fact more sensitive to changes on the mean energy than PDDs. Changes on the spatial distribution and mean angular divergence of the impinging electrons affected the distal and central parts of the wide–field profiles, respectively (see Figure 9 and Figure 12), while changes on the mean energy affects the entire profile (see Figure 10).

As oppose to determining each parameter individually a calibration protocol where a data space containing a range of combinations were compared to measurements for a 40×40 cm^2 field using a χ^2–test. All parameter combinations fulfilling an acceptance criteria were selected

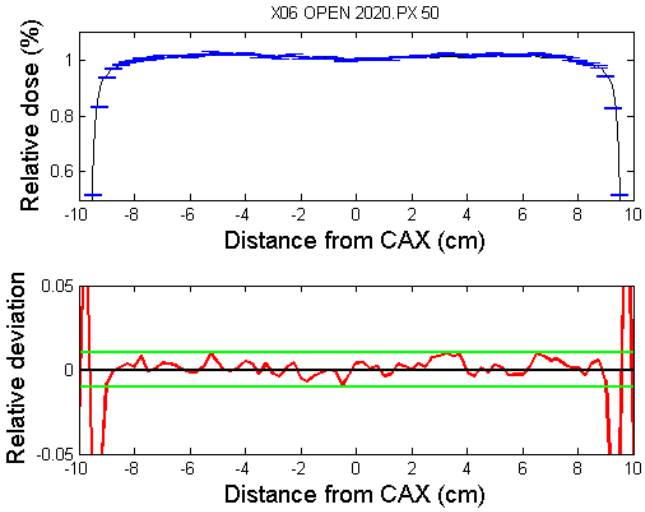

Figure 35: **Top:** Measured (black) and simulated (blue) lateral inline profile for 6MV, field size = 20×20 cm^2 and at 5 cm depth. Both curves were normalized at the central axis, using a second degree polynomial fit in the inner [-2.0;2.0] cm region. The errorbars on the MC simulated dose correspond to the statistical uncertainty (as calculated by EGSnrc). **Bottom:** relative deviation between the MC simulated and measured profile (red). Lines representing ideal agreement (black) as well as ±1% (green) are also shown.

for further investigation. ROF for a wide range of field sizes (3×3 to 20×20 cm^2) were computed and compared to measurements for all selected parameter combinations. The set of parameters yielding closest agreement with measured ROFs were then selected. The validity of the selected mean energy was verified for a 10×10 cm^2 PDD, while the spatial distribution and mean angular divergence of the impinging electrons was fine tuned individually by comparison against a 40×40 cm^2 field. ROF were then resimulated, using the fine tuned parameter set, and compared to measurements.

Verification was conducted for PDDs and lateral profiles of different field sizes, small field ROF and dose in the build up region of a 10×10 cm^2 field. The agreement with measurements was generally within 1–2%. The acceptance criteria, ±0.5% for 10×10 cm^2 PDD in the [0;40] cm range and ±1.0% for 40×40 cm^2 lateral profiles in the [0;20] cm range, were achieved. Measured ROFs were reproduced within 0.9% and 0.6% for 6MV and 15MV respectively. Morover, the MLC was commissioned seperately. This gives confidencec that any given treatment plan may be recalculated with good accuracy using the commissioned MC model.

The commissioning protocol was applied to a Varian 2300iX linac, at Copenhagen University Hospital, Herlev, using BEAMnrc/DOSXYZnrc, but could in principle be applied to any linac and MC engine.

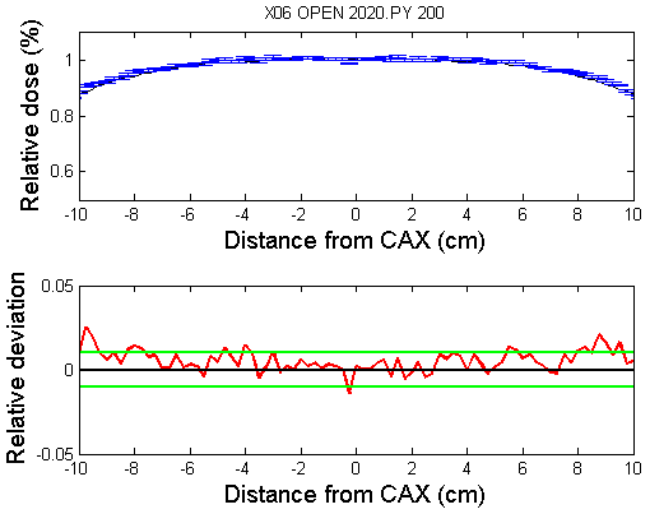

Figure 36: **Top:** Measured (black) and simulated (blue) lateral crossline profile for 6MV, field size = 20×20 cm^2 and at 20 cm depth. Both curves were normalized at the central axis, using a second degree polynomial fit in the inner [-2.0;2.0] cm region. The errorbars on the MC simulated dose correspond to the statistical uncertainty (as calculated by EGSnrc). **Bottom:** relative deviation between the MC simulated and measured profile (red). Lines representing ideal agreement (black) as well as ±1% (green) are also shown.

The geometry provided by the vendor was considered accurate and implemented from the provided drawings. Incomplete knowledge of geometry and material composition (e.g. the internal linac design) does not allow MC calculation to be performed purely from "first principles". The commissioning must be based on fitting of parameters to achieve agreement with measurements as there are no other viable options.

It should also be stated that the measurements used to determine the parameters of the MC model are not independent from the measurements used in the latter verification. The influence of this on the validity and accuracy of the dose calculated by the MC model is not further discussed.

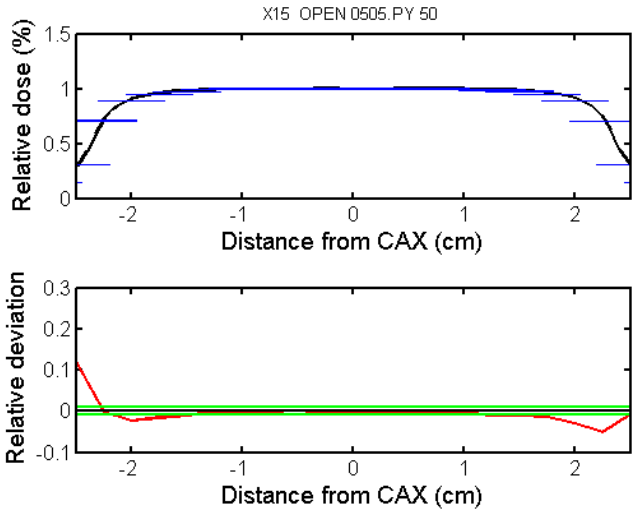

Figure 37: **Top:** Measured (black) and simulated (blue) lateral crossline profile for 15MV, field size = 5×5 cm^2 and at 5 cm depth. Both curves were normalized at the central axis, using a second degree polynomial fit in the inner [-1.25;1.25] cm region. The errorbars on the MC simulated dose correspond to the statistical uncertainty (as calculated by EGSnrc). **Bottom:** relative deviation between the MC simulated and measured profile (red). Lines representing ideal agreement (black) as well as ±1% (green) are also shown.

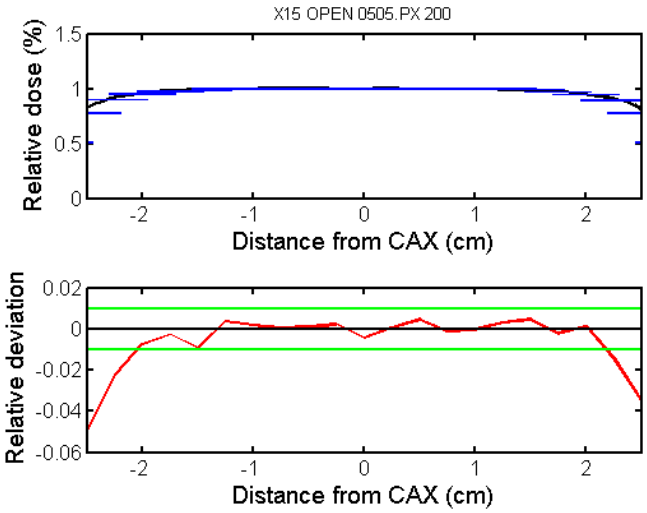

Figure 38: **Top:** Measured (black) and simulated (blue) lateral inline profile for 15MV, field size = 5×5 cm^2 and at 20 cm depth. Both curves were normalized at the central axis, using a second degree polynomial fit in the inner [-1.25;1.25] cm region. The errorbars on the MC simulated dose correspond to the statistical uncertainty (as calculated by EGSnrc). **Bottom:** relative deviation between the MC simulated and measured profile (red). Lines representing ideal agreement (black) as well as ±1% (green) are also shown.

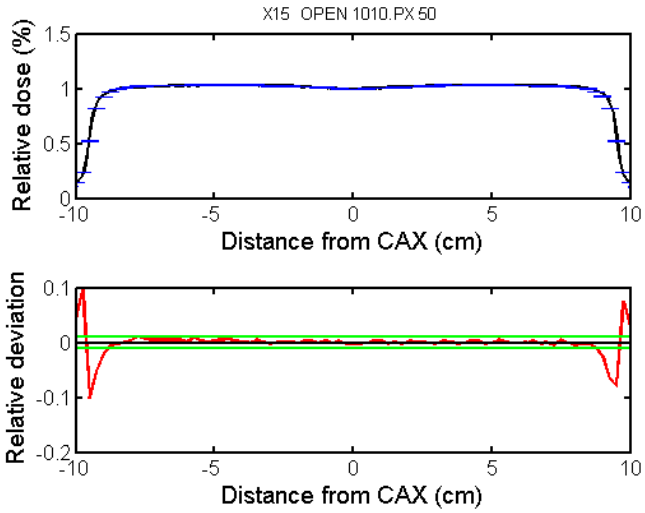

Figure 39: **Top:** Measured (black) and simulated (blue) lateral inline profile for 15MV, field size = 20×20 cm^2 and at 5 cm depth. Both curves were normalized at the central axis, using a second degree polynomial fit in the inner [-2.0;2.0] cm region. The errorbars on the MC simulated dose correspond to the statistical uncertainty (as calculated by EGSnrc). **Bottom:** relative deviation between the MC simulated and measured profile (red). Lines representing ideal agreement (black) as well as ±1% (green) are also shown.

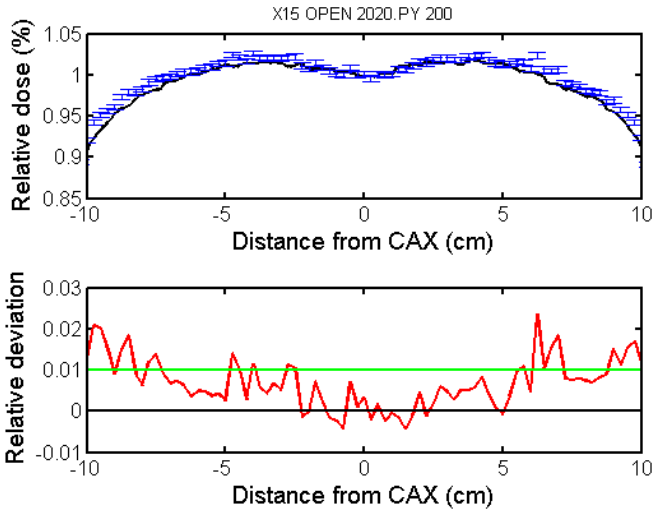

Figure 40: **Top:** Measured (black) and simulated (blue) lateral crossline profile for 15MV, field size = 20×20 cm^2 and at 20 cm depth. Both curves were normalized at the central axis, using a second degree polynomial fit in the inner [-2.0;2.0] cm region. The errorbars on the MC simulated dose correspond to the statistical uncertainty (as calculated by EGSnrc). **Bottom:** relative deviation between the MC simulated and measured profile (red). Lines representing ideal agreement (black) as well as ±1% (green) are also shown.

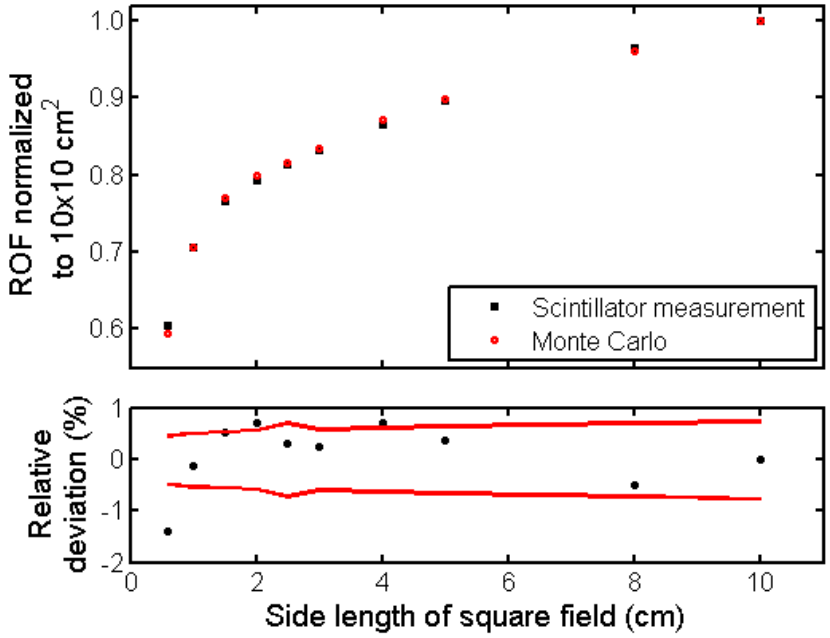

Figure 41: **Top:** ROFs, normalized to the 10×10 cm^2 field, measured using the ME40 Scintillator Dosimetry System (black) and MC simulated (red) as a function of square field side length. **Bottom:** Relative deviation between MC simulated and measured ROFs (black). Included in the figure are also lines corresponding to the statistical uncertainty of the MC simulated ROFs (red). The uncertainty of the measurements are not considered.

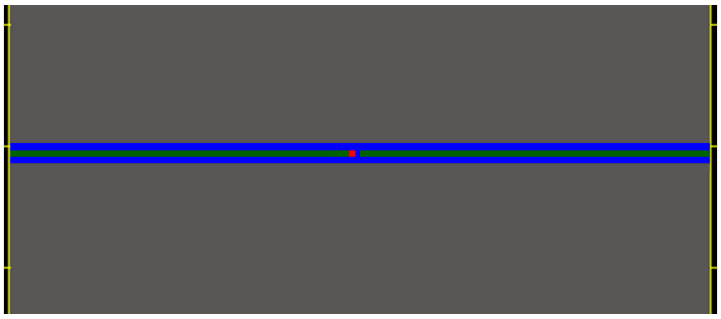

Figure 42: A schematic drawing of the geometry used for simulation of the ME40 Scintillator Dosimetry System. A 30×30×30 cm^3 Gammex 457 (grey) phantom was used. It had a 3×3 mm^2 Polyethylene (blue) outer jacket running across the phantom, a Polystyrene (red) crystal of 1×1×1 mm^3 located at (0,0,10) cm connected to a PMMA (green) optical fibers of 1×1 mm inside the outer jacket. An additional PMMA optical fibers was also placed inside the outer jacket beyond the scintillating crystal. Drawing is not to scale.

4

GENERATING THE MONTE CARLO COMPLIANT PATIENT PHANTOM

A Monte Carlo code, such as EGSnrc, computes dose based on an interaction cross–sections database, where the cross–sections depend on the particle type and energy but also on material composition and mass density of the medium. In order to perform MCTP in a patient geometry, it is therefore necessary to compute mass density as well as the (chemical) composition for each element (voxel) of the patient. The typical patient imaging modality used in radiotherapy is CT, which results in a 3D attenuation matrix of the patient. In order to build an MC compliant representation of the patient geometry it is necessary to convert the CT data to mass density and composition matrices. This topic was summarized in a MCTP review article by Reynaert et al. [2007].

4.1 CONVERSION OF CT NUMBER TO MASS DENSITY

A calibration curve linking CT numbers to mass density can be obtained by scanning different materials of known densities. The calibration curve will be a bilinear relationship divided into high–Z and low–Z materials [McCullough and Holmes, 1985]. They found an overlapping region, in which care should be taken, at HU = 100–150. Saw et al. [2005] conducted a similar study using a tissue characterization phantom, CIRS Model 062 (CIRS Tissue Simulation Technology, Norfolk, VA) which also established a bilinear relationship between CT numbers and physical density. The main difference between the studies being that McCullough and Holmes [1985] used non–tissue equivalent materials, which might explain the more distinct overlap region reported in that study. The reported point of discontinuity in the bilinear curve also varies between the two studies (HU = 0 in Saw et al. [2005] and HU = 100-150 in McCullough and Holmes [1985]). Both studies highlight the fact that calibration curves are scanner specific and that calibration therefore should be performed at each institute. This has also been reported by others (e.g. Constantinou et al. [1992] and Vanderstraeten et al. [2007]). Vanderstraeten et al. [2007] initially assigned a separate linear curve to the region [0,100] HU, but eventually concluded that they readily could be combined into a single curve representing air, lung and soft tissues together.

In this work a CIRS Model 062 phantom (CIRS Tissue Simulation Technology, Norfolk, VA, USA) was used for determination of the CT–to–density conversion relationship (figure 43). The epoxy–based

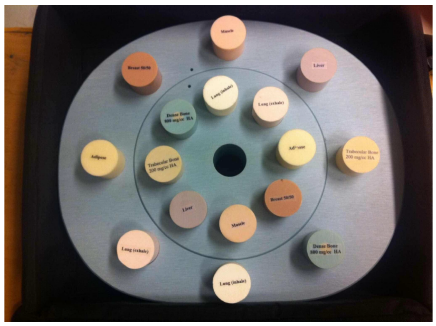

Figure 43: CIRS Model 062 phantom with tissue equivalent inserts.

phantom (ρ = 1.01 gcm^{-3}) accommodate a total of 17 inserts simultaneously.

A total of eight different tissue equivalent materials (two of each) and a water filled syringe were placed in the phantom (table 6). The phantom was placed in a Phillips Brilliance CT Big Bore (Phillips, Amsterdam, the Netherlands) such that the iso–center of the scanner was aligned with the center of the phantom. A clinical protocol with typical scanning parameters (120 kVp, 2–mm slice thickness) was selected and the scan was repeated 7 times. The CT images were read into MATLAB, using the `dicomread` function. Volume Of Interests (VOIs) were drawn around each insert for every scan. VOIs was also drawn outside of the phantom to obtain the CT number for air. The data was pooled to obtain the average CT number of each insert for the entire population of scans. The data set was fitted with linear equations for the soft tissue and bone materials, respectively:

$$\rho = 10^{-3} \times \begin{cases} 1.02H - 7.65 & : H < 55 \\ 0.58H + 467.79 & : H \geqslant 55 \end{cases} \tag{4.1}$$

The linear fits had R^2 greater than 0.99. The results are in agreement with the findings of Saw et al. [2005].

Figure 44 shows the relationship between CT numbers (H) and density. The data are plotted as the mean CT numbers[1] vs. physical densities. The size of the markers corresponds to the uncertainty in CT number (1 SD) and the average standard deviation was 15 HU.

Using dual energy CT–scanners for determination of the effective atomic numbers, Z_{eff}, and electron densities, ρ_e, in a CT–image has been suggested in several studies (e.g. [Bazalova et al., 2008; Torikoshi et al., 2003, 2004]). The mass density can subsequently be computed from the electron density through:

$$\rho = \rho_w \frac{n\rho_e}{n_w \rho_{ew}}, \tag{4.2}$$

1 I.e. the average CT number in the VOI and over all 7 scans

Table 6: Physical densities and average CT number for the scanned materials. Uncertainties on CT numbers are given as 1 SD.

Material	Physical density gcm^{-3}	CT number
Air (20 C)	1.2041×10^{-3}	-998 (±3)
Water (syringe)	1.00	-7 (±14)
Lung (inhale)	0.20	-801 (±16)
Lung (exhale)	0.50	-494 (±16)
Breast (50/50)	0.99	-33 (±16)
Liver	1.07	55 (±17)
Muscle	1.06	51 (±15)
Adipose	0.96	-64 (±16)
Trabecular Bone 200 $mgcm^{-3}$	1.16	183 (±18)
Dense Bone 800 $mgcm^{-3}$	1.53	841 (±19)

where n and n_w is the number of atomic units per electron for the specific material and water respectively and ρ_{ew} is the electron density of water [Reynaert et al., 2007]. This was not done in this study since no dual energy CT scanner was available.

4.2 CONVERSION OF CT NUMBER TO CHEMICAL COMPOSITION

Converting the CT–data to chemical composition matrix is less straight forward, since it is not possible to establish a direct relationship through measurements. It is, however, important to assign proper materials, since media assignment may heavily influences the resulting dose distribution [du Plessis et al., 1998]. Improper media assignment has been reported to lead to dose errors on the order of 10% [Ottosson and Behrens, 2011; Vanderstraeten et al., 2007; Verhaegen and Devic, 2005].

The first automated tool for conversion of CT–data to MC compliant phantoms was presented by du Plessis et al. [1998]. They demonstrated that representing the human body with seven different tissue types were enough to limit the added uncertainty on dose to within 1%. In the presented method both composition and mass density was fixed for each tissue type. For bone and lung tissues, however, additional tissue types was needed to maintain within the 1% limit. This was accomodated by creating tissue types (21 tissues corresponding to cortical bone and 31 to lung) with the same atomic composition, but different physical densities. The protocol suggested by du Plessis et al.

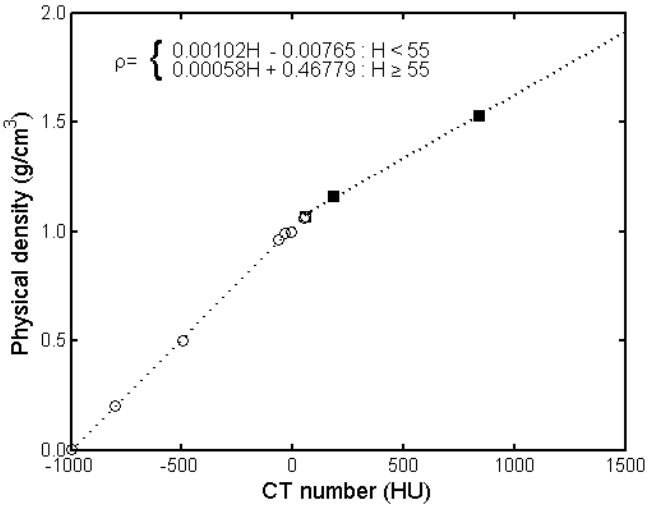

Figure 44: CT number plotted against physical density for the scanned materials for soft tissue (hollow circles) and bone material (filled squares). The size of the markers corresponds to the uncertainty in CT number (1 SD). Included in the figure are also linear fits to the data of the soft tissue and bone materials, respectively.

[1998] is limited to the beam energy under consideration and would need to be applied to all beam energies separetely.

An attempt to establish a link between composition and CT numbers was introduced by Schneider et al. [1996] and revised by Schneider et al. [2000]. It is based on a stoichiometric calibration of the CT scanner using materials of known densities and compositions. Using the stoichiometric calibration, it is possible to calculate the HU, H, for a given composition. Dividing the human tissues into soft and bone tissues, it can be noted that the bone tissues consists of a combination osseous tissue and bone marrow, whereas soft tissue mainly consists of combinations of water, fat and protein [White et al., 1987; Woodard and White, 1982, 1986]. Using the calculated H and a number of tissues with known composition (air, lung, adipose tissue 3, adrenal gland, small intestine (wall), connective tissue, red/yellow marrow and skeleton cortical bone) mass density and composition for a tissue subset of 24 different media composition were computed through:

$$\rho = \frac{\rho_1 H_2 - \rho_2 H_1 + (\rho_2 - \rho_1)\, H}{H_2 - H_1} \tag{4.3}$$

$$w_i = \frac{\rho_1\,(H_2 - H)}{(\rho_1 H_2 - \rho_2 H_1) + (\rho_2 - \rho_1)\, H}\,(w_{1,i} - w_{2,i}) + w_{2,i} \tag{4.4}$$

where media 1 and 2 are two of the basis media. $w_{1,i}$ and $w_{2,i}$ is the weight of element i in media 1 and media 2, respectively, ρ_1 and ρ_2

are the densities of media 1 and media 2, respectively and H_1 and H_2 are the HU of media 1 and media 2, respectively. Equations 4.3 and 4.4 are only valid if the basis media are chosen so that $H_1 \leqslant H \leqslant H_2$.

Vanderstraeten et al. [2007] implemented the stoichiometric calibration protocol suggested by Schneider et al. [2000] for a large number of CT–scanners and investigated the dosimetrical impact on the tissue subset selection. Moreover, they investigated the dosimetrical impact on the number of tissue types. It was found that 14 tissue types, whereof 10 corresponding to bone of different densities, was sufficient to obtain dosimetrical accuracy within 1% for photon beams. It was also found that proper diffrentiation between air and lung is the most critical task as misassignment might lead to local dose errors on the order of 10%.

4.3 ALGORITHMS FOR AUTOMATED CONVERSION OF CT–DATA TO MC COMPLIANT PHANTOMS

The method currently implemented in tools for automated conversion of CT–data to MC compliant phantoms is based on a method published by Ma et al. [1999] and Ma et al. [2002]. In short, the method consists of defining a number of bins, each corresponding to a media, over the range of CT numbers. Each bin is assigned a lower and upper value of CT number and density (this might be mass density or electron density) and the density is computed through linear interpolation. The media assignment consists of sorting the voxels on CT numbers and assigning the media corresponding to the bin it falls within. This method is implemented in algorithms for automated conversion of CT data to MC phantoms (e.g. CT–create [Walters et al., 2005] and the DICOM–RT Toolbox [Spezi et al., 2002][2]). Thus, the conversion to density might depend on the number of media and it is therefore necessary to use precaution when selecting the points and verifying them with a measured calibration curve.

The existing tools and protocols for conversion of CT data to MC parameters are limited to a global list of media, however not all medias are likely to exist within a given organ or anatomical structure (hereafter referred to as structures). This might lead to anatomically incorrect medium assignment (e.g. a dense tumor might be assigned bone in some voxels or voxels outside of the body may be classified as lung) and ultimately resulting in an error in dose. Moreover, this disables the use of media with an overlap in CT numbers, but distinct elemental compositions.

2 The conversion of CT data to MC phantom is performed by the function DICOMRT_ctcreate

4.4 CTC–ASK

A new algorithm, CTC-ask (CT create applying DICOM structure knowledge), implemented in a MATLAB software solution, enabling global density conversion using partially linear HU–to–density–relationship and local media assignment conditions within each structure was developed and is described in detail in Appendix B. Incorporation of the delineations contained in the DICOM RS file enables separation into local compartments based on anatomical regions.

4.4.1 *CTCask general work–flow*

Figure 45 illustrates the general work–flow of the program. Firstly, the CT–matrix, CT– and dose–grid are read from the DICOM files. The bilinear CT–to–density relationship is calculated based on data points submitted by the user. An option to use a pre–saved relationship is also provided. The CT matrix is globally converted to a density matrix, with a grid corresponding to the dose–grid of the DICOM RD file. The structures in the DICOM RS file are sorted according to structure types (e.g. PTV, External, Avoidance etc.) and the user is queried for structure types to be considered. A list of the structures with the desired types is created and presented to the user along with an option to exclude specific structures. The external body outline is a required structure and may not be excluded. A logical mask is generated for each selected structure, that is, a logical matrix of the same shape as the RD dose grid where true means that the voxel belongs to the specific structure. The user is requested to input names and upper CT number bounds for the possible media (hereafter refereed to as a ramp–function) for each structure (the lower CT number bound of the first medium defaults to 0, while the ith (i>1) uses the upper CT number bound of the $(i-1)$th medium). An option to use a pre–saved ramp–function is implemented. As every voxel is allowed to belong to only one structure, the program iterates over the selected structures and generates a union–structure in the regions where structure–overlaps exist. In case of structure–overlaps the ramp–function of the overlapping structures are compared. If identical, the structure–union is assigned the ramp else the user is queried to specify one. The voxels belonging to the overlapping area are set to false for the overlapping parent–structures and to true for the generated structure–union. If any unions were found during the iteration a recursive call of the function is made. Each structure undergoes a separate conversion of CT number to media based on their ramp–function. A global media list is generated and each structure correlated to the global list. An option to set voxels outside of the external body contour to air with zero density is implemented in order to emulate the procedure of treatment planning systems . The media matrices are subsequently

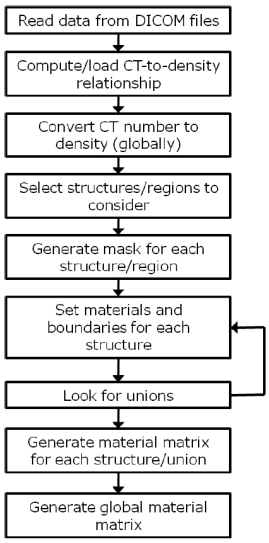

Figure 45: General work–flow of CTCask.

added to a global media matrix. Finally, the data is written to an egs4phant file.

4.4.2 *Generating a representative media set*

Using tabulated composition (NIST [2011*a*]; White et al. [1987]; Woodard and White [1986]) of a limited number of tissues and the measured relationship between density and HU it is possible to generate a representative set of media spanning the full range of HU values from air to cortical bone (Schneider et al. [2000]; Vanderstraeten et al. [2007]). The scheme suggested by Schneider et al. [2000] was adopted, with one modification: The soft tissue range was divided in accordance with Vanderstraeten et al. [2007], which assures dosimetric equivalence within 1%. In total, 19 media were generated (table 7). The first and second bins correspond to air and lung, respectively. The composition of the following bins were calculated according to equation 4.4. The integral difference between the method presented by Schneider et al. [2000] and this study is that no stochiometric calibration of the CT was conducted. The density of a media was obtained through the measured relationship (equation 4.1 and figure 44), whereas [Schneider et al., 2000] computes the density through equation 4.3. The media used for the interpolation were the same as in Schneider et al. [2000], i.e. adipose tissue 3 and adrenal gland (for bin #3), small intestine (wall) and connective tissue (for bin #4) and red/yellow marrow and cortical bone (for bins #5 through #19). The calculated compositions of the HU–bins are presented in table 7.

Table 7: The binning–schemed used for this study. The HU range was divided into 19 bins, the first corresponding to the composition of air and the second to lung. The composition of the following bins were determined by (equation 4.4) where the media used for the interpolation were adipose tissue 3 and adrenal gland (for bin #3), small intestine (wall) and connective tissue (for bin #4) and red/yellow marrow and cortical bone (for bins #5 through #19).

		Elemental weight (w_i)											
Media	HUrange	H	C	N	O	Na	Mg	P	S	Cl	Ar	K	Ca
HUrange1	-1000 – -950			75.7	23.2						1.3		
HUrange2	-950 – -100	10.3	10.5	3.1	74.9	0.2		0.2	0.3	0.3		0.2	
HUrange3	-100 – 15	11.2	50.8	1.2	36.4	0.1			0.1	0.1			
HUrange4	15 – 129	10.0	16.3	4.3	68.4	0.4			0.4	0.3			
HUrange5	129 – 200	9.7	44.7	2.5	35.9			2.3	0.2	0.1		0.1	4.5
HUrange6	200 – 300	9.1	41.4	2.7	36.8		0.1	3.2	0.2	0.1		0.1	6.3
HUrange7	300 – 400	8.5	37.8	2.9	37.9		0.1	4.1	0.2	0.1		0.1	8.2
HUrange8	400 – 500	8.0	34.5	3.1	38.8		0.1	5.0	0.2	0.1		0.1	10.0
HUrange9	500 – 600	7.5	31.6	3.2	39.7		0.1	5.8	0.2	0.1			11.6
HUrange10	600 – 700	7.1	28.9	3.4	40.4		0.1	6.6	0.2	0.1			13.1
HUrange11	700 – 800	6.7	26.4	3.5	41.2		0.2	7.2	0.3				14.4
HUrange12	800 – 900	6.3	24.2	3.7	41.8		0.2	7.8	0.3				15.7
HUrange13	900 – 1000	6.0	22.1	3.8	42.4		0.2	8.4	0.3				16.8
HUrange14	1000 – 1100	5.6	20.1	3.9	43.0		0.2	8.9	0.3				17.9
HUrange15	1100 – 1200	5.3	18.3	4.0	43.5		0.2	9.4	0.3				18.9
HUrange16	1200 – 1300	5.1	16.6	4.1	44.0		0.2	9.9	0.3				19.8
HUrange17	1300 – 1400	4.8	15.0	4.2	44.4		0.2	10.3	0.3				20.7
HUrange18	1400 – 1500	4.6	13.6	4.2	44.9		0.2	10.7	0.3				21.5
HUrange19	$>$ 1500	4.3	12.2	4.3	45.3		0.2	11.1	0.3				22.2

Table 8: List of the cases and their main properties.

Case	Tumor Site	Treatment Type	Energy (MV)
01	Prostate	IMRT	15
02	Recti	IMRT	15
03	Mammary	3DCRT	6/15
04	Lung	IMRT	6
05	Head&Neck	IMRT	6

Table 9: Specific instructions applied for conversion with CTC–ask for case 01, a prostate–case.

Structure	HUranges included	Specific media	H (HU)
Body	1,3–19		
Urinary bladder	3-4	Urinary, urine	-10 – 10
		Urinary, filled	10 – 20
		Urinary, empty	20 – 40
Rectum	3-4		
Rectum wall	3-4		
Caput femur dxt.	4-19	Cartilage	79 – 109
		Connective	109 – 144
		Femur	633 – 663
Caput femur sin.	4-19	Cartilage	79 – 109
		Connective	109 – 144
		Femur	633 – 663

4.5 COMPARISON BETWEEN CTC–ASK AND THE DICOM RT TOOLBOX

Phantoms were created utilizing the 19 media scheme as implemented in the DICOM RT toolbox as well as in CTC–ask for five patient cases (table 8). The constraints posed in CTC–ask were that HUrange2 was only allowed in anatomical structures were lung tissue was present. The specific instructions for each case and structure for the CTC–ask–scheme are listed in table 9–13. Additional tissue specific media were allowed to be included, where applicable, by CTC–ask. Media composition were taken from [NIST, 2011*a*; White et al., 1987; Woodard and White, 1986]. CTC–ask was allowed to use all of the media except HUrange2 (corresponding to lung) outside of the external (Body) contour.

Full MC simulation of a clinical treatment plan was subsequently employed[3], using MCSIM, in both of the phantoms. The number of

3 Cut off energies were 521 and 10 keV for electrons and photons respectively. The only variance reduction technique explicitly employed was electron track repeating. The number of histories were chosen so that the estimated statistical uncertainty was ≈0.5% for the voxels in the high–dose regions.

Table 10: Specific instructions applied for conversion with CTC–ask for case 02, a recti–case.

Structure	HUranges included
Body	1,3–19
Blood vessels	3–4

Table 11: Specific instructions applied for conversion with CTC–ask for case 03, a mammary–case.

Structure	HUranges included	Specific media	H (HU)
Body	1–19	Mammary gland 1	-39 – -9
		Mammary gland 2	-9 – 20
		Mammary gland 3	30 – 60
Left lung	2–4		
Heart	3–4	Heart 2	20 – 50
Cavity	1,3		

Table 12: Specific instructions applied for conversion with CTC–ask for case 04, a lung–case.

Structure	HUranges included	Specific media	H (HU)
Body	1,3–19	Adipose 3	-98 – -73
		Adipose 2	-73 – -52
		Adipose 1	-52 – -29
		Muscle 2	20 – 50
		Cartilage	79 – 109
Heart	3–4	Heart 2	20 – 50
Lungs	2–3		
Spinal cord	3–4		

Table 13: Specific instructions applied for conversion with CTC–ask for case 05, a head–and–neck–case.

Structure	HUranges included	Specific media	H (HU)
Body	1,3–19	Cartilage	79 – 109
		Cranium	962 – 992
Mandible	3–19	Mandible	1083–1113
Spinal cord	3–4		
Brain stem	3–4		
Larynx	1,3–4		
Parotid glands	3–4		

simulated histories were chosen so that the estimated statistical uncertainty was $\approx 0.5\%$ for the voxels in the high dose regions. The selected number of histories resulted in estimated statistical uncertainties below 2%, 8% and 15% for voxels recieving 50%, 20% and 10% of the

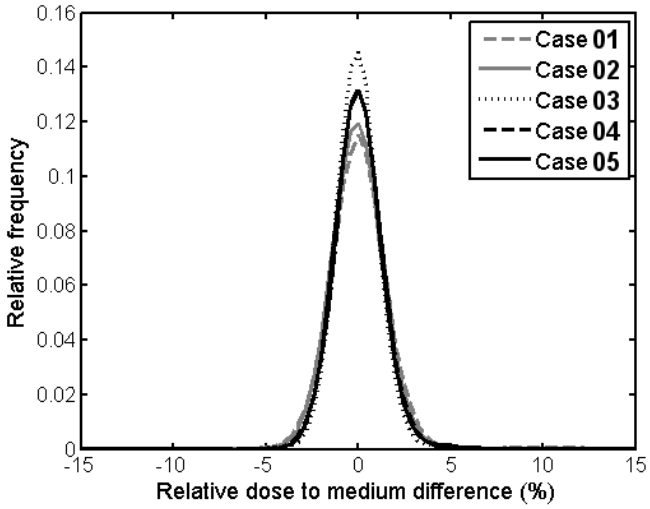

Figure 46: Histograms of the relative difference of dose distributions, calculated in the CTC–ask and DICOM RT toolbox generated phantoms, for cases 01 through 05. Each histogram was plotted with a binwidth of 0.4%. Voxels with uncertainty larger than 1% were ignored.

maximum dose, repsectively. The relative statistical uncertainty of the dose in a voxel is estimated by

$$\frac{\sigma D}{D} = \sqrt{\frac{n \sum e_i^2 - (\sum e_i)^2}{(n-1)(\sum e_i)^2}} \tag{4.5}$$

where e_i is the energy deposited in the voxel in the i^{th} energy deposition event and n is the total number of energy deposition events in the voxel. All doses are reported as dose–to–medium unless otherwise explicitly stated.

The differences in dose distribution calculated in the CTC–ask and DICOM RT toolbox generated phantoms shown in figure 46. Voxels with uncertainty larger than 1% were ignored. The dose distributions of the HU– and the CTC–ask–scheme are in good agreement, as indicated by the Gaussian–like distributions around 0%. This is not surprising as the only difference between the two phantoms are the media assignment in a relatively small fraction of the voxels (typically less than 1%). This may be interpreted as CTC–ask being robust and in agreement with the well documented DICOM RT toolbox.

CTC–ask allows the user to control which media that are allowed to be assigned to voxels within a given structure. In order to investigate the influence of this on dose distribution in detail, the dose of voxels assigned specific media as well as voxels differing in terms of air and lung between the conversion scheme as implemented in the DICOM RT toolbox and CTC–ask were studied (figure 47). For specific soft–tissue media (e.g. cartilage) the difference in D_m is small,

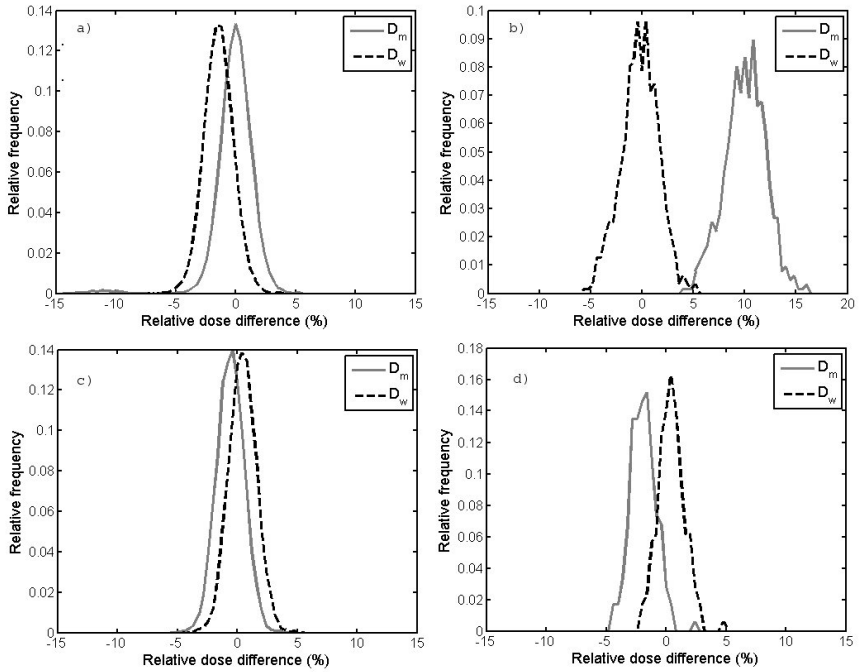

Figure 47: Histograms of the relative difference of dose distributions, for **a)** voxels of case 04 assigned to HUrange2 (corresponding to lung) by the DICOM RT toolbox and a different medium by CTC–ask, **b)** voxels of case 01 assigned to HUrange1 (corresponding to air) by the ICOM RT toolbox and a different medium by CTC–ask, **c)** voxels of case 05 assigned to cartilage by CTC–ask and **d)** voxels of case 05 assigned to cranium by CTC–ask. Each histogram was plotted with a binwidth of 0.4%. Voxels with uncertainty larger than 1% were ignored.

converting to D_w, however, introduces a systematic shift. The same applies to voxels assigned HUrange2 by the DICOM RT toolbox while a different media by CTC–ask (most of those voxels where assigned HUrange3, adipose or mammary gland and not HUrange1 – corresponding to air). For specific dense bone media (e.g. cranium) the difference in D_m is noticeable. The largest difference is noted for the voxels assigned to HUrange1 (corresponding to air) by the DICOM RT toolbox, while HUrange2 (corresponding to lung) by CTC–ask. In this case the dose–difference distribution is centered around 10% for D_m. This is however compensated by the differences in stopping power ratios when converting to D_w.

Computational Environment for Radiotherapy Research (CERR) [Deasy et al., 2003] was used to produce Dose Volume Hisotgrams (DVHs) for all cases, the DVHs of case 05 are shown in figure 48. For case 05, the conversion scheme as implemented in the DICOM RT toolbox assigned lung (HUrange2) to 9.9% of the voxels inside the external contour, to 5.2% of the PTV and to 15.1% of the larynx,

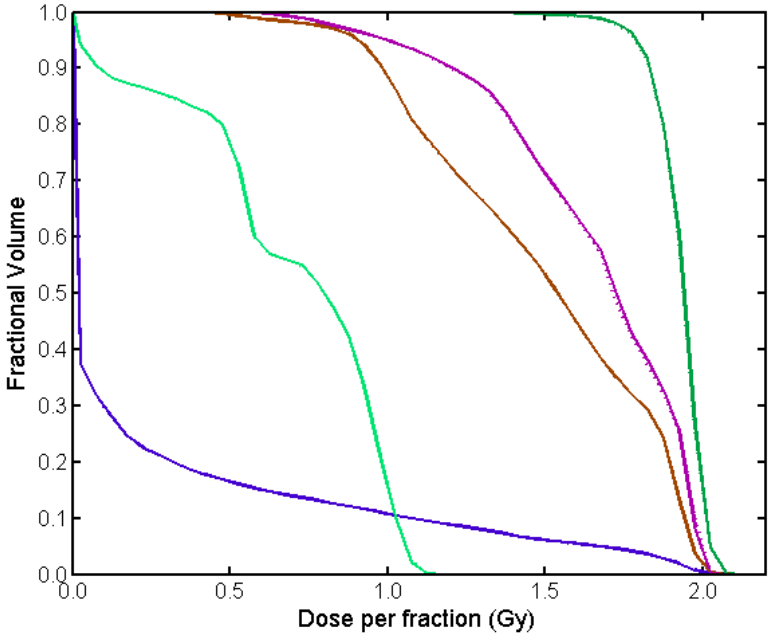

Figure 48: Dose Volume Hisotgram, in terms of D_m, for case 05 for the DICOM RT toolbox (solid) and CTC–ask (dashed). The included structures are total body (blue), PTV (dark green), mandible (brown), larynx (purple) and the medulla (light green).

whereas CTC–ask did not assign lung (HUrange2) to any of the voxels for case 05. The larynx–voxels assigned lung by the DICOM RT toolbox were assigned air by CTC–ask, which led to the decreased dose to the larynx in the CTC–ask phantom. The same effect is present for the PTV, but to a lesser extent and altmost non–detectable on the DVHs.

The accuracy of MC dose calculation is strongly influenced by the conversion of CT–number to density and media. The most crucial contributor is arguably the density conversion. When assigning media to voxels, the most critical task is to differentiate between media with distinct mass attenuation properties. It was demonstrated that misassignment between air and lung can introduce a local error in dose in the order of 10% (figure 47b), which agrees with the findings of e.g. Verhaegen and Devic [2005]. Compton effect is the dominating effect for radiotherapy beams and the probability for Compton interaction is proportional to the electron density. Hydrogen has a higher electron density than elements with higher Z, therefore the attenuation properties of media will depend heavily on the hydrogen content. This is most outspoken when comparing air and lung as lung contain 10.3% hydrogen, whearas dry air does not contain any [Vanderstraeten et al., 2007].

Media with distinct composition will likely differ in important dosimetrical properties (such as stopping power and mass energy

absorption coefficients). This is best illustrated by figure 47d, where the voxels assigned Cranium are shifted to a ≈2% lower dose for the CTC–ask generated phantoms due to lower mass stopping power of the composition corresponding to Cranium–media than that of HUrange13, which was the media assigned to the voxels in the DICOM RT toolbox generated phantom.

Erroneous assignment of media will lead to a local error in dose (figure 47), which may or may not be partially compensated for, due to the differences in mass stopping power, if converting to dose–to–water (D_w). The mass attenuation of the improper media will however also perturb the beam, leading to an error in dose downstream or laterally. In addition, an increased backscatter (or lack thereof, depending on if moving from media with high H– or Ca– content to media with low, or vice versa) is noted at the boundary. Moreover, the local dose may be affected by media misassignment of neighboring voxels. None of those effects are compensated for when converting to D_w.

4.6 CT–ARTIFACTS

The accuracy of MCTP relies on precise determination of density in the patient and/or phantom. In some cases severe artifacts are introduced in the CT data such that the reconstructed HU differs from the actual linear attenuation coefficients. Metal streaking artifacts are observed when high Z materials are present in the scanned volume, e.g dental cavity fillings or hip prostheses in a patient. Figure 49 shows a transversal CT slice of a pelvic case with bilateral hip prostheses. Metal streaking artifacts are seen throughout the slice and in between the prostheses there is a region where information not only is slightly distorted, but more or less ascent. Such artifacts may, if not corrected for, lead to erroneous density assignment, media assignment and ultimately dose distributions.

Keall et al. [2003] investigated the influence of CT artifacts, due to a hip prostheses, on the resulting dose distribution by modifying CT–data of a prostate case without hip prostheses. A spherical volume with density corresponding to stainless steel was introduced in a CT–data set to obtain an artifact–free image. Sinograms of the artifact–free image set were calculated from a number of projections through the CT–data. Filtered back projections and iterative deblurring methods were applied to reconstruct the image set from the sinograms. Thus creating reconstructed images with metal streaking artifacts. MC compliant phantoms were created based on each one of the CT–data sets. Full MC simulation of a clinical treatment plan was subsequently employed, using EGS4, in each of the three MC phantoms. No apparent differences, in terms of iso dose curves or DVHs, were observed between the simulations. Although the artifacts did not lead to significant perturbation of the dose distribution in the

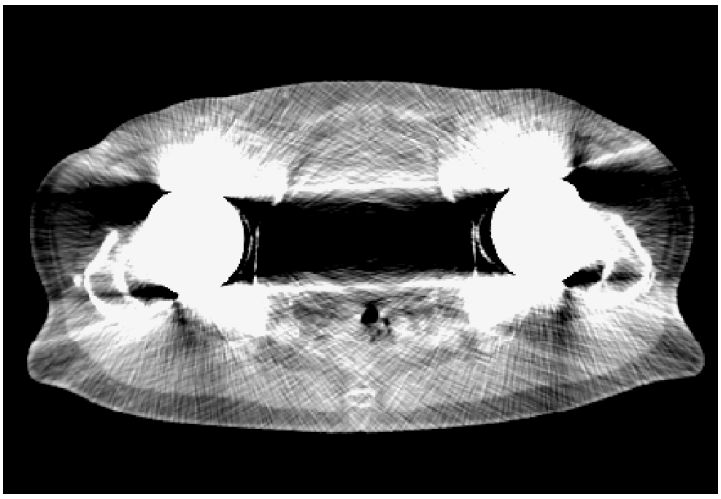

Figure 49: Transversal CT slice of a pelvic case, showing the CT–artifacts due to a bilateral hip prostheses.

study by Keall et al. [2003] it was concluded that this was not enough to make general predictions for other patient data.

In this study a 15MV 3DCRT pelvic case with substantial metal artifacts in the CT scan due to bilateral hip prostheses (figure 49) was selected in order to investigate the effect of metal artifacts on the resulting dose distribution. Phantoms were generated based on the CT–data, using the 19 media conversion scheme (table 7) as implemented in the DICOM–RT toolbox (hereafter referred to as uncorrected phantom) as well as in CTC–ask (hereafter referred to as corrected phantoms). For the corrected phantom the bilateral hip prostheses were delineated manually, all voxels belonging to the delineated prostheses were set to titanium with a density of 4.54 gcm^{-3} and in the slices containing artifacts, all voxels inside the external outline not belonging to bone nor prostheses were set to ICRUTISSUE with a density of 1.00 gcm^{-3}. Full MC simulation of a clinical treatment plan was subsequently employed[4], using MCSIM, in both of the phantoms. The number of simulated histories were chosen so that the estimated statistical uncertainty was $\approx$ 0.5% for the voxels in the high dose regions. The selected number of histories resulted in estimated statistical uncertainties below 2%, 8% and 15% for voxels recieving 50%, 20% and 10% of the maximum dose, repsectively. All doses are reported as dose–to–medium.

3D–dose distributions were converted to DICOM RD files using CERR [Deasy et al., 2003] and subsequently imported to the TPS (Varian Eclipse 10.0) to generate DVHs (figure 50). A large underdosage

4 Cut off energies were 521 and 10 keV for electrons and photons respectively. The only variance reduction technique explicitly employed was electron track repeating. The number of histories were chosen so that the estimated statistical uncertainty was $\approx$0.5% for the voxels in the high–dose regions.

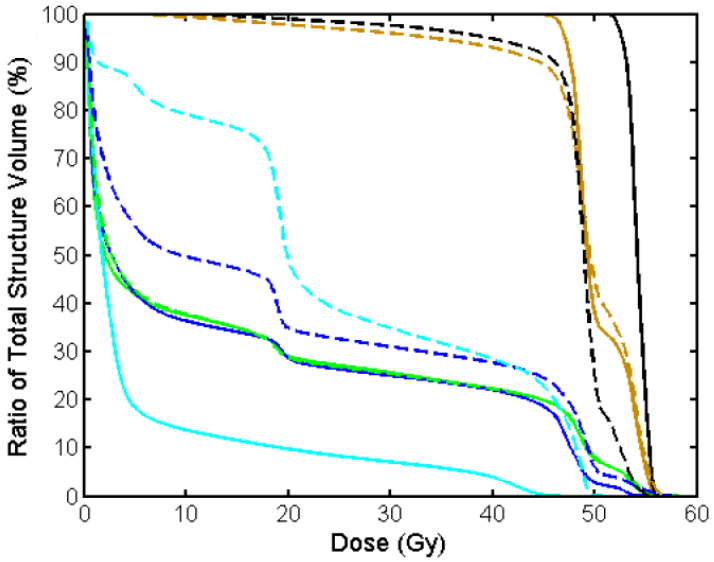

Figure 50: Cumulative Dose Volume Hisotgrams for the pelvic case using the corrected (solid) and uncorrected (dashed) phantoms. DVHs are plotted for the external outline (green), bones (blue), prostheses (cyan), PTV (brown) and the PTV excluding the rectum (black).

is noted for the uncorrected PTV and almost the entire PTV volume receives 5 Gy less dose than compared to the PTV of the corrected phantom. On the other hand the bone and prostheses structures receive higher doses in the unconstrained phantom. The substantial differences on the DVHs are a direct consequence of the erroneous assignment of media and density due to the CT artifacts.

These findings are in contradiction with those of Keall et al. [2003], indicating that CT artifacts indeed have a substantial impact on the dose distribution. However, it should also be stated that the artifacts in Keall et al. [2003] were substantially less apparent than in figure 49. The impact of CT artifacts on the dose distribution for a much more similar case (a prostate patient with bilateral hip prostheses) was presented in Bazalova et al. [2007]. They found underdosage in the target volume for the uncorrected CT–data on the same order as in figure 50. The correction method presented in Bazalova et al. [2007] is, however, more sophisticated than the one used here. In essence, an image with an unlimited HU scale is produce by filtered back projection of the sinograms. Voxels corresponding to metal are extracted to form a "metal only image" using a HU threshold level. The forward Radon transformation of the metal only image is used as a mask for the original sinograms and the missing projections (as defined by the mask) are interpolated at each projection angle. Filtered back projection of the modified sinogram generates an image in which the metal artifacts are corrected for whilst not containing information on the voxels previously identified as metal. The final

corrected image is obtained by superimposing the metal only image on the artifact–corrected image [Bazalova et al., 2007].

The similarity in results, despite the difference in correction methods, indicate that the coarse method used in this study is substantially better than making no correction at all and may readily be used as a correction method.

5

CONVERTING FROM DOSE TO MEDIUM PER INCIDENT PARTICLE TO DOSE IN WATER PER MONITOR UNIT

EGSnrc reports dose per incident particle which is useful when the relative dose distribution is of interest. In MCTP the absorbed dose, in Gy, is generally more relevant. The objective of this chapter is to present a formalism for converting from dose per incident particle to Gy. A protocol for conversion from dose per incident particle to absolute dose was described by Francescon et al. [2000]. In short, a calibration factor, K_{MC}, needs to be obtained. This is done by a simulation of reference dose, D_{ref}^{MC}, which is the dose at a reference point under reference conditions. Typically one would use the dose at 10 cm depth along the CAX in homogeneous water phantom experienced by a 10×10 cm^2 field with SSD = 100 cm. The expected reference dose per MU, D_{ref}^{meas}, can be measured following procedures in TRS–398 [Andreo et al., 2000]. The calibration factor is then given by

$$K_{MC} = \frac{D_{ref}^{meas}}{D_{ref}^{MC}} \tag{5.1}$$

The conversion is handled as a post processing step and needs to be conducted manually. The dose, in Gy, will be given by

$$D_{MC,abs} = D_{MC} \times K_{MC} \times U, \tag{5.2}$$

where U is the number of MUs for the irradiation.

In MCSIM, however, a calibration factor corresponding to K_{MC}, `drefmax`, is defined for each field. The dose distribution for the field in question will be converted to absolute dose by multiplication with `drefmax` and the number of MU which is specified explicitly for each field through the MLC sequence file.

5.1 THE BACKSCATTER EFFECT

For a given irradiation, the linac is instructed to deliver a number of MUs. This is related to a response in the monitor chamber and once that response is reached the beam is switched off. The dose experienced by the monitor chamber can be divided into two parts: dose delivered from the particles moving downstream and dose delivered by backscattered particles moving upstreams. It has been shown that the backscattered radiation increases the photon output by about 2% –

3% when moving from a 3×3 cm^3 field to a 40×40 cm^3 field on Varian 2100 accelerators [Liu et al., 1997; Verhaegen et al., 2000]. The main source of the backscattered particles are the jaw collimators, particularly the upper one. Liu et al. [2000] reported that the backscatter from the lower jaws amounts to about 10% of that from the upper jaws. As the backwards component of the dose to the monitor chamber is dependent on the jaw positions it is field size dependent. This backscatter effect needs to be compensated for and incorporated into equation 5.2 when converting to absolute dose:

$$D_{MC,abs} = D_{MC} \times K_{MC} \times BSF(Y,X) \times U, \tag{5.3}$$

where $BSF(Y,X)$ is the BackScatter correction Factor for a field with jaw settings according to (Y,X).

5.1.1 *An experimental formalism*

As the monitor chamber reading is affected by both the forward and backwards component, an alternative measurand is needed in order to separate the two components. Lam et al. proposed a formalism to measure, I_{target}, the current required to keep the linac gun target electrically neutral during irradiation [Lam et al., 1998]. Consider the assumption that the backscatter was field size independent, then the I_{target} required for a given number of MUs would be constant over all field sizes. As this is not the case the relative backscatter contribution can be obtained by I_{target} ratios:

$$BSF(Y,X) = \frac{I_{target}(Y,X)}{I_{target}(Y_{ref},X_{ref})}, \tag{5.4}$$

where $I_{target}(Y,X)$ and $I_{target}(Y_{ref},X_{ref})$ are the integrated charge over time for an irradiation, for a fixed number of monitor units, of a field with jaw openings defined by (Y,X) and a reference field, respectively.

In this work I_{target} as a function of jaw settings, for square fields, were measured for four beam matched Varian 2300 iX linacs (Figure 51). Measurements were conducted with the in–house developed ME40 Scintillator Dosimetry System (DTU, Roskilde, Denmark), which functions by connecting Burr–Brown ACF2101 switched integrator circuits [Mountford et al., 2008] to the I_{target} BNC contact of the linac. The charge built up in the 100 pF capacitor is held, integrated, and read out before it is reset at the onset of the next synchronization pulse. The charge over all gun pulses within an irradiation with collimator settings (Y,X) is accumulated to yield $I_{target}(Y,X)$. A detailed description of the methodology is given in Beierholm et al. [2011]. The backscatter correction factors were largely consistent across the linacs

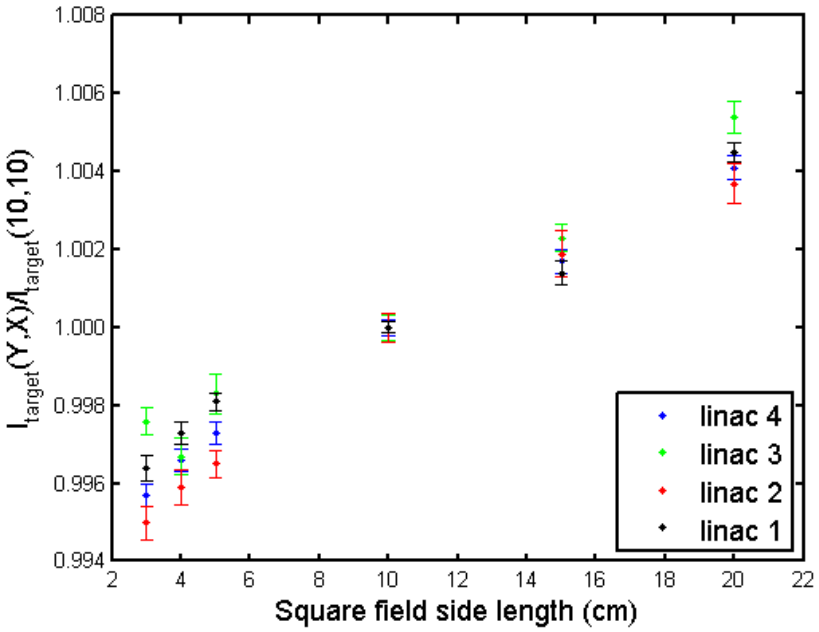

Figure 51: Measured I_{target} ratios for four beam matched Varian 2300 iX linacs. The 10×10 cm^2 field is used as the reference field and uncertainties are given as 1 SD based on 10 repeated measurements.

studied. The standard deviation of the mean of the population was 0.06%, while the maximum deviation was 0.14%. Possible sources of error are differences in geometry between the linacs and inconsistent jaw calibrations. Hereafter I_{target} measurements of linac 1 are used, since that was the linac that the MC model was commissioned to.

Charge as a function of time is shown in Figure 52 for 10×10 cm^2 fields. The I_{target} reading is obtained by integrating the charge over time for a fixed number of monitor units.

5.1.2 *A Monte Carlo formalism*

Popescu et al. [2005] published a formalism for absolute dose calculations in MC under which the field size dependent backscatter effect is taken into account. In short, it involves splitting the treatment head simulation into two parts (Figure 53): i) the static upper part of the treatment head (target through mirror), $BEAM_A$, and ii) the field specific part of the treatment head (monitor chamber through beam limiting devises), $BEAM_B$. The phase space generated by $BEAM_A$ is used as input in $BEAM_B$ and in both simulation the dose to the monitor chamber is scored.

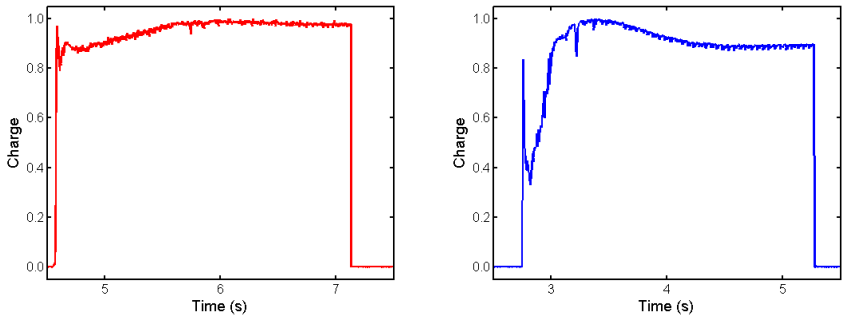

Figure 52: Charge as a function of time for 10×10 cm^2 fields in 6MV mode (left) and 15MV mode (right). The signal has been normalized to its peak charge to increase readability.

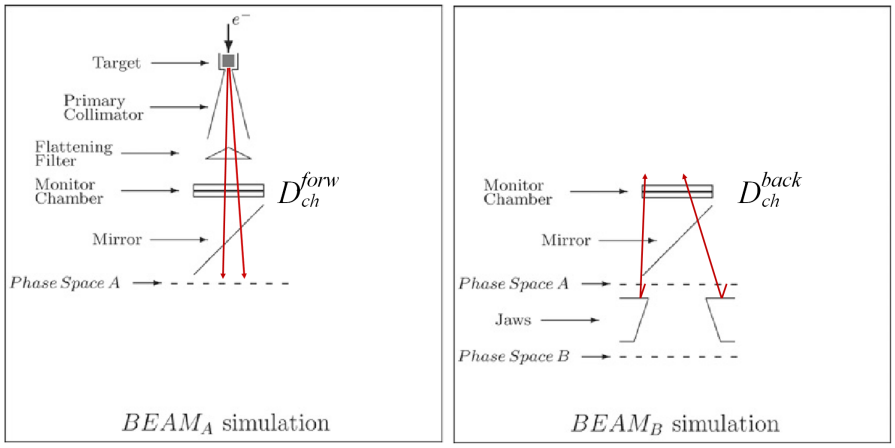

Figure 53: Schematic sketches of BEAM_A and BEAM_B on the left and right hand side, respectively. The red arrows indicate typical particle tracks that make up the forward, D_{ch}^{forw}, and the backward, D_{ch}^{back}, dose components to the monitor chambers, respectively. (Adapted from Popescu et al. [2005] with permission)

Going through the equations presented in Popescu et al. [2005] (and maintaining the nomenclature), the backscatter correction for a field with jaw settings (Y, X) is given by

$$\text{BSF}(Y,X) = \frac{D_{ch}^{forw} + D_{ch}^{back}(Y_{ref}, X_{ref})}{D_{ch}^{forw} + D_{ch}^{back}(Y,X)}, \tag{5.5}$$

where D_{ch}^{forw} is the dose deposited in the monitor chamber during the BEAM_A simulation, $D_{ch}^{back}(Y_ref,X_ref)$ is the dose deposited in the monitor chamber during the BEAM_B simulation for the reference field (10×10 cm^2) and $D_{ch}^{back}(Y,X)$ is the dose deposited in the monitor chamber during the BEAM_B simulation for an arbitrary field.

The formalism published by Popescu et al. [2005] was developed prior to the introduction of DBS [Kawrakow et al., 2004] into EGSnrc.

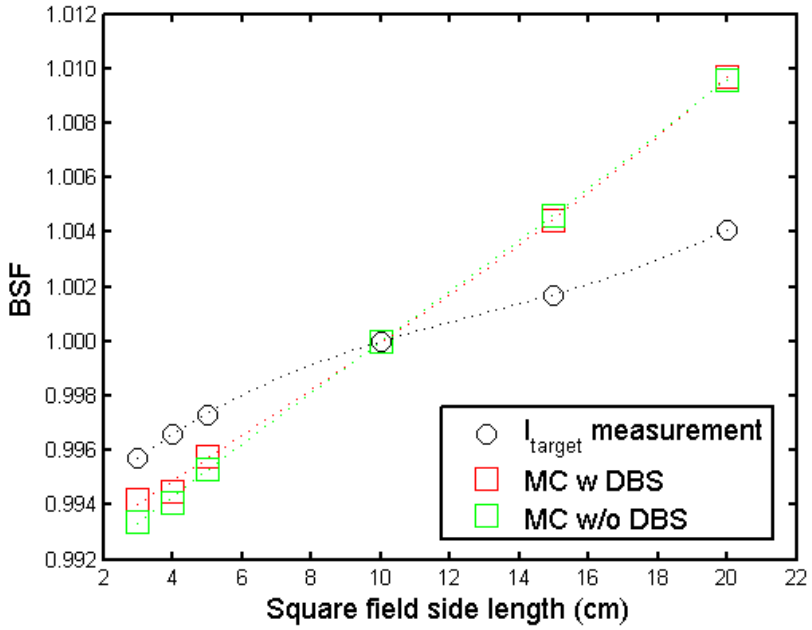

Figure 54: Backscatter correction factors as a function of square field side length for I_{target} measurements, black, the MC–formalism (Equation 5.5 with, red, and without, green, DBS turned on. The size of the markers corresponds to the uncertainties, which for the measurements are given as 1 SD and the for the MC simulations as statistical uncertainty reported by DOSXYZnrc. The dashed lines show fits to the data using a third degree polynomial and linear fit to the measured and MC data, respectively.

In order to investigate the validity of the formalism BSF were simulated[1] with and without DBS turned on for a range of 6MV field sizes Figure 54. The monitor chamber dose was scored, using a dose scoring region encompassing the air layers of the monitor chambers, in both $BEAM_A$ and $BEAM_B$ for simulations with and without DBS. The BSF were calculated according to Equation 5.5. No statistical significance was found between the two simulation types, which ensures that the formalism is vaild also with the use of DBS. Meanwhile the simulated BSF did not agree with the measured.

In order to investigate and rectify the disagreement with measurements three possible MC factors were considered: i) the mean energy of the impinging electrons, ii) the spot size FWHM of the impinging electrons and iii) the approximation of placing the jaw collimators at a fixed distance from the source and perpendicular to the beam direction in the BEAMnrc model. The first two factors were investigated

1 Simulations were conducted with ECUT = 521 keV, PCUT = 10 keV, NBRSPL = 1000. For simulations using DBS, the splitting field radius was set to twice the length of the squared field. Uniform bremsstrahlung splitting was used for the simulations not employing DBS. The number of histories were selected so that the statistical uncertainty of the dose to the monitor chamber was between 0.9% and 1.0%.

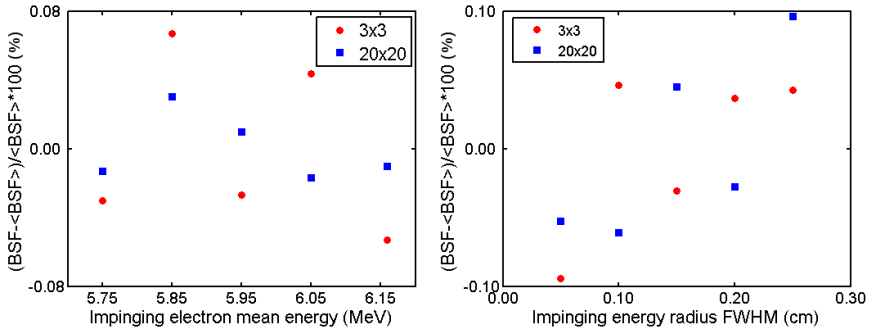

Figure 55: Backscatter correction factors as a function of impinging electron mean energy (**left**) and as a function impinging electron spot size FWHM (**right**). Data are shown for two field sizes: 3×3 cm^2 (red circles) and 20×20 cm^2 (blue squares). The figures show relative deviation from the average value of the dataset in question.

by simulating[2] BSF with i) a varying mean energy, while a constant spot size FWHM and ii) vice versa. Simulations were limited to a large (20×20 cm^2) and a small (3×3 cm^2) field size. It was demonstrated that the BSF was rather insensitive (variation were within 0.1%) within the range of impinging electron mean energy and spot size FWHM that were considered (Figure 55). This is in agreement with the findings of Verhaegen et al. [2000], where it was demonstrated that the backscatter contribution as a function of field size changes no more than a percent for two different beam qualites (6 MV and 10 MV). The effect of such small changes in impinging electron beam parameters investigated in this study is therefore expected to have little, or even neglectable, impact.

The third factor considered, the approximation of placing the jaw collimators at a fixed distance from the source and perpendicular to the the beam direction, is justified by conclusions drawn in previous studies. An empirical formalism for calculation of monitor chamber backscatter was derived by Liu et al. [2000]. They conclude that the majority of the backscatter radiation originate from the jaw collimators, the upper collimator in particular, for a Varian 2100 linac. Moreover, they showed that the backscattered radiation consist mostly of low energy photons and electrons. Liu et al. [1997] concluded that the backscatter is dependent on the accelerator geometry. The approximation to model the jaw collimators as perpendicular to the beam direction placed at a fixed distance from the source might be justifiable when investigating lateral profiles, but not for a parameter that is highly dependent on the precise geometry of the linac treatment head in general and the collimator jaws in particular.

2 Simulations were conducted with ECUT = 521 keV, PCUT = 10 keV, NBRSPL = 1000 and using uniform bremsstrahlung splitting. The number of histories were selected so that the statistical uncertainty of the dose to the monitor chamber was between 0.9% and 1.0%.

The upper collimators on a Varian 2100 and 2300 are in fact pivoting on an axis Verhaegen and Liu [2001]. There is, however, currently no CM able to model pivoting jaws available in EGSnrc. The existing CMs that model the collimator jaws (JAWS and SYNCJAWS) all employ the approximation of using a surface perpendicular to the beam direction. This infers that the effective distance between the collimating jaws and the monitor chamber varies with collimation settings. The relative change in distance can be accounted for by shifting the jaw position in z–direction in the MC model. The following equations[3] yields the shifted jaw positions for the collimation setting in question:

$$
\begin{aligned}
htY2 &= zrady * SAD/\sqrt{y2^2 + SAD^2} \\
htY1 &= zrady * SAD/\sqrt{y1^2 + SAD^2} \\
htY &= (htY2 + htY1)/2 \\
hbY2 &= htY2 + wjaws * SAD/\sqrt{y2^2 + SAD^2} \\
hbY1 &= htY1 + wjaws * SAD/\sqrt{y1^2 + SAD^2} \\
hbY &= (hbY2 + hbY1)/2, \\
htX1 &= zradx \\
htX2 &= zradx - wjaws * 20/\sqrt{20.0^2 + SAD^2} \\
htX &= (htX2 + htX1)/2 \\
hbX2 &= htX + wjaws * SAD/\sqrt{x2^2 + SAD^2} \\
hbX1 &= htX + wjaws * SAD/\sqrt{x1^2 + SAD^2} \\
hbX &= (hbX2 + hbX1)/2
\end{aligned}
\tag{5.6}
$$

where zrady is the distance between the source and the upper jaws, SAD is the Source to Axis Distance (SAD) (the distance between the target and the ISO–center), y1 and y2 define the field opening, in y–direction, at SAD, htY1 and htY2 is then the jaw position corresponding to the accurate effective distance between the source and the upper collimator jaws. Analogously zradx is the distance between the source and the lower jaws, x1 and x2 define the field opening, in x–direction, at SAD, htX1 and htX2 is then the jaw position corresponding to the accurate effective distance between the source and the lower collimator jaws, while wjaws is the nominal thickness of the jaws, As it is not possible to define a pair of collimator jaws as located at different z–locations in BEAMnrc, the average distance, htY or htX, is used. Simulations[4], with compensated z–positions of the upper collimator, were conducted and results compared to I_{target} measurements

3 Equations derived by IA Popescu and C Shaw, published with permission.

4 Simulations were conducted with ECUT = 521 keV, PCUT = 10 keV, NBRSPL = 1000. DBS was turned on and the splitting field radius was set to twice the length of the squared field. The number of histories were selected so that the statistical uncertainty of the dose to the monitor chamber was between 0.9% and 1.0%.

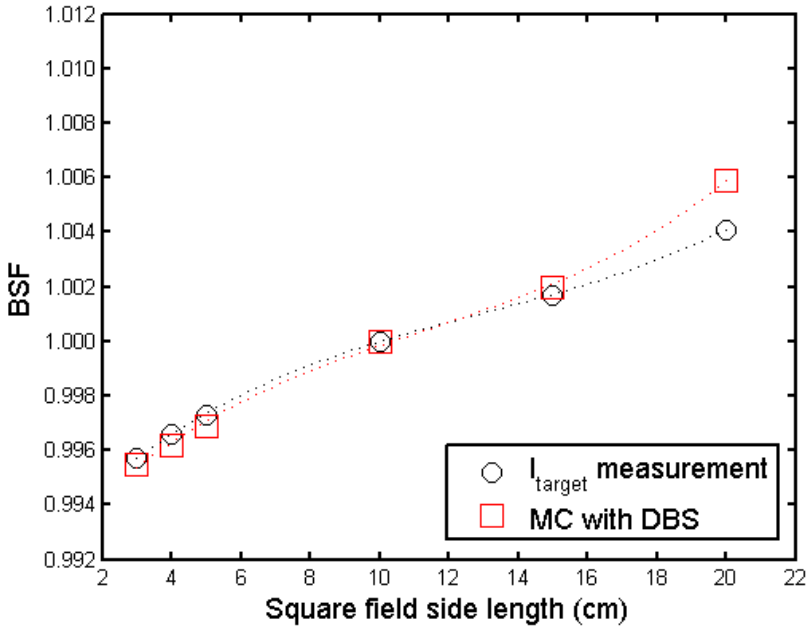

Figure 56: Backscatter correction factors as a function of square field side length for I_{target} measurements, black, the MC–formalism (Equation 5.5 with DBS turned on, red. The size of the markers corresponds to the uncertainties, which for the measurements are given as 1 SD and the for the MC simulations as statistical uncertainty reported by DOSXYZnrc. Third degree polynomial fits to the data are shown as dashed lines.

(Figure 56). When compensating for the effective distance between the jaws and the monitor chamber, much better agreement was found between measurements and simulations. The deviation was within 0.2%, but seemed to follow a trend where the deviation increased when moving furhter away from the reference field (10×10 cm^2). This is likely due to the fact that the jaws are modeled as perpendicular to the source as oppose to pivoting on an axis. Developement of a CM able to simulate the non–perpendicular jaws may improve the simulation of BSFs for Varian linacs.

5.1.3 *Backscatter correction in MCSIM*

As stated on page 99, `drefmax`, is defined for each field in MCSIM. This means that the field specific BSF correction can be implicitly handled by MCSIM. This comes at the cost of the need for prior knowledge of the BSF correction for any collimating aperture. Liu et al. [2000] derived empirical formula for the backscattered radiation to the monitor chamber as function of jaw settings for a Varian 2100 linac. A simplified study was in this work conducted to obtain prior knowledge

Table 14: Measured and MCSIM simulated ROFs for a range of field sizes.

Field opening	6 MV			15 MV		
(Y×X)	Measured	Simulated	Difference	Measured	Simulated	Difference
(cm)	ROF	ROF	(%)	ROF	ROF	(%)
10.0×10.0	1.000	1.000	0.0	1.000	1.000	0.0
3.0×10.0	0.878	0.888	1.1	0.907	0.913	0.7
5.0×10.0	0.930	0.937	0.8	0.952	0.958	0.6
8.0×10.0	0.979	0.981	0.2	0.986	0.988	0.2
12.0×10.0	1.015	1.013	-0.2	1.010	1.008	-0.2
15.0×10.0	1.032	1.027	-0.5	1.020	1.016	-0.4
20.0×10.0	1.048	1.041	-0.7	1.031	1.024	-0.7
30.0×10.0	1.067	1.055	-1.1	1.045	1.036	-0.9
10.0×3.0	0.886	0.892	0.7	0.914	0.911	-0.3
10.0×5.0	0.939	0.940	0.1	0.960	0.958	-0.2
10.0×8.0	0.984	0.982	-0.2	0.990	0.991	0.1
10.0×12.0	1.012	1.013	0.1	1.007	1.007	0.0
10.0×15.0	1.024	1.026	0.2	1.014	1.014	0.0
10.0×20.0	1.037	1.038	0.1	1.022	1.021	-0.1
10.0×30.0	1.051	1.049	-0.2	1.029	1.023	-0.6

of the BSFs. Simulations were conducted using MCSIM[5] (with `drefmax` set to 1) where the upper, Y, collimater was fixed at defining a 10 cm field opening (at ISO center) and the lower, X, collimator was varied between defining a field openings of 3 and 30 cm. Corresponding simulations in which the reciprocal conditions were applied to the collimators were also conducted. The dose to water voxel, at 10 cm depth, in a homogenous water phantom with SSD = 90 cm was used to compute ROFs (Table 14). The MC simulated ROFs were compared the corresonding measured ROFs, under the same conditions, and the difference was assumed to be due to monitor chamber backscatter.

The backscatter effect for each field setting was expressed as the ratio between the measured and simulated ROF. The ratio between measured and simulated ROF were plotted as a function of field opening and fitted to a third degree polynomial function (Figure 57). The data points conform nicely to the polynomial functions and they may therefore be used as to asses the back scatter effect for a given field setting. Two statements made by Liu et al. [2000] were taken into consideration when computing back scatter effects for combined settings of Y– and X–jaws: The off–axis location does not significantly impact the back scatter effect. The lower jaws contribute approximately 10% of the ammount of backscatter compared to the upper jaws. With that, the off–axis was neglected and only the field opening considered and contribution from the upper jaws was set to 1/1.1, while the

5 A dose scoring grid of $0.5 \times 0.5 \times 0.5 \text{cm}^3$ was used, ECUT and PCUT were set to 700 keV and 10 keV, respectively. The source input was an energy specific phase space file scored directly below the flattening filter. The number of histories were selected so that the statistical uncertainty along the CAX (past build up) was less than 0.5%.

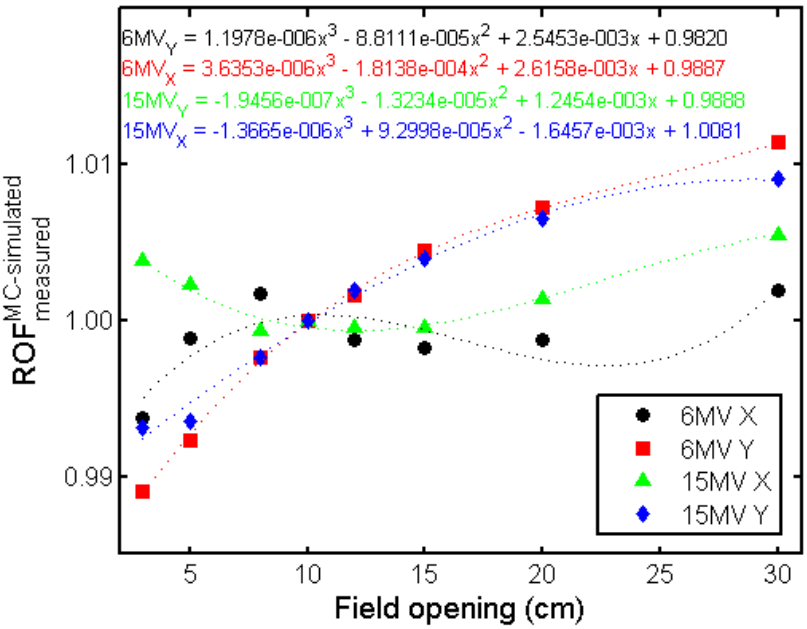

Figure 57: The ratio between simulated and measured ROFs for 6 and 15 MV for various field sizes. For the simulations with varying X–jaw settings, the Y–jaws were fixed at defining an opening of 10 cm (at ISO center) and vice versa. Included in the figure are also third degree polynomial fits to the data points (dashed lines) as well as the equations for the resulting functions.

contribution from the lower jaws were set to 1-1/1.1. Part of the backscattered radiation from the lower jaws will not reach the monitor chamber, but instead be blocked by the upper jaws. This perturbation is dependent on the upper jaw settings in question. This effect was also studied by Liu et al. [2000] but is neglected here.

The backscatter for a given field is computed using the fitted polynomial functions of the individual collimators for the field opening in question. In effect the backscatter correction given by:

$$\begin{aligned} BSF_{6MV} &= (1/1.1)(k_1^1(FS_Y)^3 + k_2^1(FS_Y)^2 + k_3^1(FS_Y) + k_4^1) \\ &\quad +(1-1/1.1)(k_1^2(FS_X)^3 + k_2^2(FS_X)^2 + k_3^2(FS_X) + k_4^2) \\ BSF_{15MV} &= (1/1.1)(k_1^3(FS_Y)^3 + k_2^3(FS_Y)^2 + k_3^3(FS_Y) + k_4^3) \\ &\quad +(1-1/1.1)(k_1^4(FS_X)^3 + k_2^4(FS_X)^2 + k_3^4(FS_X) + k_4^4) \end{aligned} \tag{5.7}$$

with

$$\mathbf{k} = \begin{bmatrix} 1.1978\times10^{-6} & 3.6353\times10^{-6} & -1.9456\times10^{-7} & -1.3665\times10^{-6} \\ -8.8111\times10^{-5} & -1.8138\times10^{-4} & -1.3234\times10^{-5} & -1.8138\times10^{-4} \\ 2.5453\times10^{-3} & 2.6158\times10^{-3} & 1.2454\times10^{-3} & 2.6158\times10^{-3} \\ 0.9820 & 0.9887 & 0.9888 & 0.9887 \end{bmatrix}$$

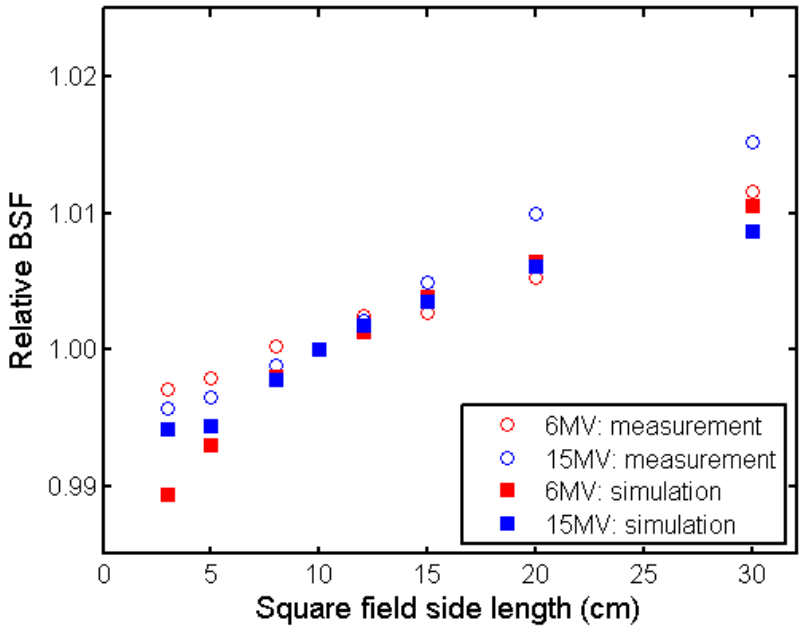

Figure 58: Measured and calculated backscatter correction factors. Measurements not conducted yet. For now 6MV I_{target} measurements for those field sizes available are included.

for 6MV and 15MV, respectively and where FS_Y and FS_X are the projected field openings defined by the upper and lower collimators, respectively.

Backscatter correction factors calculated using Equation 5.7 were compared to relative I_{target} measurements (see Section 5.1.1). Measured and calculated back scatter correction factors are shown in (Figure 58). The error introduced by the calculated BSF is small, especially for intermediate field sizes. Most of the fields simulated with MCSIM throughout this study was between 5×5 and 20×20 cm^2. No fields smaller than 3×3 or larger than 30×30 cm^2 were encountered and thus no extrapolation was conducted.

5.2 CONVERTING FROM DOSE–TO–MEDIA TO DOSE–TO–WATER

EGS4 and EGSnrc both report dose–to–media, D_m, whereas most TPS report dose–to–water, D_w Knöös et al. [2006]; Ottosson, Karlsson and Behrens [2010]. In order for an intercomparison between MC, reporting D_m, and a TPS, reporting D_w, a conversion method between them is needed. An analytical procedure based on Bragg–Gray cavity theory was proposed by Siebers et al. [2000]. They concluded that Spencer–Attix mass restricted collision stopping–power ratios can be used as conversion factors between the two quantities. Moreover, they concluded that a single correction factor can be used for each particular media throughout the field for a given photon beam energy.

The exception from this is for air, but as we are rarely interested in dose to air in clinical considerations and that the conversion is done locally for each voxel this can be disregarded from. An empirical formula relating the nominal acceleration potential to the effective energy is provided:

$$E_{eff} = 0.081P + 0.41, \tag{5.8}$$

where P is the nominal acceleration potential. Conversion factors are then calculated as the ratio of tabulated stopping power for water and the medium in question at E_{eff}.

The EGSnrc user code SPRRZnrc calculates Spencer–Attix mass restricted collision SPR for a given geometry and beam. Thus it can readily be used, as an alternative method, to obtain the factors needed to convert between D_m and D_w. As an example, SPRRZnrc was used to simulate[6] Spencer–Attix mass restricted collision stopping–power ratios for tissue vs water as defined by ICRU [NIST, 2011*b*] (`ICRUTISSUE521ICRU` and `H2O521ICRU`, respectively) using a cylindrical beam, with a radius of 5 cm for a parallel spectra corresponding to a 6 MV beam (Figure 59). The results show that the Spencer–Attix mass restricted collision stopping–power ratio is constant over the voxels occupied by tissue although the energy spectra is not (not shown). This is a verification of the conclusion made by Siebers et al. [2000], that a single correction factor can be used for each particular media throughout the field for a given photon beam energy.

Conversion factors were calculated for the 18 media (excluding HUrange1, corresponding to air) listed in Table 7 using the method described by Siebers et al. [2000] and for an effective energy according to Equation 5.8. SPRRZnrc was used to simulate[7] stopping power ratios for the same set of media. SPRRZnrc uses a fixed track end term cut off energy, Δ, of 10 keV, which is relevant for air–water–SPR but less so for media that can not be considered Spencer Attix cavities. Therefore SPRRZnrc was modified to use the Δ corresponding to the dimension of the voxel of interest each medium. The energies were selected using the continious slowing down approximation ranges calculated by the ESTAR code [NIST, 2011*b*]. The resulting corrections factors from the two methods are listed in Table 15. Conversion factors computed for the two methods follow the same trend and are in

6 A parallel beam incident from the front with a radius of 5 cm using the mohan6.spectra was employed in the simulation. ECUT was set to 521 keV, while PCUT was set to 10 keV. Default EXACT parameters were used for the boundary crossing algorithm

7 An energy specific phase space file corresponding to a $10 \times 10 cm^2$ field of the commissioned MC linac was incident on a water phantom with a voxel (radius = 0.25 cm, thickness = 0.5 cm) of the medium to be investigated at 10 cm depth and along the CAX. Cut off energies were set to 521 keV and 10 keV for electrons and photons respectively. The number of histories were chosen so that the relative statistical uncertainty was below 0.2% in the voxel of interest.

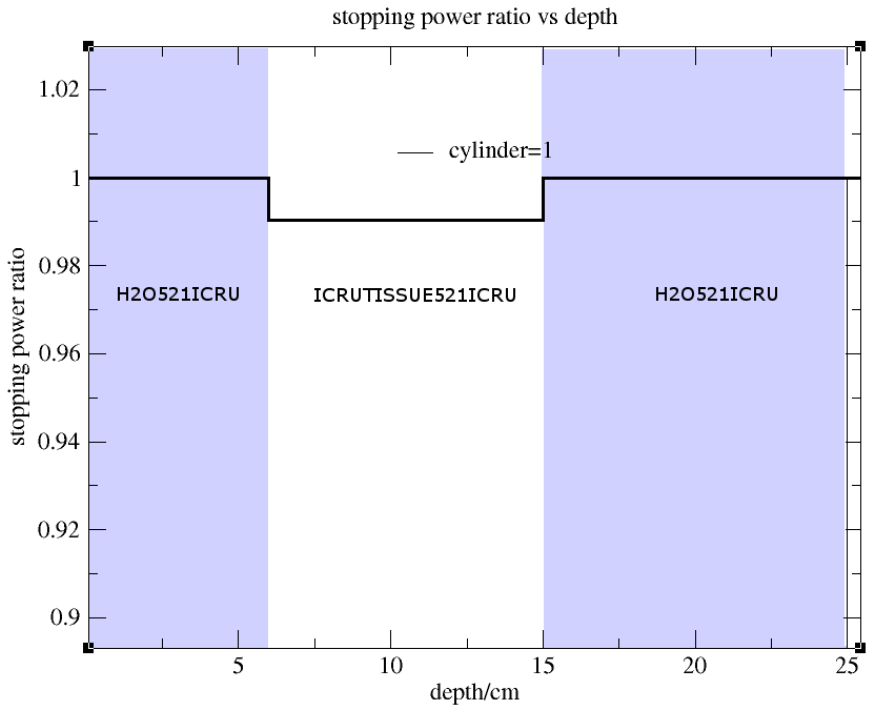

Figure 59: The figure shows Spencer–Attix mass restricted collision stopping–power ratios as a function of depth along the central axis (r = 1.0 cm). Inserted is a schematic sketch of the geometry, which shows that the voxels between 6 and 15 cm, along the CAX, are assigned ICRUTISSUE521ICRU. The calculated Spencer–Attix mass restricted collision stopping–power ratios are constant over those voxels.

agreement for most of the medias. For the densest media, however, disagreement on the order of 2% are noted. It should be stated that the expression for E_{eff} (Equation 5.8) corresponds to the linacs used in the study conducted by Siebers et al. [2000] and is not neccessarily applicable to linacs in this study. The SPRRZnrc method employs no fits to data (apart from the selection of Δ) and/or approximation and is therefore likely to be more reliable. Moreover, conversion factors can be obtained for the actual linac in question directly.

In conclusion, conversion from D_m to D_w for the beam quality, Q, and medium, m, can be conducted using the following equation:

$$D_w^{xyz} = D_m^{xyz} \times SPR_m^w(Q, m) \tag{5.9}$$

where D_w^{xyz} and D_m^{xyz} is the dose to voxel xyz in dose–to–water and dose–to–medium, respectively and $SPR_m^w(Q, m)$ is the SPRRZnrc simulated Spencer–Attix mass restricted collision stopping–power ratio.

Table 15: Analytically calculated and SPRRZnrc simulated dose–to–medium to dose–to–water conversion factors for the two linac potentials considered in this study and range of tissue equivalent media covering the span in density from lung to cortical bone.

Media	6MV			15MV		
	Analytical	SPRRZnrc	Difference (%)	Analytical	SPRRZnrc	Difference (%
HUrange2	0.9989	0.9977	0.1	0.9808	0.9843	-0.4
HUrange3	0.9936	0.9832	1.1	0.9968	0.9825	1.5
HUrange4	1.0130	1.0088	0.4	1.0143	1.0066	0.8
HUrange5	1.0185	1.0104	0.8	1.0199	1.0085	1.1
HUrange6	1.0268	1.0217	0.5	1.0279	1.0192	0.9
HUrange7	1.0207	1.0334	-1.2	1.0228	1.0305	-0.7
HUrange8	1.0330	1.0443	-1.1	1.0343	1.0406	-0.6
HUrange9	1.0563	1.0541	0.2	1.0544	1.0503	0.4
HUrange10	1.0641	1.0632	0.0	1.0617	1.0589	0.3
HUrange11	1.0714	1.0727	-0.1	1.0684	1.0672	0.1
HUrange12	1.0794	1.0811	-0.2	1.0753	1.0756	-0.0
HUrange13	1.0856	1.0894	-0.3	1.0810	1.0825	-0.1
HUrange14	1.0926	1.0972	-0.4	1.0880	1.0909	-0.3
HUrange15	1.0984	1.1136	-1.4	1.0932	1.1136	-1.8
HUrange16	1.1035	1.1196	-1.4	1.0977	1.1191	-1.9
HUrange17	1.1094	1.1266	-1.5	1.1030	1.1259	-2.0
HUrange18	1.1134	1.1325	-1.7	1.1070	1.1311	-2.1
HUrange19	1.1193	1.1390	-1.7	1.1123	1.1379	-2.2

6 THE MCTP WORKFLOW

The term Monte Carlo Treatment Planning is currently limited to the act of using an MC dose engine to recalculate an existing treatment plan, hence the actual treatment planning is done a priori and is not a part of MCTP.

The three cornerstones of MCTP are i: the linac model (Chapter 3), ii: the patient (or phantom) representation (Chapter 4) and iii: the translation of the treatment plan parameters, as given by the TPS, to MC compliant input files. The realization of dynamic delivery (i.e. changing with time during irradiation) in MC must be given special consideration. Separate building blocks aiming at solving the three cornerstones exist, but in order to routinely perform MCTP, an automated workflow considering the three tasks needs to be constructed. No such package is available to date. Furthermore, in–house constructed building blocks may increase flexibility and be better suited to the desired functionalities. This chapter describes the MCTP workflow developed and employed in this study. A schematic drawing of the MCTP workflow is given in Figure 60.

6.1 WORKFLOW OUTLINE

The starting point of the MCTP workflow is the conventional TPS, from which the following DICOM files are exported:

RP which holds all the information of the treatment plan parameters (e.g. gantry, collimator and couch angles, jaw collimator and MLC settings etc.)

CT the planning CT scan of the patient, which holds the HU matrix of the patient geometry

RD which holds information on the TPS calculated dose distribution

RS which holds information on all delineated structures

The set of DICOM files is imported to Computational Environment for Radiotherapy Research [Deasy et al., 2003] and saved for later usage.

A MC compliant representation of the patient is generated using either the DICOM RT–toolbox [Spezi et al., 2002] or CTC–ask [Ottosson and Behrens, 2011] as described in Chapter 4. Either of the two methods will maintain the dose grid set in the TPS.

MC dose engines are generally not integrated in the commercial TPS. Moreover most MC codes do not accept treatment plan information as

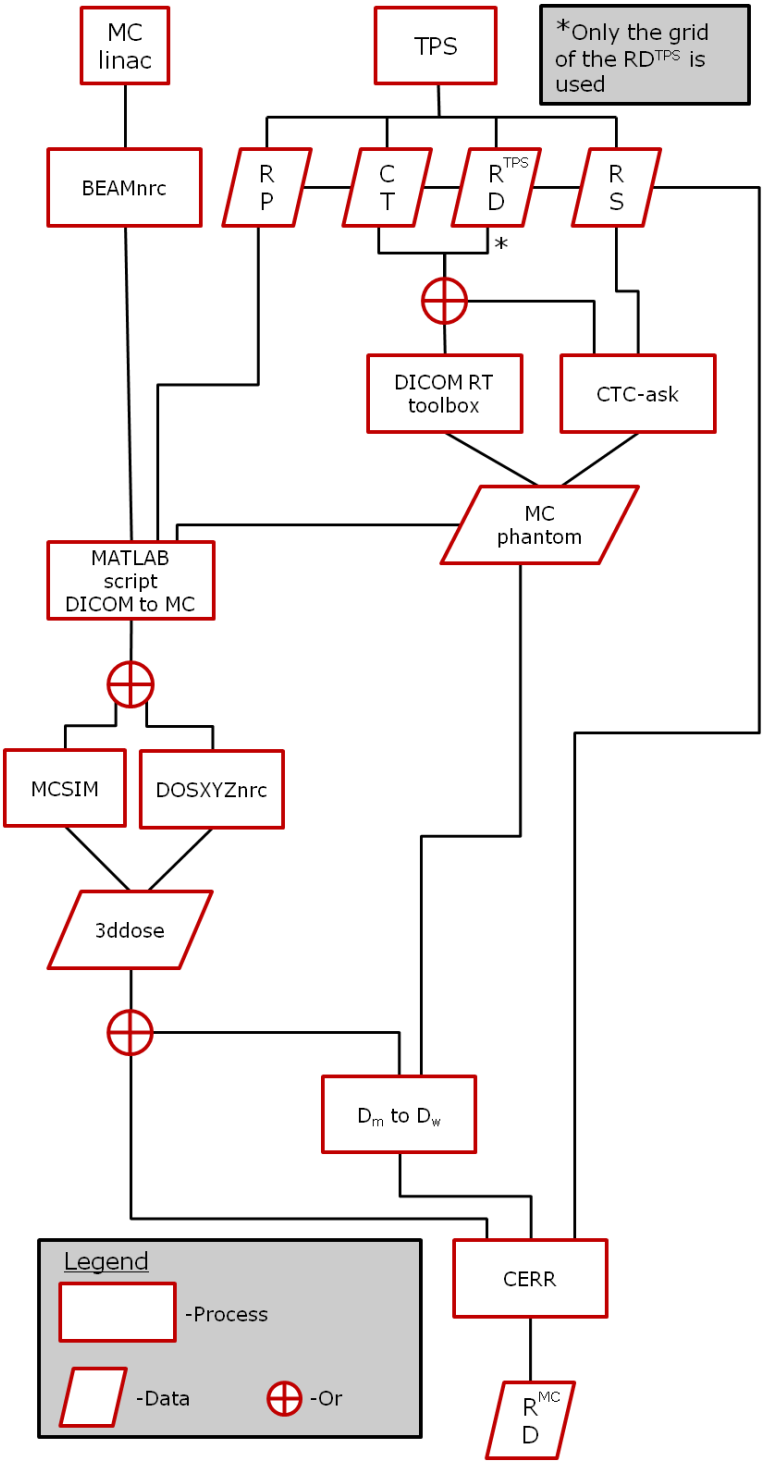

Figure 60: A schematic drawing of the MCTP workflow developed and employed in this study.

exported from the TPS (e.g. DICOM data) as input directly. Therefore it is necessary to translate the plan specific data (such as collimator settings, MLC sequence, gantry angle, iso center position etc.) to a format compatible with the MC code.

Full MC dose calculation is then conducted, using either MCSIM or BEAMnrc/DOSXYZnrc, resulting in a 3D dose distribution given as dose in medium per incident particle. The 3D dose distribution is converted to absolute dose (either as dose to medium or dose to water) and imported to CERR, which is capable of exporting the MC computed dose distribution in DICOM format.

The end point of the workflow described here is a MC computed 3D dose matrix in DICOM format, RD^{MC}, which has the same size and resolution as the TPS calculated dose distribution, RD^{TPS}.

6.2 TRANSLATING THE TREATMENT PLAN PARAMETERS TO MONTE CARLO INPUT

The following section addresses the issues one encounters when constructing a input file compatible with MCSIM or EGSnrc based on treatment plan parameters in DICOM format. Various tools for reading DICOM files exist (e.g. VEGA DICOM library [Locke and Zavgorodni, 2009], pydicom [Mason, 2011]), in this study the intrinsic MATLAB function `DICOMinfo` was used. `DICOMinfo` takes a single input argument: the path of the DICOM compliant file in question and returns the metadata in a data structure.

MATLAB scripts were created for extraction of the plan specific data and construction of input files for BEAMnrc, DOSXYZnrc and MCSIM. The following issues needed to be considered:

I/ DICOM lists all distances in mm, whereas EGSnrc and EGS4 user codes expects cm.

II/ The information on beam limiting devices is found under the DICOM field "BeamSequence" under which each individual beam is listed as a subfield. The information on fractionation (i.e. the number of MU per beam) is located under the DICOM field "FractionGroupSequence" under which each individual beam is listed as a subfield. It is however important to realize that the individual beams are not necessarily listed in the same order with regards to beams. The individual beams are linked through the variables "ReferencedBeamNumber" in the FractionGroupSequence and "BeamNumber" in the BeamSequence. This relates to DICOM files generated by the Varian Eclipse TPS, but might be implemented differently in other Treatment Planning System.

III/ The coordinate system differs between DICOM and that of EGSnrc and EGS4.

IV/ The MLC positions are listed as a single vector, as oppose to a vector for each MLC bank, for each control point.

V/ A DICOM file lists a set of static control points, whereas the delivery simulated may be dynamical.

The first and second issues are easily negotiated and does not merit further mentioning. The latter three issues will be discussed below.

6.2.1 *Coordinate system transformation*

The DICOM RP file holds information on the gantry, couch and collimator angles, whereas DOSXYZnrc utilizes the parameters θ, ϕ and ϕ_{Col}. Definitions of the three parameters depend on the source type in question. The source types used in this study are 2 (Phase-Space Source Incident from Any Direction), 9 (BEAM Treatment Head Simulation Incident from Any Direction), 20(Simulation through moving MLC with multiple variable settings) and 21(Full BEAM treatment head simulation through moving MLC with multiple variable settings), which all share the same coordinate system A set of equations rotating the TPS coordinate system to that of DOSXYZnrc was reported by Bush [2009]; Bush and Zavgorodni [2010]; Thebaut and Zavgorodni [2006]. However, the origin of the phase space file used in these studies was scored in negative z–direction, which is in contradiction with the origin of the source types used in this study. The particles travel in positive zdirection for θ=0 and ϕ=0. [Spezi et al., 2002] derived another set of equations for the coordinate transformation. The equations were not published in that paper but can be found in the source code of the DICOM–RT toolbox.

$$\theta = 90 \tag{6.1}$$

$$\phi = -90 + \theta_{gantry} \tag{6.2}$$

$$\phi_{Col} = -90 - \theta_{collimator} \tag{6.3}$$

where θ_{gantry} and $\theta_{collimator}$ are the gantry and collimator angles, respectively. The drawback of the transformation equations is that they are valid for coplanar treatments only.

MCSIM uses the same coordinate system as described above, but conveniently also offers the possibility to use the DICOM coordinate system.

6.2.2 *Field specific treatment head simulation*

The in–house written MATLAB scripts took the RP file as input and produced MC input files for either MCSIM or BEAMnrc/DOSXYZnrc

(using DOSXYZnrc source 2 for non–VMAT and source 20 for VMAT simulations). In either case the simulation starts from an energy specific phase space file scored below the monitor chamber ($BEAM_A$). The simulations were conducted using cut off energies of 521 keV (including rest mass) and 10 keV for electrons and photons, respectively. Uniform bremsstrahlung splitting was turned on, using NBRSPL = 1000 (maximum splitting factor). In order to maintain good electron statistics in the build up region, Russian roulette was switched off. This phase space was used directly as input in the patient simulations in MCSIM, while for patient simulations utilizing DOSXYZnrc, a second phases space file ($BEAM_B$) was scored at a distance of 60 cm from the target. Cut off energies were 521 keV (including rest mass) and 10 keV for electrons and photons, respectively. Directional bremsstrahlung splitting was employed, with SSD = 100 cm, NBRSPL = 1000 and FS[1] equal to the largest field side length defined by the jaw collimators (as projected at an SSD of 100 cm).

6.2.3 *The MLC position*

An MLC consists of two opposing banks of leafs: A and B. For the Varian Millennium MLC each bank houses 60 leafs. The two immediately opposing leafs are called a leaf pair and the opening of a leaf pair is governed by the distance[2] between the opposing leafs. An MLC leaf sequence file as exported from the TPS holds the lateral distance from the CAX of each leaf for every control point. This value refers to the projected distance at the ISO–center as oppose to physical position. Each leaf is represented by a number and the bank it belongs to (the leafs in bank A are referred to as [1A,2A,...,N-1A,NA] and the leafs in bank B are referred to as [1B,2B,...,N-1B,NB]). In the DICOM file the MLC positions are given by a vector of length 2N. Apart from being given in mm, there are two distinct differences between the MLC sequence file and the DICOM vector: i the (projected) distance from the CAX of the B–bank leafs are given by elements [1;N], while the (projected) distance from the CAX of the A–bank leafs are given by elements [N+1;2N] and ii the (projected) distance from the CAX of the B–bank leafs are given with inverted sign in the MLC sequence file compared to that of the DICOM file (figure 61). The interpretation of this is that a directional vector is assumed for each leaf bank in the MLC sequence file and that they are directed away from the CAX. In the DICOM RP file where all leaf positions are given in a single vector this is obviously not possible and therefore the (projected) leaf position, relative to the CAX, must be given for the two banks.

1 The radius of field into which bremsstrahlung photons must be directed if they are to be split

2 Two distance are of concern: the physical distance and the distance projected at the ISO–center plane.

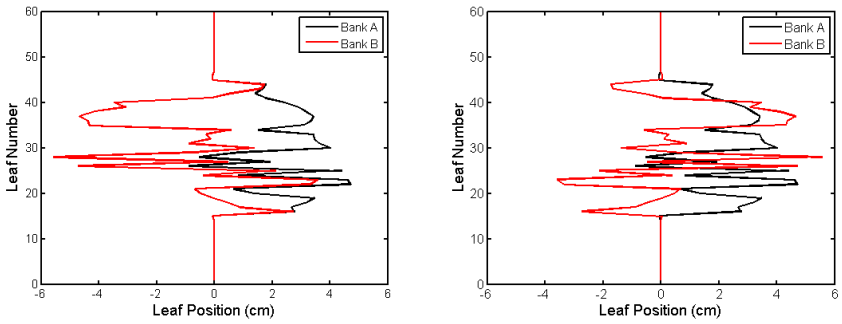

Figure 61: MLC positions for a typical Rapid Arc control point as listed in the DICOM RP file (left) and in the MLC sequence file (right). The single vector of leaf positions in the DICOM RP file have been separated into bank A and B. It can be seen that the bank A positions are identical whereas the bank B positions differ in sign.

Both MCSIM and the particle dMLC library takes, slightly, modified MLC leaf sequence files as input. The DYNVMLC CM also takes a slightly modified MLC leaf sequence file as input with one distinct difference: the lateral distance from the CAX for an individual leaf is the actual distance as oppose to the projected distance. This can be computed using simple trigonometry.

6.2.4 *The realization of dynamic delivery in Monte Carlo*

Advance radiotherapy (e.g. IMRT and VMAT) is often delivered dynamically, i.e. one or more component of the linac are moving during the irradiation. For dynamic IMRT[3] (also referred to as sliding window IMRT) the MLC is dynamically moving during the irradiation. For VMAT, in addition to MLC movement, the gantry and the collimator may also be rotating during irradiation. In the DICOM files, the motion is expressed as a number of control points which dictate the state of each linac component at a specific point in the delivery process. Attributed to each control point is also the fraction of the total accumulated MU to be delivered when arriving at the state dictated by the specific control point. This effectively sets the time scale of the dynamic delivery.

MCSIM

In order to implement the time scale in the MC simulation, intermediate control points are typically computed between two adjacent control points (as given by the DICOM file). This was implemented directly in the in–house script generating the MC input file for MCSIM.

3 IMRT may also be delivered by multiple static segments - so called "step and shoot IMRT".

Each leaf moves with constant speed between positions specified by two adjacent control points [Siebers et al., 2002]. Intermediate control points were thus computed at the mid–point between two adjacent original control point and the fractional delivery index associated to the i^{th} intermediate control point was taken as the average of the fractional delivery index for the adjacent original control points. This is a justifiable approximation if, and only if, the difference between any two adjacent control point is small.

Testing of MLC movement between control points

The MLC leaf movement between control points was in this study investigated for 100 clinical IMRT beams covering the most common treatment sites (e.g. head and neck, rectum, prostate and lung). The maximum movement of any individual leaf (between any two adjacent control points) was between 0.14 and 0.19 cm, while the average leaf movement was between 0.03 and 0.05 cm (static leafs disregarded from the average). Considering that the maximum leaf movement is on the order of the positioning accuracy for a detector and that the average movement is on the order of the precision of the MLC positioning, the approximation can be justified. The dynamic gantry angle was treated analogously, which is justified by the fact that it is the dose rate, rather than the gantry rotation speed, that is adjusted to ensure the correspondence between gantry angle and fractional photon fluence delivered (as stated by the control points). Thus, it may be assumed that the gantry rotates at a constant speed between two adjacent control points. Dose rate is not considered in MC, since there is no notation of time. Therefore the intermediate control points were assigned the average of the angles of two adjacent control points of the original data set. Thus, a beam specified by N control points is simulated as $N - 1$ static segments. The cumulative MU index was renormalized for the intermediate control points so that it ranged from 0 (for the the first segment) to 1 (for the last segment).

DYNVMLC and particle DMLC

The dynamic MLC as modelled in DYNVMLC [Heath and Seuntjens, 2003] and the particle DMLC [Siebers et al., 2002] operates in a similar fashion as MCSIM, but computes an intermediate control point for each particle. This is realized by drawing a random number that is related to a fractional MU index, and the leaf position is then linearly interpolated from the positions specified by the original control points.

DOSXYZnrc sources 20/21

Simulation of a VMAT treatment plan can be achieved with the DOSXYZnrc sources 20/21 as introduced by Lobo and Popescu [2010]. The input files lists a number of control points each attributed with a

set of angles, describing the gantry, couch and collimator angles in the BEAMnrc coordinate system (see Section 6.2.1) and a fractional index. A random number between 0 and 1 is drawn, which becomes the MU index of the particle to be simulated. The corresponding settings for the MLC is interpolated, as described above, and the particle is transported through it and then directed onto the phantom by using angles (θ_G, θ_T and θ_C) interpolated from the input file corresponding to that index.

MLC simulation example

Figure 62 shows the MLC settings for four control points of a clinical IMRT beam. Simulations were conducted for the dynamic plan, a step and shoot plan based on intermediate control points as described above as well as for the 74^{th} and 75^{th} segments (in static mode). All simulations were performed using BEAMnrc and DOSXYZnrc. The treatment head was simulated using BEAMnrc, and the MLC simulated using DYNVMLC, scoring a phase space file, containing $\approx 5 \times 10^7$ particles, at 90 cm distance from the target. The electron cut off energies (ECUTIN) of the jaw collimators and the MLC leaves were set to 1.8 MeV in order to reduce computation time. This effectively means that all electrons entering, or produced in, the collimator jaws and/or the MLC leaves were terminated. This is justifiable if comparisons are done at depths larger than the range of those electrons. The phase space file was incident on a homogenous water phantom (SSD = 100 cm) and gantry, collimator and couch angles were adjusted to 0° in DOSXYZnrc. The number of histories simulated were 3.6×10^8, thereby recycling each particle of the phase space seven times. The resulting statistical uncertainty for relative dose levels above 20% was less than 0.7%. The resulting dose distributions are illustrated in Figure 63. As can be expected, when viewing the MLC settings, the two adjacent control points yeild very similair dose distributions. The relative difference between the clinical IMRT plan simulated fully dynamically and in "step and shoot" mode using intermediate control points is shown in Figure 64. The relative difference for voxel (i,j,k) was computed as $(D_{i,j,k}^{stepNshoot} - D_{i,j,k}^{dynamic})/D_{i,j,k}^{dynamic} * 100$ and voxels with uncertainty > 1% in either of the dose distributions were omitted. The difference histogram exhibited close to normal distribution. A fit to a normal distribution yielded a standard deviation of 0.9%, while the average deviation was 0.5%. As the average deviation as well as the standard deviation was found to be small, one can infer that the error introduced by using intermediate static segmenets, as oppose to fully dynamic delivery, also is small. The error will however scale with the modulation of the treatment plan.

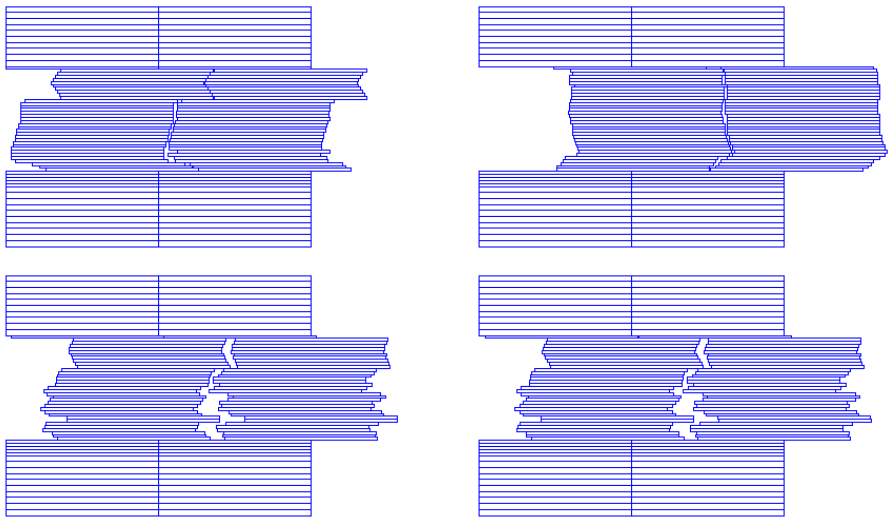

Figure 62: The figure shows the MLC settings for four control points (**top left**: segment 1/150, **top right**: segment 150/150, **bottom left**: segment 74/150 and **bottom right**: segment 75/150) of a clinical IMRT beam.

6.3 MC SIMULATION IN PATIENT GEOMETRY

MC simulation in patient geometry can be conducted utilizing MCSIM or DOSXYZnrc. Common for the two methods is that the patient specific MC compliant phantom is used to defined the geometry. For simulations in MCSIM, the $BEAM_A$ phase space file is used as input and simulation of beam modifiers (jaw collimators and MLC) are integrated in the patient dose simulation. Therefore, the information of jaw collimator and MLC settings is required in the patient simulations utilizing MCSIM. The only variance reduction technique switched on was IETRACK (electron track repeating) and cut off energies were set to 521 keV (including rest mass) and 10 keV for electrons and photons, respectively.

For simulation of clinical treatment plans in DOSXYZnrc different approaches were applied for simulations of VMAT and non–VMAT plans. In the first case the simulation started from $BEAM_A$ scoring a secondary phase space file ($BEAM_B$) below the jaw collimators using BEAMnrc and subsequently the MLC simulated using DOSXYZnrc source 20 to score dose to the patient while utilizing the particle DMLC code to simulate the MLC. For non–VMAT plans the beam modifiers were simulated using BEAMnrc, scoring a phase space file ($BEAM_B$) at a distance of 60 cm from the target and the MLC was simulated using DYNVMLC. The DOSXYZnrc simulation was then conducted using source 2. In both cases photon and electron splitting was set to

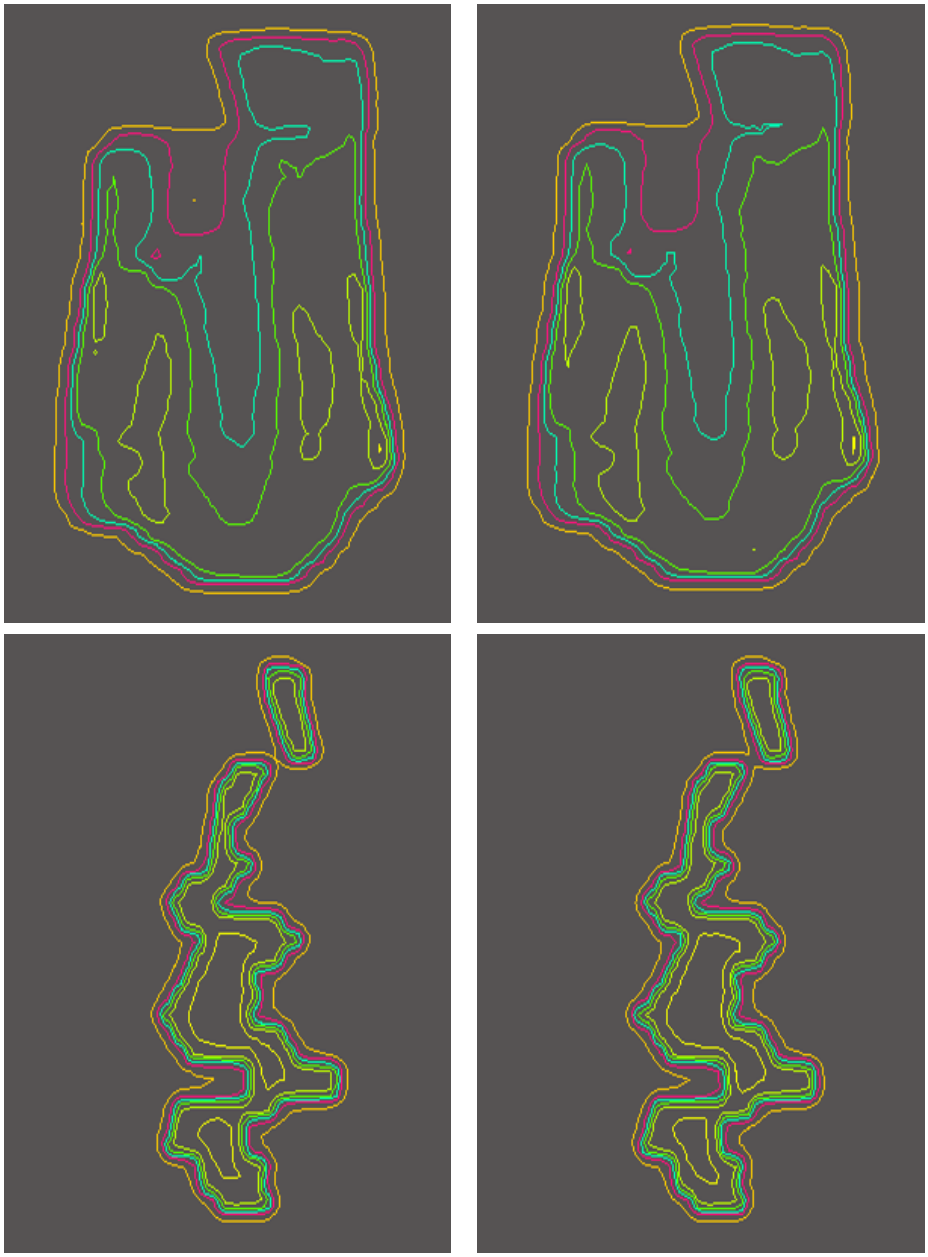

Figure 63: Relative 2D–dose distributions at 10 cm depth in a homogenous water phantom simulated by DOSXYZnrc. The ISO dose lines corresponds to 10% (dark yellow), 20% (pink), 30% (cyan), 40% (green), 50% (olive) and 60% (yellow) of D_{max}, respectively. Shown in the figure are dose distribution from a clinical IMRT plan simulated fully dynamically (top left), in "step and shoot" mode using intermediate control points (top right), statically for segment 74/150 (bottom left) and for segment 75/150 (bottom right).

25, PCUT was set to 10 keV while ECUT was computed using the rule of thumb[4] given in Rogers et al. [2009].

4 Choosing ECUT so that the range of electrons at ECUT is less than approximately a third of the smallest dimension in the dose scoring region ensures that energy is transported and deposited in the proper region

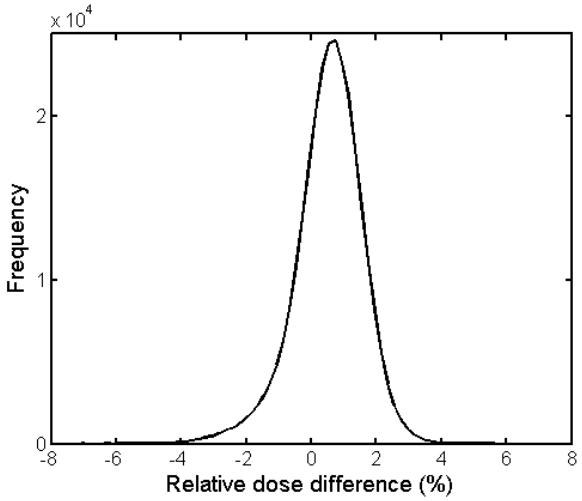

Figure 64: Local relative dose difference between the clinical IMRT plan simulated fully dynamically and in "step and shoot" mode using intermediate control points (taking the fully dynamical simulation as a reference). Voxels with uncertainty > 1% in either of the dose distributions were disregarded. The histogram is plotted using a bin widht of 0.2%.

Particles in the phase space file may originate from the same primary electron and thus be correlated. A latent variance [Sempau et al., 2001] in the phase space file may propagate to the final dose calculations leading to an underestimation of the uncertainty [Walters et al., 2002]. This is taken into account in the uncertainties reported by DOSXYZnrc [Kawrakow and Watlers, 2006; Walters et al., 2005], but not for MCSIM. The probability of two correlated phase space particles depositing dose in the same voxel is difficult to estimate, but considered small. In order to minimize the effect of the propagation of latent variance the recycle rate of phase space particle was limited by using a phase space containing a large number of particles. In MCSIM no phase space particle was used more than once, for each field, during the patient simulations while in DOSXYZnrc the particle were allowed to be recycled maximum 5 times. The difference was necessary in order to reduce disk space since the patient and field specific BEAM_B phase space files utilized by DOSXYZnrc are on the order of 5–10 Gb in file size.

6.4 CONVERTING THE MC DOSE DISTRIBUTION TO DICOM FORMAT

The resulting 3D–dose distribution was imported to CERR using an in–house written MATLAB script. In short the 3ddose file was read into MATLAB using the DICOM RT–toolbox function `dicomrt_read3ddose` and converted to absolute dose as described in Chapter 5. This does not pose a problem for multiple beam IMRT simulations utilizing MC-

SIM as a field specific calibration factor can be applied to each field individually and thereby correcting for monitor chamber backscatter effects (see Section 5.1). For multiple beam IMRT simulations using DOSXYZnrc a field specific post correction, as described in Section 5.1.2, is needed. In DOSXYZnrc each IMRT beam/VMAT arc was simulated individually, resulting in a dose distribution per field/arc, which simply was added to a dose distribution corresponding to the full treatment. Uncertainties were computed using error propagation procedures, assuming that the covariance between the beams was zero. The procedure results in a conservative estimate of the uncertainty. The previosly imported CERR plan was loaded and if the same dose grid was used, the TPS calculated dose was replaced by the MC calculated one. If the dose grids did not match, the CERR parameters were conformed to that of the MC dose grid. The MC dose distribution was multiplied by the number of planned fractions for the treatment. The CERR plan was saved (as a new file) and the CERR DICOM export, modified so as to only export the DICOM RD file, was executed yielding a DICOM RD file.

COMPUTATION DETAILS

EGSnrc computations were conducted on a dedicated 47 node, standard dual core 3.0 GHz PCs, cluster using a PBS queue system. A typical IMRT–$BEAM_B$ simulation in BEAMnrc took ≈147 hours (≈3.7 hours running on 40 nodes) resulting in a phase space file of $\approx 5.0\times10^7$ particles (depending on collimator and MLC settings). A typical IMRT field simulated in DOSXYZnrc using the $BEAM_B$ phase space had NCASE set to 3.6×10^8, ran for 150 hours (i.e. ≈3.8 hours running on 40 nodes) and resulted in a statistical uncertainty of ≈0.7% in the high dose regions. A VMAT–$BEAM_B$ simulation in BEAMnrc took ≈15 hours (≈0.4 hours running on 40 nodes) resulting in a phase space file of $\approx 6\times10^5$ particles per cm^2. A typical single arc Rapid Arc treatment plan simulated in DOSXYZnrc using the $BEAM_B$ phase space had NCASE[5] set to 5.0×10^7, ran for ≈60 hours (i.e. ≈1.5 hours running on 40 nodes) and resulted in a statistical uncertainty of ≈0.6% in the high dose regions.

MCSIM simulations were conducted on a stand alone dual core 3.0 GHz computer. A typical IMRT simulation (using N_{beams} fields) had NCASE set to $2\times10^9/N_{beams}$ and ran for ≈54 hours, resulting in an uncertainty of ≈0.7% in the high dose regions.

5 The actual number of histories to simulate is determined by deviding NCASE by the MLC survival fraction, which is computed by making a presimulation of 1×10^6 histories

7

MCTP VS CLINICAL DOSE CALCULATION ALGORITHMS

Currently available dose calculation algorithms (e.g. PBC and AAA) rely on approximations which might compromise accuracy of the final dose distribution (see Section 1.3.3.1). MC methods consider all aspects of the particle transport through the linac and in the patient and is therefore the most accurate dose calculation method. For that very reason it is of interest to compared dose distributions generated by MC to those calculated by clinical dose calculation algorithms. Such studies have been conducted by many groups [Aarup et al., 2009; Arnfield et al., 2000; Chow et al., 2003; Fogliata et al., 2007; Fotina et al., 2011, 2009; Francescon et al., 2000; Gagne et al., 2008; Hasenbalg et al., 2007; Jeraj et al., 2002; Keall et al., 2001; Knöös et al., 2006; Krieger and Sauer, 2005; Linthout et al., 2002; Ma et al., 1999; Ottosson and Behrens, 2011; Ottosson, Karlsson and Behrens, 2010; Paelinck et al., 2005; Reynaert et al., 2005; Seco et al., 2005; Sterpin et al., 2009; Vanderstraeten et al., 2006; Wang et al., 2002] in heteregenous phantoms as well as in patient geometry. Some of the studies focus on extreme cases where a single beam progresses through a boundary between high and low density materials.

7.1 REVIEW OF LITERATURE

Paelinck et al. [2005] compared two different superposition/convolution algorithms to MC for single beam impinging on a polystyrene phantom with a large centrally placed cavity consisting of a lung–equivalent material. For one of the algorithms agreement was found within the lung cavity whereas an over response of 3.6% was noted behind the cavity. The second algorithm was in better agreement with MC behind the cavity but showed an underresponce of 5.6% within the lung cavity. MC was in agreeement with radiochromic film in the lung cavity as well as behind it.

Arnfield et al. [2000] compared a generalized Batho algorithm and a superposition/convolution algorithm to MC and Thermo Luminescent Dosimeter (TLD) and IC measurements for beams impinging on a tissue–equivalent phantom with a centrally placed cavity consisting of a lung–equivalent material. The comparison was done for PDDs along the CAX. Agreement was found between measurements and MC while both algorithms over responded in the lung cavity. The effect was inversely proportional to field size proportional to the energy of the impinging photons.

Francescon et al. [2000] compared MC simulation to a superposition/convolution algorithm for mediastinal and breast treatment plans. Deviations between MC and the TPS were in the range of 0% to 2.6% even in areas of large density inhomogeneities as well as for single beam calculations.

Reynaert et al. [2005] compared a superposition/convolution algorithm to two different MC dose engines for a head and neck IMRT treatment. The superposition/convolution algorithm agreed with one of the MC simulations whereas deviations of up to 10% were noted between the two different MC simulations. This illustrates the importance of accurately modeling the linac. The difference was thought to be due to improper commissioning of the MLC model for the MC dose engine not in agreemnet with the superposition/convolution algorithm. It should be noted that the deviating MC dose enginge was a beta release.

Sterpin et al. [2009] compared a superposition/convolution algorithm to MC simulations both in idealized phantom geometries as well as for patient calculations. Dose was calculated for a beam impinging on a heterogeneous phantom consisting of two slabs of polystyrene separated with Styrofoam and compared to radiochromic film measurements. The deviation for the transversal dose plane, of the polystyrene slab, was within 2%/1 mm for a 1.25×2.5 cm^2 field. Similar agreement was found between MC and the superposition/-convolution algorithm for the transversal dose plane. Compared to MC, an overresponce of the superposition/convolution alogorithm of up to 8% was noted behind the polystyrene/styrofoam interface. The largest deviation was found for the smallest field size investigated. The deviation between TPS calculated and MC computed dose was, however, within 2% in most situations.

The lesson learned from previous studies are, unsurprisingly, that the largest deviations are found in the extreme situations were a single beam is progressing through a phantom with large cavities. The deviations increase with increasing photon energy and decreasing field sizes. Better agreement is found when comparing situations resembling clinical treatment plans (e.g. multiple beams, real patient geometry). Finally, superposition/convolution algorithms are generally in better agreement with MC than less sophisticated algorithms (e.g. PBC and Batho methods).

In the following sections comparisons between commercially available algorithms and MC are presented for clinical treatment plans.

7.2 COMPARISON FOR CLINICAL TREATMENT PLANS

In order for a comparison between MC dose calculation algorithms and TPS to be fair a number of circumstances needs to be considered. The dose calculation algorithms in commercial TPS usually report

D_w [Knöös et al., 2006], while MC report D_m. The method for conversion between the quantities was discussed in Section 5.2 and is well documented in the literature [Siebers et al., 2000]. Moreover the commercially available dose calculation algorithms treat voxels differently depending on weather they are located within the external contour or not. Typically voxels outside the external outline are set to a density corresponding to 0 HU. Corrections methods for support structures (e.g. the couch and immobilization devices) may be conducted based on transmission measurements. For some commercial algorithm, advanced models of support structures may be incorporated in the treatment planning. In MC the dose calculation grid is typically defined so that the patient couch is omitted, but the voxels outside the external outline is typically not considered differently than those inside during the CT to phantom conversion. As discussed on page 86 a function for setting voxels outside the external contour to air with a density of 1.2041×10^{-3} gcm^{-3} was implemented in CTC–ask. Thus, replicating the typical procedure of commercial dose calculation algorithms. As for support structures, if no reliable drawings can be obtained and converted to a structure in the MC simulation a pragmatic solution is to omit them in the dose calculation all together.

In order to investigate the influence of setting voxels located outside the external outline to air with a density of 1.2041×10^{-3} gcm^{-3} a head and neck case planned for IMRT was converted to a MC compliant phantom using CTC–ask, and the media set described in Section 4.4.2. Two phantoms were generated, one where all voxels outside the external contour were explicitly set to air with a density of 1.2041×10^{-3} ($phant_A$) and one where they were not ($phant_B$). The phantoms were idenctical for all voxels inside the external contour. The MCTP workflow illustrated in Figure 60 was employed in order to recalculate the treatment plan using an MC dose algorithm. The MCSIM dose engine was selected[1], conversion to D_w was conducted.

It can clearly be seen that the dose outside of the external contour is higher for the simulation based on $phant_A$ than compared to that of $phant_B$ (Figure 65). Apart from the decreased dose outside of the patient geometry, two effects can be noted for the simulation based on $phant_B$: (i) the surface dose of the actual patient is lower as the build–up region is effectively shifted deeper into the patient and (ii) a higher dose in the central regions of the patient. Shifting the build–up region deeper implies that the beam will be less attenuated at a given distance beyond d_{max} and thus will give rise to a higher dose. This is illustrated by a shift towards higher doses for the centrally located structures, predominantly the PTV and the CTV, as seen on the DVHs in Figure 66. This effect will be somewhat compensated for distal

1 Cut off energies were 521 and 10 keV for electrons and photons respectively. The only variance reduction technique explicitly employed was electron track repeating. The number of histories were chosen so that the estimated statistical uncertainty was ≈0.5% for the voxels in the high–dose regions.

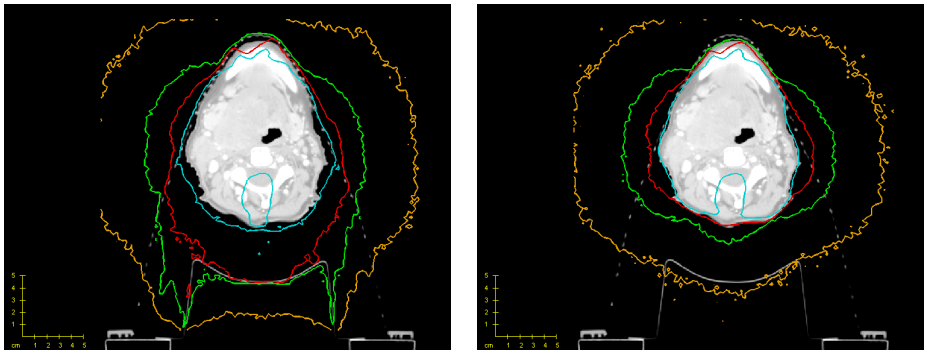

Figure 65: MC simulated isodose lines for a head and neck IMRT case. Simulations conducted using MCSIM for a phantom were no considerations were made for the voxels outside the external outline (**left**) and a phantom were the voxels outside the external outline were set to air with a density of 1.2041×10^{-3} gcm^{-3}. The isodose lines corresponds to 10% (brown), 20% (green), 30% (red) and 50% (blue) of the prescribed dose.

voxels when using opposing beams while it will be further enhanced for central voxels.

Assigning all of the voxels outside the external contour to air might not be accurate from a dosimetric point of view since the patient might be covered by a mask, be placed in a fixation and the treatment couch might be in the beam. For inter comparison between MC and TPS dose calculation algorithms it is a sound strategy if such a feature is implemented in the TPS. In CTC–ask, delineated support structures may, like any other delineated structure, be assigned the actual density and media composition should it be known.

7.2.1 *Monte Carlo vs AAA*

MC simulation was conducted for five clinical dual arc RapidArc and two IMRT treatment plans all calculated with AAA as implemented in Varian Eclipse TPS build 8.2.24.10720 (Varian Medical Systems, Inc. Palo Alto, CA, USA). DICOM files were exported form the TPS and imported to CERR. The MCTP workflow illustrated in Figure 60 was employed in order to recalculate the treatment plan using an MC dose algorithm. MC compliant phantoms were generated from the DICOM files using the 19 media set (described in Section 4.4.2) implemented in CTC–ask. Voxels outside the external contour were explicitly set to air with a density of 1.2041×10^{-3} for all phantoms. The DOSXYZnrc

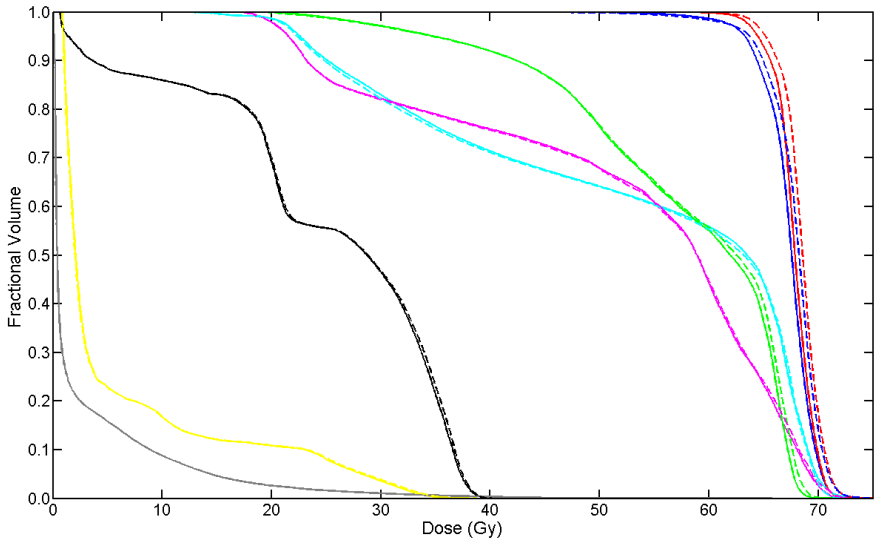

Figure 66: DVHs for MC simulations for a head and neck IMRT based on two different geometries, one where all voxels outside of the external contour actively was set to air with a density of 1.2041×10^{-3} gcm^{-3} (dashed) and another where no special considerations were made for the voxels located outside the external contour (solid). DVHs of the following structures are shown: CTV(red), PTV (blue), parotis dx (cyan), parotis sin (magenta), larynx (green), brain stem (yellow), spinal cord (black), lung (grey).

dose engine was selected[2] and conversion to D_w was conducted. The resulting dose distributions were imported to CERR. The CT data and structures imported to CERR from the TPS DICOM files were used in the computation of DVHs.

In geometries with small variations in density the AAA calculated and MC simulated dose distributions are in good agreement (Figure 67). The voxels failing the 2D gamma evaluation (2% dose, 0.2% mm Distance To Agreement (DTA)) for a prostate dual arc RapidArc case are all either located in the build up region or at bone–tissue interfaces (Figure 67). For the lung IMRT case shown in Figure 68, differences are found at lung–tisue interfaces as well. Dose differences of up to 6% were found at the lung–heart and the lung–tumor interfaces for the lung IMRT case.

The difference in agreement between AAA and MC for cases with (e.g. lung) or without (e.g. prostate) large regions of substantial variation in density and elemental composition, can clearly be seen on DVHs (Figure 69 and Figure 70). For the lung IMRT case (Figure 70), the MC DVHs of the PTV and the CTV are shifted to lower doses

2 Cut off energies were 700 and 10 keV for electrons and photons respectively. Photon splitting and electron splitting were set to a value of 25. The number of histories were chosen so that the estimated statistical uncertainty was ≈0.5% for the voxels in the high–dose regions. Source 20 was selected and particle Dmlc was employed to simulate the MLC

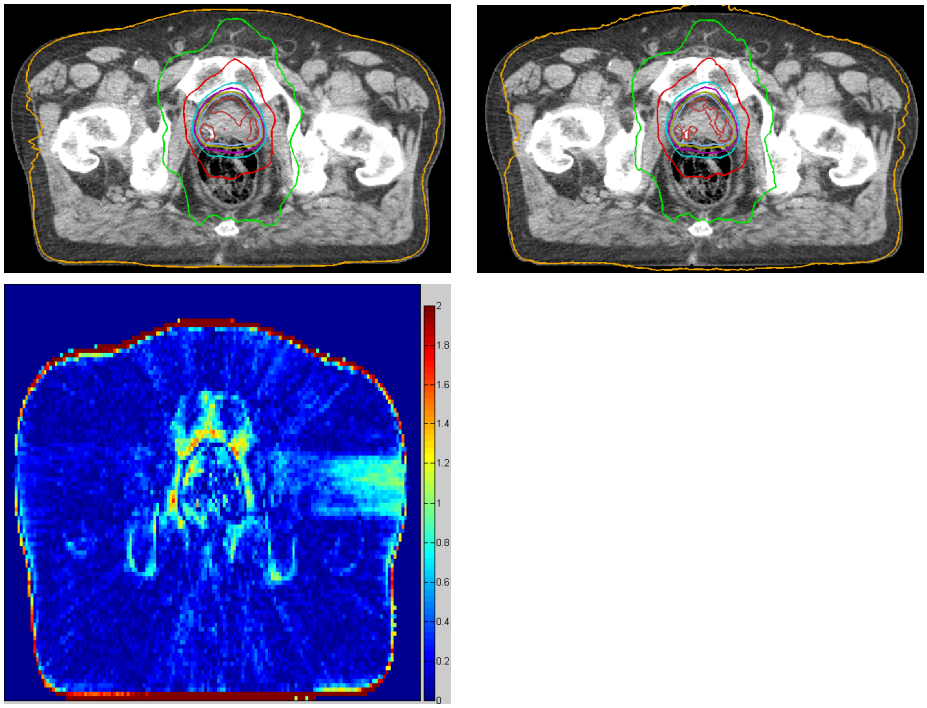

Figure 67: **Top panel:** A transversal CT slice of a prostate dual arc RapidArc case calculated by AAA (left) and MC simulated using DOSXYZnrc (right). The isodose lines corresponds to 10% (orange), 30% (green), 50% (red), 70% (cyan), 80% (purple), 90% (gold), 95% (light blue) and 100% (deep red). **Bottom:** 2D gamma analysis (2%/0.2 mm). Voxels outside the external contour were set to gamma = 0.

compared to AAA (mean doses were 0.7 and 0.5 Gy lower, respectively). This is explained by the over estimation of scattered dose from lung in AAA. For the prostate case, however, no monotonous shift is noted for the PTV or the CTV, instead the MC DVHs of these structures are tilted about the average dose. Part of this is a result of the stochastic nature of MC. The effect exists for all structures, but is less clearly visible for structures receiving lower doses. The mean doses of the structures considered agreed within 0.3 Gy for the structures considered (Table 16).

[Fippel, 2003; Jiang et al., 2000; Kawrakow, 2002; Naqa et al., 2005; Smedt et al., 2006] investigate the possibility of using smoothing filters on MC simulated dose distribution as a mean of reducing the influence of statistical noise. Jiang et al. [2000] proposed an iterative algorithm, in which the uncertainty of the MC simulation is used to construct a blurring function, which in turn is used to produce noiseless DVHs. They found that the influence of noise was largest for structures with steep DVH gradient (e.g. typically the target volumes). Moreover they stated that the influence of the statistical noise, depending on the un-

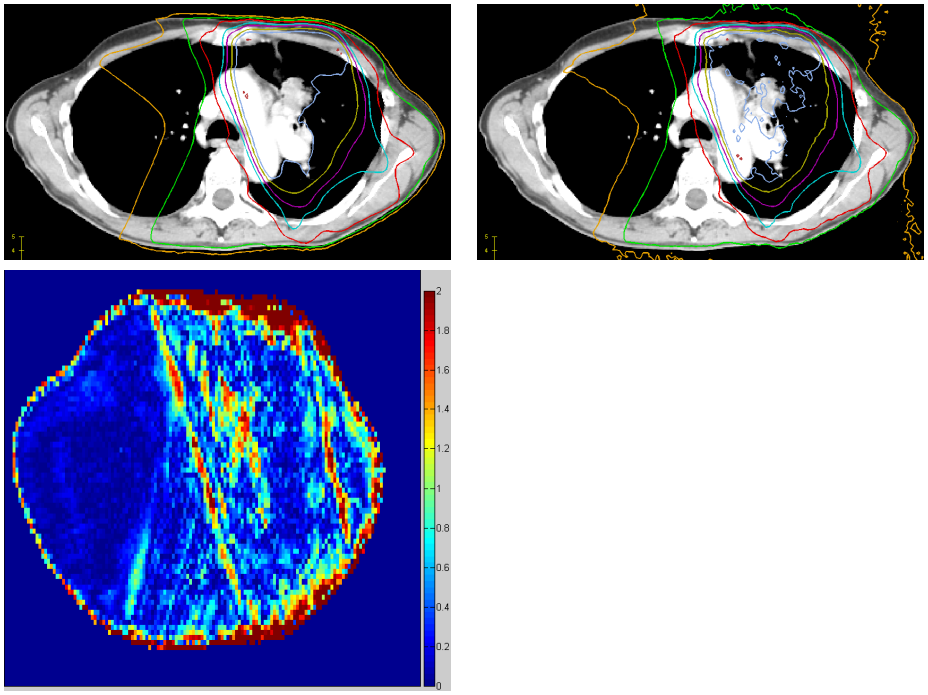

Figure 68: **Top panel:** A transversal CT slice of a head and neck dual arc RapidArc case calculated by AAA (left) and MC simulated using DOSXYZnrc (right). The isodose lines corresponds to 10% (orange), 30% (green), 50% (red), 70% (cyan), 80% (purple), 90% (gold), 95% (light blue) and 100% (deep red). **Bottom:** 2D gamma analysis (2%/0.2 mm). Voxels outside the external contour were set to gamma = 0.

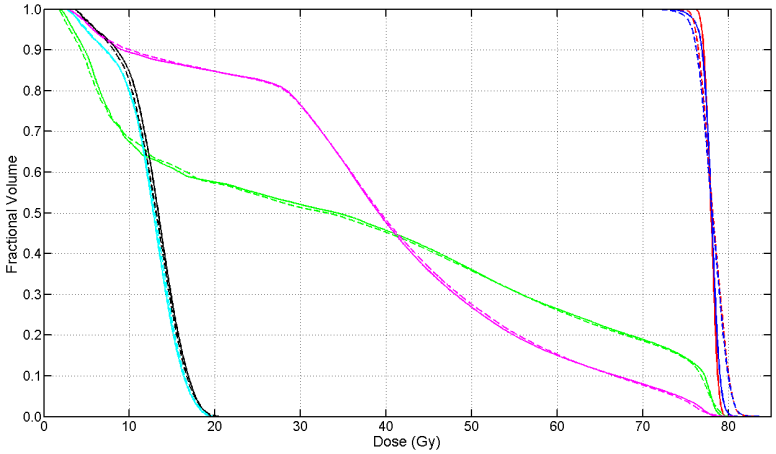

Figure 69: DVHs for a prostate dual arc RapidArc case calculated by AAA (solid) and MC simulated using DOSXYZnrc (dashed). The DVHs shown correspond to CTV (red), PTV (blue), rectum (magenta), bladder (green), caput femur sin (black) and caput femur dx (cyan)

.

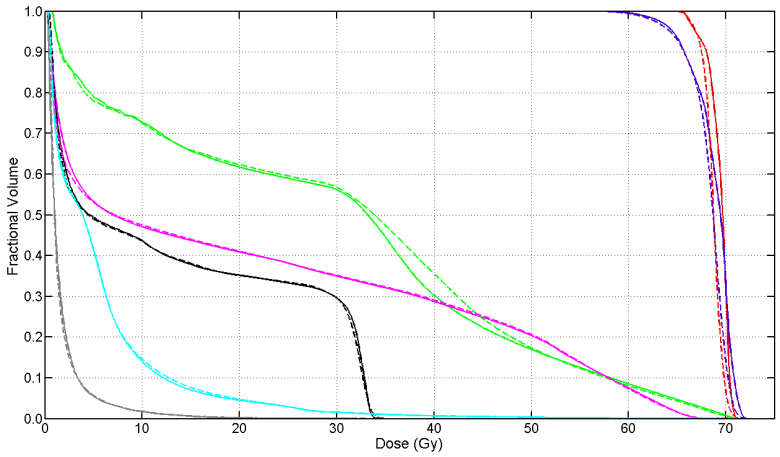

Figure 70: DVHs for a seven field IMRT lung case calculated by AAA (solid) and MC simulated using DOSXYZnrc (dashed). The DVHs shown correspond to CTV (red), PTV (blue), the right lung (cyan), the left lung (magenta), the oesephagos (green), the spinal cord (black) and the heart (grey)

.

certainty of the simulation, could be of clinical importance. Smoothing of dose distribution and DVHs were, however, not employed in this study.

An aspect worth mentioning is that AAA calculates the dose as N static segments (where N is the number of control points), whereas the MC, as implemented here, calculates the dose as being delivered fully dynamically. Thus, it might seem like a case of comparing apples and oranges, but in fact is not since the approach employed in the AAA dose calculation is an inherent limitation of the algorithm itself. The approximation of calculating a dynamical delivery as N static segments also infers that the difference between AAA and MC calculated dose will increase with the modulation of the treatment plan if N is kept constant as for RapidArc treatment plans.

7.3 HIGH VS LOW ENERGY FOR LUNG TREATMENTS

PBC dose calculation is frequently used for lung cancer treatment planning. If PBC based treatment plans generated with high and low energy (e.g. 15 MV or 18 MV and 4 MV or 6 MV, respectively) are compared, the ones based on the higher energies will in many cases appear more favorable. However, it is well known that the inaccuracies introduced by the PBC dose calculation generally are larger for higher energies and depend on several parameters such as field size and geometry (e.g. [Behrens, 2006], [Klein et al., 1993], [Tsiakalos et al., 2006], [Vanderstraeten et al., 2006], [Krieger and Sauer, 2005]). Therefore, usually low energy is chosen as default for lung

Table 16: Average dose to specific structures for a dual arc RapidArc prostate case as calculated by AAA and MC. The MC dose was considered as the reference.

Structure	AAA (Gy)	MC (Gy)	Difference (Gy)
CTV	78.0	78.3	-0.3
PTV	78.0	78.1	-0.1
Bladder	35.9	35.7	0.3
Rectum	39.9	40.1	-0.2
Caput femur dx	12.3	12.5	-0.1
Caput femur sin	13.0	12.8	0.2

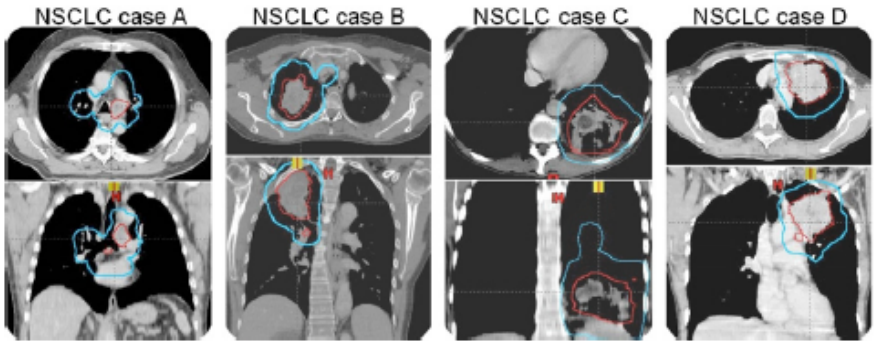

Figure 71: NSCLC cases (A)–(D). Transversal and coronal CT slices, illustrating the tumor location and extension. Red and light blue lines are delineations of the GTVs and PTVs, respectively.

treatments. This begs the question whether this always is the best choice. For some cases, treatment plans based on higher energies may be more favorable. In order to address this question, more accurate dose calculation methods (e.g. MC) must be employed. PBC and a more sophisticated superposition/convolution algorithm, AAA, were compared to MC–based dose calculations clinical IMRT and AP–PA lung treatments.

Four non-small cell lung cancer (NSCLC) cases with apparent differences in tumor location, were selected for this study. The cases exhibited geometrical properties where one could expect a significant discrepancy between analytical and MC dose calculation algorithms (Figure 71). CTV and OAR were delineated by a radiologist. PTV margins were added in accordance with the protocol used at Copenhagen University Hospital Herlev.

7.3.1 *Treatment Planning*

For inverse planning, Varian EclipseTM build 8.2.24.10720 (Varian Medical Systems, Inc. Palo Alto, CA, USA) modeling a Varian 2300 iX (Varian Medical Systems, Inc., Palo Alto, CA, USA) was used.

35×2 Gy was prescribed to the PTV and a maximum dose constraint of 45 Gy was applied to the spinal cord. The lungs were assigned a dose volume constraint of $V20 \leqslant 50\%$, while the constraints for the heart were $V30 \leqslant 100\%$, $V45 \leqslant 65\%$ and $V60 \leqslant 25\%$.

As an initial step of the treatment planning, the optimal numbers of beams, gantry and collimator angles were determined individually for each case and energy (6 and 15 MV) by Varians geometrical optimization module utilizing the Plan Geometry Optimization (PGO) algorithm (Varian Medical Systems 2007). The PGO takes the specific geometry of the case and the DVO constraints into account.

Hereafter, a number of isocentric dynamic (sliding window) IMRT treatment plans, ranging from PTV conformity weighted to normal tissue sparing weighted, were created for each case and beam energy. Thus, the PTV coverage, from one plan to the next, deteriorated as sparing of the normal tissue in general, and the lungs specifically, increased. In total 31 treatment plans, distributed amongst the 4 cases, were created. For the optimization, a PBC algorithm was used as Eclipse offers no other option. Full dose calculation was undertaken for each treatment plan, employing the Eclipse PBC algorithm and the AAA using identical MLC settings and monitor units.

7.3.2 *Monte Carlo simulations*

Voxalized phantoms were created via the DICOM RT toolbox using the planning CT set as input. The phantom grid was matched to the dose grid of the TPS. A set of in–house MATLAB scripts was used to generate input files for MCSIM from the DICOM RP files. Thus, all parameters of the treatment plans were recreated in the simulations. The treatment plan simulations were performed in MCSIM using an energy specific phase space, scored above the jaw collimators, as source input. A total number of $0.5–1 \times 10^9$ histories was simulated for each treatment plan, resulting in a statistical uncertainty of 0.3–0.6% at the global dose maximum. Cut off energies of 521 keV (including rest mass) and 10 keV for electrons and photons, respectively were used. The only variance reduction technique switched on was IETRACK (electron track repeating). Backscatter corrections were calculated for each field using the method described in Section 5.1.3.

Since the TPS reports dose to water and MCSIM dose to media, a conversion was necessary in order to ensure a fair comparison. The procedure suggested by Siebers et al. [2000] as implemented in

the DICOM RT toolbox was employed in order to convert the MC-calculated dose into dose to water.

7.3.3 *Evaluation*

For each treatment plan and algorithm, DVHs were created. The DVHs were used to evaluate the volume of the PTV receiving less than 95% of the prescribed dose $\left(1 - V_{95}^{PTV}\right)$. The lung NTCP for pneumonitis was calculated using an Equivalent Uniform Dose (EUD)-based formalism Gay and Niemierko [2007]. The parameters used for the NTCP calculation were a = 1, γ_{50} = 2, TD_{50} = 24.5 Gy and α/β = 3 Gy, as suggested by [Gay and Niemierko, 2007].

The results were evaluated using a Pareto front comparison method Ottosson et al. [2009]; Steneker et al. [2006]. The general idea of this concept is to compare sets of plans, belonging to different classes (e.g. high versus low energy) as opposed to a traditional plan-to-plan comparison procedure. Comparative treatment planning has hitherto often been rather inconclusive. For instance, when comparing different IMRT delivery techniques (e.g. step and shoot versus sliding windows), it may have been found that one of the techniques is capable of better target coverage, while the other is better at sparing risk organs. This leaves room for a subjective interpretation. By sampling the entire Pareto front for a case, it may be possible to make a much more just and comprehensive comparison of the two systems. Utilizing this concept elements such as treatment planner dependence and misfortunate plan selections can be minimized.

In order to visualize the comparison between energies and algorithms, Pareto fronts based on $\left(1 - V_{95}^{PTV}\right)$ and the lung NTCP were produced for all algorithms and cases. Plans belonging to the same class (beam energy and algorithm) constitute the Pareto front for that specific class, enabling comparison of class to class rather than plan to plan.

7.3.4 *Results*

All algorithms (PBC, AAA and MC) used identical setups for each treatment plan and all differences in the resulting dose distributions were solely due to discrepancies between the dose calculation algorithms. Throughout this study MC is considered the golden standard or "ground truth". Unless explicitly stated all references to dose distributions or dose differences are based on the MC calculations.

Considering MC as the golden standard, the inaccuracy of the other algorithms, in terms of NTCP and PTV underdosage, is illustrated and quantified by the Pareto fronts. The results illustrate that PBC significantly miscalculates the dose for all treatment plans, independent of tumor geometry. AAA is in much better agreement with MC.

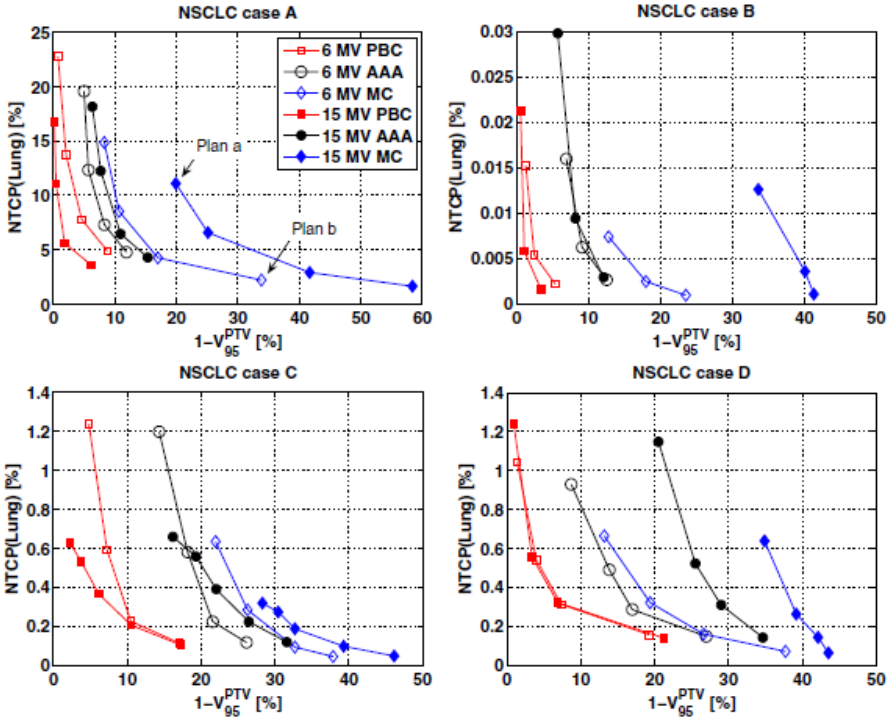

Figure 72: Pareto fronts for NSCLC cases (A)–(D). Treatment plans a and b for case A (marked in the plot) illustrate the potential problem in a plan to plan comparison study. Which one is the better plan, and should we prefer 6 or 15 MV? This question is impossible to answer based on these two treatment plans alone. However, when the Pareto fronts are plotted, it is clear that 6 MV is preferable to 15 MV for this case.

Generally, the differences between PBC and AAA/MC are larger for 15 MV. PBC and AAA overestimate the dose to the PTV, compared to MC (Figure 72). Even a small overestimation in dose can lead to a large impact on $(1 - V_{95}^{PTV})$ due to the conformal nature of the dose distribution.

The dose to the total lung volume was significantly higher for case A. This is due to the fact that the PTV in case A is located in the mediastinum and extends into both lungs. For cases B–D, the PTV is confined to one lung, making it possible to spare the contralateral lung to a large extent. The NTCP(lung) values for cases B–D are very low. However, plotting V20 as a function of $(1 - V_{95}^{PTV})$ yields results similar to those illustrated in figure 5 and leads to the same conclusions. For the MC calculations, the ranges of V20 values are [34;53], [12;19], [18;29], [21;25]%, for cases A, B, C, and D, respectively.

For cases A–C, 15 MV appears favorable as compared to 6 MV based on the PBC treatment plans, while for case D, no significant difference is observed. However, this is not the case as more accurate dose calculation algorithms are employed. All cases exhibit a better combination of target coverage and NTCP(lung) for 6 MV than for 15

MV, i.e. for a range of treatment plans, the Pareto front for 6 MV MC is closer to origin than the corresponding 15 MV MC front (Figure 72). The difference is least pronounced for case C. From the treatment plans generated, it is clear that 6 MV is more favorable than 15 MV in general.

Even though 6 MV was generally found to be more favorable for the cases studied, one should not set aside the possibility of using higher energies, as there might be cases or classes of cases benefiting from high energy–based treatment plans. It would be advantageous if patients could be sorted prior to treatment planning, identifying those with potential benefit from high energy–based treatment. Sorting criteria could include patient size and tumor location, tumor size and proximity to other structures, etc. For example, due to the larger dose deposition at depth, high energy-based treatment plans might be more advantageous for deep seated tumors. However, several other factors are important, e.g. the larger penumbra region and primary and secondary build-up effects for the higher energy. A large secondary build–up effect might be advantageous when a beam passing through lung enters high-density healthy tissue, while a small build–up effect is beneficial when a beam passing through lung enters high density tumor tissue. Based on the present work, it has not been possible to identify suitable sorting criteria. Possibly, too many different effects interplay and the potential benefit for a patient is based on the exact geometry of the case including the specific beam configuration. One might find that for some patients and a given beam configuration, high energy might be advantageous while low energy is advantageous for another beam configuration. In fact, it might be that some patients could benefit from a mixed energy setup, i.e. using high energy for some gantry angles and low energy for others. This is beyond the scope of this work and the subject of future investigations.

7.3.5 *Conclusions*

This study clearly demonstrates that the PBC dose calculation algorithm is clinically insufficient for patient geometries such as cases A–D. This is line with the study by [Jeraj et al., 2002] where the conclusion was that PBC algorithms should be replaced by superposition/convolution algorithms or MC for inverse treatment planning. AAA is generally in closer agreement with MC than PBC, which also was the result of the study conducted by [Knöös et al., 2006].

For the more simple AP–PA treatment plans both the AAA and PBC calculation algorithms predicts the trends in the differences between 15 and 6 MV plans, except in the lungs for the PBC algorithm. Both the AAA and the PBC algorithm sufficiently accurately predicts the absolute dose levels for the palliative patients studied. This indicate that PBC still may be a viable choice in the case of forward planning.

A number of the PBC–calculated treatment plans appeared significantly better for 15 MV than for 6 MV. However, considering MC as the golden standard, the dose distributions that would actually be delivered to the patient are significantly better for 6MV for the IMRT plans. Yet, one should not completely set aside the possibility of using higher energies for sites covering the lungs or other inhomogeneous sites, as there might be cases, or classes of cases, where the resulting plans prove to be better. However, it is still advisable to use low energies as default for tumor sites involving large inhomogeneities unless a precise dose calculation algorithm is available.

7.4 THE INFLUENCE OF THE FITTED PARAMETERS OF THE MONTE CARLO MODEL

Although the particle transport in MC does not rely on inherent approximations, it is important to remember that the calibration of the linac model typically is conducted by tweaking parameters of the particles incident on the linac target until an acceptable agreement between simulations and measurements is achieved. Moreover, the validation typically encompasses only a limited number of simulation geometries. It is by no means trivial to translate the influence of the uncertainty on the fitted model parameters to differences on dose distribution in a heterogeneous patient geometry and for a complex treatment delivery. [Chetty et al., 2005] investigated the influence of the model parameters of an Equivalent Path Length algorithm for a conformal treatment plan involving the thorax region. An initial model was determined by choosing a set of parameters so that agreement was found with an MC simulation along the CAX of a heterogeneous phantom. The model parameters were subsequently optimized so that agreement with MC simulation was found also in the penumbra– and low dose regions. The optimized Equivalent Path Length (EPL) model calculated dose well within $\pm 3\%$ of the MC calculated dose distribution, wheras deviations of 10% to 15% were noted when comparing the dose predicted by the initial model with that of the MC algorithm.

The statistical tests employed in the calibration of the MC model described in Section 3.3 estimate not only the optimal parameter values but the standard deviation of each parameter value. The value minimizing the χ^2/NDF corresponds to the optimal value while one standard deviation of that parameter is the value resulting in $\min(\chi^2/\mathrm{NDF})+1$ [Berendsen, 2011; Hughes and Hase, 2010]. The optimal value was chosen by fitting a second degree polynomial to a data set representing χ^2/NDF as a function of spot size FWHM and the value corresponding to +1 SD is that resulting in $\min(\chi^2/\mathrm{NDF})+1$ (Figure 73). Although the optimal value was revised later in the calibration protocol the value of the SD may still be representable.

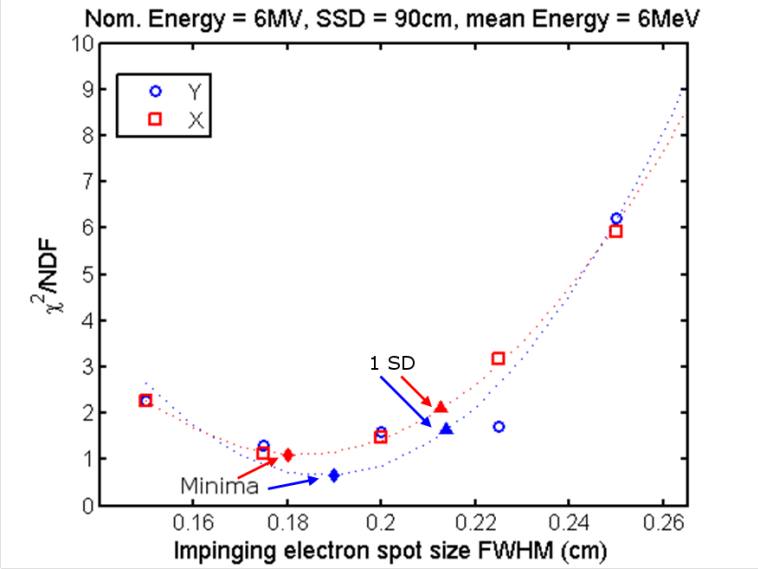

Figure 73: χ^2/NDF as a function of spot size FWHM, for X (red square) and Y (blue circle) direction individually, for the 6MV model. A second degree polynomial fit to the data is included (dashed). The values minimizing the χ^2/NDF as well as those corresponding to +1 SD are included in the figure (diamonds and triangles, respectively).

In order to investigate the influence of the fitted parameters of the model, MC simulation was conducted for five clinical dual arc RapidArc treatment plans. The MCTP workflow illustrated in Figure 60 was employed in order to recalculate the treatment plan using an MC dose algorithm. MC compliant phantoms were generated from the DICOM files using the 19 media set (described in Section 4.4.2) implemented in CTC–ask. The DOSXYZnrc dose engine was selected[3] and conversion to D_w was conducted.

Simulations were conducted for two MC models: MC_{opt} where parameters were chosen in accordance with the previously conducted commissioning (i.e. mean impinging electron energy: 6.00 MeV, radial spot size FWHM: 0.155 and 0.170 cm for the X– and Y–directions, respectively) and MC_{1SD} where the spot size FWHM was chosen as +1 SD (i.e. mean impinging electron energy: 6.00 MeV, radial spot size FWHM: 0.188 and 0.194 cm for the X– and Y–directions, respectively). The lateral dose profiles is not heavily sensitive to changes in spot size FWHM even for field sizes of 20×20 cm^2 (see Figure 8). Therefore no large deviations are to be expected between the dose distributions.

Looking at iso dose lines for a dual arc RapidArc prostate case (Figure 74) the limited difference observed can be confirmed. The

3 Cut off energies were 700 and 10 keV for electrons and photons respectively. Photon splitting and electron splitting were set to a value of 25. The number of histories were chosen so that the estimated statistical uncertainty was ≈1.0% for the voxels in the high–dose regions. Source 20 was selected and particle Dmlc was employed to simulate the MLC

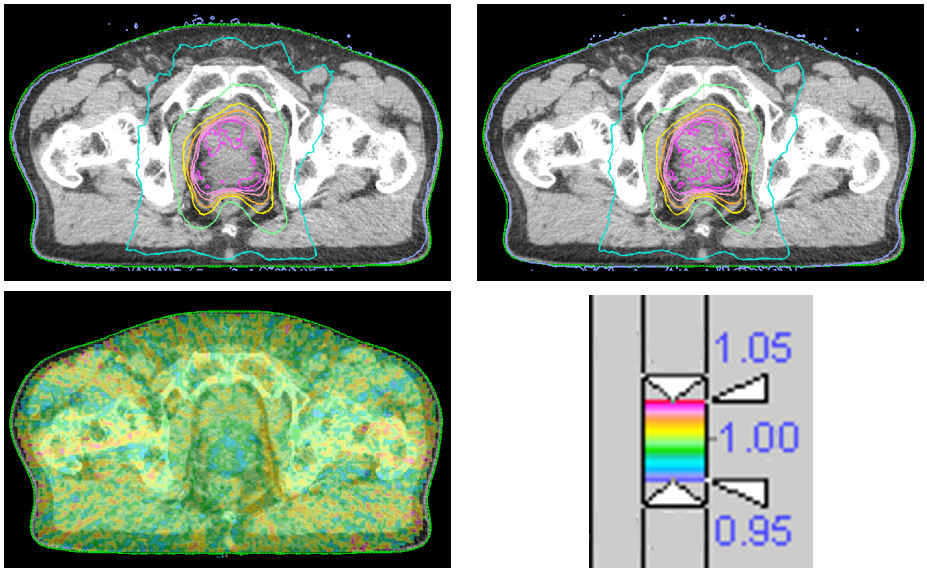

Figure 74: **Top panel:** A transversal CT slice of a prostate dual arc RapidArc case simulated with an optimal MC model (left) and one were the electron spot size FWHM was set to +1SD (right). The isodose lines corresponds to 10% (blue), 30% (cyan), 50% (green), 70% (lime), 80% (yellow), 90% (orange), 95% (deep orange), 100% (light pink), 105% (pink) and 110% (deep pink). **Bottom panel:** Difference of the dose distributions computed as $200 - D_{MC_{1SD}}/D_{MC_{opt}} \times 100$. Only voxels with dose $\geqslant$ 10% of the prescribed dose in both of the simulates were considered. The dose colorwash ranges from 95% (i.e. a 5% lower dose in the MC_{opt} simulation) (blue) to 105% (i.e. a 5% higher dose in the MC_{opt} simulation) (red).

difference dose map in Figure 74 illustrates that for most voxels the dose is well within 2% and at most 5% occuring occasionally for distal voxels where the abslute dose is lower. Looking at the DVHs no substantial difference between the two models are observed either (Figure 75). The dose recieved by 90% and 95% of the PTV and the CTV was slightly higher for the MC_{1SD} model. This is expected since penumbra widening is one of the effects of an increased spot size.

The resulting dose distributions for the two MC models of a dual arc RapidArc head and neck case also show no dramatic differences (Figure 76). However, small islet of "hot–" and "cold–spots" can be observed on the dose difference map. Moreover, the differences appear within the high dose regions. The treatment plan delivered for a head and neck case is typically more modulated than a prostate case and is therefore more susceptible to changes of the model. The maximum dose difference was however within 5% for all voxels. Looking at the resuting DVHs no substantial difference can be observed (Figure 77). Some fractional volumes of the PTV and the CTV receive higher doses in the MC_{opt} simulation, while for other fractional volumes the MC_{1SD} simulation results in higher doses. This can be possibly partly

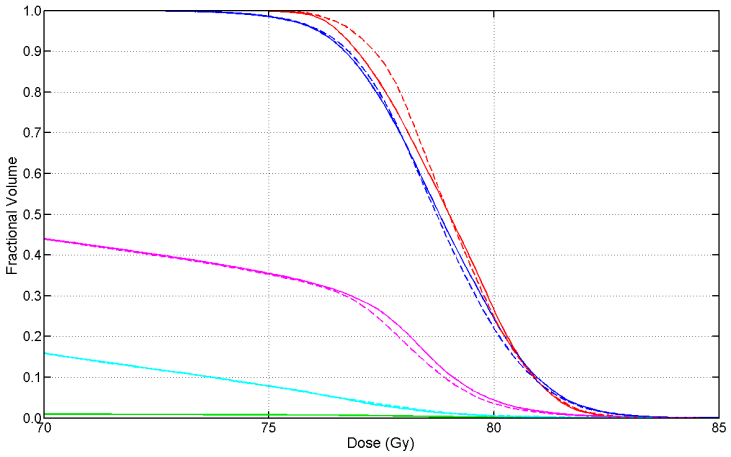

Figure 75: DVHs for a prostate dual arc RapidArc case simulated with an optimal MC model (solid) and one were the electron spot size FWHM was set to +1SD (dashed). The DVHs shown correspond to CTV (red), PTV (blue), bladder (magenta), rectum (cyan) and the entire external outline (green)

.

be explained by the stochastical nature of MC. Observing the dose difference map (Figure 76) more closely it can be seen that the large deviations are found either in regions where the absolute dose is low or in high dose regions where the density is far from unity.

The finding of this study indicate that a suboptimal MC model potentially can lead to dose deviations of 5% even in the high dose regions. The deviations seems to be larger in regions with large density variations. Moreover, the difference is most likely proportional to the modulation of the treatment plan. This is so since the largest difference between lateral profiles for models with different spot sizes are observed at the field edges and in the penumbra regions. With incerasing modluation, the relative penumbra dose contribution to the total dose will increase. In order to draw any clear conclusions of the impact of the MC model parameters on the resulting dose distributions for clinically relevant cases a large study including several cases is needed. The statistical uncertainty should also be low so that the any real effects can be clearly seperated from effects due to statistical noise.

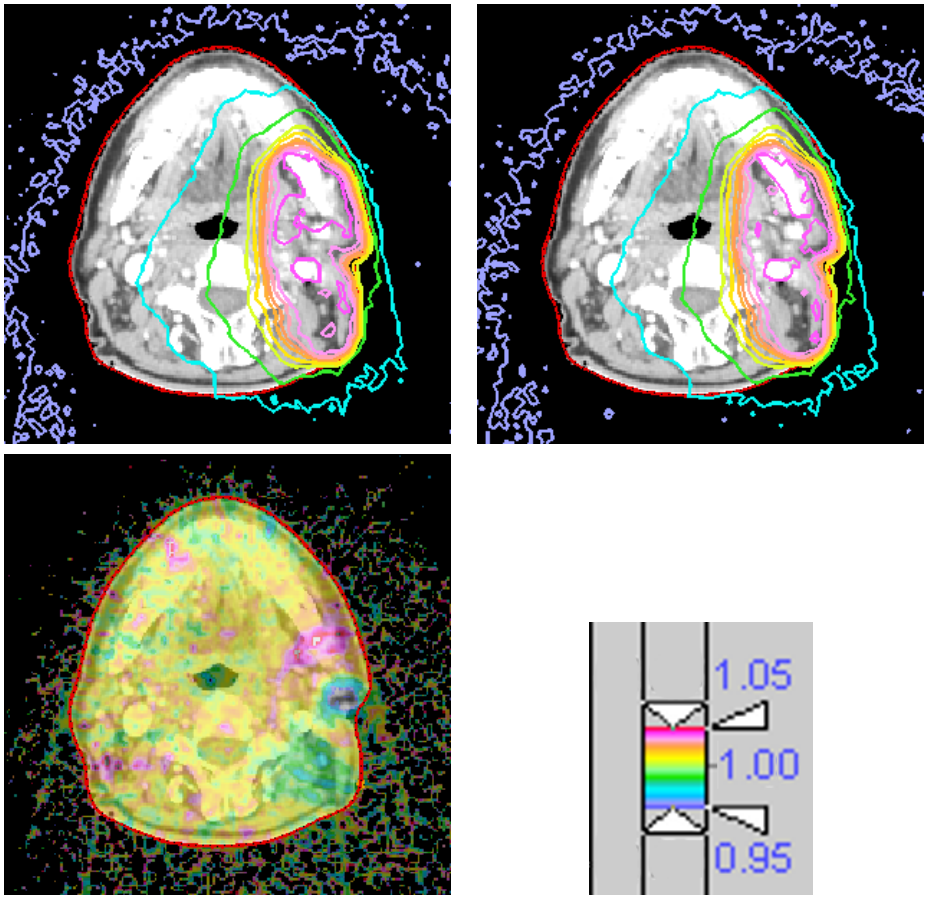

Figure 76: **Top panel:** A transversal CT slice of a seven field IMRT lung case simulated with an optimal MC model (left) and one were the electron spot size FWHM was set to +1SD (right). The isodose lines corresponds to 10% (blue), 30% (cyan), 50% (green), 70% (yellow), 80% (orange), 90% (light pink), 95% (pink) and 100% (deep pink). **Bottom panel:** Difference of the dose distributions computed as $200 - D_{MC_{1SD}}/D_{MC_{opt}} \times 100$. Only voxels with dose $\geqslant$ 10% of the prescribed dose in both of the simulates were considered. The dose colorwash ranges from 95% (i.e. a 5% lower dose in the MC_{opt} simulation) (blue) to 105% (i.e. a 5% higher dose in the MC_{opt} simulation) (red).

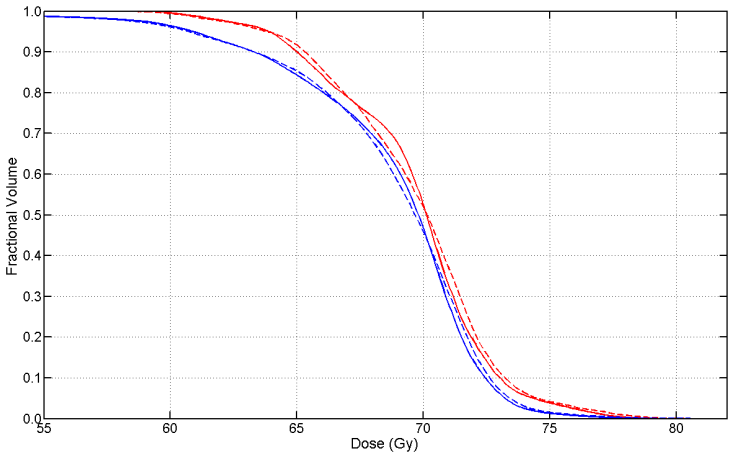

Figure 77: DVHs for a head and neck dual arc RapidArc case simulated with an optimal MC model (solid) and one were the electron spot size FWHM was set to +1SD (dashed). The DVHs shown correspond to CTV (red) and PTV (blue), bladder (magenta), rectum (cyan) and the entire external outline (green).

8

ENERGY AND PERTURBATION FACTORS FOR DOSIMETRY IN SMALL, MV PHOTON RADIOTHERAPY BEAMS

Alanine/EPR has been suggested as a suitable system for radiotherapy dosimetry ([Anton, 2005, 2006]), in particular, for non–reference situations, such as for small field sizes and composite beam delivery (e.g. IMRT and VMAT). The appealing features of alanine are close–to–water equivalent interaction properties, dose linearity up to the kGy range, small energy and dose rate dependence, limited influence of environmental factors, non destructive read out, and small size. The EPR signal from the detector irradiated with an unknown dose is related to dose to water through a calibration curve obtained by measuring the EPR signal from detectors irradiated to known doses in a large ^{60}Co field under conditions of Charged Particle Equilibrium. Sanches-Doblado et al. [2003] demonstrated that the beam energy spectrum are significantly different for small field sizes compared to a 10×10 cm^2 field size situation. For small field sizes, lateral CPE does not even exist along the CAX and Li et al. [1995] found that it requires a field diameter of at least 2.6 cm to have lateral CPE along the CAX in a 6 MV photon beam. The photon spectrum emitted by the linac will also differ between small and large field sizes due to differences in scatter contribution [Sanches-Doblado et al., 2003]. Moreover, the perturbation on the field by the detector itself becomes increasingly important with decreasing field size [Das et al., 2008]. The energy dependence of alanine in the MV photon range has been studied previously (Anton et al. [2008]; Bergstrand et al. [2003]; Waldeland and Malinen [2011]; Zeng et al. [2004]), but the studies have been limited to situations under which reference conditions apply (i.e. large fields, high dose, low gradient, CPE), which may not be the case in IMRT and small fields.

In small–field MV photon beam dosimetry (e.g. output factor measurements), the general aim is to determine the absorbed dose, D, at a single mathematical point. Alanine detectors, however, have a finite size and they therefore provide an average dose over the detector volume, $\overline{D}$ [Aspardakis et al., 2010]. For large, homogeneous irradiation fields, D and $\overline{D}$ are identical, but for small fields, correction factors are needed to estimate D from $\overline{D}$. The volume averaging effect can be eliminated if the detector is made sufficiently small or if the EPR–spectrometer only reads parts of the detector signal [Anton et al., 2011].

Two important factors that influences the dose to the detector compared to that of water are: i) the energy dependence of the active part of the detector material and ii) the perturbation of the beam induced by the detector itself. In this work the ratio of the volume–averaged dose to the alanine detector versus the volume–average dose over a voxel of water of the same size as the detector ($f \equiv D_{alan}/D_{H_2O}$) was studied as function of detector and field size and depth. This was accomplished by Monte Carlo simulation of the relevant geometries in a 6 MV photon beam.

Harwell alanine probes (batch AM 576C) (Harwell Dosimeters, Harwell, UK) were considered as these are used by the authors for dose measurements. The nominal composition of Harwell alanine probes (90.9% L–α–alanine and 9.1% parrafin binder) were processed through EGSnrc (Kawrakow [2000*a*,*b*]) to compute interaction cross sections. The density was determined by weighing and measuring 15 probes from the same batch and found to be ρ=1.24 gcm^{-3}.

DOSrz was employed to score the dose to an alanine voxel ($\overline{D}_{alan}$) in an otherwise homogeneous water phantom with an outer radius of 20 cm. Each simulation geometry was reproduced for a homogeneous water phantom, using the same dimensions, and thereby obtaining the dose to water, $\overline{D}_{H_2O}$. The center of the alanine/H_2O voxel, where the dose was recorded, was located at a depth of 10 cm on the central axis. The 6 MV photon spectrum previously published by Mohan et al. [1985] was used as the input for the simulation throughout the study. The advantage of using this spectrum is that it is well documented and public available as it is distributed with EGSnrc. Moreover it is computationally efficient to use a spectrum file, rather than a phase space file and/or a beam treatment head simulation, as input to DOSrz. The spectrum in question corresponds to the bremsstrahlung spectrum for a 10×10 cm^2 field emitted by a Varian Clinac (in 6 MV mode). The spectrum file was used in combination with DOSrz source 0 (i.e. parallel beam incident from the front). The number of histories were chosen so that the statistical uncertainty was no larger than 0.4% in the voxel of interest. The only variance reduction turned on was photon forcing (for the first generation particles only) and cut off energies were 521 keV (including rest mass) and 10 keV for electrons and photons, respectively.

The ratio of volume averaged doses $f \equiv \overline{D}_{alan}/\overline{D}_{H_2O}$ was studied as function of the field diameter for two different detector sizes i.e. with detector diameter (ø) and height (h): (ø,h)=(5,2.5) mm and (ø,h)=(1,2.5) mm, respectively (figure 78). A correction factor of $f \approx 0.98$ is needed to correct $\overline{D}_{alan}$ to $\overline{D}_{H_2O}$ for fields with a diameter of $\approx$ 1 cm and above for both detector sizes. However, f increases more rapidly for the larger detector as the field diameter decrease below 1 cm, e.g. $f \approx 1.03$ and $f \approx 1.00$ for a field diameter of 0.5 cm for the larger and smaller detector, respectively.

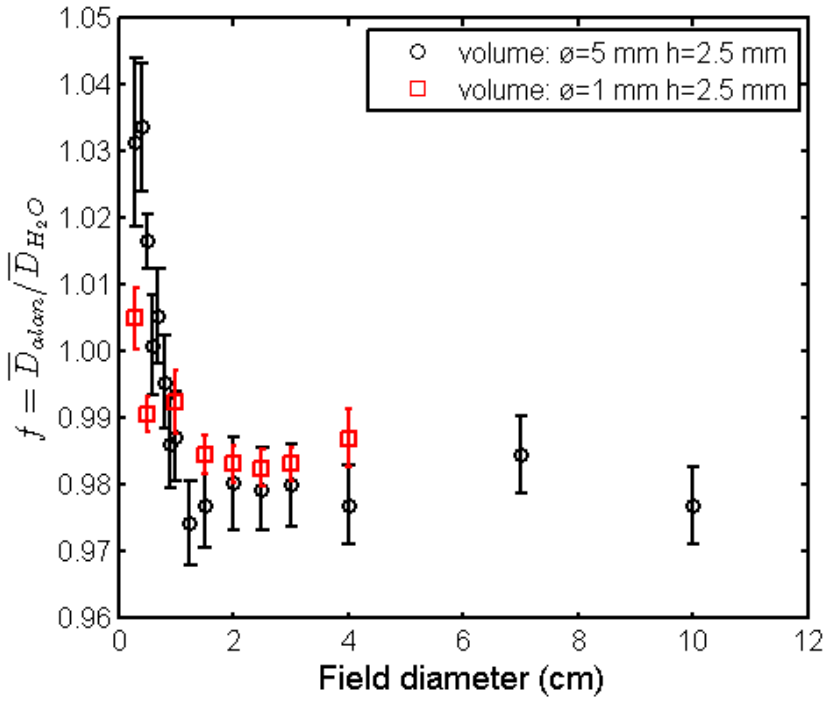

Figure 78: The ratio of volume averaged doses, f, as function of field diameter for two detector sizes. $f \approx 0.98$ for fields with a diameter of ≈ 1 cm and above. Error bars are the combined statistical uncertainty of the MC simulations.

In order to further study the dependency of f on field– and detector size, f was evaluated for a range of detector sizes for three field diameters: 0.5, 1.0, 4.0 cm (Figure 79). For the two largest fields $f \approx 0.98$ for all detector sizes except, possibly, for the smallest detector (ø=1 mm). However, for the smallest field size (0.5 cm) f increases with the detector diameter, illustrating that the detector needs to be very small for such a small field size.

In order to evaluate whether f is depth dependent, f was evaluated as a function of depth for a 10 cm diameter field and a detector size of (ø,h)=(5,2.5) mm (figure 80). f is fairly constant for depths $\geqslant$1 cm, but deviates for shallower depths. A correction factor of 0.9779($\pm$0.0067)[1] was found for depths $\geqslant$1 cm. A ratio of volume averaged doses of 0.9779 is on the order of what to be expected when looking at alanine/water restricted mass stopping power ratios and mass energy absorbtion coefficient ratios.

A depth independent detector is a much desired feature as measurements may be conducted at any depth without additional considerations. Depth invariance is to be expected as alanine is rather

1 The reported uncertainty is the standard deviation of the average value for depths $\geqslant$1 cm.

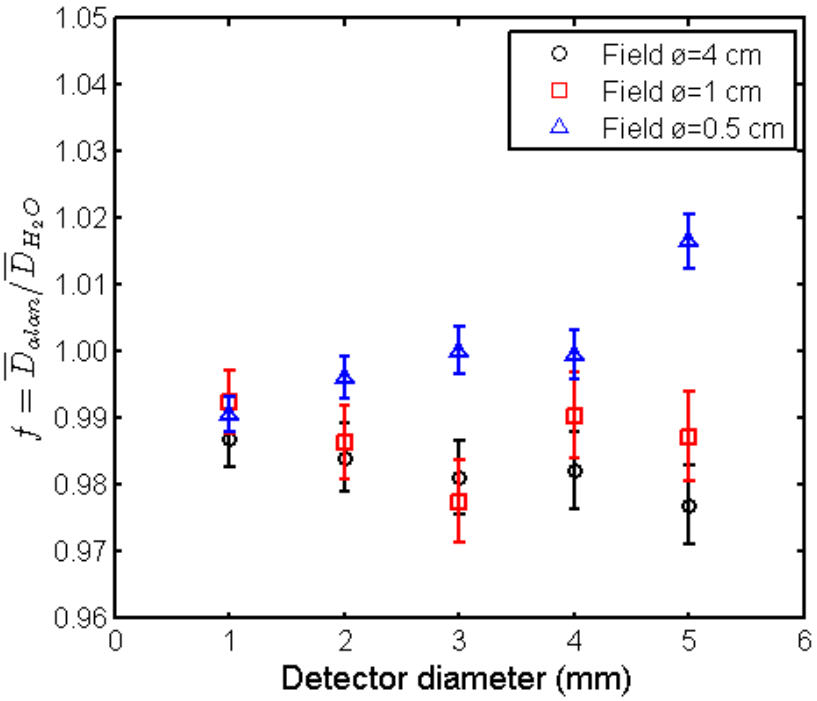

Figure 79: The ratio of volume averaged doses, f, as function of detector diameter (ø) for three field sizes. f is fairly constant over the range of detector sizes for the larger two field sizes whereas this does not hold true for the smallest field size. Error bars are the combined statistical uncertainty of the MC simulations.

water equivalent. For the shallowest depth, however, f was $\approx$ 1.01. This might be due to the substantially different energy spectrum at such a shallow depth. The result may not be accurate as contaminating electrons, which contribute to the dose at shallow depths, were omitted in the simulation. The impact of contaminating electrons on f for shallow depths was not further studied.

If alanine is to be used as a detector for radiotherapy the correction factor f needs to be constant or its variation known. Obviously, in the ideal case f is constant and thus calibrated out of the equation and one does not need to think further thereof. Second best, is that its variation as function of e.g. field size and detector size is known. The results of this study illustrates that f is constant for a large range of field sizes, detector sizes and depths. However, as the field size becomes of the order of the detector size or the field size becomes very small (e.g. a diameter of 0.5 cm) this breaks down. The detector cannot be made infinitely small. One practical obstacle is that the handling of the detector becomes cumbersome if it is too small and further the signal to noise ratio gets lower as the detector becomes smaller. However, a detector size of (ø,h)=(5,2.5) mm is easily handled and as illustrated f is constant down to field sizes of the order of ø=1 cm for such a

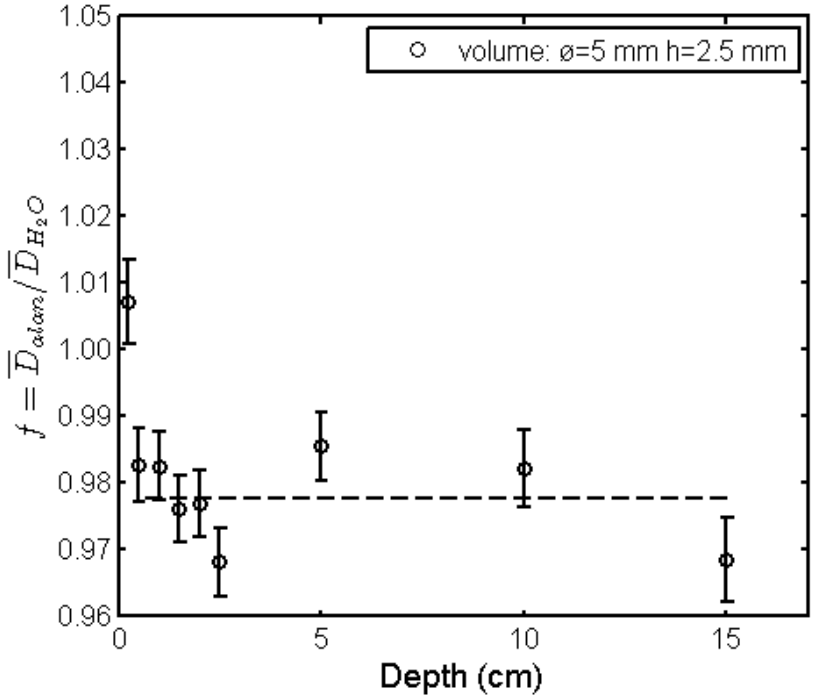

Figure 80: The ratio of volume averaged doses, f, as function of depth (d) for a field with a diameter of 10 cm and detector size (ø,h)=(5,2.5) mm. The ratio of volume averaged doses, f, was fairly constant at depths $\geqslant$1 cm, with an average of $\approx$ 0.98. For the shallowest depth (0.5 cm), a value of $\approx$ 1.01 was needed in order to correct $\overline{D}_{alan}$ to $\overline{D}_{H_2O}$. Error bars are the combined statistical uncertainty of the MC simulations. The average f for $1 \leqslant d \leqslant 15$ cm is included in the figure (dashed line).

detector size. This will most likely be sufficient for most applications within radiotherapy. Even for field sizes of this order, and certainly for smaller field sizes, other problems arise anyhow such as position inaccuracies of the detector in the beam. For instance, Beierholm et al. [2011] states that a 1 mm misalignment between the isocenter and a 1 mm wide scintillator probe for a 0.6×0.6 mm^2 square field leads to a dose measurement error (at 20 cm's depth) in the order of 6%.

This work demonstrates that f is constant for a large range of depths, detector– and field sizes. This range is sufficient for most applications in radiation therapy. Thus, only in extreme cases are f of concern in dosimetry for radiotherapy and in those cases can f potentially be determined by Monte Carlo simulations.

9

ON THE POTENTIAL USE OF AN ALANINE-BASED PROTOCOL FOR SMALL FIELD RELATIVE OUTPUT FACTOR DETERMINATION IN HIGH ENERGY PHOTON BEAMS

Dosimetry in small fields is problematic for a number of reasons [Aspardakis et al., 2010]. A trivial, but important, reason is that the positioning of the detector device becomes increasingly important when the field size decreases. For a 10×10 cm^2 field a displacement of 1 mm will not significantly influence the detector signal, but for a field size of 0.6×0.6 cm^2 it can lead to a signal decrease in the order of 6% [Beierholm et al., 2011]. The purturbation introduced by the detector becomes increasingy apparent with decreasing field sizes, this is further enhanced if wires or cables are attached to the detector. Furthermore, as the size of the field becomes comparable to the range of the secondary electrons lateral CPE is no longer fulfilled [Liu et al., 1997]. Loss of lateral CPE leads to changes in the fluence spectra compared to a 10×10 cm^2 field which typically is used as a reference [Sanches-Doblado et al., 2003; Yin et al., 2004]. The change in the fluence spectra is not a dosimetrical issue per se, however many detector systems are calibrated, and thus only valid, using a fluence spectra corresponding to that of a 10×10 cm^2. Moreover, the photon fluence spectra will change with field size, due to beam hardening effects and different scatter contributions. Chosing a detector material with high water equivalence implies that it also is insensitive to changes in the fluence spectra. Moreover, the perturbation effect decreases for highly water equivalent detector materials. Loss of lateral CPE also has implications in terms of the so called volume averaging effect. The dose reading of a detector will be the average signal over the entire sensitive volume. This is a non–issue in the case of a 10×10 cm^2 field since the lateral profiles are flat. However, as the field size grows smaller, the lateral penumbra regions will be more centrally located. When lateral CPE is lost, the opposing penumbrae will overlap resulting in dose gradients over the entire lateral dose profile. As the dose at a specific point typically is what is sought after, this becomes an issue since the average dose over the sensitive volume of the detector no longer will be representative of the point dose.

Figure 81 shows restricted mass Stopping Power Ratio and mass energy absorption coefficient ratios, compared to water, for a range of common detector materials. It can clearly be seen that alanine indeed is a potentially suitable detector material since it is highly water equivalent in terms of restricted mass stopping power and mass

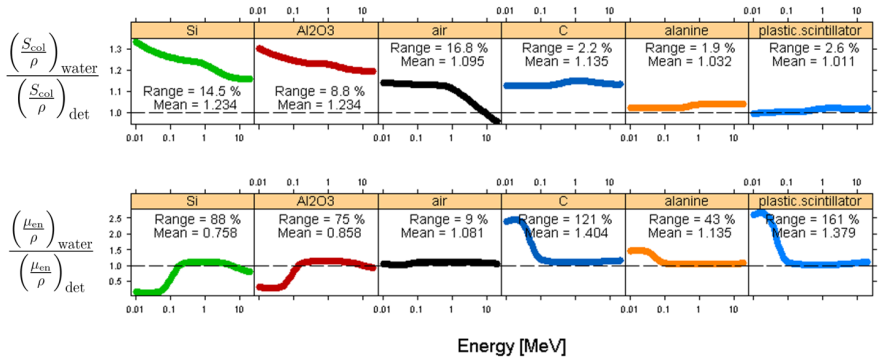

Figure 81: **Top panel:** Mass Stopping Power Ratio for a range of common detector materials compared to water. **Bottom panel:** Mass energy absorption coefficient ratios for a range of common detector materials compared to water. Data taken from NIST [2011*b*,*c*]

energy absorption coefficient. Moreover, it is possible to fabricate alanine detectors in small sizes.

Monte Carlo has the potential to overcome all of the above mentioned issues, since an ideal detector can be defined for any given situation. However, an MC model is often calibrated using measurements of large field only and is not necessarily validated for small fields. Moreover, the validity of an MC model is limited to the specific linac it is calibrated against. Therefore, a more practical approach is to conduct MC simulations of a measurement system and validate the results by measurements on the very same linac. Concurrent results should give confidence of the validity of the measurement system, which in turn can be used for measurements on any given linac.

In this chapter such a comparison will be conducted for an alanine/EPR dosimetry system on a Varian 2300 iX linac, which has been accurately modeled and validated for MC (see Chapter 3).

9.1 ALANINE MEASUREMENTS

Alanine dosimeters from Harwell Dosimeters (Batch AM576C) were used. These dosimeters consisted of 90.9% L–α–alanine and 9.1% parrafin binder. The cylindrical dosimeters were 4.83 mm in diameter and 2.54 mm in thickness[1].

Measurements were conducted on a Varian 2300 iX linac located at the Copenhagen University Hospital, Herlev. All measurements were conducted with the linac operating in 6 MV mode and with the dose repetition rate set to 600 MU/min, which corresponds to the maximum dose repetition rate. Gammex 457 solid water slabs with a total outer dimension of 30×30×30 cm^3 were placed at the table top.

1 The physical dimensions were measured for 15 individual dosimeters and the variation were ±0.00 mm and ±0.02 mm in diameter and thickness, respectively.

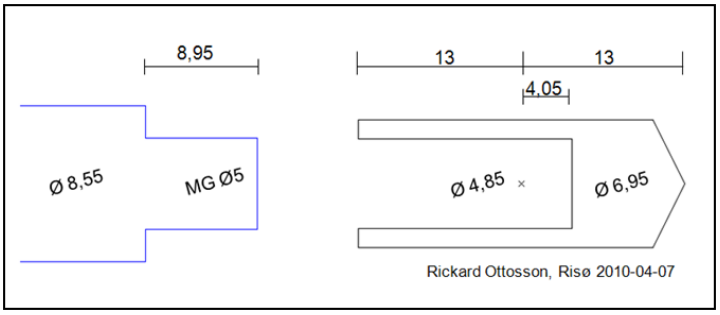

Figure 82: Schematic illustration of the modifications made on Gammex 457 solid water Farmer chamber dummy. All measures are in mm

In order to increase friction and thereby reduce the risk of the phantom moving during and/or between irradiations, a rubber mat was placed under the bottom solid water slab. The phantom was positioned at a SSD of 90 cm using a front pointer attached to the linac head. The Gammex 457 slabs were arranged so that a 10 cm thick slab, with a hole suited for a Farmer ionization chamber insert, was located with its hole at 10 cm depth (i.e at the beam isocenter). The arrangement was conducted so that a Farmer chamber insert could slide in and out of the phantom without disturbing the positioning.

A Gammex 457 solid water Farmer chamber dummy was modified so that it could house three alanine dosimeters (Harwell Dosimeters Batch AM576C) (Figure 82). A single alanine dosimeter was placed in the holder, surrounded by disks of Gammex 457 ensuring that the entire cavity was filled. The alignment with the beam CAX was conducted by replacing the alanine dosimeter with an in–house made lead marker of the same dimensions. The Farmer chamber dummy, with the lead marker inserted, was positioned in the phantom and the phantom was approximately aligned with the beam CAX using the treatment room laser guide markers. The OBI system was used to take a portal image of the phantom. The high density lead marker was highly visible on the portal image and was aligned with the field center by carefully repositioning the phantom. A second portal image was acquired in order to verify the positioning. If the lead piece still was not aligned with the beam isocenter, the procedure was reiterated until agreement. The positioning procedure was conducted for the smallest (i.e. 0.6×0.6 cm^2) field size.

Each individual dosimeter was irradiated to a dose in the range of 10 Gy, using estimated Relative Output Factors. The number of MUs was logged for later purposes. Three consecutive measurements were conducted for each measurement and the 10×10 cm^2 was repeated three times during the measuring session.

9.2 EPR SPECTROSCOPY

The EPR spectroscopy was conducted in accordance with the method described in Helt-Hansen et al. [2009]. A Bruker EMX–micro EPR spectrometer (Bruker, Billerica, MA, USA) was used for measurements of the alanine dosimeters. The alanine resonance spectra were acquired by placing the individual dosimeters in a quartz tube which was positioned in the rectangular cavity of the spectrometer. For each dosimeter, six repeated scans were conducted prior to removing the dosimeter from the cavity. The acquisition parameters were:

microwave power: 9.0 mW

modulation amplitude: 1.0 mT

time constant: 20.5 ms

conversion time: 20.5 ms

The resonance spectrum of un–irradiated, control, dosimeters are subtracted from the dosimeters in order to produce background free spectra. The central peak position is determined from a spectrum from a dosimeter irradiated to a known dose (100 Gy). The EPR intensities between the central peaks of the dosimeter in question is plotted as a function of the corresponding intensities of the EPR spectrum of the reference dosimeter. A slope is found by performing a least–square fit to a linear function of the part of the curve that is most linear (i.e. yields the highest R^2 value). The absorbed dose is then determined by multiplying the amplitude of the slope with the known dose.

The mass of each individual dosimeter is taken into account when computing the dose of a given dosimeter. The dose is then normalized by the MUs the individual detector was irradiated to. As demonstrated in Chapter 8, no field size specific correction factor is needed over the range of field sizes studied (with a possible exception for the smallest field size).

9.3 MONTE CARLO SIMULATION

EGSnrc (Kawrakow [2000*a*,*b*]) was used to compute interaction cross sections for the alanine dosimeters and the Gammex 457 solid water material. The nominal composition of Harwell alanine probes (90.9% L–α–alanine and 9.1% parrafin binder) was used and the density was determined by weighing and measuring 15 probes from the same batch and found to be ρ=1.24 gcm^{-3}. For the Gammex 457 phantom, calibration protocols of the actual Gammex 457 phantom slabs used during the measurements were used to determine the composition and density.

Table 17: Relative Output Factor measured with alanine/EPR and IC for a range of field sizes. The alanine/EPR measurements were conducted in Gammex 457 solid water whereas the IC measurements were conducted in liquid water. The difference was calculated as ($ROF_{alanine}$-ROF_{IC})/ROF_{IC}*100.

Field size	ROF		Difference
(cm^2)	Alanine	ICt	(%)
10×10	1.000	1.000	—
8×8	0.963	0.963	0.0
5×5	0.887	0.891	-0.5
3×3	0.824	0.827	-0.4

A Gammex 457 phantom with outer dimensions of 30×30×30 cm^3 with an alanine dosimeter (2.54×4.83×4.83 mm^3) placed at 10 cm depth along the central line of the phantom was defined. Simulations were conducted using DOSXYZnrc[2]. The linac model defined in BEAMnrc corresponded to the Varian 2300 iX linac used during mesurements (see Section 3.3). The center of the alanine dosimeter was defined to be at the beam isocenter and at an SSD of 90 cm. The BSF was accounted for using relative I_{target} measurements as described in Section 5.1.1.

9.4 RESUTLS

The results of the alanine measurements were initially validated against IC measurements[3] for field sizes in the range of 10×10 to 3×3 cm^2 (Table 17). Agreement within 0.5% was found.

The comparison between simulated and measured ROFs is shown in Table 18. The agreement was generally within 2%. However, statistical significant difference was found for all field sizes $\leqslant$ 2.5×2.5 cm^2. The

2 The number of histories were chosen so that the statistical uncertainty for the alanine voxel was ≈0.3%. Simulation properties were ECUT = 521 keV, PCUT = 10 keV, nsplit = 25, esplit = 25. The treatment head was simulated using source 9 in DOSXYZnrc. Simulation properties were ECUT = 700 keV, PCUT = 10 keV, direction bremsstrahlung splitting was used (FS, defined at SSD = 100 cm, was set equal to the side length of the square field for field sizes $\geqslant$ 5×5 cm^2 and to 5 cm otherwise), NBRSPL was set to 1000, with the splitting plane for electrons (ZPLANE_DBS) defined as the bottom of the flattening filter and russian roulette conducted for electron at a plane 0.20 cm above the bottom of the flattening filter.

3 Measurements were with a Wellhöfer/IBA CC13 (IBA Dosimetry AB, Uppsala, Sweden) Ionization Chamber (0.13 cm^3 active volume) in a Blue Phantom (IBA Dosimetry AB, Uppsala, Sweden) 48×48×48 cm^3 water tank (± 0.1 mm position accuracy) and the data acquisition was controlled by the OmniPro Accept v.6.5A (IBA Dosimetry AB, Uppsala, Sweden) software. An SSD of 90 cm was used and the measurements were conducted at 10 cm depth.

Table 18: MC simulated and measured ROFs for a range of field sizes. The reported uncertainties computed using common uncertainty propagation considering the statistical uncertainties for the individual simulations combined with the uncertainty of the relative I_{target} measurement for MC and the standard deviation of measurements for the field in question as well as the reference field (10×10 cm^2). The difference was calculated as (ROF_{MC}-$ROF_{measured}$)/$ROF_{measured}$*100.

Field size	ROF		Difference
(cm^2)	MC	Alanine	(%)
10×10	1.000(±0.005)	1.000(±0.015)	—
5×5	0.895(±0.004)	0.887(±0.007)	0.9(±1.1)
3×3	0.834(±0.003)	0.824(±0.007)	1.2(±1.4)
2.5×2.5	0.818(±0.004)	0.804(±0.008)	1.8(±1.6)
2×2	0.793(±0.003)	0.781(±0.003)	1.5(±0.8)
1.5×1.5	0.756(±0.005)	0.749(±0.001)	0.9(±0.7)
1×1	0.660(±0.002)	0.672(±0.003)	-1.8(±1.1)
0.6×0.6	0.460(±0.001)	0.503(±0.005)	-8.5(±3.3)

actual position of the jaw collimators was not not monitored during the measurements, thereby there is an uncertainty on the field size that is not accounted for. The relative uncertainty will increase as the field size decreases. This does not explain the 8.5% deviation for the smallest field size, nor can it be explained by a positioning error since the alignment was conducted for that very field setting. Part of the discrepancy might be due to differences between the actual geometry and that modeled in the simulation. Particularly the dosimeter which in the simualtion is modeled as a cube, wheras it in fact is a cylinder. The deviation can be explained by the inhomogene sensitivity profile over the EPR cavity used (see Figure 83). The sensitivity profile is unimportant if the dosimeter is homogeneously irradiated, but becoms importat if a dose graident is present over the detector volume. This is indeed the case for field sizes < 3×3 cm^2 and as a consequence the dose reported by the EPR spectroscopy will overestimate the dose. In order to correct for the inhomogeneous sensitivity profile one would have to know the exact shape of the dose profile, which, for the reasons discussed on page 151, is not easy to measure accurately for small fields.

9.5 CONCLUSIONS

Alanine/EPR measured ROFs agreed well with ROFs measured with an IC as well as with MC simulations in the field size range 10×10

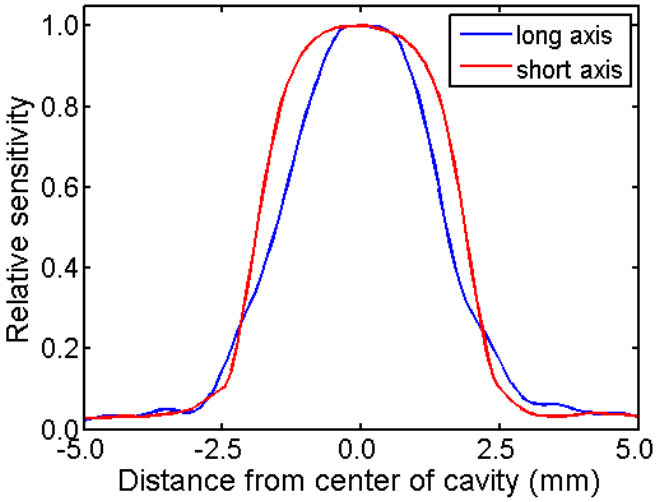

Figure 83: The sensitivity profile, normalized at the center of the cavity, at the horizontal plane for a Bruker EMX–micro EPR spectrometer cavity. The data were provided by Bruker.

to 3×3 cm^2. For smaller field sizes significant differences between measurements and MC simulations were observed. The deviation was largest for the smallest field sizes. The deviation can, at least partly, be explained by the inhomogeneous sensitivity profile of the EPR cavity. Results of alanine/EPR dosimetry needs to be corrected for if the dose gradient over the detector becomes apparent. This is by no means a trivial correction as the actual dose profiles needs to be known.

Alanine/EPR dosimetry is suitable for field sizes where the dose profile over the detector is homogeneous, i.e. $\geqslant 3\times3$ cm^2 for 6 MV photon beams. For smaller field sizes, correction factors that are not commonly know or easily derived.

Part I

APPENDIX

A

PAPER I

Appendix A is a paper published in Physics in Medicine and Biology in 2010. The choice between low and high energy photon energy for Intensity Modulated RadioTherapy treatment of non–small lung cell cancer is investigated using Pareto front analysis. The included dose calculation algorithms are the Pencil Beam Convolution algorithm, the Analytical Anisotropical Algorithm and Monte Carlo.

Pareto front analysis of 6 and 15 MV dynamic IMRT for lung cancer using pencil beam, AAA and Monte Carlo

2010 Phys. Med. Biol. 55 4521

(http://iopscience.iop.org/0031-9155/55/16/S07)

IOP PUBLISHING PHYSICS IN MEDICINE AND BIOLOGY

Phys. Med. Biol. **55** (2010) 4521–4533 doi:10.1088/0031-9155/55/16/S07

Pareto front analysis of 6 and 15 MV dynamic IMRT for lung cancer using pencil beam, AAA and Monte Carlo

R O Ottosson, A Karlsson and C F Behrens

Department of Oncology (R), Division of Radiophysics (52AA), Copenhagen University Hospital Herlev, Herlev Ringvej 75, DK–2730 Herlev, Denmark

E-mail: riolot01@heh.regionh.dk

Received 14 January 2010, in final form 9 May 2010
Published 29 July 2010
Online at stacks.iop.org/PMB/55/4521

Abstract

The pencil beam dose calculation method is frequently used in modern radiation therapy treatment planning regardless of the fact that it is documented inaccurately for cases involving large density variations. The inaccuracies are larger for higher beam energies. As a result, low energy beams are conventionally used for lung treatments. The aim of this study was to analyze the advantages and disadvantages of dynamic IMRT treatment planning for high and low photon energy in order to assess if deviating from the conventional low energy approach could be favorable in some cases. Furthermore, the influence of motion on the dose distribution was investigated. Four non-small cell lung cancer cases were selected for this study. Inverse planning was conducted using Varian Eclipse. A total number of 31 dynamic IMRT plans, distributed amongst the four cases, were created ranging from PTV conformity weighted to normal tissue sparing weighted. All optimized treatment plans were calculated using three different calculation algorithms (PBC, AAA and MC). In order to study the influence of motion, two virtual lung phantoms were created. The idea was to mimic two different situations: one where the GTV is located centrally in the PTV and another where the GTV was close to the edge of the PTV. PBC is in poor agreement with MC and AAA for all cases and treatment plans. AAA overestimates the dose, compared to MC. This effect is more pronounced for 15 than 6 MV. AAA and MC both predict similar perturbations in dose distributions when moving the GTV to the edge of the PTV. PBC, however, predicts results contradicting those of AAA and MC. This study shows that PB-based dose calculation algorithms are clinically insufficient for patient geometries involving large density inhomogeneities. AAA is in much better agreement with MC, but even a small overestimation of the dose level by the algorithm might lead to a large part of the PTV being underdosed. It is advisable to use low energy as a default for tumor sites involving lungs. However, there might be situations where it is favorable to use high energy.

In order to deviate from the recommended low energy convention, an accurate dose calculation algorithm (e.g. MC) should be consulted. The study underlines the inaccuracies introduced when calculating dose using a PB-based algorithm in geometries involving large density variations. PBC, in contrast to other algorithms (AAA and MC), predicts a decrease in dose when the density is increased.

(Some figures in this article are in colour only in the electronic version)

1. Introduction

Pencil beam (PB) dose calculation algorithms are the most widespread in modern treatment planning for radiation therapy. The accuracy of these algorithms is in many cases sufficient and the difference in dose distribution calculated with PB and more sophisticated methods such as Monte Carlo (MC) is not of clinically importance. However, in cases involving significant density variations, such as metal implants, air cavities and low density lung tissue, the inaccuracies in dose distribution calculated with the PB algorithms may become clinically significant. The accuracy of the PB algorithms depends on several parameters such as beam energy, field size and geometry as reported in numerous studies (e.g. Behrens (2006), Klein *et al* (1993), Tsiakalos *et al* (2006), Vanderstraeten *et al* (2006), Krieger and Sauer (2005)).

PB dose calculation algorithms are, nevertheless, frequently used for lung cancer treatment planning. If PB-based treatment plans generated with high and low energy (e.g. 15 or 18 MV and 4 or 6 MV, respectively) are compared, the high energy-based dose distributions will in many cases appear more favorable. However, it is well known that the inaccuracies introduced by the PB dose calculation in general are larger for higher energies. As a result, low energy-based treatment plans are chosen as default for lung treatments. This begs the question whether this is always the best choice. For some cases, treatment plans based on higher energies may be more favorable. In order to address this question, more accurate dose calculation methods (e.g. MC) must be employed. Studies aiming at this have been published (e.g. Tsiakalos *et al* (2006), Vanderstraeten *et al* (2006), Krieger and Sauer (2005), McDermott *et al* (2003), Weiss *et al* (2007), Madani *et al* (2007)). However, only a few involve MC calculation methods for IMRT treatment planning (e.g. Vanderstraeten *et al* (2006), McDermott *et al* (2003), Madani *et al* (2007)) and most consider static as opposed to dynamic IMRT.

The aim of this study was to analyze the advantages and disadvantages of high and low photon energy dynamic IMRT treatment planning for lung tumors. Furthermore, the influence of motion on the dose distribution was investigated.

PB and a more sophisticated dose calculation algorithm, the anisotropic analytical algorithm (AAA), were compared to MC-based dose calculations utilizing a Pareto front comparison method (Ottosson *et al* 2009, Steneker *et al* 2006). The general idea of this concept is to compare sets of plans, belonging to different classes (e.g. high versus low energy) as opposed to a traditional plan-to-plan comparison procedure. Comparative treatment planning has hitherto often been rather inconclusive. For instance, when comparing different IMRT delivery techniques (e.g. step&shoot versus sliding windows), it may have been found that one of the techniques is capable of better target coverage, while the other is better at sparing risk organs. This leaves room for a subjective interpretation. By sampling the entire Pareto front for a case, it may be possible to make a much more just and comprehensive comparison of the two systems. Utilizing this concept elements such as treatment planner dependence and misfortunate plan selections can be minimized.

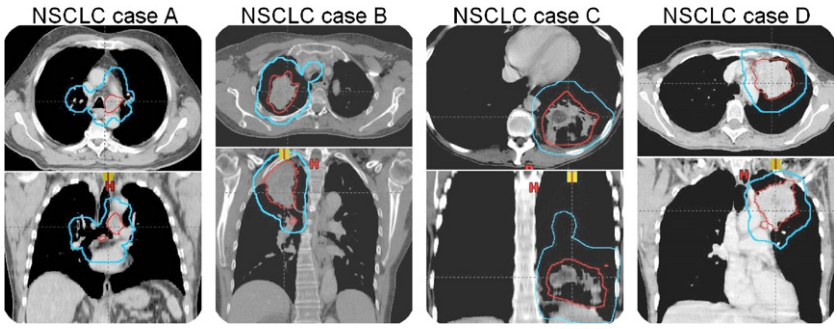

Figure 1. NSCLC cases (A)–(D). Transversal and coronal CT slices, illustrating the tumor location and extension. Red and light blue lines are delineations of the GTVs and PTVs, respectively.

2. Materials and methods

Four non-small cell lung cancer (NSCLC) cases, with apparent differences in tumor location, were selected for this study (figure 1). The cases exhibited geometrical properties where one could expect a significant discrepancy between analytical and MC dose calculation algorithms. CTV and OAR were delineated by a radiologist. PTV margins were added in accordance with the protocol used at Copenhagen University Hospital Herlev.

2.1. Treatment planning

For inverse planning, Varian Eclipse^{TM} build 8.2.24.10720 (Varian Medical Systems, Inc., Palo Alto, CA, USA) modeling a Varian 2300 iX (Varian Medical Systems, Inc., Palo Alto, CA, USA) was used.

35 $\times$ 2 Gy was prescribed to the PTV and a maximum dose constraint of 45 Gy was applied to the spinal cord. The lungs were assigned a dose volume constraint of $V_{20} \leqslant 50\%$, while the constraints for the heart were $V_{30} \leqslant 100\%$, $V_{45} \leqslant 65\%$ and $V_{60} \leqslant 25\%$.

As an initial step of the treatment planning, the optimal numbers of beams, gantry and collimator angles were determined individually for each case and energy (6 and 15 MV) by Varians geometrical optimization module utilizing the plan geometry optimization (PGO) algorithm (Varian Medical Systems 2007). The PGO takes the specific geometry of the case and the DVO constraints into account.

Hereafter, a number of isocentric dynamic (sliding window) IMRT treatment plans, ranging from PTV conformity weighted to normal tissue sparing weighted, were created for each case and beam energy. Thus, the PTV coverage, from one plan to the next, deteriorated as sparing of the normal tissue in general, and the lungs specifically, increased. In total 31 treatment plans, distributed amongst the 4 cases, were created. For the optimization, a PB algorithm was used as Eclipse offers no other option.

Full dose calculation was undertaken for each treatment plan, employing the Eclipse pencil beam (PBC) algorithm and the AAA using identical MLC settings and monitor units.

2.2. Monte Carlo modeling

EGSnrc and BEAMnrc (Kawrakow 2000a, 2000b, Rogers *et al* 2005) were used to build and commission Monte Carlo models for each energy of the Varian 2300 iX linear accelerators (6 and 15 MV). The commissioning procedure utilized the same measurements as the

configuration and commissioning of the PBC and AAA algorithms for the TPS. The MC commissioning followed the protocol suggested by Pena *et al* (2004), where the general idea is to compare simulated central-axis (CAX) depth–dose profiles and lateral dose profiles to corresponding measurements. The commissioning procedure included 10 × 10 and 20 × 20 cm^2 open fields in water. Furthermore, the MC model was tested for a large number of quadratic and rectangular field sizes ranging from 3 × 3 to 30 × 30 cm^2. Once a satisfactory agreement between simulations and measurements was obtained, BEAMnrc was used to simulate the treatment head. A phase space file (PHSP) was scored just below the flattening filter for each beam energy. The PHSPs were scored by simulation of 2.5 × 10^6 histories with cut off energies of 521 keV (including rest mass) and 10 keV for electrons and photons, respectively. Directional bremsstrahlung splitting was turned on, using the following parameters: SSD = 100 cm, NBRSPL = 1000 (maximum splitting factor) and FS = 30 cm (radius of field into which bremsstrahlung photons must be directed if they are to be split). In order to maintain good electron statistics in the build up region, Russian roulette was switched off.

The beam modifiers were simulated in MCSIM (Jin *et al* 2007, Ma *et al* 2002), using the PHSP as a source input. Since the MLC geometry in MCSIM is hard coded, employing a set of specific input parameters (inter- and intra-MLC leaf leakage), it was commissioned separately. Specifically, a field with fully closed leaves was compared with film measurements. GafChromic EBT film (International Specialty Products, NJ, USA) was placed at 5 cm depth in a Gammex 457 solid water phantom (Gammex–RMI, Nottingham, UK) with an SSD of 95 cm. The field size was 10 × 30 cm^2 and all leaf pairs were fully closed 10 cm off CAX. Corresponding simulations were performed, using a voxel size of 2.0 × 0.1 × 0.5 cm^3 for 9 × 10^9 histories with cut off energies of 521 keV (including rest mass) and 10 keV for electrons and photons, respectively. The only variance reduction technique switched on was IETRACK (electron track repeating).

2.3. Monte Carlo simulations

Voxalized phantoms were created via the DICOM RT toolbox (Spezi *et al* 2002) using the planning CT set as input. The phantom grid was matched to the dose grid of the treatment planning system (TPS). For two of the cases (A and C), the CT slice thickness was larger than the dose grid spacing. The voxel sizes were expanded, in the slice direction, to match the CT scan grid for those cases. The final voxel size was 2.5 × 2.5 × 2.5 mm^3 and 2.5 × 2.5 × 5.0 mm^3 for cases B and D, and cases A and C, respectively. A set of in-house MATLAB scripts was used to generate input files for MCSIM from the DICOM RP files. Thus, all parameters of the treatment plans were recreated in the simulations. The treatment plan simulations were performed in MCSIM using the BEAMnrc-simulated PHSP as a source input. A total number of 1 × 10^9 histories was simulated for each treatment plan, resulting in a statistical uncertainty of 0.3–0.6% at the global dose maximum. Particles in the PHSP may originate from the same primary electron and thus be correlated. A latent variance (Sempau *et al* 2001) in the PHSP may propagate to the final dose calculations leading to an underestimation of the uncertainty (Walters *et al* 2002). This was not taken into account in the reported MC uncertainties. The probability of two correlated PHSP particles depositing dose in the same voxel is difficult to estimate, but considered small. In order to minimize the effect of the propagation of latent variance no phase space particle was used more than once, for each field, during the patient simulations. Cut off energies and variance reduction techniques were applied as described in subsection 2.2. Backscatter corrections were calculated for each field using the formalism described by Liu *et al* (2000).

Since the TPS reports dose to water and MC dose to media, a conversion was necessary in order to ensure a fair comparison. The procedure suggested by Siebers *et al* (2000) as implemented in the DICOM RT toolbox was employed in order to convert the MC-calculated dose into dose to water.

2.4. Evaluation

All algorithms (PB, AAA and MC) used identical setups for each treatment plan and all differences in the resulting dose distributions were solely due to discrepancies between the dose calculation algorithms. For each treatment plan and algorithm, dose–volume histograms (DVHs) were created. The DVHs were used to evaluate the volume of the PTV receiving less than 95% of the prescribed dose $\left(1 - V_{95}^{\mathrm{PTV}}\right)$. The lung normal tissue complication probability (NTCP) for pneumonitis was calculated using an equivalent uniform dose (EUD)-based formalism (Gay and Niemierko 2007). The parameters used for the NTCP calculation were $a = 1$, $\gamma_{50} = 2$, $TD_{50} = 24.5$ Gy and $\alpha/\beta = 3$ Gy, as suggested by Gay and Niemierko (2007). In order to visualize the comparison between energies and algorithms, Pareto fronts based on $\left(1 - V_{95}^{\mathrm{PTV}}\right)$ and the lung NTCP were produced for all algorithms and cases.

2.5. Influence of motion

The GTV and CTV move within the PTV due to respiratory motion and other anatomical changes. Usually part of the PTV receives less than the prescribed dose. Thus, part of the GTV and CTV might be underdosed. However, the dose distribution is perturbed due to motion of the GTV and CTV. In order to study this effect, two phantoms ($\mathrm{Ph_A}$ and $\mathrm{Ph_B}$) were created in the TPS and for MC dose calculations (figure 2). In $\mathrm{Ph_A}$ the GTV was located in the center of the PTV while for $\mathrm{Ph_B}$ the GTV was moved 1.5 cm in three dimensions to the corner of the PTV (figure 2). The Hounsfield units (HU) for the lungs were set to -800 while HU $= 0$ was used for the rest of the phantoms, including the GTV. This corresponds to the densities of $\sim$0.2 g cm^{-3} and $\sim$1 g cm^{-3}, respectively.

One 6 MV dynamic IMRT treatment plan ($\mathrm{TP_{Ph}}$) was generated. In order to stress the optimization algorithm similar to a clinical situation, cubic optimization structures mimicking the heart and the spine were utilized in addition to constraints for the lungs and PTV. $\mathrm{TP_{Ph}}$ was normalized to 35 fractions of 2 Gy mean dose to the PTV, based on the PBC calculation. Final dose calculation of $\mathrm{TP_{Ph}}$ was undertaken for PBC, AAA and MC on both phantoms.

The volume containing the solid tumor in $\mathrm{Ph_A}$ is denoted as GTVA while the volume containing the solid tumor in $\mathrm{Ph_B}$ is denoted as GTVB. Thus, the HU for GTVA on $\mathrm{Ph_A}$ is $\mathrm{GTVA_{HU}|_{PhA}} = 0$ and $\mathrm{GTVB_{HU}|_{PhB}} = 0$. Since the overlap between GTVA and GTVB is 12.5% of the GTV volume, the HU for GTVA on $\mathrm{Ph_B}$ is $\mathrm{GTVA_{HU}|_{PhB}} = -800$ and $\mathrm{GTVA_{HU}|_{PhB}} = 0$ for 87.5% and 12.5% of the GTVA volume, respectively (and analogously for GTVB on $\mathrm{Ph_A}$).

The same MC settings, except the number of histories, as in the patient treatment plan simulations were used in the phantom study. In total 2×10^9 histories were simulated for each plan. This together with the fact that only five fields were utilized in the phantom study caused a restart of the PHSP twice per field. Thus, the uncertainty in the uncertainty estimate is larger. Nevertheless, the uncertainty in the calculated dose is expected to be less than or equal to that obtained for the patient simulations.

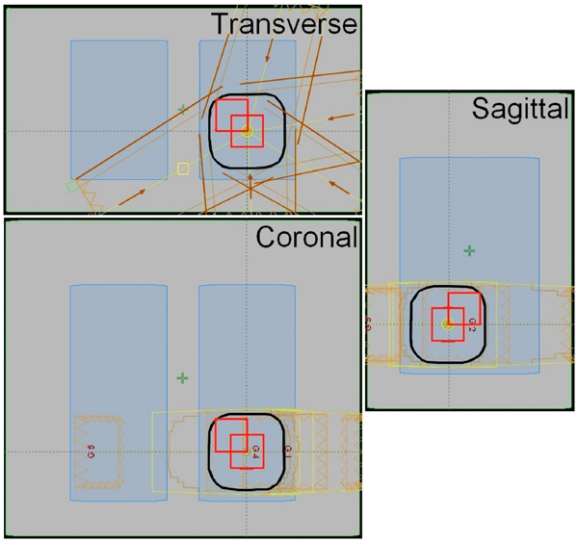

Figure 2. Superimposed illustrations of the two lung tumor phantoms Ph_A and Ph_B. For Ph_A the lower red cube represents the GTV in the center of the PTV (black line), while for Ph_B the GTV is displaced 1.5 cm cranial, right and anterior to the corner of the PTV. HU $= -800$ in the lungs and HU $= 0$ for the rest of the phantoms (including the GTV). The phantoms measure (left/right, anterior/posterior, cranial/caudal): $33 \times 19 \times 29$ cm^3, the lungs: $9 \times 13 \times 20$ cm^3 and the GTV $3 \times 3 \times 3$ cm^3. The beam arrangement for the treatment plan (TP_{Ph}) used is also visible in the transverse plane.

3. Results and discussion

3.1. Monte Carlo model

The combination of the incident electron beam parameters resulting in the best fit to measurements was found to be 6.0 MeV; 3%; 0.05 cm and 14.4 MeV; 3%; 0.12 cm (mean electron energy; FWHM Gaussian energy spread; target spot size) for 6 and 15 MV, respectively. For the CAX depth–dose profiles, agreement was within 2% beyond 1.2 cm for both energies (figure 3). For the lateral dose profiles, 98.2% and 100% of the data points were within 2%/2 mm (dose difference/distance to agreement) for 6 and 15 MV, respectively, for doses higher than 15% of the maximum dose ($D_{max}(d)$) for that depth (figure 3). The corresponding percentages were 98.2; 90.5 and 98.8; 91.7 for 1.5%/1.5 mm and 1%/1 mm for 6 and 15 MV, respectively. For comparison, the PBC and AAA algorithms agreed with the measurements within 2% for the CAX depth–dose profiles beyond 0.6 cm and 0.9 cm for 6 and 15 MV, respectively, whereas for the lateral dose profiles, agreement was within 2%/2 mm for doses higher than 15% of $D_{max}(d)$.

The inner 40 leaf pairs of the Varian Millennium 120 leaf MLC are arranged in an alternating pattern of two leaf types. This design results in transmission and leakage profiles resembling a saw-blade pattern with alternating tooth heights (Heath and Seuntjens 2003, Siebers *et al* 2002) as seen in the film measurements (figure 3). The effect was most distinguished for 6 MV. Due to limitations in leaf shape modeling, the MC simulations did not reproduce this pattern. However, the average leaf leakage effect agreed well between

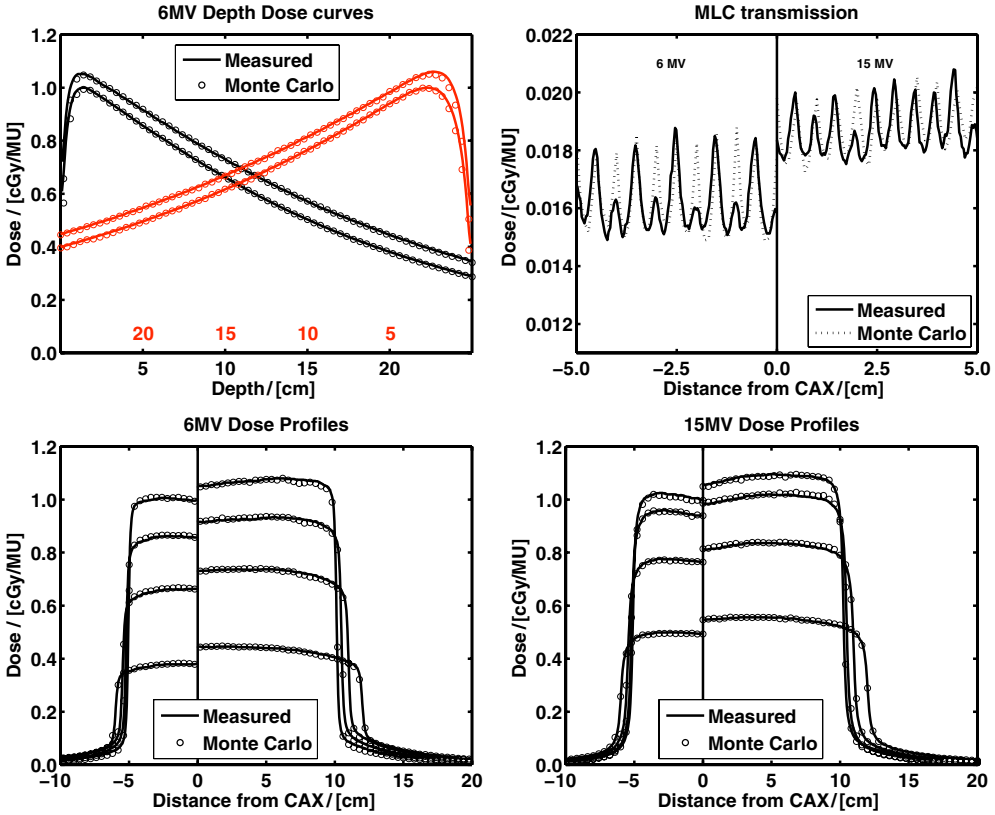

Figure 3. Top left: CAX depth–dose profiles for 10 × 10 and 20 × 20 cm^2 square fields for 6 MV (black: left to right) and 15 MV (red: right to left). Top right: lateral dose profiles for a field with a fully closed MLC. The film measurements illustrate a leaf pair effect (most distinguished for 6 MV) that was not reproduced by the MC simulations. Bottom (left 6 MV; right 15 MV): lateral dose profiles for 10 × 10 and 20 × 20 cm^2 square fields at d_{max}, 5 cm, 10 cm and 20 cm depth. The left-hand side of the figures shows the 10 × 10 cm^2 fields, while the right-hand side shows the 20 × 20 cm^2 fields.

film measurements and simulations. The small discrepancy is unlikely to have any significant effect on the reported DVH parameters below.

3.2. Cases A–D

The PTV coverage deteriorated as the dose to the total lung volume decreased. Thus, for a treatment plan with high PTV conformity, the lung dose will be higher compared to a treatment plan with a less conformal PTV dose (figure 4).

In order to visualize the comparison between energies and algorithms, the Pareto fronts for cases A–D are shown in figure 5. The abscissa indicates the percentage of the PTV volume that receives less than 95% of the prescribed dose $\left(1 - V_{95}^{\mathrm{PTV}}\right)$, while the ordinate indicates the calculated NTCP for the lungs.

Plans belonging to the same class (beam energy and algorithm) constitute the Pareto front for that specific class, enabling comparison of class to class rather than plan to plan. Treatment plans a and b for case A (figure 5) illustrate the potential problem in a plan-to-plan comparison

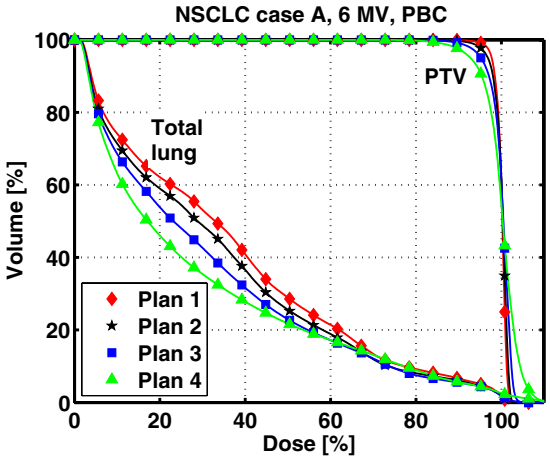

Figure 4. The 6 MV PBC DVHs of case A. Note the deterioration of the PTV coverage as the dose to the lungs is decreased.

study. Which one is the better plan, and should we prefer 6 or 15 MV? This question is impossible to answer based on these two treatment plans. However, when the Pareto fronts are plotted, it is clear that 6 MV is preferable compared to 15 MV for this case.

Considering MC as the golden standard, the inaccuracy of the other algorithms, in terms of NTCP and PTV underdosage, is illustrated and quantified by the Pareto fronts. The results illustrate that PBC significantly miscalculates the dose for all treatment plans, independent of tumor geometry. AAA is in much better agreement with MC. Generally, the differences between PBC and AAA/MC are larger for 15 MV. PBC and AAA overestimate the dose to the PTV, compared to MC (figure 5). Even a small overestimation in dose can lead to a large impact on $\left(1 - V_{95}^{\mathrm{PTV}}\right)$ due to the conformal nature of the dose distribution.

The dose to the total lung volume was significantly higher for case A. This is due to the fact that the PTV in case A is located in the mediastinum and extends into both lungs. For cases B–D, the PTV is confined to one lung, making it possible to spare the contralateral lung to a large extent. The NTCP(lung) values for cases B–D are very low. However, plotting V_{20} as a function of $\left(1 - V_{95}^{\mathrm{PTV}}\right)$ yields results similar to those illustrated in figure 5 and leads to the same conclusions. For the MC calculations, the ranges of V_{20} values are [34;53], [12;19], [18;29], [21;25]%, for cases A, B, C, and D, respectively.

For cases A–C, 15 MV appears favorable as compared to 6 MV based on the PBC treatment plans, while for case D, no significant difference is observed. However, this is not the case as more accurate dose calculation algorithms are employed. All cases exhibit a better combination of target coverage and NTCP(lung) for 6 MV than for 15 MV, i.e. for a range of treatment plans, the Pareto front for 6 MV MC is closer to origin than the corresponding 15 MV MC front (figure 5). The difference is least pronounced for case C. From the treatment plans generated, it is clear that 6 MV is more favorable than 15 MV in general.

Even though 6 MV was generally found to be more favorable for the cases studied, one should not set aside the possibility of using higher energies, as there might be cases or classes of cases benefiting from high energy-based treatment plans. It would be advantageous if patients could be sorted prior to treatment planning, identifying those with potential benefit from high energy-based treatment. Sorting criteria could include patient size and tumor location, tumor size and proximity to other structures, etc. For example, due to the larger dose

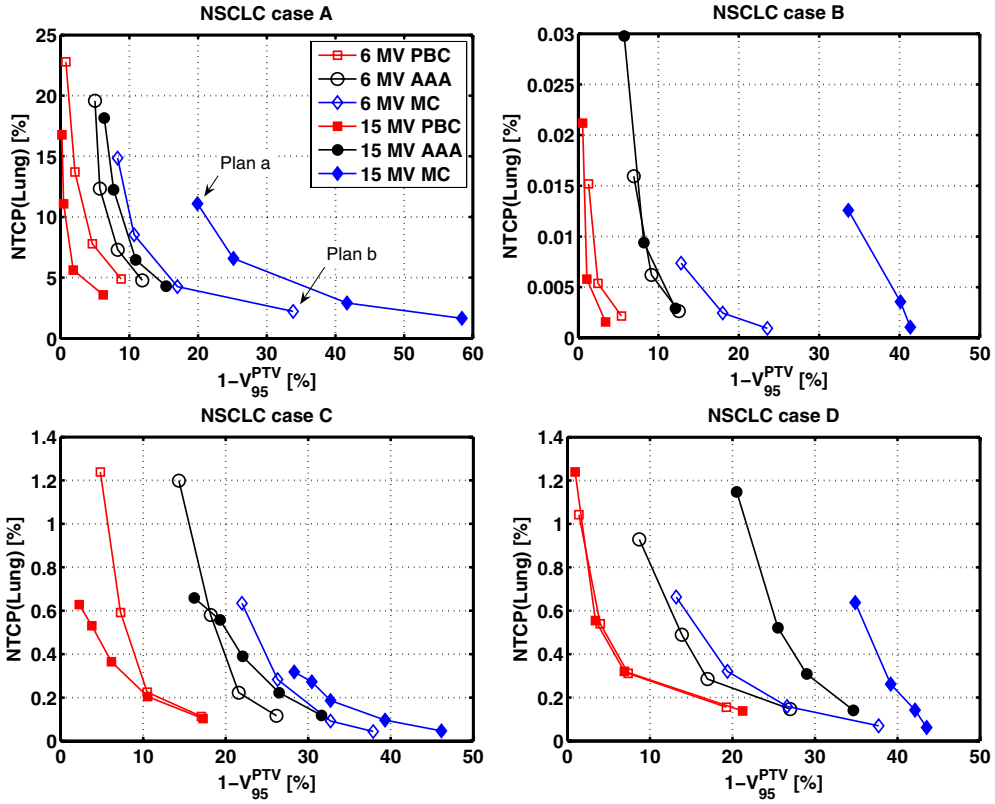

Figure 5. Pareto fronts for cases (A)–(D). Treatment plans a and b for case A (marked in the plot) illustrate the potential problem in a plan to plan comparison study. Which one is the better plan, and should we prefer 6 or 15 MV? This question is impossible to answer based on these two treatment plans. However, when the Pareto fronts are plotted, it is clear that 6 MV is preferable compared to 15 MV for this case.

deposition at depth, high energy-based treatment plans might be more advantageous for deep-seated tumors. However, several other factors are important, e.g. the larger penumbra region and primary and secondary build-up effects for the higher energy. A large secondary build-up effect might be advantageous when a beam passing through lung enters high-density healthy tissue, while a small build-up effect is beneficial when a beam passing through lung enters high-density tumor tissue. Based on the present work, it has not been possible to identify suitable sorting criteria. Possibly, too many different effects interplay and the potential benefit for a patient is based on the exact geometry of the case including the specific beam configuration. One might find that for some patients and a given beam configuration, high energy might be advantageous while low energy is advantageous for another beam configuration. In fact, it might be that some patients could benefit from a mixed energy setup, i.e. using high energy for some gantry angles and low energy for others. This is beyond the scope of this work and the subject of future investigations.

It is important to remember that the plans were generated utilizing the implemented PB-based optimization algorithm in Eclipse. Thus, it is possible that better treatment plans could be generated had MC been implemented in the optimization algorithm itself (Mihaylov

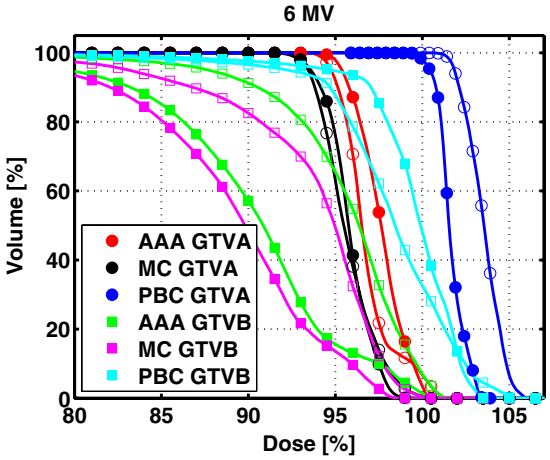

Figure 6. Closed symbols are for Ph_A (central tumor, $GTVA_{HU} = 0$) and open symbols are for Ph_B (displaced tumor, $GTVB_{HU} = 0$). For both phantoms: squares and circles represent GTVA and GTVB, respectively.

and Siebers 2008). Moreover, it is possible that having a more precise optimization algorithm at hand would lead to some high energy-based treatment plans being more favorable than those based on low energy.

3.3. Influence of motion

As shown, part of the PTV may be underdosed for a given treatment plan. Neither from the DVHs nor the Pareto fronts is it possible to evaluate where, within the PTV, the underdosage is. However, this may be clinically important. In many cases, the underdosage is found near the edges of the PTV surrounded by lung tissue and in the vicinity of critical normal tissue, e.g. the heart. In principle, the underdosage only becomes a problem if the GTV or CTV at some point during irradiation moves into the underdosed region. This can happen for several reasons, such as setup errors, changes in anatomy and inter- and intra-fractional motion of the GTV and CTV relative to the structures used for patient setup. For some lung patients, respiratory intra-fractional motion of the GTV (and CTV) may be several centimeters. If a solid tumor moves into an underdosed volume previously occupied by lung tissue, the dose distribution will be perturbed.

When moving from Ph_A to Ph_B, which corresponds to moving the tumor from the center to the edge of the PTV (figure 2), the PBC algorithm incorrectly predicts a decrease in dose for GTVB (figure 6). Knowing the limitations of the PBC algorithm, this is expected. However, the AAA algorithm as well as MC predicts an increase in dose in accordance with what is expected based on the principles of physics. The relatively high density tumor 'enhances' the dose in the volume previously occupied by lower density lung tissue (figure 7) and vice versa. Therefore, the underdosage of the GTV, as it moves to a low dose region previously occupied by lung tissue, will not be as large as predicted by the AAA or MC dose calculation in Ph_A (table 1). Thus, the underdosage of the PTV may be less critical than predicted if only looking at the original CT set (Ph_A). However, as the GTV moves into a lower dose region so may the CTV. Volumes with a relatively low number of clonogenic cells, possibly with lower density and incidence of hypoxic subvolumes, such as the CTV, may not require as high a dose as

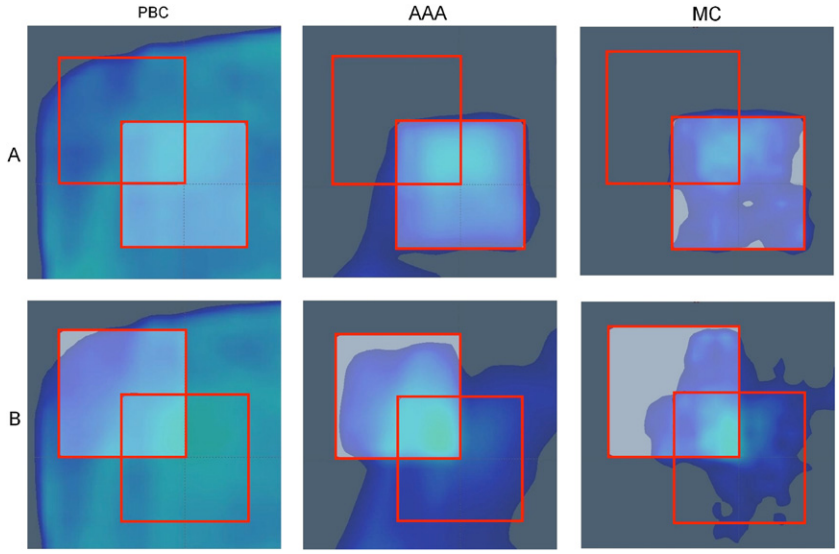

Figure 7. Dose distributions calculated utilizing PBC (first column), AAA (second column) and MC (third column) for the same treatment plan (TP_{Ph}) on Ph_A (upper row) and Ph_B (lower row). The red squares in the lower-right and upper-left corners (of each of the six illustrations) represent GTVA and GTVB, respectively. The lower colorwash dose limit was set to 95%, i.e. the visible dose cloud has a calculated dose $\geqslant$95% of the prescription dose.

Table 1. Summary of PBC, AAA and MC calculated $1 - V_{95}^{GTV}$ values for the two volumes GTVA and GTVB for the same treatment plan (TP_{Ph}) calculated on the two virtual phantoms: Ph_A and Ph_B.

$1 - V_{95}^{GTV}$	PBC		AAA		MC	
(%)	Ph_A	Ph_B	Ph_A	Ph_B	Ph_A	Ph_B
GTVA	0	0	2	8	24	37
GTVB	5	12	84	34	86	51

the solid tumor. Further investigation of these issues is beyond the scope of this work. The fractions of the GTV receiving less than 95% of the prescribed dose $\left(1 - V_{95}^{GTV}\right)$ are listed in table 1. The predicted perturbation of the dose distribution moving from Ph_A to Ph_B is similar for AAA and MC. However, the general dose level is overestimated by ~1.5% by the AAA algorithm (figure 6), i.e. if the AAA-calculated dose is lowered by 1.5%, the DVHs will be similar to those for the MC-calculated dose distributions.

As the tumor moves during respiration, the lung density will change, which will have further influence on the dose distributions (e.g. Aarup *et al* (2009)). This effect was not considered in the present work.

4. Conclusions

This study clearly demonstrates that the PBC dose calculation algorithm is clinically insufficient for patient geometries such as cases A–D. AAA is generally in closer agreement with MC than PBC. However, the inaccuracies in the calculated dose distributions are clinically

significant for both PBC and AAA. The results indicate that the AAA algorithm is in better agreement with the MC calculations for lower photon beam energies. Both AAA and PBC overestimate the dose to the PTV. Due to the conformity of the PTV dose, even a small overestimation of dose may lead to a large decrease in PTV dose coverage and tumor control probability.

A number of the PBC-calculated treatment plans appeared significantly better for 15 MV than for 6 MV. However, considering MC as the golden standard, the dose distributions that would actually be delivered to the patient are significantly better for 6 MV. Therefore, it is still advisable to use low energies as default for tumor sites involving large inhomogeneities unless a precise dose calculation algorithm is available. Yet, one should not completely set aside the possibility of using higher energies for sites covering the lungs or other inhomogeneous sites, as there might be cases, or classes of cases, where the resulting plans prove to be better. This study only encompasses MC-recalculated IMRT plans that were optimized using a simplistic PB-based algorithm. It is plausible that better treatment plans could have been generated had the optimization been based on an MC algorithm. Thus, the results indicate that it may be advantageous to have a more precise dose calculation algorithm, e.g. MC, implemented in the optimization process itself. Moreover, it is possible that having a more precise optimization algorithm at hand would lead to some high energy-based treatment plans being more favorable than those based on low energy.

The phantom study illustrates that as the relative high density GTV moves within the PTV to a location previously occupied by low density lung tissue, the dose in that volume is enhanced, as predicted by MC and AAA. In contrast, PBC predicts a decrease in dose when the density is increased. Thus, the phantom study underlines the inaccuracies introduced when calculating dose using a PB-based algorithm in geometries involving large density variations. The relative increase predicted by AAA is similar to what is predicted by MC, even though AAA overestimates the dose in absolute terms. However, the study of the effects this has on TCP and NTCP values is beyond the scope of this work. Additionally, the changes in lung density and other geometrical deformations were not considered and are the subject of further investigations.

Acknowledgments

The project is granted by The Danish Cancer Society with 885.600 DKK and supported by CIRRO—The Lundbeck Foundation Center for Interventional Research in Radiation Oncology and The Danish Council for Strategic Research. The hardware used for the MC calculations was donated by Toyota-Fonden, Denmark.

References

Aarup L R, Nahum A E, Zacharatou C, Juhler-Nøttrup T, Knöös T, Nyström H, Specht L, Wieslander E and Korreman S S 2009 The effect of different lung densities on the accuracy of various radiotherapy dose calculation methods: implications for tumour coverage *Radiother. Oncol.* **91** 405–14

Behrens C F 2006 Dose build-up behind air cavities for Co–60, 4, 6 and 8 MV. Measurements and Monte Carlo simulations *Phys. Med. Biol.* **51** 5937–50

Gay H A and Niemierko A 2007 A free program for calculating EUD-based NTCP and TCP in external beam radiotherapy *Phys. Medica* **23** 115–25

Heath E and Seuntjens J 2003 Development and validation of a BEAMnrc component module for accurate Monte Carlo modelling of the Varian dynamic Millennium multileaf collimator *Phys. Med. Biol.* **48** 4045–63

Jin L, Wang L, Li J, Luo W, Feigenberg S J and Ma C M 2007 Investigation of optimal beam margins for stereotactic radiotherapy of lung-cancer using Monte Carlo dose calculations *Phys. Med. Biol.* **52** 3549–61

Kawrakow I 2000a Accurate condensed history Monte Carlo simulation of electron transport: I. EGSnrc, the new EGS4 version *Med. Phys.* **27** 485–98

Kawrakow I 2000b Accurate condensed history Monte Carlo simulation of electron transport: II. Application to ion chamber response simulations *Med. Phys.* **27** 499–513

Klein E E, Chin L M, Rice R K and Mijnheer B J 1993 The influence of air cavities on interface doses for photon beans *Int. J. Radiat. Oncol. Biol. Phys.* **27** 419–27

Krieger T and Sauer O A 2005 Monte Carlo- versus pencil-beam-/collapsed-cone-dose calculation in a heterogeneous multi-layer phantom *Phys. Med. Biol.* **50** 859–68

Liu H H, Mackie T R and McCullough E C 2000 Modeling photon output caused by backscattered radiation into the monitor chamber from collimator jaws using a Monte Carlo technique *Med. Phys.* **27** 737–44

Ma C M, Li J S, Pawlicki T, Jiang S B, Deng J, Lee M C, Koumrian T, Luxton M and Brain S 2002 A Monte Carlo dose calculation tool for radiotherapy treatment planning *Phys. Med. Biol.* **47** 1671–89

Madani I, Vanderstraeten B, Bral S, Coghe M, Gersem W D, Wagter C D, Thierens H and Neve W D 2007 Comparison of 6 MV and 18 MV photons for IMRT treatment of lung cancer *Radiother. Oncol.* **82** 63–9

McDermott P N, He T and DeYoung A 2003 Dose calculation accuracy of lung planning with a commercial IMRT treatment planning system *J. Appl. Clin. Med. Phys.* **4** 341–51

Mihaylov I B and Siebers J V 2008 Evaluation of dose prediction errors and optimization convergence errors of deliverable-based head-and-neck IMRT plans computed with a superposition/convolution dose algorithm *Med. Phys.* **35** 3722–7

Ottosson R O, Engström P E, Sjöström D, Behrens C F, Karlsson A, Knöös T and Ceberg C 2009 The feasibility of using Pareto fronts for comparison of treatment planning systems and delivery techniques *Acta Oncol.* **48** 233–7

Pena J *et al* 2004 Commissioning of a medical accelerator photon beam Monte Carlo simulation using wide field profiles *Phys. Med. Biol.* **49** 4929–42

Rogers D W O, Walters B and Kawrakow I 2005 *BEAMnrc User's Manual* pp 1–236 http://www.irs.inms.nrc.ca/BEAM/user_manuals/pirs0509/index.html

Sempau J, Sánchez-Reyes A, Salvat F, Tahar H O B, Jiang S B and Fernández-Varea J M 2001 Monte Carlo simulation of electron beams from an accelerator head using PENELOPE *Phys. Med. Biol.* **46** 1163–86

Siebers J V, Keall P J, Kim J O and Mohan R 2002 A method for photon beam Monte Carlo multileaf collimator particle transport *Phys. Med. Biol.* **47** 3225–49

Siebers J V, Keall P J, Nahum A E and Mohan R 2000 Converting absorbed dose to medium to absorbed dose to water for Monte Carlo based photon beam dose calculations *Phys. Med. Biol.* **45** 983–95

Spezi E, Lewis D G and Smith C W 2002 A DICOM-RT-based toolbox for the evaluation and verification of radiotherapy plans *Phys. Med. Biol.* **47** 4223–32

Steneker M, Lomax A and Schneider U 2006 Intensity modulated photon and proton therapy for the treatment of head and neck tumors *Radiother. Oncol.* **80** 263–7

Tsiakalos M F, Stathakis S, Plataniotis G A, Kappas C and Theodorou K 2006 Monte Carlo dosimetric evaluation of high energy vs low energy photon beams in low density tissues *Radiother. Oncol.* **79** 131–8

Vanderstraeten B, Reynaert N, Paelinck L, Madani I, Wagter C D, Gersem W D, Neve W D and Thierens H 2006 Accuracy of patient dose calculation for lung IMRT: a comparison of Monte Carlo, convolution/superposition, and pencil beam computations *Med. Phys.* **33** 3149–58

Varian Medical Systems 2007 *Eclipse Algorithms Reference Guide (P/N B500298R01C).* (Palo Alto, CA: V M Systems)

Walters B R B, Kawrakow I and Rogers D W O 2002 History by history statistical estimators in the BEAM code system *Med. Phys.* **29** 2745–52

Weiss E, Siebers J V and Keall P J 2007 An analysis of 6-MV versus 18-MV photon energy plans for intensity-modulated radiation therapy (IMRT) of lung cancer *Radiother. Oncol.* **82** 55–62

B

PAPER II

Appendix B is a paper published in Physics in Medicine and Biology in 2011. A new algorithm, using delineation of structures in order to include and/or exclude certain media in various anatomical regions, for the conversion of CT data to a MC compliant phantom is presented and tested for a number of clinical cases.

CTC-ask: a new algorithm for conversion of CT numbers to tissue parameters for Monte Carlo dose calculations applying DICOM RS knowledge

2011 Phys. Med. Biol. 56 N263

(http://iopscience.iop.org/0031-9155/56/22/N01)

IOP PUBLISHING PHYSICS IN MEDICINE AND BIOLOGY

Phys. Med. Biol. **56** (2011) N263–N274 doi:10.1088/0031-9155/56/22/N01

NOTE

CTC-ask: a new algorithm for conversion of CT numbers to tissue parameters for Monte Carlo dose calculations applying DICOM RS knowledge

Rickard O Ottosson[1,2,3] **and Claus F Behrens**[2]

[1] Risø National Laboratory, Technical University of Denmark, Roskilde, Denmark
[2] Copenhagen University Hospital Herlev, Department of Oncology (R), Division of Radiophysics (52AA), Herlev, Denmark

E-mail: ctcask@gmail.com

Received 14 July 2011, in final form 12 September 2011
Published 25 October 2011
Online at stacks.iop.org/PMB/56/N263

Abstract

One of the building blocks in Monte Carlo (MC) treatment planning is to convert patient CT data to MC compatible phantoms, consisting of density and media matrices. The resulting dose distribution is highly influenced by the accuracy of the conversion. Two major contributing factors are precise conversion of CT number to density and proper differentiation between air and lung. Existing tools do not address this issue specifically. Moreover, their density conversion may depend on the number of media used. Differentiation between air and lung is an important task in MC treatment planning and misassignment may lead to local dose errors on the order of 10%. A novel algorithm, CTC-ask, is presented in this study. It enables locally confined constraints for the media assignment and is independent of the number of media used for the conversion of CT number to density. MC compatible phantoms were generated for two clinical cases using a CT-conversion scheme implemented in both CTC-ask and the DICOM-RT toolbox. Full MC dose calculation was subsequently conducted and the resulting dose distributions were compared. The DICOM-RT toolbox inaccurately assigned lung in 9.9% and 12.2% of the voxels located outside of the lungs for the two cases studied, respectively. This was completely avoided by CTC-ask. CTC-ask is able to reduce anatomically irrational media

[3] Author to whom any correspondence should be addressed.

assignment. The CTC-ask source code can be made available upon request to the authors.

(Some figures in this article are in colour only in the electronic version)

1. Introduction

One of the building blocks in Monte Carlo (MC) treatment planning is to convert CT numbers to an MC compatible phantom, consisting of a density and a media matrix. A protocol for automatic conversion was suggested by du Plessis *et al* (1998). That protocol is, however, limited to the beam quality under consideration. The MC framework EGSnrc is distributed with a tool called *ctcreate* for this task (Walters *et al* 2005, Kawrakow 2000a). The modus operandi for this tool is to read and sort CT files from a directory, prompt the user for a subset and resample the data on a user-specified grid. The actual conversion is performed by sorting the CT numbers into a user-specified number of bins corresponding to different media. All voxels are assigned the medium of the bin its CT number belongs to. Each bin has a lower and upper value in terms of CT number and density. A linear relationship between CT number and density is established within each bin. Thus, the conversion to density might depend on the number of media. The DICOM-RT toolbox (Spezi *et al* 2002) has its own version of this tool. The general workflow is similar and the conversion is performed using the same principles. The DICOM-RT toolbox allows the user to read the dose grid of a DICOM RD file and use it as the voxel grid. This ensures that the MC simulation will be on the same grid as dose calculated by the treatment planning system (TPS).

A stoichiometric calibration protocol establishing a direct relationship between medium composition and Hounsfield units (HU) was suggested in Schneider *et al* (1996) and Schneider *et al* (2000). Moreover, they suggested that the media within the human body readily can be represented by a limited number of media. Vandersraeten *et al* (2007) showed that the number of media can be chosen so that the error in dose, due to media assignment, is less than 1%. Implementation of the protocol suggested by Schneider *et al* (2000) requires measurements as well as access to tissue-like materials with precise known chemical composition. Vandersraeten *et al* (2007) highlight the importance of differentiating between media with discrepancies in H and Ca content as this has a significant impact on the attenuation properties of a medium. They suggest tweaking of the CT-number boundaries between air and lung for each tumor site, depending on the presence of lung.

Using dual-energy CT scanners for the determination of the effective atomic numbers, Z, and the relative electron densities, ρ_e, in a CT image has been suggested in several studies (e.g. Bazalova *et al* 2008, Torikoshi *et al* 2003, 2004).

The existing tools and protocols for conversion of CT data to MC parameters are limited to a global list of media; however, not all media are likely to exist within a given organ or anatomical structure (hereafter referred to as structures). This might lead to anatomically incorrect medium assignment (e.g. a dense tumor might be assigned bone in some voxels or voxels outside of the body may be classified as lung) and ultimately resulting in an error in dose. Furthermore, this disables the use of media with an overlap in CT numbers, but distinct elemental compositions.

The purpose of this work was to develop, evaluate and test a new algorithm, implemented in a MATLAB (Mathworks, Natlick, MA, USA) software solution, enabling global density conversion using piece-wise linear HU-to-density relationship while using structure specific media conversion ramps (i.e. the list of media eligible for assignment and their HU ranges).

Table 1. Physical densities and average CT number for the scanned materials. Uncertainties on CT numbers are given as 1 SD.

Material	Physical density (g cm^{-3})	CT number
Air (20 C)	1.2041×10^{-3}	−998 (±3)
Water (syringe)	1.00	−7 (±14)
Lung (inhale)	0.20	−801 (±16)
Lung (exhale)	0.50	−494 (±16)
Breast (50/50)	0.99	−33 (±16)
Liver	1.07	55 (±17)
Muscle	1.06	51 (±15)
Adipose	0.96	−64 (±16)
Trabecular bone 200 mg cm^{-3}	1.16	183 (±18)
Dense bone 800 mg cm^{-3}	1.53	841 (±19)

Incorporation of the delineations contained in the DICOM RS file enables separation into local compartments based on anatomical regions.

2. Materials and methods

2.1. CT calibration

A CIRS Model 062 phantom (CIRS Tissue Simulation Technology, Norfolk, VA, USA) was used for the determination of the CT-to-density conversion relationship. The epoxy-based phantom ($\rho = 1.01$ g cm^{-3}) accommodates a total of 17 inserts simultaneously.

A total of eight different tissue equivalent materials (two of each) and a water-filled syringe were placed in the phantom (table 1). The phantom was placed in a Phillips Brilliance CT Big Bore (Phillips, Amsterdam, the Netherlands) such that the iso-center of the scanner was aligned with the center of the phantom. A clinical protocol with typical scanning parameters (120 kVp, 2 mm slice thickness) was selected and the scan was repeated seven times. The CT images were read into MATLAB, using the dicomread function. Volumes of interest (VOIs) were drawn around each insert for every scan. VOIs were also drawn outside of the phantom to obtain the CT number for air. The data were pooled to obtain the average CT number of each insert for the entire population of scans. The data set was fitted with linear equations for the soft tissue and bone materials, respectively:

$$\rho = 10^{-3} \times \begin{cases} 1.02H - 7.65: & H \leqslant 55 \\ 0.58H + 467.79: & H > 55. \end{cases} \tag{1}$$

The linear fits had R^2 greater than 0.99. The results are in agreement with the findings of Saw *et al* (2005).

2.2. Generating a representative media set

Using tabulated composition (Woodard and White 1986, White *et al* 1987, NIST 2011) of a limited number of tissues and the measured relationship between density and HU, it is possible to generate a representative set of media spanning the full range of HU values from air to cortical bone (Schneider *et al* 2000, Vandersraeten *et al* 2007). The scheme suggested by Schneider *et al* (2000) was adopted, with one modification: the soft tissue range was divided

Table 2. The binning-scheme used for this study. The HU range was divided into 19 bins, the first corresponding to the composition of air and the second to lung. The compositions of the following bins were determined by equation (2) where the media used for the interpolation were adipose tissue 3 and adrenal gland (for bin 3), small intestine (wall) and connective tissue (for bin 4) and red/yellow marrow and cortical bone (for bins 5 through 19).

		Elemental weight (w_i)											
Media	H	H	C	N	O	Na	Mg	P	S	Cl	Ar	K	Ca
HUrange1	−1000 to −950			75.7	23.2						1.3		
HUrange2	−950 to −100	10.3	10.5	3.1	74.9	0.2		0.2	0.3	0.3		0.2	
HUrange3	−100 to 15	11.2	50.8	1.2	36.4	0.1			0.1	0.1			
HUrange4	15 to 129	10.0	16.3	4.3	68.4	0.4			0.4	0.3			
HUrange5	129 to 200	9.7	44.7	2.5	35.9			2.3	0.2	0.1		0.1	4.5
HUrange6	200 to 300	9.1	41.4	2.7	36.8		0.1	3.2	0.2	0.1		0.1	6.3
HUrange7	300 to 400	8.5	37.8	2.9	37.9		0.1	4.1	0.2	0.1		0.1	8.2
HUrange8	400 to 500	8.0	34.5	3.1	38.8		0.1	5.0	0.2	0.1		0.1	10.0
HUrange9	500 to 600	7.5	31.6	3.2	39.7		0.1	5.8	0.2	0.1			11.6
HUrange10	600 to 700	7.1	28.9	3.4	40.4		0.1	6.6	0.2	0.1			13.1
HUrange11	700 to 800	6.7	26.4	3.5	41.2		0.2	7.2	0.3				14.4
HUrange12	800 to 900	6.3	24.2	3.7	41.8		0.2	7.8	0.3				15.7
HUrange13	900 to 1000	6.0	22.1	3.8	42.4		0.2	8.4	0.3				16.8
HUrange14	1000 to 1100	5.6	20.1	3.9	43.0		0.2	8.9	0.3				17.9
HUrange15	1100 to 1200	5.3	18.3	4.0	43.5		0.2	9.4	0.3				18.9
HUrange16	1200 to 1300	5.1	16.6	4.1	44.0		0.2	9.9	0.3				19.8
HUrange17	1300 to 1400	4.8	15.0	4.2	44.4		0.2	10.3	0.3				20.7
HUrange18	1400 to 1500	4.6	13.6	4.2	44.9		0.2	10.7	0.3				21.5
HUrange19	>1500	4.3	12.2	4.3	45.3		0.2	11.1	0.3				22.2

in accordance with Vandersraeten *et al* (2007), which assures dosimetric equivalence within 1%. In total, 19 media were generated (table 2). The first and second bins correspond to air and lung, respectively. The compositions of the following bins were calculated according to equation (18) in Schneider *et al* (2000):

$$w_i = \frac{\rho_1(H_2 - H)}{(\rho_1 H_2 - \rho_2 H_1) + (\rho_2 - \rho_1)H}(w_{1,i} - w_{2,i}) + w_{2,i} \tag{2}$$

with

$$H_1 \leqslant H \leqslant H_2,$$

where H is the average HU of the bin, ρ is the density of the media and w_i is the weight of element i. The media used for the interpolation were the same as in Schneider *et al* (2000), i.e. adipose tissue 3 and adrenal gland (for bin 3), small intestine (wall) and connective tissue (for bin 4) and red/yellow marrow and cortical bone (for bins 5 through 19). The calculated compositions of the HU bins are presented in table 2.

2.3. CTC-ask general work-flow

A MATLAB program, called CTC-ask (CT Create Applying DICOM RS Knowledge), was developed. CTC-ask uses the DICOM-RT toolbox to a large extent, either through function calls or by direct reuse of code segments. Figure 1 illustrates the general work-flow of the program.

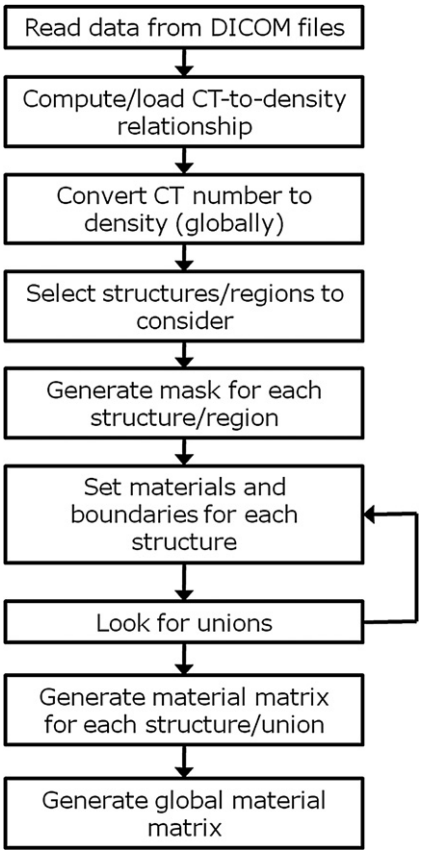

Figure 1. General work-flow of CTC-ask.

Firstly, the CT matrix, CT and dose grid are read from the DICOM files. The bilinear CT-to-density relationship is calculated based on data points submitted by the user. An option to use a pre-saved relationship is also provided. The CT matrix is globally converted to a density matrix, with a grid corresponding to the dose grid of the DICOM RD file. The structures in the DICOM RS file are sorted according to structure types (e.g. PTV, External, Avoidance etc) and the user is queried for structure types to be considered. A list of the structures with the desired types is created and presented to the user along with an option to exclude specific structures. The external outline is a required structure and may not be excluded. A logical mask is generated for each selected structure, that is, a logical matrix of the same shape as the RD dose grid where true means that the voxel belongs to the specific structure. The user is requested to input names and upper CT number bounds for the possible media (hereafter referred to as a ramp function) for each structure (the lower CT number bound of the first medium defaults to -1000, while the ith ($i > 1$) uses the upper CT number bound of the $(i-1)$st medium). An option to use a pre-saved ramp function is also implemented. As every voxel is allowed to belong to only one structure, the program iterates over the selected structures and generates a union structure in the regions where structure-overlaps exist. In the case of structure-overlaps, the ramp functions of the overlapping structures are compared. If identical, the structure union is assigned the ramp, else the user is queried to specify one. The voxels belonging to the overlapping area are set to false for the overlapping parent structures

and to true for the generated structure union. If any unions were found during the iteration, a recursive call of the function is made. Each structure undergoes a separate conversion of CT number to media based in its ramp-function. A global media list is generated and each structure correlated to the global list. An option to set voxels outside of the external outline to air with zero density is implemented in order to emulate the procedure of TPSs. The media matrices are subsequently added to a global media matrix. Finally, the data are written to an egs4phant file.

2.4. Patient cases

Two cases where one may expect improvements due to the specific considerations in CTC-ask were selected: a 15 MV 3D-CRT pelvic case with substantial metal artifacts in the CT scan due to bilateral hip prostheses and a 6 MV IMRT head and neck case including lung as well as air-filled cavities. Phantoms were generated based on the CT-data, using the 19-media conversion scheme as implemented in the DICOM-RT toolbox (hereafter referred to as unconstrained phantoms) as well as in CTC-ask (hereafter referred to as constrained phantoms). For the constrained pelvic phantom, the bilateral hip prostheses were delineated, all voxels belonging to the delineated prostheses were set to titanium with a density of 4.54 g cm^{-3} and in the slices containing artifacts, all voxels inside the external outline not belonging to bone nor prostheses were set to ICRUTISSUE with a density of 1.00 g cm^{-3}. For the constrained head and neck phantom, only voxels belonging to the lungs were allowed to be assigned lung. Voxels inside the external outline, not belonging to any other specific structure, were allowed also to be assigned Cranium. As the mandible was outlined, voxels belonging to that structure were allowed to be assigned mandible as well. Compositions and densities of specific media were taken from Woodard and White (1986). A second constrained phantom was generated for the head and neck case (hereafter referred to as the constrained$_{\text{air outside}}$ phantom) where, in addition to previously mentioned considerations, all voxels outside of the external outline were assigned HUrange1 (corresponding to air) with a density of 1.2041×10^{-3} g cm^{-3}. The rationale behind this was to exclude the neck support tray and the fixation mask from the MC simulation.

2.5. MC simulation

The MC simulations followed the procedure reported in Ottosson *et al* (2010). In short, EGSnrc and BEAMnrc (Kawrakow 2000a, 2000b, Rogers *et al* 1995) were used to build and commission MC models for each energy (6 and 15 MV) of a Varian 2300 iX linear accelerator (Varian Medical Systems, Palo Alto, CA, USA). A phase space file (PHSP) was scored just below the flattening filter for each of the energies. The PHSPs were scored by simulation of 2.5×10^6 histories with cut-off energies of 521 keV (including rest mass) and 10 keV for electrons and photons, respectively. The beam modifiers and patient geometry were simulated in MCSIM (Jin *et al* 2007, Ma *et al* 2002) using the EGSnrc-generated PHSP as the source. A set of in-house MATLAB scripts were used to generate input files for MCSIM from the DICOM RP files. Thus, all parameters of the treatment plans were recreated in the simulations. The number of simulated histories were chosen so that the estimated statistical uncertainty[4]

[4] MCSIM estimates the relative statistical uncertainty of the dose in a voxel is estimated by

$$\frac{\sigma D}{D} = \sqrt{\frac{n\sum e_i^2 - \left(\sum e_i\right)^2}{(n-1)\left(\sum e_i\right)^2}}, \tag{3}$$

where e_i is the energy deposited in the voxel in the ith energy deposition event and n is the total number of energy deposition events in the voxel.

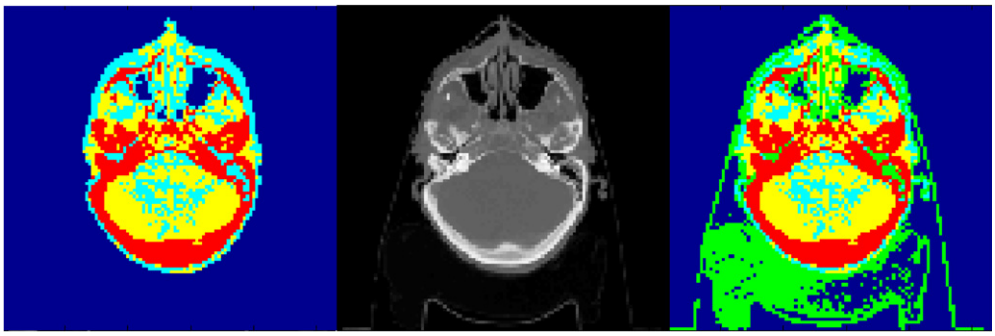

Figure 2. Transversal slice of the head and neck case showing media assignment for the constrained$_{\text{air outside}}$ phantom (left), HU-map (center) and media assignment for the unconstrained phantom (right). The colors correspond to air (dark blue), lung (green), soft tissue (cyan), connective tissue (yellow) and bone (red). (Note that all media corresponding to bone appear in red.)

was ≈0.5% for the voxels in the high-dose regions. The selected number of histories resulted in estimated statistical uncertainties below 2%, 8% and 15% for voxels receiving 50%, 20% and 10% of the maximum dose, respectively. All doses are reported as dose to medium.

3D-dose distributions were converted to DICOM RD files using CERR (Deasy *et al* 2003) and subsequently imported to the TPS (Varian Eclipse 10.0) to generate DVHs.

3. Results

The unconstrained phantoms were assigned HUrange2 (corresponding to lung) in 9.9% and 12.2% of voxels inside the external outline (excluding voxels belonging to lung structures) for the head and neck and the pelvic case, respectively. Moreover, 15.1% of the larynx in the head and neck case was assigned lung in the unconstrained phantom. No voxel outside of the lung structures was assigned lung for the constrained phantoms (figure 2). The unconstrained phantoms also were assigned lung to voxels outside of the external outline. This was avoided for the constrained phantoms (figure 2).

Local differences in dose, for the clinically used treatment plans, were computed between constrained and unconstrained phantoms (the unconstrained phantoms were used as references). Histograms of the local differences for voxels inside the external outline and with statistical uncertainty on dose $\leqslant$ 2% were produced (figures 3(a) and (b)). Gaussian-like distributions, with mean value close to zero, are noted when comparing constrained and unconstrained phantoms globally. For the head and neck case, the comparison between the constrained$_{\text{air outside}}$ and the unconstrained phantom deviates from this behavior. Figure 3(b) shows two things in particular for the constrained$_{\text{air outside}}$ phantom: (i) a low dose tail and (ii) a shift toward higher doses for the remaining distribution.

The user can make restrictions on which media CTC-ask is allowed to assign to voxels within a given structure. In order to investigate the influence of this on the dose distribution in detail, the dose of voxels assigned specific media as well as voxels differing in terms of air and lung between the constrained and unconstrained phantoms were studied (figures 3(c) and (d)). When comparing dose in voxels assigned to lung in the unconstrained phantom while a different media in the constrained phantoms for the head and neck case, two peaks are

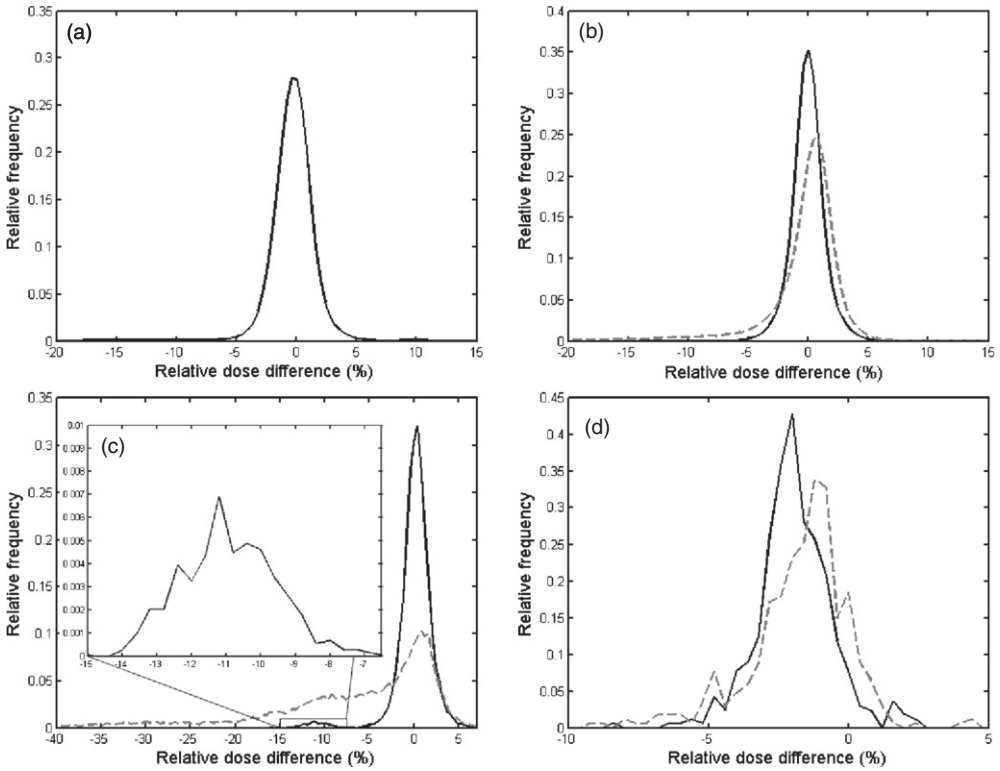

Figure 3. Histograms over local dose differences (calculated as ($\text{dose}_{\text{constrained}}-\text{dose}_{\text{unconstrained}}$)/$\text{dose}_{\text{unconstrained}} \times 100$) between constrained and unconstrained phantoms (solid) as well as $\text{constrained}_{\text{air outside}}$ and unconstrained phantoms (dashed) for the head and neck case. The histogram was plotted with a binwidth of 0.4% and normalized to the integral. Voxels outside the external outline or with uncertainty larger than 2% were ignored. (a) Pelvic case. (b) Head and neck case. (c) Voxels in the head and neck case assigned HUrange2 (lung) in the unconstrained phantom and non-HUrange2 in the constrained phantoms. Two frequency peaks are noted for the comparison with the constrained phantom (solid): around 0% and around −11%. The 0% peak corresponds to voxels assigned HUrange3 (soft tissue), while the −11% peak (also shown in the inset figure) corresponds to voxels assigned HUrange1 (air) in the constrained phantoms, respectively. (d) Voxels in the head and neck case assigned Cranium in the constrained phantoms (the corresponding voxels were assigned HUrange13 in the unconstrained phantom).

observed (figure 3(c)). The peaks are less distinct, but still existing, for the $\text{constrained}_{\text{air outside}}$ phantom. The dose for voxels assigned Cranium (figure 3(d)) in the constrained phantoms was lowered by ≈2% on average.

The Gaussian-like distribution around 0% for the pelvic case indicates that dose distributions generally agree. This is confirmed by the virtually indistinguishable DVHs of the external outline (figure 4(a)). For other structures, the differences are more noticeable. A large underdosage is noted for the unconstrained PTV and almost the entire PTV volume receives 5 Gy less dose. On the other hand, the bone and prostheses structures receive higher doses in the unconstrained phantom. This is caused by the misassignment of media and density due to the metal artifacts. Differences in DVHs of the constrained and $\text{constrained}_{\text{air outside}}$ phantoms for the head and neck case are not as dramatic as the 5 Gy shift for the PTV of the pelvic case. Nevertheless, it is evident that a larger volume receives high doses for the $\text{constrained}_{\text{air outside}}$

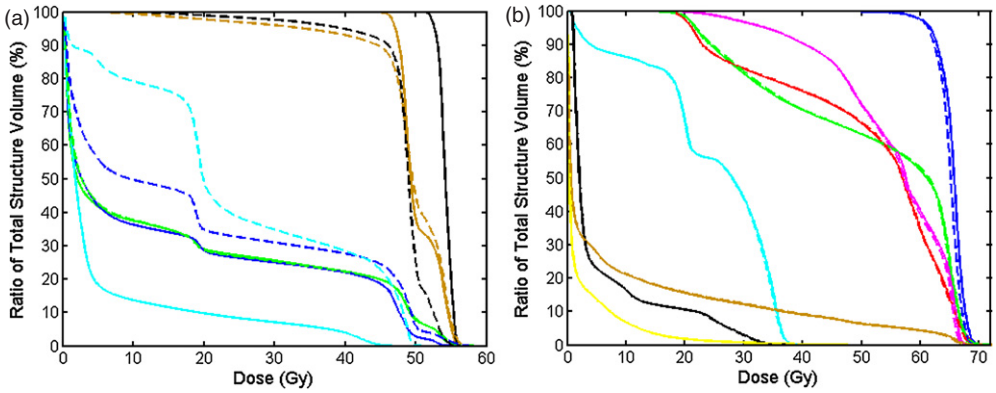

Figure 4. (a) Cumulative dose volume histograms for the pelvic case using the constrained (solid) and unconstrained (dashed) phantoms. DVHs are plotted for the external outline (green), bones (blue), prostheses (cyan), PTV (brown) and the PTV excluding the rectum (black). (b) Cumulative dose volume histograms for the head and neck case using the constrained$_{\text{air outside}}$ (solid) and constrained (dashed) phantoms. DVHs are plotted for the external outline (brown), PTV (blue), left parotid gland (red), right parotid gland (green), spinal cord (cyan), brainstem (black), larynx (magenta) and the lungs (yellow).

(figure 4(b)). The effect is particularly noticeable for deep-seated structures (e.g. PTV, larynx and spinal cord).

4. Discussion

The accuracy of MC dose calculation is strongly influenced by the conversion of CT number to density and media. The most crucial contributor is arguably the density conversion. When assigning media to voxels, the most critical task is to differentiate between media with distinct mass attenuation properties. It was demonstrated that misassignment between air and lung can introduce a local error in dose in the order of 10% (figure 3(c)), which agrees with the findings of e.g. Verhaegen and Devic (2005).

CTC-ask is run interactively and allows for manual manipulation at any point. This is useful in the case of CT scans obtained with contrast enhancing agents and/or metal artifacts. For those cases, the CT number will not represent the actual density if not corrected for manually and dose calculation will be performed using the inaccurate densities and/or media. This can be solved by delineating the area containing the affected voxels and applying a filter that compensates for the shift in density (or CT-number) on those voxels. This was done for the constrained pelvic phantom, where voxels in slices containing metal artifacts were set to ICRUTISSUE with a density of 1.00 g cm^{-3} unless the voxels belonged to the delineated prostheses or bone structures. This heavily influenced the dose distribution of most structures (figure 4(a)). An alternative method of correcting for metal artifacts was presented by Bazalova *et al* (2007) where the general idea is to apply a metal filter and then by interpolating missing projections of the filtered sinograms. CTC-ask may be used in combination with the method suggested by Bazalova *et al* (2007).

The inclusion of an 'outside' structure, the inverse of the external outline, gives rise to the possibility of specifying which media are allowed to be assigned outside of the patient. This is a unique feature of CTC-ask. Other existing tools allow any voxel to be assigned any of the media regardless of whether it is located within the body or not. Moreover, CTC-ask allows

post-conversion manipulation of the density and/or media assignment for any structure. Hence, it is possible to set objects (couch, clothes, support structures, etc) to air with zero density and thereby removing their influence on the dose calculation. This may influence the entire dose distribution. When setting all voxels outside of the external outline to air for the head and neck case, the build-up region is effectively shifted deeper into the patient. This is what causes the low-dose tail (compared to the unconstrained phantom) for the constrained$_{\text{air outside}}$ phantom (figure 3(b)). Shifting the build-up region deeper also means that the beam will be less attenuated at a given distance beyond d_{max} and thus will give rise to a higher dose. This is the explanation for the shift toward higher doses for the constrained$_{\text{air outside}}$ phantom (figures 3(b) and 4(b)). This effect will be somewhat compensated for distal voxels when using opposing beams while it will be further enhanced for central voxels. Assigning all of the voxels outside the external contour to air might not be accurate from a dosimetric point of view since the patient might be covered by a mask, be placed in a fixation and the treatment couch might be in the beam. In CTC-ask, delineated support structures may, like any other delineated structure, be assigned the actual density and media composition should it be known.

Vandersraeten *et al* (2007) stress the importance of differentiating between air and lung (i.e. HUrange1 and HUrange2 in this study) and media with different Ca content. Their suggested solution is to tune the CT-number boundary between air and lung depending on the tumor site and to include a number of media, with increasing Ca content, representing bone of various densities. The CT numbers of air and lung are however not likely to differ depending on tumor site. Another way to address the issue would be to exclude air and/or lung from areas where they are not likely to exist. This is what is done in CTC-ask. Moreover, it is possible to tune the HUrange corresponding to a given media individually for each structure. Thus, a voxel with a HU of −940 might be assigned air, lung or gas depending on which structure it belongs to. In addition to the possibility of using a range of interpolated media representing tissues of various densities, CTC-ask allows for inclusion of tissue-specific media (and non-tissue media), and for confinement of the eligibility of those media to structures where they are likely to exist.

Media with distinct composition will likely differ in important dosimetrical properties (such as stopping power and mass energy absorption coefficients). This is illustrated by figure 3(d), where the voxels assigned Cranium are shifted to a lower dose for the constrained phantoms due to lower mass stopping power of the composition corresponding to Cranium media than that of HUrange13, which was the media assigned to the corresponding voxels in the unconstrained phantom.

Compton effect is the dominating effect for radiotherapy beams and the probability for Compton interaction is proportional to the electron density. Hydrogen has a higher electron density than elements with higher Z; therefore, the attenuation properties of media will depend heavily on the hydrogen content. This is most outspoken when comparing air and lung as lung contains 10.3% hydrogen, whereas dry air does not contain any (Vandersraeten *et al* 2007). This is illustrated by figure 3(c) where two peaks are evident for the constrained phantom (solid line). The voxels constituting the largest peak, around 0%, were assigned HUrange3 (soft tissue), whereas the voxels in the peak around −11% (see the inset in figure 3(c)) were assigned HUrange1 (air). The difference in hydrogen content is small (0.9%) when moving from HUrange2 to HUrange3 and thus no large effect on dose is expected for those voxels. The peaks are not as distinct for the constrained$_{\text{air outside}}$ phantom since the build-up region is shifted deeper into the patient in the constrained$_{\text{air outside}}$ phantom and a large fraction of the voxels are situated at shallow depths.

Erroneous assignment of media might lead to a local error in dose (figures 3(c) and (d)), which may or may not be partially compensated for, due to the differences in mass stopping

power, if converting to dose to water (D_w). The mass attenuation of the improper media will however also perturb the beam, leading to an error in dose downstream and/or laterally. In addition, an increased backscatter (or lack thereof, depending on if moving from media with high H or Ca content to media with low, or vice versa) is noted at the boundary. Moreover, the local dose may be affected by media misassignment of neighboring voxels. None of those effects are compensated for when converting to D_w.

As CTC-ask utilizes delineated structures in the DICOM data, it is integral to ensure that the structures of consideration were properly delineated.

5. Conclusions

CTC-ask utilizes delineated structures in the DICOM data to set local conversion constraints for each structure and thus greatly reduces the probability of voxels being assigned anatomically irrational media. Furthermore, CTC-ask uses the CT number to density relationship without any linear interpolation within the range of a given media. Thus, the density matrix generated by CTC-ask will be independent of the number of media considered.

CTC-ask is run interactively and density and media matrices can be manually modified at any point. This gives rise to the possibility of applying filters to specific regions affected by contrast enhancing agents, metal artifacts, etc during the CT scan.

As CTC-ask relies on delineated structures in the DICOM set, it is integral to ensure that all structures are properly delineated as irrational media assignment otherwise may be introduced.

Acknowledgments

This project was granted by the Danish Cancer Society and supported by CIRRO—the Lundbeck Foundation Center for Interventional Research in Radiation Oncology and the Danish Council for Strategic Research. The hardware used for the MC calculations was donated by Toyota-Fonden, Denmark.

References

Bazalova M, Beaulieu L, Pefalsky S and Verhaegen F 2007 Correction of CT artifacts and its influence on Monte Carlo dose calculations *Med. Phys.* **34** 2119–31

Bazalova M, Carrier J F, Beaulieu L and Verhaegen F 2008 Tissue segmentation in Monte Carlo treatment planning: a simulation study using dual-energy CT images *Radiother. Oncol.* **86** 93–8

Deasy J O, Blanco A I and Clark V H 2003 CERR: a computational environment for radiotherapy research *Med. Phys.* **30** 979–85

du Plessis F C, Willemse C A, Lötter M G and Goedhals L 1998 The indirect use of CT numbers to establish material properties needed for Monte Carlo calculation of dose distributions in patients *Med. Phys.* **25** 1195–201

Jin L, Wang L, Li J, Luo W, Feigenberg S J and Ma C M 2007 Investigation of optimal beam margins for stereotactic radiotherapy of lung-cancer using Monte Carlo dose calculations *Phys. Med. Biol.* **52** 3549–61

Kawrakow I 2000a Accurate condensed history Monte Carlo simulation of electron transport: I. EGSnrc, the new EGS4 version *Med. Phys.* **27** 485–98

Kawrakow I 2000b Accurate condensed history Monte Carlo simulation of electron transport: II. Application to ion chamber response simulations *Med. Phys.* **27** 499–513

Ma C M, Li J S, Pawlicki T, Jiang S B, Deng J, Lee M C, Koumrian T, Luxton M and Brain S 2002 A Monte Carlo dose calculation tool for radiotherapy treatment planning *Phys. Med. Biol.* **47** 1671–89

NIST 2011 http://physics.nist.gov/cgi-bin/Star/compos.pl?ap

Ottosson R O, Karlsson A and Behrens C F 2010 Pareto front analysis of 6 and 15 MV dynamic IMRT for lung cancer using pencil beam, AAA and Monte Carlo *Phys. Med. Biol.* **55** 4521–33

Rogers D W O, Faddegon B A, Ding G X, Ma C M, We J and Mackie T R 1995 BEAM: a Monte Carlo code to simulate radiotherapy treatment units *Med. Phys.* **22** 503–24

Saw C B, Loper A, Komanduri K, Combine T, Huq S and Scicutella C 2005 Determination of CT-to-density conversion relationship for image-based treatment planning systems *Med. Dosim.* **30** 145–8

Schneider U, Pedroni E and Lomax A 1996 The calibration of CT Hounsfield units for radiotherapy treatment planning *Phys. Med. Biol.* **41** 111–24

Schneider W, Bortfeld T and Schlegel W 2000 Correlation between CT numbers and tissue parameters needed for Monte Carlo simulation of clinical dose distributions *Phys. Med. Biol.* **45** 459–78

Spezi E, Lewis D G and Smith C W 2002 A DICOM-RT-based toolbox for the evaluation and verification of radiotherapy plans *Phys. Med. Biol.* **47** 4223–32

Torikoshi M, Tsunoo T, Sasaki M, Endo M, Noda Y, Ohno Y, Kohno T, Hyodo K, Uesugi K and Yagi N 2003 Electron density measurement with dual-energy x-ray CT using synchrotron radiation *Phys. Med. Biol.* **48** 673–85

Torikoshi T T M, Ohno Y, Endo M, Natsuhori M, Kakizaki T, Yamada N, Ito N, Yagi N and Uesugi K 2004 Measurement of electron density and effective atomic number using dual-energy x-ray CT *Nuclear Science Symp. Conf. Record, IEEE* vol 6 pp 3764–8

Vandersraeten B *et al* 2007 Conversion of CT numbers into tissue parameters for Monte Carlo dose calculations: a multi-centre study *Phys. Med. Biol.* **52** 539–62

Verhaegen F and Devic S 2005 Sensitivity study for CT image use in Monte Carlo treatment planning *Phys. Med. Biol.* **50** 937–46

Walters B, Kawrakow I and Rogers D W O 2005 *DOSXYZnrc User's Manual* pp 1–109 http://irs.inms.nrc.ca/software/beamnrc/documentation/pirs794.pdf

White D R, Woodard H Q and Hammond S M 1987 Conversion of CT numbers into tissue parameters for Monte Carlo dose calculations: a multi-centre study *Br. J. Radiol.* **60** 907–13

Woodard H Q and White D R 1986 The composition of body tissues *Br. J. Radiol.* **59** 1209–19

C

PAPER III

Appendix C is a paper published in Physics in Medicine and Biology in 2011. A dosimetry system based on fiber–coupled organic scintillators is presented. It has the potential to conduct point measurements of absorbed dose in radiotherapy beams involving high spatial and temporal dose gradients. The system is tested against Monte Carlo simulations for Percentage Depth Dose curve and Relative Output Factor for square fields down to 0.6×0.6 cm^2 size.

Characterizing a pulse-resolved dosimetry system for complex radiotherapy beams using organic scintillators

2011 Phys. Med. Biol. 56 3033

(http://iopscience.iop.org/0031-9155/56/10/009)

IOP PUBLISHING PHYSICS IN MEDICINE AND BIOLOGY

Phys. Med. Biol. **56** (2011) 3033–3045 doi:10.1088/0031-9155/56/10/009

Characterizing a pulse-resolved dosimetry system for complex radiotherapy beams using organic scintillators

Anders R Beierholm[1,3], Rickard O Ottosson[1,2], Lars R Lindvold[1], Claus F Behrens[2] and Claus E Andersen[1]

[1] Radiation Research Division, Risoe National Laboratory for Sustainable Energy, Technical University of Denmark, Frederiksborgvej 399, DK-4000, Roskilde, Denmark
[2] Division of Radiophysics, Department of Oncology, Copenhagen University Hospital Herlev, Herlev Ringvej 75, DK-2730 Herlev, Denmark

E-mail: abei@risoe.dtu.dk

Received 3 January 2011, in final form 23 March 2011
Published 20 April 2011
Online at stacks.iop.org/PMB/56/3033

Abstract

A fast-readout dosimetry system based on fibre-coupled organic scintillators has been developed for the purpose of conducting point measurements of absorbed dose in radiotherapy beams involving high spatial and temporal dose gradients. The system measures the dose for each linac radiation pulse with millimetre spatial resolution. To demonstrate the applicability of the system in complex radiotherapy fields, output factors and per cent depth dose measurements were performed in solid water for a 6 MV photon beam and compared with Monte Carlo simulated doses for square fields down to 0.6 cm × 0.6 cm size. No significant differences between measurements and simulations were observed. The temporal resolution of the system was demonstrated by measuring dose per pulse, beam start-up transients and the quality factor for 6 MV. The precision of dose per pulse measurements was within 2.7% (1 SD) for a 10 cm × 10 cm field at 10 cm depth. The dose per pulse behaviour compared well with linac target current measurements and accumulated dose measurements, and the system was able to resolve transient dose delivery differences between two Varian linac builds. The system therefore shows promise for reference dosimetry and quality assurance of complex radiotherapy treatments.

(Some figures in this article are in colour only in the electronic version)

1. Introduction

The use of organic scintillators for dosimetry in complex radiotherapy fields, such as the ones used in stereotactic radiotherapy or intensity-modulated radiotherapy (IMRT), has been studied

[3] Author to whom correspondence should be addressed.

extensively (Létourneau *et al* 1999, Beddar *et al* 2001, Lambert *et al* 2010, Klein *et al* 2010). However, no experimental studies have so far verified the use of organic scintillators by direct comparison with Monte Carlo (MC) simulations of beam output in small fields, nor taken advantage of the fast response of commercial organic scintillators to measure doses delivered in radiotherapy beams on the actual timescale of the pulsed linac output. Dose measurements in small fields put high demands on the dosimeters used, and present a rapidly evolving field of research (IPEM 2010). Because of the lack of reference data for small fields, the best way to verify dose measurements seems to be a comparison between different dosimetry methods and MC simulations, as demonstrated in e.g. Das *et al* (2008), Cheng *et al* (2007) and Scott *et al* (2008).

As for the temporal structure of dose delivery, detailed knowledge of the dose deposition with time is of potential relevance for quality assurance (QA) purposes—especially for dynamic treatments like IMRT, where small dose segments on the order of a cGy are not uncommon. In general, the instantaneous dose rate within the μs duration linac radiation pulses is very high, easily reaching 50 Gy s^{-1} for normal beam delivery and well over 100 Gy s^{-1} for flattening-filter-free delivery (Vassiliev *et al* 2006). Therefore, pulse-resolved dose measurements will arguably provide physical insight into modern radiotherapy beam delivery. Also, some microdosimetric and spectroscopic information about the irradiation process might be uncovered, as suggested by Illemann *et al* (2009). An array of organic scintillators using charge-coupled device (CCD) and electron multiplying charge-coupled device (EMCCD) cameras has recently been developed for radiotherapy QA (Lacroix *et al* 2008), *in vivo* dosimetry (Archambault *et al* 2010), and small field dosimetry (Klein *et al* 2010). To accumulate a satisfactory signal-to-noise ratio, dose measurements have been performed with an integration time of approximately 5 s (for the CCD) or 150 ms (for the EMCCD). However, such data acquisition times cannot resolve the μs duration pulsed dose delivery of a medical linac, which typically has a frequency of 300–400 Hz. Studies of the theoretical precision limits of these CCD-based systems (Lacroix *et al* 2010) reveal that integration times as low as 0.1 ms can be achieved while maintaining a precision within 2%.

This study presents further development on the fast-readout dosimetry system introduced by Beierholm *et al* (2010). The system is based on two fibre-coupled organic scintillators coupled to photomultiplier tubes (PMTs). Our approach was to focus on the basic dosimetric challenges presented by small fields and non-continuous dose delivery by making measurements with a small number of point dosimeters. Our claim is that a thorough study of the basic mechanisms of spatial and temporal dose delivery will further the knowledge of the dosimetric challenges associated with modern radiotherapy. The purpose of the work was to support that the method provides detailed and highly accurate dose measurements in modern radiotherapy applications involving small fields and dynamic dose delivery. This was achieved in a twofold process: first, we critically examined the accuracy that can be obtained with organic scintillators in small field dosimetry by comparing dose measurements with MC simulations in small static fields. Secondly, we demonstrated that new dosimetric information can be uncovered with pulse resolution. We also provided experimental determination of the uncertainties associated with pulse-resolved dose measurements.

2. Materials and methods

2.1. Organic scintillator probes

The organic scintillators employed in this study were 1 mm diameter, polystyrene-based scintillating fibres (BCF-60, Saint-Gobain Ceramics & Plastics Inc., France). This type of a

plastic scintillator is well characterized and has been used for similar purposes in the studies by Fontbonne *et al* (2002) and Frelin *et al* (2005). The scintillating fibres were cut to a desired length and coupled to PMMA-based optical fibres (ESKA GH-4001P, Mitsubishi-Rayon Co., Japan) of 1 mm core diameter, 2.2 mm outer jacket diameter and approximately 10 m length, terminated by an SMA connector. Before coupling, the exposed ends of the scintillator and the optical fibre were polished using aluminium oxide polishing paper of 5, 3, 1 and 0.3 μm grain size (Thorlabs Sweden AB) and cleaned using water and pressurized air. The two components were aligned using a mechanical fixation mount and a stereo microscope, before making the coupling permanent using UV-curing, refractive index-matching glue (NOA68, Norland Products Inc., USA). Finally, a jacket of black epoxy cement (EPOTEK 320, Epoxy Technology Inc., USA) was moulded around the exposed junction to light-tighten the probe. The scintillators used for probes in this study were between 1 mm and 10 mm in length.

2.2. ME04 detector system

The ME04 dosimetry system (Risø DTU, Denmark) is designed as a hardware basis for the fibre-coupled organic scintillators. The ME04 hardware handles the input of two dosimeter probes. The optical fibres are long enough for the detection equipment to be placed outside the main treatment room. This prevents interference from stray radiation on the detector electronics. Parasitic fibre luminescence and Cerenkov radiation (the so-called stem signal) was suppressed using the chromatic removal method originally introduced by Fontbonne *et al* (2002). For each probe, light of wavelengths corresponding to mostly stem signal (designated A) and scintillation (designated B) is chromatically separated using yellow and magenta 45° dichroic mirrors (Edmund Optics Ltd, UK) and subsequently detected using two Hamamatsu H5784 PMT modules (Hamamatsu GmbH, Germany) operated in current mode at 0.3 V gain. Calibration links the absorbed dose, D, to the stem signal contribution, A, and the scintillator signal contribution, B. The data acquisition is synchronized with the pulsed synchronization output of the linac. The ME04 system makes use of a 'sample-hold' setup using Burr–Brown ACF2101 switched integrator circuits (Mountford *et al* 2008). The charge built up in the 100 pF capacitor is held, integrated, and read out before it is reset at the onset of the next synchronization pulse. The system handles five input channels, with four of these being used by the PMTs. The fifth is used for measuring the linac target current, which is the current required to keep the linac gun target electrically neutral when the target is hit by the accelerated electron bunches during irradiation. The temperature inside the hardware casing is measured by a thermistor to correct for the temperature-dependent sensitivity of the PMTs (approximately 0.1% per °C). The voltage signals are acquired using a NI 6218 DAQ card and a data acquisition software interface in-house developed in LabVIEW (National Instruments Inc., USA).

2.3. Setup for irradiation and dose measurement

A flow chart of the measurement setup is shown in figure 1. Dose measurements were made using 6 MV x-rays delivered by a Varian 2300 iX medical linac at Copenhagen University Hospital, Herlev. The linac was calibrated to deliver a dose to water of 1 cGy per monitor unit (MU) for a 10 cm × 10 cm field at 100 cm source to surface distance (SSD), at the depth of maximum dose delivery (d_{max}) which is approximately 1.5 cm at this energy. The details of linac calibration can be found in Sjöström *et al* (2009). The ME04 system was connected to the SYNC and I_TARGET BNC output of the linac to enable synchronized pulse counting of the synchronization signal and target current. In this way, the synchronization pulses as well

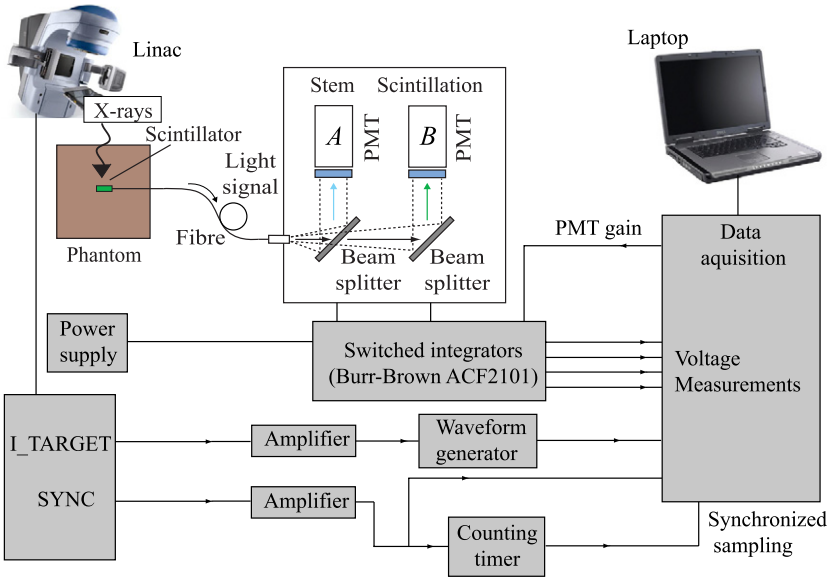

Figure 1. Flow chart of light detection and linac-synchronized data acquisition. For each linac SYNC pulse, the light from fibres and scintillators is chromatically discriminated and converted into voltage readings using Burr–Brown switched integrator circuits.

as the target current pulses of the linac were recorded. The time structure of the Varian 2300 iX linac was determined using an oscilloscope as well as the ME04 system in non-synchronized (continuous) sampling mode. Using the oscilloscope, the duration of the linac gun pulse was measured to be 4 μs long and starting approximately 12.5 μs after the synchronization signal leading edge. As expected, the pulse period was seen to change with dose rate, with the pulse width being constant. Based on this, a sampling time of 80 μs was chosen. The charge integration started 6 μs after the synchronization pulse leading edge and terminated after 86 μs.

As emphasized in the studies by Chow *et al* (2005) and Klein *et al* (2010), the dosimetric characteristics of a small field depends on the beam-shaping geometry. In this study, the linac was operated in service mode with the multi-leaf collimators parked, and the square field size varied between 0.6 cm $\times$ 0.6 cm and 10 cm $\times$ 10 cm using the secondary collimator jaws. All irradiations were performed at 100 cm SSD with the linac gantry and collimators at 0° and 90° rotation, respectively. The probes were irradiated in a 30 cm $\times$ 30 cm $\times$ 21 cm solid water phantom (CTG-457, Gammex Ltd, UK). 2.5 mm $\times$ 2.5 mm $\times$ 300 mm grooves were drilled along the centre of some of the slabs for a tight housing of the dosimeter probes.

A critical point of small field measurements is to ensure correct alignment of the dosimeter with the beam isocentre. In the case of scanning water tanks, this can be achieved by scanning the dosimeter through the tank until the signal is at a maximum in the lateral and longitudinal directions. This cannot be done in a solid water phantom, where the position of the dosimeter is fixed. In the present case, we used a lead piece of the same dimensions as the scintillator. The lead piece was aligned with the apparent beam isocentre using the positioning lasers and alignment light field. A portal image was then obtained using the linac on-board imaging device, confirming the actual position of the beam isocentre. In case of an offset, the solid water phantom was carefully repositioned to correct for the offset and another portal image was obtained to verify correct positioning of the dosimeter probe. For most irradiations, 25 MU were delivered at a dose rate of 300 MU min^{-1}. The only exceptions were irradiations

performed at different dose rates, made to investigate the dose per pulse dependence on dose rate. Dosimeter calibration was carried out for each scintillator probe using the same 10 cm × 10 cm field size, but for two distinct measurement configurations: (i) an irradiation with the scintillator positioned in the field isocentre; (ii) an irradiation with the fibre going straight through the beam and the scintillator positioned approximately 20 cm outside the beam and phantom. The shift in fibre position is minimized to ensure that the optical spectra of the two channels are not changed significantly, since the chromatic removal method depends on a constant stem signal spectrum (Frelin *et al* 2005, Beierholm *et al* 2008). The dosimeter probes were calibrated at 10 cm depth, to follow the standards of the TRS-398 protocol (IAEA 2000). A water-to-solid water depth correction factor of 1.011 was applied to account for differences in electron density (Seuntjens *et al* 2005). Three consecutive measurements were used for each of the two calibration configurations.

To demonstrate the spatial resolution of our dosimeter probes in the context of small radiation fields, we used a probe of 1 mm scintillator length to measure output factors (OFs) for collimator settings from 10 cm × 10 cm down to 0.6 cm × 0.6 cm, as well as per cent depth dose (PDD) for the largest and smallest field. The OF for a given field is a measure of the dose absorbed at the field isocentre per delivered MU, relative to a reference field which is typically 10 cm × 10 cm. The OFs are normally defined at d_{max}, but to avoid electron contamination, it is common practice to perform the measurements at a larger depth, and then extrapolate to d_{max} using PDD reference measurements (Dutreix *et al* 1997). However, this cannot be done for small fields, as reference measurements are normally not available for fields smaller than 3 cm × 3 cm. In this study, the hospital reference depth was 10 cm, and therefore we conducted our OF measurements at that depth. PDD measurements were performed by moving the dosimeter slab down the stack for each measurement depth. A portal image was taken at each depth using the lead piece to improve the dosimeter–isocentre alignment. The normalization depth was 1.5 cm (d_{max}). An additional 9 cm solid water stack was added to the phantom to ensure satisfactory backscatter conditions for measurements at 20 cm depth. To assess the degree of dose underestimation due to volume averaging, dose was measured for the 0.6 cm × 0.6 cm field at d_{max} as a function of scintillator size, for scintillators of 1 mm to 10 mm length.

2.4. Additional dosimetry methods

Independent dose measurements using LiF thermoluminescence dosimeters (TLDs) were made for the out-of-field calibration configuration, to measure the out-of-field dose to the scintillator. The TLDs were subsequently read out using a Dosacus TLD-reader (Alnor Oy, Finland) at the Radiation Research Division, Risø DTU. Reference OF measurements, performed in a water tank using a waterproof standard ionization chamber (IC) of the Farmer 30006/30013 type (PTW Freiburg GmbH, Germany) were included in the OF study for verification of the MC model. These reference measurements were originally presented by Sjöström *et al* (2009). Because of large cavity volume (0.6 cm^3), the IC was however not used for fields smaller than 3 cm × 3 cm. For the volume averaging experiment, lateral profiles of the 0.6 cm × 0.6 cm field were measured at d_{max} using GAFchromic EBT2 film (Radiation Products Design Inc., USA), which was calibrated in the 1–5 Gy dose range and read out using a Canon LiDE 90 scanner and RisøScan (Helt-Hansen and Miller 2004).

2.5. Monte Carlo simulations

The OF measurements were compared with MC simulations of (i) a 1.0 mm × 1.0 mm × 1.0 mm polystyrene scintillator in a 30 cm × 30 cm × 21 cm solid water volume and

(ii) a 1.0 mm × 1.0 mm × 1.0 mm water voxel in a homogenous 30 cm × 30 cm × 21 cm water volume. For the volume averaging experiment, dose was calculated for 1–10 mm long scintillators in a 0.6 cm × 0.6 cm field at d_{max}. For MC calculations of PDD, an additional 9 cm of solid water was included to allow for sufficient backscatter conditions. The linac was modelled (Ottosson *et al* 2010) using the BEAMnrc user code (Rogers *et al* 1995 and 2009), and the MC model was commissioned for field sizes between 3 cm × 3 cm and 30 cm × 30 cm. Dose to scintillator/water was scored using DOSXYZnrc (Walters *et al* 2009) with a precision of approximately 0.5% for 10 cm × 10 cm at 10 cm depth. Collimator jaw positioning uncertainty was not evaluated, and the cladding and jacket of the scintillator probe were not included in the MC simulations. The MC data included corrections for collimator backscatter in the linac monitor chambers, in accordance with the method described by Lam *et al* (1998).

3. Results and discussion

3.1. Measurement precision

Because the number of scintillation photons detected by the ME04 system is linearly related to the dose absorbed in the scintillator, measurement precision depends on the accumulated dose. The precision of pulse-resolved dose measurements was defined as the relative standard deviation of the dose per pulse (DPP). Although a 25 MU irradiation typically consists of approximately 900 radiation pulses, we used a subset consisting of the last 500 pulses to establish a plateau value where accelerator dose rate fluctuations were minimized. In this way, the precision of individual DPP measurements was found to be 2.7% (1 SD) at 10 cm depth (approximately 0.182 mGy per pulse), using the smallest scintillator (1 mm length). The reproducibility obtained from consecutive irradiations was found to be within 0.4% (1 SD) for a 16.6 cGy accumulated dose. It should be emphasized that linac-inherent DPP fluctuations always contribute to the uncertainty of dose estimates. Measuring the target current within the 500 pulse interval revealed fluctuations of approximately 1.5% (1 SD).

The feasibility of dose-per-pulse measurements in medical dosimetry requires sufficient signal per pulse to provide high sensitivity and dosimetric precision. The DPP precision depends on the overall system throughput and therefore on the size of both detected signal contributions (A and B). Parameters such as the PMT cathode luminous sensitivity, the attenuation through the optical fibre, the scintillator size and the fibre–scintillator coupling efficiency all affect the system throughput and must all be optimized to enhance the system sensitivity and DPP precision. Depending on the scintillator length, fibre length, coupling efficiency, field size and irradiation depth, the uncertainty of DPP measurements presented in this study varied between 0.9% and 4.1% (1 SD). A clear correlation between the magnitude of the detected signal and the relative standard deviation was evident from measurements for arbitrary depths, field sizes and probes of different scintillator sizes, emphasizing the importance of optimizing the light collection efficiency through the entire dosimetry system. While the first version of the ME04 system sampled the decay of an RC circuit at 50 kHz sampling rate with several samples per pulse (Beierholm *et al* 2010), the new switched-integrator method has reduced timing errors and intrinsic voltage fluctuations of the hardware. This development has improved the measurement precision of the system by approximately a factor 2. In addition, since each synchronization pulse is only sampled once, the amount of data is reduced while maintaining the same pulse-inherent information.

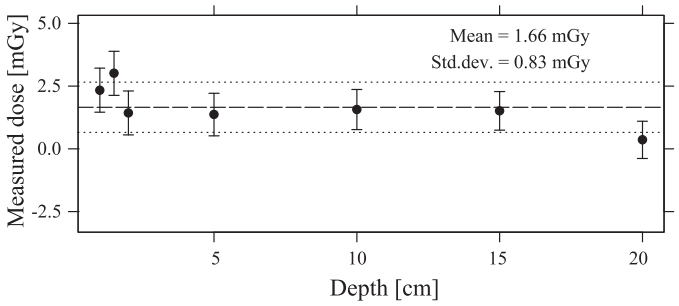

Figure 2. Measured dose versus depth for a maximal stem signal configuration of a 25 MU irradiation. Assessment of the success of stem signal removal. Only the fibre is in the beam; for an ideal dosimeter, the dose measured would be equal to the out-of-field dose at the point of measurement. Error bars (1 SD) correspond to the accumulated dose uncertainty.

3.2. Stem signal removal accuracy and calibration stability

When using fibre-coupled organic scintillators, the largest source of systematic measurement errors is the parasitic stem signal originating from the optical fibre itself. Therefore, the accuracy of such a dosimetry system is critically dependent on the ability to suppress the stem signal. If correctly calibrated, the signal contribution from the optical fibre should be completely suppressed and the dose measurements should be independent of the orientation of the optical fibre, the length of irradiated fibre, or the irradiation depth. Lambert *et al* (2009) suggested a dependence of the stem signal spectrum on the incident energy spectrum in a water phantom, and recommended that any stem signal removal procedure that relied on the constancy of the stem signal spectrum be tested as a function of depth. This test was performed and the results are shown in figure 2, where estimated dose to the scintillator is plotted against depth. The scintillator was in this case outside the main radiation field with the fibre going straight through the field. Therefore, the dose absorbed in the scintillator should be independent of the position of the fibre in the phantom. No significant deviation from the mean value was seen with depth, and the standard deviation of 0.8 mGy was comparable to the overall 0.6 mGy measurement reproducibility.

The dose to the TLDs out-of-field was measured to be 1.3 ± 0.4 mGy for a 10 cm $\times$ 10 cm field. The uncertainty on the out-of-field dose during calibration hereby induces a 0.4 mGy systematic uncertainty on dose estimates. This is not significant compared with measurement reproducibility, although measurements of doses out-of-field would be more severely affected than in-field measurements. This error is circumvented if applying the calibration configuration described in Lacroix *et al* 2008 and Beierholm *et al* 2010, which however requires irradiations at known doses at small and large field sizes.

Measurement reproducibility, calibration uncertainty and PMT temperature correction uncertainty all contribute to the overall measurement uncertainty of the ME04 system. An uncertainty budget, giving approximate values of the combined uncertainties of pulse-resolved as well as accumulated dose measurements, is presented in table 1 for a 1 mm length scintillator in a 10 cm $\times$ 10 cm field, at 1.5 and 10 cm depths.

3.3. Small static field measurements

OF measurements for 10 cm $\times$ 10 cm down to 0.6 cm $\times$ 0.6 cm fields at 10 cm depth are presented in figure 3, where they are compared with MC simulations of a scintillator in solid

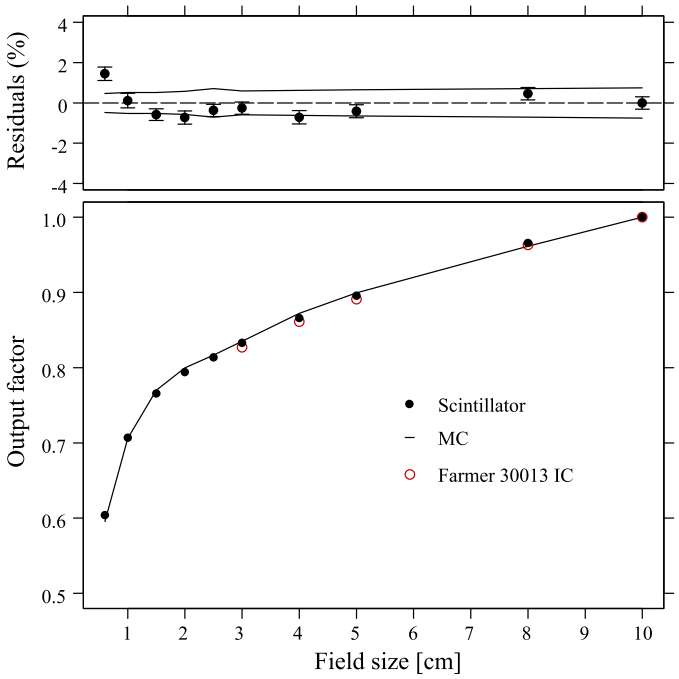

Figure 3. OF measurements for field sizes of 10 cm × 10 cm down to 0.6 cm × 0.6 cm at 10 cm depth. Filled circles: organic scintillator probes in solid water. Solid line: MC calculated dose to the scintillator in solid water. Hollow circles: reference IC measurements in water. Solid lines in residual plot represent uncertainties on MC simulations. Error bars (1 SD) correspond to the accumulated dose uncertainty.

Table 1. Uncertainty budget for pulse-resolved and accumulated dose measurements. All uncertainties are given as 1 SD.

Depth (cm)	Measurement	Delivered dose (mGy)	Reproducibility (%)	Calibration (%)	PMT (%)	Total uncertainty (%)	Total uncertainty (mGy)
1.5	Per pulse	0.277	2.13	0.17	0.10	2.14	0.006
1.5	Accumulated	250.0	0.28	0.17	0.10	0.34	0.850
10.0	Per pulse	0.182	2.72	0.26	0.10	2.73	0.005
10.0	Accumulated	166.0	0.40	0.26	0.10	0.49	0.807

water as well as to IC measurements in water. The scintillator measurements agreed with MC calculations with a maximum deviation of 1.5%. Considering the IC measurements, the scintillator measurements agreed to within 0.7%, while the MC simulations differed from the IC measurements by maximum 1.3%. An agreement within 1.4% was observed between measurements and MC calculated dose to water (plot not shown). It should be noted that the scintillator OF measurements also compared well with the ones recently presented by Klein *et al* (2010).

PDD measurements for the 10 cm × 10 cm and 0.6 cm × 0.6 cm fields are presented in figure 4, for depths of 1 cm down to 20 cm. For both field sizes, measured dose to the scintillator is compared with MC calculated dose. For the 10 cm × 10 cm field, measurements agreed with MC simulations to within 0.9%. For the 0.6 cm × 0.6 cm field, most measurements

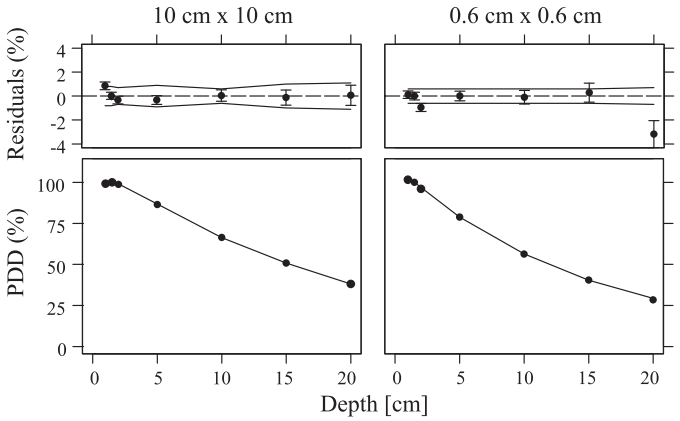

Figure 4. PDD measurements for an organic scintillator probe in solid water for 10 cm × 10 cm field size (left), and for 0.6 cm × 0.6 cm field size (right). Solid line: MC simulated dose to the scintillator in solid water. Solid lines in residual plot represent uncertainties on MC simulations. Error bars (1 SD) correspond to the accumulated dose uncertainty.

were within 0.9% agreement with MC while the measurement at 20 cm depth displayed a 3.2% lower PDD value compared with MC. Similarly, the measurements agreed within 1.8% with MC-simulated PDD for water, except for the measurement at 20 cm depth which was 5.0% too low compared with MC (plot not shown). The discrepancy at 20 cm depth was likely caused by erroneous probe–isocentre alignment, as a probe in solid water is hard to align with the field isocentre compared with a probe in a water tank for small fields, especially at large depths. Measurements using radiochromic film as well as MC simulations suggested that a misalignment between the scintillator and the beam isocentre of 1 mm in either direction leads to a dose underestimation of approximately 6%.

The volume averaging effect was examined by using scintillators of 1–10 mm lengths to measure isocentre dose as a function of dosimeter size in a 0.6 cm × 0.6 cm field at d_{max}. The measurements were compared with MC calculations and radiochromic film measurements, and are shown in figure 5. The insert of figure 5 shows the lateral dose profile of the field, measured with radiochromic film. For a 1 mm long scintillator, the dose estimate is averaged over a 1 mm interval around the central axis of the field profile; for a longer scintillator, the dose is averaged over a larger area and the peak dose is underestimated accordingly. The use of scintillators longer than 2 mm was found to induce a dose underestimation of 2% or higher. The use of dosimeters this large is therefore strongly discouraged in small field dosimetry, since the enhancement in signal magnitude and precision comes at the expense of systematic measurement errors due to volume averaging. Large discrepancies between the scintillator, MC and film are evident when the dosimeter is comparable to or much larger than the size of the field. For lengths shorter than 5 mm, the OF estimates obtained with the scintillator, film and MC agree within 2.1%.

3.4. Pulse-resolved measurements

Figures 6(a) and (b) show an example of DPP measurements for the first 20 gun pulses of beam delivery, performed using two probes at 10 cm and 20 cm depth. Part (a) shows the response of the probe at 10 cm depth for the first 20 gun pulses of beam delivery. For each synchronization pulse, the response of the scintillator is compared with the measured target

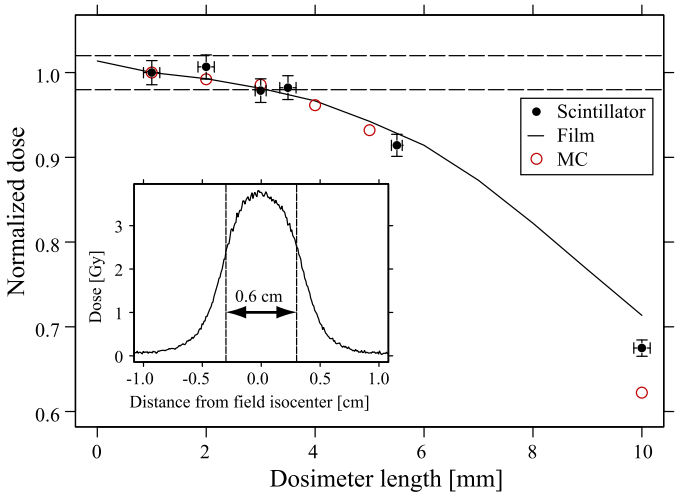

Figure 5. Estimated isocentre dose in a 0.6 cm × 0.6 cm field at d_{max} as a function of dosimeter size. Data are normalized to values corresponding to 1 mm length. Solid circles: dose measured with organic scintillator probes in solid water. The *x* and *y* error bars are the uncertainty estimates of the scintillator length and probe–isocentre alignment, respectively. Hollow circles: MC calculated dose for a scintillator in solid water. Error bars are smaller than the symbols. Solid line: dose measured with radiochromic film. The dashed lines indicate the ±2% deviation from the normalization point. Insert: lateral dose profile of the 0.6 cm × 0.6 cm field, measured with radiochromic film subjected to a 500 MU irradiation at d_{max}.

current, which has been normalized to the same scale as the measured mean DPP. Every second measurement yields zero DPP because the pulse repetition frequency (dose rate) is half of the maximum value, meaning that there is no gun pulse for every second synchronization pulse. The transient behaviour is evident and comparable for both the scintillator and target current measurements. Part (b) shows the measured quality factor of the radiation beam, represented by the $TPR_{20,10}$ value, obtained from the DPP simultaneously measured using the probe at 10 cm depth and the one at 20 cm depth. The $TPR_{20,10}$ value is seen to fluctuate with a 5.8% standard deviation around a constant value of 0.667 for the first 20 pulses. For the total number of pulses a mean value of 0.666 ± 0.001 was obtained, being comparable to the expected value of 0.669 measured using a Farmer chamber (Sjöström *et al* 2009). This shows that the radiation quality of the beam can be considered constant on the per-pulse level, for the whole irradiation as well as in the transient. The transient behaviour is characteristic to the individual Varian 2300 iX linac used in this study, and is distinctively different from previous experiments performed on an older linac model (Varian 21 EX), as depicted in figure 6, part (c).

The figure shows the start-up transient (normalized DPP) for five irradiations using the 2300 iX compared with an irradiation using the 21 EX, all at 300 MU min^{-1} dose rate. The data for the 21 EX were part of the study presented in Beierholm *et al* (2010). While the 21 EX apparently reaches stable dose per pulse after 20–30 pulses, the 2300 iX reaches a stable level after merely 5–10 pulses. These measurements show a clear dosimetric difference between the linacs concerning dose rate stability, potentially influencing the accuracy of linac dose delivery for small dose segments (on the order of 1 cGy). According to Konnoff *et al* (2011), there appears to be general consensus in the literature on the under-delivering of dose for small dose segments, regardless of linac build. However, figure 6 indicates that the degree of

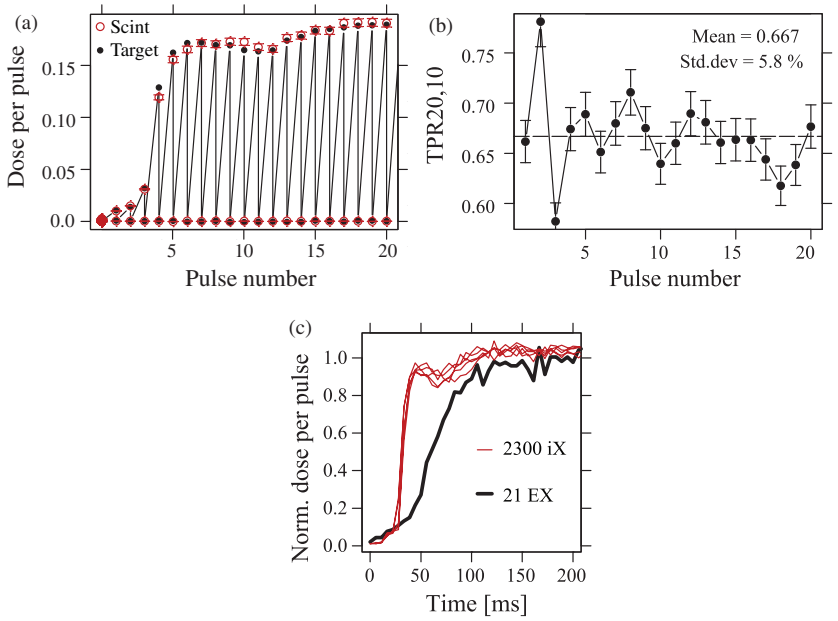

Figure 6. Transient behaviour for dose delivery at 300 MU min^{-1} dose rate. (a) DPP measured at 10 cm depth (hollow circles), with the linac target current (filled circles and lines) normalized to the mean DPP of the irradiation. (b) Measured $TPR_{20,10}$ per pulse, obtained using two scintillator probes positioned at 10 and 20 cm depth. Error bars (1 SD) correspond to the uncertainty on DPP and $TPR_{20,10}$ per pulse, respectively. (c) Transient behaviour for the Varian 2300 iX (thin lines) and a Varian 21 EX (thick line).

Table 2. Transient behaviour, number of pulses, DPP precision (1 SD), and the difference between measured and excepted DPP for irradiations at different field sizes, depths and dose rates.

Field side (cm)	Depth (cm)	Dose rate (MU min^{-1})	Total dose (Gy)	Total no of pulses	Transient no of pulses	DPP precision (%)	Meas. DPP (mGy)	Exp. DPP (mGy)	DPP diff. (%)
10.0	1.5	100	0.250	896	16	2.2	0.2792	0.2790	0.1
10.0	1.5	200	0.250	899	18	2.3	0.2784	0.2781	0.1
10.0	1.5	300	0.250	900	15	2.1	0.2773	0.2778	−0.2
10.0	1.5	400	0.250	903	17	2.2	0.2769	0.2769	0.0
10.0	1.5	500	0.250	903	15	2.3	0.2757	0.2769	−0.4
10.0	1.5	600	0.250	905	20	2.2	0.2760	0.2762	−0.1
10.0	10.0	300	0.166	903	14	2.7	0.1826	0.1823	−0.6
10.0	20.0	300	0.095	902	15	3.6	0.1052	0.1039	−0.3
0.6	1.5	300	0.175	903	11	2.3	0.1937	0.1942	−0.2
0.6	10.0	300	0.099	902	10	3.1	0.1091	0.1096	−0.4
0.6	20.0	300	0.051	903	14	4.1	0.0551	0.0577	−3.4

under-dosing is linac specific. An interesting application of the new dosimetry system would be to compare the precision of dose delivery on a pulse scale for a representative assortment of linac builds used in hospitals, not only for static beam delivery but also for small IMRT plan segments. Table 2 shows examples of beam characteristics for various dose-per-pulse values

(i.e. field sizes and depths) and pulse repetition frequencies (i.e. dose rates). The transient pulses at the start of irradiation were defined as the pulses exhibiting a dose value being lower than the mean plateau value by more than two standard deviations. For each irradiation, the expected DPP was calculated from the MC simulations of the scintillator in solid water and the total number of pulses. A small change in the total number of pulses was seen with dose rate. The DPP values for different field sizes and depths were comparable to the PDD values presented in section 3.3, confirming the correlation between pulse-resolved dose and accumulated dose.

4. Conclusion

We present a dosimetry system based on fibre-coupled organic scintillators to be used for dose measurements in dynamic and stereotactic radiotherapy. Due to 0.1 ms readout time, the system can measure the dose delivered for each individual linac radiation pulse, enabling detailed time-resolved QA of small dynamic radiotherapy dose increments. The presented system configuration measures the absorbed dose with an uncertainty within 2.7% per pulse and within 0.5% for the accumulated dose (1 SD) at 10 cm $\times$ 10 cm field size and 10 cm depth. No significant discrepancies were found between measurements and MC simulations for field sizes down to 0.6 cm $\times$ 0.6 cm. The significance of the pulse-resolution capability of the system can be further explored by comparing the fluctuations in dose rate during irradiations for different linacs and beam energies, and ultimately by performing pulse-resolved QA of gated 4D radiotherapy and IMRT segments. This study therefore shows that the system presents a suitable and promising choice for reference dosimetry and quality assurance in advanced radiotherapy.

Acknowledgments

This work was supported by the Danish Cancer Society and CIRRO—Center for Interventional Research in Radiation Oncology, supported by the Lundbeck Foundation. The hardware used for the MC calculations was donated by the Toyota Foundation, Denmark.

References

Archambault L, Briere T M, Pönisch F, Beaulieu L, Kuban D A, Lee A and Beddar A S 2010 Toward a real-time *in vivo* dosimetry system using plastic scintillation detectors *Int. J. Radiat. Oncol. Biol. Phys.* **78** 280–7

Beddar A S, Kinsella T J, Ikhlef A and Sibata C H 2001 A miniature 'scintillator-fiberoptic-PMT' detector system for the dosimetry of small fields in stereotactic radiosurgery *IEEE Trans. Nucl. Sci.* **48** 924–8

Beierholm A R, Andersen C E, Lindvold L R and Aznar M C 2010 Investigation of linear accelerator pulse delivery using fast organic scintillator measurements *Radiat. Meas.* **45** 668–70

Beierholm A R, Andersen C E, Lindvold L R, Kjaer-Kristoffersen F and Medin J 2008 A comparison of BCF-12 organic scintillators and Al_2O_3:C crystals for real-time medical dosimetry *Radiat. Meas.* **43** 898–903

Cheng C-W, Cho S H, Taylor M and Das I J 2007 Determination of zero-field size percent depth doses and tissue maximum ratios for stereotactic radiosurgery and IMRT dosimetry: comparison between experimental measurements and Monte Carlo simulation *Med. Phys.* **34** 3149–57

Chow J C L, Seguin M and Alexander A 2005 Dosimetric effect of collimating jaws for small multileaf collimated fields *Med. Phys.* **32** 759–65

Das I J, Ding G X and Ahnesjö A 2008 Small fields: nonequilibrium radiation dosimetry *Med. Phys.* **35** 206–15

Dutreix A, Bjärngard B E, Bridier A, Mijnheer B, Shaw J E and Svensson H 1997 Monitor unit calculation for high energy photon beams *Physics for Clinical Radiotherapy Booklet* 3 (Brussels: European Society for Therapeutic Radiology and Oncology)

Fontbonne J-M *et al* 2002 Scintillating fiber dosimeter for radiation therapy accelerator *IEEE Trans. Nucl. Sci.* **49** 2223–7

Frelin A-M, Fontbonne J-M, Ban G, Colin J, Labalme M, Batalla A, Isambert A, Vela A and Leroux T 2005 Spectral discrimination of Cerenkov radiation in scintillating dosimeters *Med. Phys.* **32** 3000–6

Helt-Hansen J and Miller A 2004 RisøScan—a new dosimetry software *Rad. Phys. Chem.* **71** 361–4

IAEA 2000 Absorbed dose determination in external beam radiotherapy: an international code of practice for dosimetry based on standards of absorbed dose to water *Technical Report Series* No. 398 (Vienna: International Atomic Energy Agency)

Illemann J 2009 Single-pulse-resolved dosimetry with miniaturized detectors in teletherapy *IFMBE Proc.* **25** 932–5

IPEM 2010 Small field MV photon dosimetry *IPEM Report* No. 103 (York: Institute of Physics and Engineering in Medicine)

Klein D M, Taylor R C, Archambault L, Wang L, Therriault-Proulx F and Beddar A S 2010 Measuring output factors of small fields formed by collimator jaws and multileaf collimator using plastic scintillation detectors *Med. Phys.* **37** 5541–9

Konnoff D C, Plant T K and Shiner E 2011 SSPM based radiation sensing: preliminary laboratory and clinical results *Radiat. Meas.* **46** 76–87

Lacroix F, Archambault L, Gingras L, Guillot M, Beddar A S and Beaulieu L 2008 Clinical prototype of a plastic water-equivalent scintillating fiber dosimeter array for QA applications *Med. Phys.* **35** 3682–90

Lacroix F, Beaulieu L, Archambault L and Beddar A S 2010 Simulation of the precision limits of plastic scintillation detectors using optimal component selection *Med. Phys.* **37** 412–8

Lam K L, Muthuswamy M S and Ten Haken R K 1998 Measurement of backscatter to the monitor chamber of medical accelerators using target charge *Med. Phys.* **25** 334–8

Lambert J, Yin Y, McKenzie D R, Law S and Suchowerska N 2009 Cerenkov light spectrum in an optical fiber exposed to a photon or electron radiation therapy beam *Appl. Opt.* **48** 3362–7

Lambert J, Yin Y, McKenzie D R, Law S H, Ralston A and Suchowerska N 2010 A prototype scintillation dosimeter customized for small and dynamic megavoltage radiation fields *Phys. Med. Biol.* **55** 1115–26

Létourneau D, Pouliot J and Roy R 1999 Miniature scintillating detector for small field radiation therapy *Med. Phys.* **26** 2555–61

Mountford J, Porrovecchio G, Smid M and Smid R 2008 Development of a switched integrator amplifier for high-accuracy optical measurements *Appl. Opt.* **47** 5821–8

Ottosson R O, Karlsson A and Behrens C F 2010 Pareto front analysis of 6 and 15 MV dynamic IMRT for lung cancer using pencil beam, AAA and Monte Carlo *Phys. Med. Biol.* **55** 4521–33

Rogers D W O, Faddegon B A, Ding G X, Ma C-M, Wei J and Mackie T R 1995 BEAM: a Monte Carlo code to simulate radiotherapy treatment units *Med. Phys.* **22** 503–24

Rogers D W O, Walters B and Kawrakow I 2009 BEAMnrc users manual *NRCC Report* PIRS-0509(A)revK http://irs.inms.nrc.ca/software/beamnrc/documentation/pirs0509/pirs0509.pdf

Scott A J D, Nahum A E and Fenwick J D 2008 Using a Monte Carlo model to predict dosimetric properties of small radiotherapy photon fields *Med. Phys.* **35** 4671–84

Seuntjens J, Olivares M, Evans M and Podgorsak E 2005 Absorbed dose to water reference dosimetry using solid phantoms in the context of absorbed-dose protocols *Med. Phys.* **32** 2945–53

Sjöström D, Bjelkengren U, Ottosson W and Behrens C F 2009 A beam-matching concept for medical linear accelerators *Acta Oncol.* **48** 192–200

Vassiliev O N, Titt U, Pönisch F, Kry S F, Mohan R and Gillin M T 2006 Dosimetric properties of photon beams from a flattening filter free clinical accelerator *Phys. Med. Biol.* **51** 1907–17

Walters B, Kawrakow I and Rogers D W O 2009 DOSXYZnrc users manual *NRCC Report* PIRS-794revB http://irs.inms.nrc.ca/software/beamnrc/documentation/pirs794.pdf

D

PAPER IV

Appendix D is a paper submitted for publication in Radiation Measurements in 2012. The need for additional correction factors for alanine dosimetry in small field photon beams is investigated using MC.

Energy and perturbation correction factors for alanine dosimetry in small, MV photon radiotherapy beams

Rickard O Ottosson†‡[1], Claus E Andersen† Claus F Behrens‡, and Jakob Helt–Hansen†

† *Center for Nuclear Technologies, Technical University of Denmark, Risø Campus Build. 201, Roskilde, Denmark*

‡ *Copenhagen University Hospital Herlev, Department of Oncology (R), Division of Radiophysics (52AA), Herlev, Denmark*

Abstract

The EPR signal of an alanine dosimeter is typically converted to dose by using a reference spectrum. Spectral differences might necessitate correction factors. In this study, the need for energy and perturbation correction factors in small field dosimetry of MV photon beams were investigated by means of Monte Carlo simulations. The intrinsic dependencies of the detector material alone rather than that of the entire dosimetry system was studied.

DOSRZnrc was employed to score the dose to an alanine voxel ($\overline{D}_{alan}$) in an otherwise homogeneous water phantom with an outer radius of 20 cm. The ratio of volume averaged doses, $f \equiv \overline{D}_{alan}/\overline{D}_{H_2O}$, was studied for three situations: as a function of the field diameter (i), as a function of the detector size (ii) and as a function of depth for a large field (iii).

A correction factor of $f \approx 0.98$ was found for most situations. However, as the field diameter approached the detector diameter the correction factor increased. The same effect was found for very shallow depths (< 1 cm) for a 10 cm diameter field.

The results of this study illustrates that f is constant for a large range of field sizes, detector sizes and depths. However, as the field size becomes of the order of the detector size or the field size becomes very small (e.g. a diameter of 0.5 cm) this breaks down.

The range of siutations exhibiting a constant f is likely to be sufficient

[1]To whom correspondence should be addressed (riot@risoe.dtu.dk)

for most applications in radiation therapy. Thus, only in extreme cases are f of concern in dosimetry for radiotherapy and in those cases can f potentially be determined by Monte Carlo simulations.

Keywords: alanine, small field, correction factor, Monte Carlo

1. Introduction

Alanine/EPR has been suggested as a suitable system for radiotherapy dosimetry ((Anton, 2005, 2006)), in particular, for non–reference situations, such as for small field sizes and composite beam delivery (e.g. IMRT and VMAT). The appealing features of alanine are close–to–water equivalent interaction properties, dose linearity up to the kGy range, small energy and dose rate dependence, limited influence of environmental factors, non destructive read out, and small size. The EPR signal from the detector irradiated with an unknown dose is related to dose to water through a calibration curve obtained by measuring the EPR signal from detectors irradiated to known doses in a large ^{60}Co field under conditions of CPE. Sanches-Doblado et al. (2003) demonstrated that the beam energy spectrum are significantly different for small field sizes compared to a 10×10 cm^2 field size situation. For small field sizes, lateral CPE does not even exist along the CAX and Li et al. (1995) found that it requires a field diameter of at least 2.6 cm to have lateral CPE along the CAX in a 6 MV photon beam. The photon spectrum emitted by the linac will also differ between small and large field sizes due to differences in scatter contribution (Sanches-Doblado et al., 2003). Moreover, the perturbation on the field by the detector itself becomes increasingly important with decreasing field size (Das et al., 2008). The energy dependence of alanine in the MV photon range has been studied previously (Waldeland and Malinen (2011); Anton et al. (2008); Bergstrand et al. (2003); Zeng et al. (2004)), but the studies have been limited to situations under which reference conditions apply (i.e. large fields, high dose, low gradient, CPE), which may not be the case in IMRT and small fields.

In small–field MV photon beam dosimetry (e.g. output factor measurements), the general aim is to determine the absorbed dose, D, at a single mathematical point. Alanine detectors, however, have a finite size and they therefore provide an average dose over the detector volume, $\overline{D}$ (Aspardakis et al., 2010). For large, homogeneous irradiation fields, D and $\overline{D}$ are identical, but for small fields, correction factors are needed to estimate D from

$\overline{D}$. The volume averaging effect can be eliminated if the detector is made sufficiently small or if the EPR–spectrometer only reads parts of the detector signal (Anton et al., 2011).

The purpose of this study was to use Monte Carlo (MC) simulations in order to investigate the effect of the perturbation and the energy response of alanine for dosimetry in small 6 MV photon beams as function of detector and field size and depth. The prime quantity of interest is the ratio of the volume–averaged dose to the alanine detector versus the volume–average dose over a voxel of water of the same size as the detector ($f \equiv D_{alan}/D_{H_2O}$).

2. Material and Methods

2.1. Alanine Probes

Harwell alanine probes (batch AM 576C) were considered as these are used by the authors for dose measurements. The nominal composition of Harwell alanine probes (90.9% L–α–alanine and 9.1% parrafin binder) were processed through EGSnrc (Kawrakow (2000a), Kawrakow (2000b)) to compute interaction cross sections. The density was determined by weighing and measuring 15 probes from the same batch and found to be ρ=1.24 gcm^{-3}.

2.2. Monte Carlo Simulation

DOSRZnrc was employed to score the dose to an alanine voxel ($\overline{D}_{alan}$) in an otherwise homogeneous water phantom with an outer radius of 20 cm. Each simulation geometry was reproduced for a homogeneous water phantom, using the same dimensions, and thereby obtaining the dose to water, $\overline{D}_{H_2O}$. Thus, the doses scored are averaged over the same volume. The center of the alanine/H_2O voxel, where the dose was recorded, was located at a depth of 10 cm on the central axis. The 6 MV photon spectrum previously published by Mohan et al. (1985) was used as the input for the simulation throughout the study. The advantage of using this spectrum is that it is well documented and public available as it is distributed with EGSnrc. Moreover it is computationally efficient to use a spectrum file, rather than a phase space file and/or a beam treatment head simulation, as input to DOSRZnrc. The spectrum in question corresponds to the bremsstrahlung spectrum for a 10×10 cm^2 field emitted by a Varian Clinac (in 6MV mode). The spectrum file was used in combination with DOSRZnrc source 0 (i.e. parallel beam incident from the front). The number of histories were chosen so that the statistical uncertainty was no larger than 0.4% in the voxel of interest. The

only variance reduction turned on was photon forcing (for the first generation particles only) and cut off energies were 521 keV (including rest mass) and 10 keV for electrons and photons, respectively.

3. Results

The ratio of volume averaged doses $f \equiv \overline{D}_{alan}/\overline{D}_{H_2O}$ was studied as function of the field diameter for two different detector sizes i.e. with detector diameter (ø) and height (h): (ø,h)=(5,2.5) mm and (ø,h)=(1,2.5) mm, respectively (figure 1). A correction factor of $f \approx 0.98$ is needed to correct $\overline{D}_{alan}$ to $\overline{D}_{H_2O}$ for fields with a diameter of ≈ 1 cm and above for both detector sizes. However, f increases more rapidly for the larger detector as the field diameter decrease below 1 cm, e.g. $f \approx 1.03$ and $f \approx 1.00$ for a field diameter of 0.5 cm for the larger and smaller detector, respectively.

In order to further study the dependency of f on field– and detector size, f was evaluated for a range of detector sizes for three field diameters: 0.5, 1.0, 4.0 cm (figure 2). For the two largest fields $f \approx 0.98$ for all detector sizes except, possibly, for the smallest detector (ø=1 mm). However, for the smallest field size (0.5 cm) f increases with the detector diameter, illustrating that the detector needs to be very small for such a small field size.

In order to evaluate whether f is depth dependent, f was evaluated as a function of depth for a 10 cm diameter field and a detector size of (ø,h)=(5,2.5) mm (figure 3). f is fairly constant for depths $\geq$1 cm, but deviates for shallower depths. A correction factor of 0.9779($\pm$0.0067)[1] was found for depths $\geq$1 cm. A ratio of volume averaged doses of 0.9779 is on the order of what to be expected when looking at alanine/water restricted mass stopping power ratios and mass energy absorbtion coefficient ratios.

A depth independent detector is a much desired feature as measurements may be conducted at any depth without additional considerations. Depth invariance is to be expected as alanine is rather water equivalent. For the shallowest depth, however, f was ≈ 1.01. This might be due to the substantially different energy spectrum at such a shallow depth. The result may not be accurate as contaminating electrons, which contribute to the dose at shallow depths, were omitted in the simulation. The impact of contaminating electrons on f for shallow depths was not further studied.

[1]The reported uncertainty is the standard deviation of the average value for depths $\geq$1 cm.

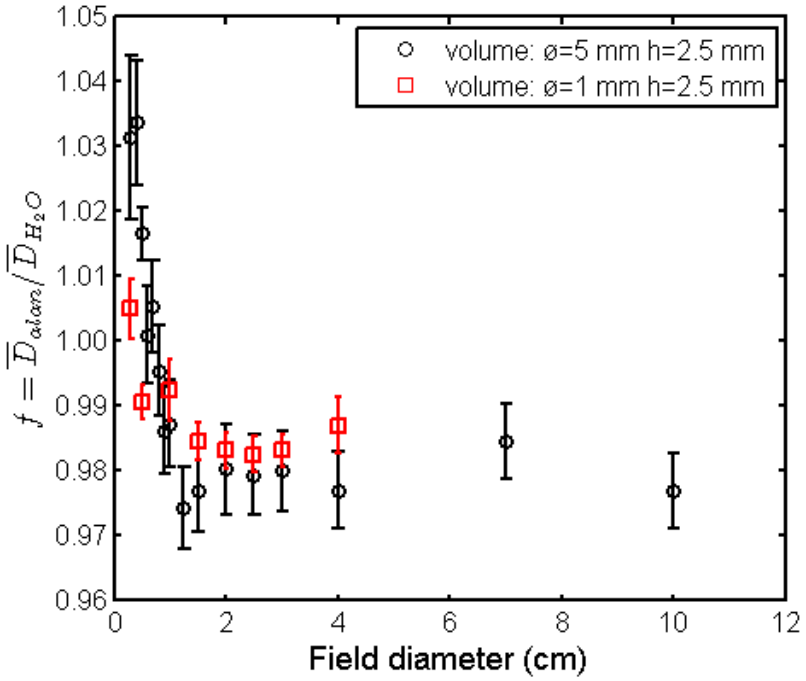

Figure 1: The ratio of volume averaged doses, f, as function of field diameter for two detector sizes. $f \approx 0.98$ for fields with a diameter of ≈ 1 cm and above. Error bars are the combined statistical uncertainty of the MC simulations.

4. Discussion

If alanine is to be used as a detector for radiotherapy the correction factor f needs to be constant or its variation known. Obviously, in the ideal case f is constant and thus calibrated out of the equation and one does not need to think further thereof. Second best, is that its variation as function of e.g. field size and detector size is known. The results of this study illustrates that f is constant for a large range of field sizes, detector sizes and depths. However, as the field size becomes of the order of the detector size or the field size becomes very small (e.g. a diameter of 0.5 cm) this breaks down. The detector cannot be made infinitely small. One practical obstacle is that the handling of the detector becomes cumbersome if it is too small and further the signal to noise ratio gets lower as the detector becomes smaller. However,

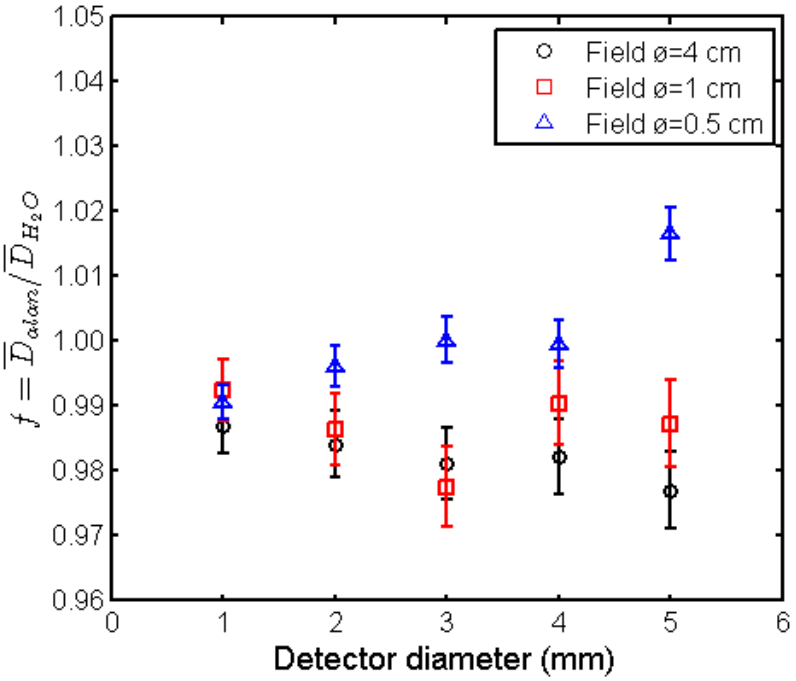

Figure 2: The ratio of volume averaged doses, f, as function of detector diameter (ø) for three field sizes. f is fairly constant over the range of detector sizes for the larger two field sizes whereas this does not hold true for the smallest field size. Error bars are the combined statistical uncertainty of the MC simulations.

a detector size of (ø,h)=(5,2.5) mm is easily handled and as illustrated f is constant down to field sizes of the order of ø=1 cm for such a detector size. This will most likely be sufficient for most applications within radiotherapy. Even for field sizes of this order, and certainly for smaller field sizes, other problems arise anyhow such as position inaccuracies of the detector in the beam. For instance, Beierholm et al. (2011) states that a 1 mm misalignment between the isocenter and a 1 mm wide scintillator probe for a 0.6×0.6 mm^2 square field leads to a dose measurement error (at 20 cm's depth) in the order of 6%.

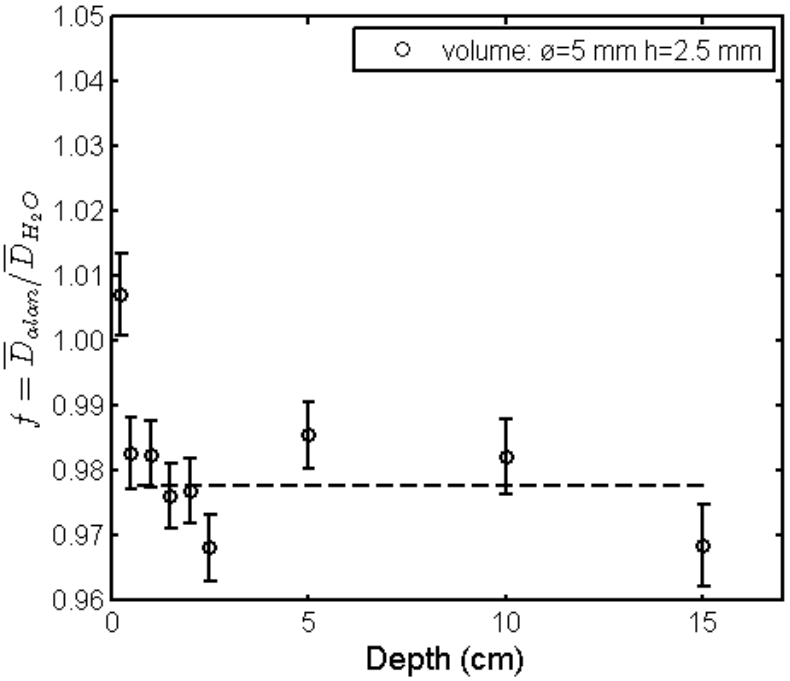

Figure 3: The ratio of volume averaged doses, f, as function of depth (d) for a field with a diameter of 10 cm and detector size (ø,h)=(5,2.5) mm. The ratio of volume averaged doses, f, was fairly constant at depths $\geq$1 cm, with an average of ≈ 0.98. For the shallowest depth (0.5 cm), a value of ≈ 1.01 was needed in order to correct $\overline{D}_{alan}$ to $\overline{D}_{H_2O}$. Error bars are the combined statistical uncertainty of the MC simulations. The average f for $1 \leq d \leq 15$ cm is included in the figure (dashed line).

5. Conclusions

This work demonstrates that f is constant for a large range of depths, detector– and field sizes. This range is sufficient for most applications in radiation therapy. Thus, only in extreme cases are f of concern in dosimetry for radiotherapy and in those cases can f potentially be determined by Monte Carlo simulations.

6. Acknowledgements

This project was granted by The Danish Cancer Society and supported by CIRRO - The Lundbeck Foundation Center for Interventional Research in Radiation Oncology and The Danish Council for Strategic Research. The hardware used for the MC calculations was donated by Toyota-Fonden, Denmark.

References

Anton, M., 2005. Development of a secondary standard for the absorbed dose to water based on the alanine EPR dosimetry system. Appl Radiat Isot 62, 779–795.

Anton, M., 2006. Uncertainties in alanine/ESR dosimetry at the physikalisch–technische bundesanstalt. Phys Med Biol 51, 5419–5440.

Anton, M., Hackel, T., Rouijaa, M., von Voigts-Rhetz, P., 2011. Measurements in small fields using alanine/ESR, Presented at the 2011 Conference on Advanced Metrology for Cancer Therapy, Braunschweig, Germany.

Anton, M., Kapsch, R., Kyrstek, M., Renner, F., 2008. Response of the alanine/esr dosimetry system to mv x–rays relative to ^{60}co radiation. Phys Med Biol 52, 2753–2770.

Aspardakis, M.A., Byrne, J.P., Palmans, H., Conway, J., Rossler, K., Warrington, J., Duane, S., 2010. IPEM Report 103: Small Field MV Photon Dosimetry. Institute of Physics and Engineering in Medicine, York.

Beierholm, A.R., Ottosson, R.O., Lindvold, L.R., Behrens, C.F., Andersen, C.E., 2011. Characterizing a pulse–resolved dosimetry system for complex radiotherapy beams using organic scintillators. Phys Med Biol 56, 3033–3045.

Bergstrand, E.S., Shortt, K.R., Ross, C.K., Hole, E.O., 2003. An investigation of the photon energy dependence of the epr dosimetry system. Phys Med Biol 48, 1753–1771.

Das, I.J., Ding, G.X., Ahnesjö, A., 2008. Small fields: Nonequilibrium radiation dosimetry. Med Phys 35, 206–597.

Kawrakow, I., 2000a. Accurate condensed history monte carlo simulation of electron transport. I. EGSnrc, the new EGS4 version. Med Phys 27, 485–498.

Kawrakow, I., 2000b. Accurate condensed history monte carlo simulation of electron transport. II. application to ion chamber response simulations. Med Phys 27, 499–513.

Li, X.A., Soubra, M., Szanto, J., Gerig, L.H., 1995. Lateral electron equilibrium and electron contamination in measurements of head-scatter factors using miniphantoms and brass caps. Med Phys 22, 499–513.

Mohan, R., Chui, C., Lidofsky, L., 1985. Energy and angular distributions of photons from medical linear accelerators. Med Phys 12, 592–597.

Sanches-Doblado, F., Andreo, P., Capote, R., Leal, A., Perucha, M., Arrans, R., Nunez, L., Mainegra, E., Lagares, J.I., Carrasco, E., 2003. Ionization chamber dosimetry of small photon fields: a monte carlo study on stopping–power rations for radiosurgery and imrt beams. Phys Med Biol 48, 2081–2099.

Waldeland, E., Malinen, E., 2011. Review of the dose–to–water energy dependence of alanine and lithium formate epr dosimeters and lif tl–dosimeters e comparison with monte carlo simulations. Radiat Meas 46, 945–951.

Zeng, G.G., McEwen, M.R., Rogers, D.W.O., Klassen, N.V., 2004. Monte carlo investigation of the energy dependence of alanine/epr dosimetry: I. clinical x–ray beams. Phys Med Biol 49, 257–270.

E

PREPARATORY STUDY COMPARING MCTP TO CLINICAL DOSE CALCULATION ALGORITHMS

A preparatory study using the workflow, as described in Chapter 6, was conducted for ten palliative lung cancer patients, in which MC computed dose distribution was compared to that generated by clinically available dose calculation algorithms. However, the MC model used was not identical to that described in Chapter 3. The error introduced by using a non–optimal MC model is not accounted for. Phantoms were created using the HU–to–density–relationship given in Kawrakow et al. [1996], rather than one obtained for the CT scanner used. Moreover, no specific considerations were made to the voxels outside of the patient external outline, as is done by the TPS. Errors due to improper patient modeling are also not considered.

E.1 INTRODUCTION

PB dose calculation is frequently used for lung cancer treatment planning. If PB based treatment plans generated with high and low energy (e.g. 15 MV or 18 MV and 4 MV or 6 MV, respectively) are compared, the ones based on the higher energies will in many cases appear more favorable. However, it is well known that the inaccuracies introduced by the PB dose calculation generally are larger for higher energies and depend on several parameters such as field size and geometry (e.g. [Behrens, 2006], [Klein et al., 1993], [Tsiakalos et al., 2006], [Vanderstraeten et al., 2006], [Krieger and Sauer, 2005]). Therefore, usually low energy is chosen as default for lung treatments. This begs the question whether this always is the best choice. For some cases, treatment plans based on higher energies may be more favorable. In order to address this question, more accurate dose calculation methods (e.g. MC) must be employed. PB and a more sophisticated superposition/convolution algorithm, AAA, were compared to MC–based dose calculations clinical IMRT and AP–PA lung treatments.

E.2 MATERIAL AND METHODS

All patients previously treated with AP–PA 6 MV irradiation based on PB dose calculation at the Copenhagen University Hospital, Herlev. All patients were planned to a total of 25 Gy to the normalization point delivered in five fractions. For each patient a treatment plan for 15 MV was generated based on the 6 MV treatment plan. All treatment plan geometries were kept the same including field sizes, MLC and

collimator rotations. Only the beam energy were changed to 15 MV and the plan recalculated with the PB algorithm giving the same dose to the prescription point as for the 6 MV plan (i.e. 5 Gy×5). Both the 6 and 15 MV treatment plans were recalculated with the AAA using identical MLC settings and monitor units. Dose calculation was conducted using Varian Eclipse build 8.2.24.10720 (Varian Medical Systems, Inc. Palo Alto, CA, USA) modeling a Varian 2300 iX (Varian Medical Systems, Inc., Palo Alto, CA, USA). Except for special cases only the patient outline is delineated for palliative lung treatments at our institution. Therefore a GTV, the esophagus, the lungs, and the spinal cord were delineated retrospectively for this study by a radiation oncologist with specialized knowledge in lung radiation therapy.

When it comes to target coverage, generally, a PTV generated by adding a symmetric or asymmetric margin to the GTV or CTV is the most interesting volume to study for curative patients. However, for palliative patients this may not be the case. For the patients in this study the delineated GTV is the volume of primary interest. There is no CTV as microscopic spread is not of primary concern. Obviously, in order to cover the GTV some margin must be added to adequately take systematic and random positional errors, beam penumbra and organ motion into account (e.g. Ottosson, Baker, Hedman, Behrens and Sjöström [2010]). Such a margin is added in the sense that the field size is always made 1-2 cm larger (in all directions) than what is considered the visual target on the CT.

All algorithms (PB, AAA and MC) used identical setups for each treatment plan and all differences in the resulting dose distributions were solely due to discrepancies between the dose calculation algorithms. Throughout this study MC is considered the golden standard or "ground truth". Unless explicitly stated all references to dose distributions or dose differences are based on the MC calculations.

E.3 RESULTS AND DISCUSSION

In general, the GTV coverage was better for the 15 MV plans and the dose was more homogeneous i.e. for the 6 MV plans the minimum dose to the GTV was lower and the maximum dose to the GTV was higher. These trends were also reflected in the PB and AAA calculations (Figure 84). However, the calculated dose to the prescription point (Table 19) varied between the algorithms and resulted in shifts of the DVHs to higher and lower dose levels. Compared to PB a higher dose to the prescription point was calculated by MC in eight and six (out of the ten) treatment plans for 15 MV and 6 MV, respectively. On average there was close agreement between the algorithms in the prescription point dose with a maximum deviation of 3.2% (Table 19).

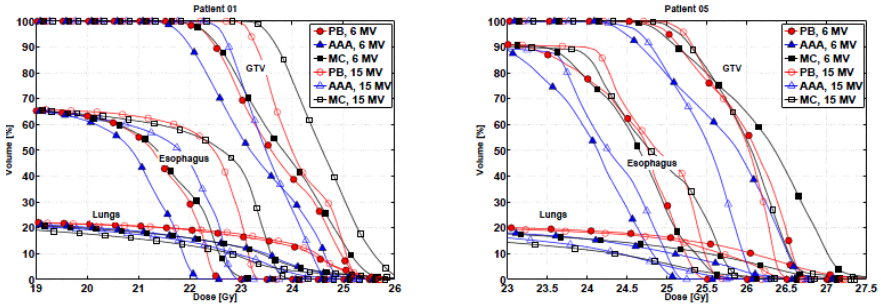

Figure 84: DVH (GTV, esophagus, and total lung volume) for patients 01 and 05 to the left and right, respectively. MC was used as ground truth. The dose to the GTV was more homogeneous for 15 MV (as compared to 6 MV). For the esophagus more dose was delivered utilizing 15 MV. These trends were also reflected in the PB and AAA calculations. The dose to the lungs were lower for 15 MV. This was reflected in the AAA calculations but not in general predicted by PB.

In the border regions between tissues of different density there will be build up and –down effects. For instance, if a beam passes though the series of tissues: lung – tumor – lung, there will be a build up effect in the more dense tumor tissue at the proximal (entrance) side and a much smaller build down in the tumor at the distal (exit) side of the tumor. These effects are more pronounced for higher energies. Thus, it might be anticipated that a small part of the GTV would be underdosed by the higher energy as compared to the lower energy. However, as seen above this was not the case. In order to investigate the reasons for this the AP–PA profiles through the normalization point (Norm. point) for patient 01 were examined (Figure 85). Based on both PB, AAA and MC it was clear that the dose to the lung was lower for 15 MV than for 6 MV along this profile. For the PB and AAA calculations the dose to the GTV was very similar for 6 MV and 15 MV, though sightly more homogeneous for 15 MV. However, the MC calculations clearly showed a better and slightly more homogeneous GTV coverage for 15 MV (Figure 85A).

The build up effect on the anterior part of the GTV for the AP beam for 15 MV was larger than for 6 MV. However, this was counter balanced by a higher dose in the same volume from the PA beam for 15 MV as compared to 6 MV (close to X, Figure 85B). Similar, for the posterior part of the GTV the build up effect of the 15 MV PA beam was counter balanced by the higher dose of the AP beam as compared to 6 MV. At the same time the build down effect was negligible. Therefore, for 15 MV there was not a small part of the GTV that received less dose as compared to 6 MV. For patient 01 there was a small volume containing both lung tissue and more dense soft tissue close the anterior border of the GTV (between V and X, Figure 85).

Table 19: AAA and MC calculated dose to the prescription point as percentage of the prescribed dose (all PB calculations resulted in 100% to the precription point).

Dose [%]	6MV		15MV	
Patient	AAA	MC	AAA	MC
01	97.8	100.2	97.9	102.6
02	99.2	101.3	99.1	100.9
03	99.2	101.2	99.4	100.3
04	100.3	101.8	99.7	101.5
05	97.7	100.5	98.1	99.7
06	100.3	97.8	100.4	100.7
07	96.8	99.9	97.4	100.9
08	99.0	102.1	98.2	100.9
09	101.9	99.9	100.5	101.4
10	98.5	98.6	97.4	98.7
Interval	[96.8;101.9]	[97.8;102.1]	[97.4;100.5]	[98.7;102.6]
Average	99.1	100.3	98.8	100.8

This may enhance the dose in the anterior part of the GTV slightly. Considering this volume as part of the GTV corresponds to a "very bad scenario" for utilizing 15 MV. However, even in this case, the dose for 15 MV was higher than for 6 MV along the studied profile (Figure 85A assuming the GTV to be between V and Y).

For patients 02, 09 and 10 the dose to the esophagus is irrelevant since the esophagus is not within the irradiated volume. For all other patients similar trends are seen as for the GTV i.e. more dose was delivered to the esophagus for the 15 MV plans. This trend was reflected in the PB and AAA calculations. However, as for the GTV, there was a shift in the calculated dose level between the algorithms (Figure 84).

In general a lower dose was delivered to the total lung volume for the 15 MV plans. This trend was reflected for AAA but not in general for PB (figure Figure 84). However, for patient 05 and 07 this trend was even reflected in the PB calculations. For the other eight patients in the study PB predicts a higher lung dose delivered by the 15 MV plans. This defect of the PB calculations is well known and expected (e.g. Ottosson, Karlsson and Behrens [2010]).

In summery the differences between the three calculation algorithms are of limited concern when it comes to the palliative patients included in this study. The AAA calculations reflect the trends in the relative differences between 15 and 6 MV plans e.g. more homogeneous dose

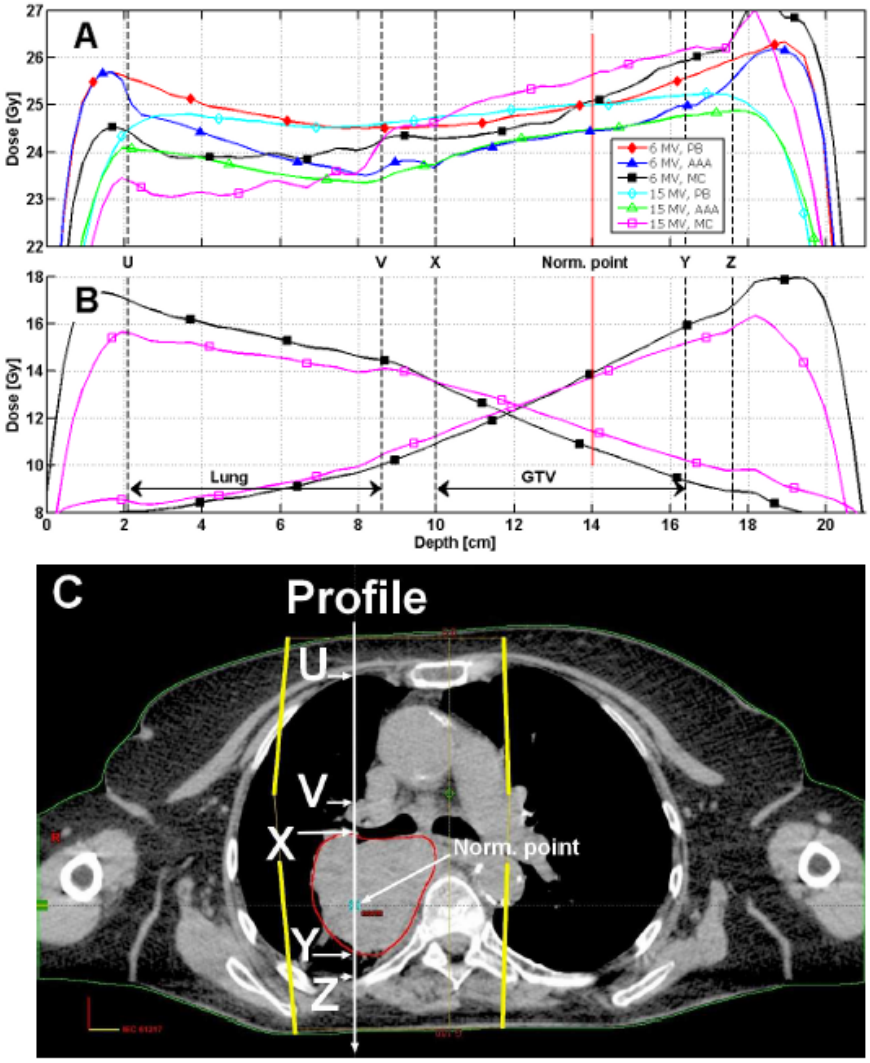

Figure 85: Profiles in the AP direction through the normalization point (Norm. point) for patient 01. In A profiles for all calculation algorithms and energies are shown. In B the profiles for the MC calculations are shown separately for each of the two beams i.e. the sum of the profiles for a given energy in B is equal to the profile for the corresponding MC profile in A. The vertical dashed lines (U, V, X, Y and Z) in A and B indicate borders between different tissue types e.g. lung, soft tissue. The corresponding points are indicated in C where also the line along which the profile is plotted is indicated. Further the Norm. point is indicated in both A, B and C. The yellow lines in C indicate the field borders and the structure drawn in read is the GTV. The little bump (higher dose) in the MC profiles at $\approx$ 18 cm depth is caused by a few voxels of bone.

to the GTV for the 15 MV plans. The same is true for PB except in the lung. The absolute dose levels are shifted and the trend is that the PB calculations actually is closer to MC than AAA except for the

lungs. However, the largest differences between the three calculation algorithms found in the ten patients were for patient 01 where the differences still is within clinical acceptable levels for the palliative patients in this study (Figure 84).

E.4 CONCLUSIONS

The 15 MV AP–PA treatment plans for the palliative lung tumor patients included in this study consistently resulted in more homogeneous target (GTV) coverage regardless of dose calculation method. This came at the expense of a higher dose to the esophagus for the patients where the esophagus was within the irradiated volume. The lung dose was also lower for 15 MV compared to 6 MV, based on AAA and MC dose calculations, but not for PB.

Based on the findings of this study, there is no reason to abandon 15 MV for AP–PA lung irradiations of the type studied. The choice whether to use 6 or 15 MV can be based on AAA or PB calculations. However, it is still advisable to use low energies as default for tumor sites involving large inhomogeneities unless a precise dose calculation algorithm is available.

The large disagreement between the analytical algorithms (PB and AAA) and MC (see Figure 85) is most likely attributed to improper calibration of the MC model and erroneous patient modeling rather than the particle transport itself. The magnitude of the error introduced was not further investigated.

BIBLIOGRAPHY

Aarup L R, Nahum A E, Zacharatou C, Juhler-Nø ttrup T, Knöös T, Nyström H k, Specht L, Wieslander E and Korreman S S 2009 *Radiotherapy and Oncology* **91**(3), 405–414.

Ahnesjö A and Aspardakis M M 1999 *Physics in Medicine and Biology* **44**(11), R99–R155.

Almond P R, Biggs P J, Coursey B M, Hanson W F, Huq M S, Nath R and Rogers D W 1999 *Medical physics* **26**(9), 1847–70.

Andreo P 1991 *Physics in Medicine and Biology* **36**(7), 891–920.

Andreo P, Burns D T, Hohlfeld K, Huq M S, Kanai T, Laitano F, Smyth V and Vynckier S 2000 *IAEA Technical Report Series No 398* .

Anton M 2005 *Applied Radiation and Isotopes* **62**(5), 779–795.

Anton M 2006 *Physics in Medicine and Biology* **51**(21), 5419–5440.

Anton M, Hackel T, Rouijaa M and von Voigts-Rhetz P 2011 Presented at the 2011 Conference on Advanced Metrology for Cancer Therapy, Braunschweig, Germany.

Anton M, Kapsch R, Kyrstek M and Renner F 2008 *Physics in Medicine and Biology* **52**(10), 2753–2770.

Arnfield M R, Siantar C H, Siebers J, Garmon P, Cox L and Mohan R 2000 *Medical Physics* **27**(6), 1266–1274.

Aspardakis M A, Byrne J P, Palmans H, Conway J, Rossler K, Warrington J and Duane S 2010 *IPEM Report 103: Small Field MV Photon Dosimetry* Institute of Physics and Engineering in Medicine, York.

Attix F H 1986 *Introduction to Radiological Physics and Radiation Dosimetry* John Wiley and Sons, New York.

Bazalova M, Beaulieu L, Palefsky S and Verhaegen F 2007 *Medical Physics* **34**(6), 2119–2131.

Bazalova M, Carrier J F, Beaulieu L and Verhaegen F 2008 *Radiotherapy and Oncology* **86**(1), 93–98.

Behrens C F 2006 *Physics in Medicine and Biology* **51**(22), 5937–50.

Beierholm A R, Ottosson R O, Lindvold L R, Behrens C F and Andersen C E 2011 *Physics in Medicine and Biology* **56**(10), 3033–3045.

Belec J, Patrocinio H and Verhaegen F 2005 *Physics in Medicine and Biology* **50**(5), 787–799.

Berendsen H J C 2011 *A Student's Guide to Data and Error Analysis* Cambridge Universtiy Press, New York.

Berger M 1993 *Monte Carlo calculation of the penetration and diffusion of fast charged particles, In: Methods in computational physics vol. I* Academic Press, New York, NY.

Bergstrand E S, Shortt K R, Ross C K and Hole E O 2003 *Physics in Medicine and Biology* **48**(12), 1753–1771.

Borges C, Zarza-Moreno M, Heath E, Teixeira N and Vaz P 2012 *Medical Physics* **39**(1), 415–423.

Boyer A, Biggs P, Galvin J, Klein E, LoSasso T, Low D, Mah K and Yu C 2001 *AAPM REPORT NO. 72* .

Bradshaw W W, Cadena D G, Crawford G W and Spetzler H A W 1962 *Radiation Research* **17**(1), 11–21.

Burlin T E 1966 *British Journal of Radiology* **39**(466), 727–734.

Bush K K 2009 Monte Carlo Dose Calculations in Advanced Radiotherapy PhD thesis University of Victoria.

Bush K and Zavgorodni S 2010 *Australasian Physical & Engineering Sciences in Medicine* **33**(4), 351–355.

Bush K, Zavgorodni S and Beckham W 2009 *Medical Physics* **36**(6), 2309–2319.

Chetty I J, Curran B, Cygler J E, DeMarco J J, Ezzell G, Faddegon B a, Kawrakow I, Keall P J, Liu H, Ma C M C, Rogers D W O, Seuntjens J, Sheikh-Bagheri D and Siebers J V 2007 *Medical Physics* **34**(12), 4818–4853.

Chetty I J, Rosu M, McShan D L, Fraass B a and Ten Haken R K 2005 *Physics in Medicine and Biology* **50**(5), 801–815.

Chibani O 2004 'On the discrepancies between Monte Carlo-based dose calculations and measurements in the buildup region of megavoltage Varian photon beams' AAPM meeting, Pittsburgh.

Chibani O, Moftah B and Ma C M 2011 *Medical Physics* **38**(1), 188–201.

Chow J C L, Wong E, Chen J Z and Van Dyk J 2003 *Medical Physics* **30**(10), 2686–2694.

Constantinou C, Harrington J and DeWerd L 1992 *Medical Physics* **19**(2), 325–327.

Craft D and Bortfeld T 2008 *Physics in Medicine and Biology* **53**(11), 2785–2796.

Das I J, Ding G X and Ahnesjö A 2008 *Medical Physics* **35**(1), 206–597.

De Smedt B, Reynaert N, Flachet F, Coghe M, Thompson M G, Paelinck L, Pittomvils G, De Wagter C, De Neve W and Thierens H 2005 *Physics in Medicine and Biology* **50**(24), 5935–5951.

Deasy J, Blanco A and Clark V 2003 *Medical Physics* **30**(5), 979–985.

Deng J, Jiang S B, Kapur A, Li J, Pawlicki T and Ma C M 2000 *Physics in Medicine and Biology* **45**(2), 411–427.

Department of Radiation Oncology, Fox Chase Cancer Center 2008 *MCSIM Users Manual*.

Devic S, Seuntjens J, Sham E, Podgorsak E B, Schmidtlein C R, Kirov A S and Soares C G 2005 *Medical Physics* **32**(7), 2245–2253.

Ding G 2002 *Physics in Medicine and Biology* **47**(7), 1025–1046.

Ding G X 2003 *Physics in Medicine and Biology* **48**(23), 3865–3874.

du Plessis F C, Willemse C A, Lötter M G and Goedhals L 1998 *Medical Physics* **25**(7), 1195–1201.

Ferreira B C, Lopes M C and Capela M 2009 *Physics in Medicine and Biology* **54**(4), 1073–1085.

Fippel M 2003 *Physics in Medicine and Biology* **48**(10), 1289–1304.

Fix M K, Stampanoni M, Manser P, Born E J, Mini R and Ruegsegger P 2001 *Physics in Medicine and Biology* **46**(5), 1407–1427.

Fix M K, Volken W, Frei D, Frauchiger D, Born E J and Manser P 2011 *Medical Physics* **38**(10), 5311–5320.

Fogliata A, Vanetti E, Albers D, Brink C, Clivio A, Knöös T, Nicolini G and Cozzi L 2007 *Physics in Medicine and Biology* **52**(5), 1363–1385.

Followill D S, Tailor R C, Tello V M and Hanson W F 1998 *Medical Physics* **25**(7), 1202–1205.

Fotina I, Kragl G, Kroupa B, Trausmuth R and Georg D 2011 *Strahlentherapie und Onkologie* **187**(7), 433–441.

Fotina I, Winkler P, Künzler T, Reiterer J, Simmat I and Georg D 2009 *Radiotherapy and Oncology* **93**(3), 645–653.

Fraass B A, Smathers J and Deye J 2003 *Medical Physics* **30**(12), 3206–3216.

Fraass B, Doppke K, Hunt M, Kutcher G, Starkschall G, Stern R and Van Dyke J 1998 *Medical Physics* **25**(10), 1773–1829.

Francescon P, Cavedon C, Reccanello S and Cora S 2000 *Medical Physics* **27**(7), 1579–1587.

Gagne I M, Ansbacher W, Zavgorodni S, Popescu C and Beckham W a 2008 *Physics in Medicine and Biology* **53**(24), 7167–7185.

Galvin J M, Smith A R and Lally B 1993 *International Journal of Radiation Oncology Biology Physics* **25**(2), 181–192.

Gay H A and Niemierko A 2007 *Physica Medica* **23**(3–4), 115–125.

Gerbi B J and Khan F M 1990 *Medical Physics* **17**(1), 17–26.

González W, Lallena a M and Alfonso R 2011 *Physics in Medicine and Biology* **56**(11), 3417–3431.

Halton J H 1970 *SIAM Review* **12**(1), 1–63.

Hartmann B, Martišikova M and Jäkel O 2010 *Medical Physics* **37**(4), 1753–1756.

Hartmann Siantar C L, Walling R S, Daly T P, Faddegon B, Albright N, Bergstrom P, Bielajew A F, Chuang C, Garrett D, House R K, Knapp D, Wieczorek D J and Verhey L J 2001 *Medical Physics* **28**(7), 1322–1337.

Hasenbalg F, Neuenschwander H, Mini R and Born E J 2007 *Physics in Medicine and Biology* **52**(13), 3679–3691.

Heath E and Seuntjens J 2003 *Physics in Medicine and Biology* **48**(24), 4045–4063.

Helt-Hansen J, Rosendal F, Kofoed I M and Andersen C E 2009 *Acta Oncologica* **48**(2), 216–222.

Hughes I G and Hase T P A 2010 *Measurements and their Uncertainties* Oxford Universtiy Press Inc., New York.

International Commission on Radiation Units and Measurements 1976 *ICRU Report 24: Determination of absorbed dose in a patient irradiated by beams of x or gamma rays in radiotherapy*.

Jaffray D A, Battista J J, Fenster A and Munro P 1993 *Medical Physics* **20**(5), 1417–1427.

Jang S Y, Vassiliev O N, Liu H H, Mohan R and Siebers J V 2006 *Medical Physics* **33**(3), 770–781.

Jeraj R, Keall P J and Siebers J V 2002 *Physics in Medicine and Biology* **47**(3), 391–407.

Jiang S B, Pawlicki T and Ma C M 2000 *Physics in Medicine and Biology* **45**(8), 2151–2161.

Kairn T, Kenny J, Crowe S B, Fielding a L, Franich R D, Johnston P N, Knight R T, Langton C M, Schlect D and Trapp J V 2010 *Medical Physics* **37**(4), 1761–1767.

Karzmark C J, Nunan C S and Tanabe E 1993 *Medical electron accelerators* McGraw–Hill Inc, York.

Kawrakow I 2000*a* *Medical Physics* **27**(3), 485–498.

Kawrakow I 2000*b* *Medical Physics* **27**(3), 499–513.

Kawrakow I 2002 *Physics in Medicine and Biology* **47**(17), 3087–3103.

Kawrakow I 2006 *Medical Physics* **33**(6), 1829–1839.

Kawrakow I, Fippel M and Friedrich K 1996 *Medical Physics* **23**(4), 445–457.

Kawrakow I and Rogers D W O 2012 'The EGSnrc code system: Monte Carlo simulations of electron and photon transport. NRCC Report PIRS–701'.
URL: *http://www.irs.inms.nrc.ca/BEAM/user_manuals/pirs701/index.html*

Kawrakow I, Rogers D W O and Walters B R B 2004 *Medical Physics* **31**(10), 2883–2898.

Kawrakow I and Watlers B R B 2006 *Medical Physics* **33**(8), 3046–3056.

Keall P, Chock L, Jeraj R, Siebers J and Mohan R 2003 *Medical Dosimetry* **28**(2), 113–117.

Keall P, Siebers J, Arnfield M, Kim J and Mohan R 2001 *Physics in Medicine and Biology* **46**(4), 929–941.

Klein E E, Chin L M, Rice R K and Mijnheer B J 1993 *International Journal of Radiation Oncology Biology Physics* **27**(2), 419–427.

Klein E E, Harms W B, Low D A, Willcut W and Purdy A 1995 *International Journal of Radiation Oncology Biology Physics* **33**(5), 1195–1208.

Knöös T, Wieslander E, Cozzi L, Brink C, Fogliata A, Albers D, Nyström H and Lassen S 2006 *Physics in Medicine and Biology* **51**(22), 5785–5807.

Krieger T and Sauer O a 2005 *Physics in Medicine and Biology* **50**(5), 859–868.

Künzler T, Fotina I, Stock M and Georg D 2009 *Physics in Medicine and Biology* **54**(24), 7363–7377.

Lam K L, Muthuswamy S and Ten Haken R K 1998 *Medical Physics* **25**(3), 334–338.

Leal A, Sánchez-Doblado F, Arráns R, Capote R, Lagares J I, Pavón E C and Roselló J 2004 *International journal of radiation oncology, biology, physics* **59**(5), 1548–1559.

Lewis R D, Ryde S J, Hancock D A and Evans C J 1999 *Physics in Medicine and Biology* **44**(5), 1219–1230.

Li J S, Lin T, Chen L, Price R a and Ma C M 2010 *Medical Physics* **37**(6), 2491–2500.

Li X A, Soubra M, Szanto J and Gerig L H 1995 *Medical Physics* **22**(7), 499–513.

Libby B, Siebers J and Mohan R 1999 *Medical Physics* **26**(8), 1476–1482.

Linthout N, Verellen D, Van Acker S, Voordeckers M, Bretz A and Storme G 2002 *Radiotherapy and Oncology* **64**(1), 85–95.

Liu H H, Mackie T R and McCullough E C 1997 *Medical Physics* **24**(12), 1975–1985.

Liu H H, Mackie T R and McCullough E C 2000 *Medical Physics* **27**(4), 737–744.

Lobo J and Popescu I 2010 *Physics in Medicine and Biology* **55**(16), 4431–4443.

Locke C and Zavgorodni S 2009 *Medical Physics* **31**(4), 290–299.

Lovelock D M J, Chui C S and Mohan R 1995 *Medical Physics* **22**(9), 1387–1394.

Lund E, Gustafsson H, Danilczuk M, Sastry M D, Lund A, Vestad T A, Malinen E, Hole E O and Sagstuen E 2003 *Applied Radiation and Isotopes* **62**(2), 317–324.

Ma C, Li J, Pawlicki T, Jiang S, Deng J, Lee M, Koumrian T, Luxton M and Brain S 2002 *Physics in Medicine and Biology* **47**(10), 1671–1689.

Ma C M and Jiang S B 1999 *Physics in Medicine and Biology* **44**(12), R157–R189.

Ma C, Mok E, Kapur A, Pawlicki T, Findley D, Brain S, Forster K and Boyer A 1999 *Medical Physics* **26**(10), 325–327.

Mack A, Mack G, Weltz D, Scheib S G, Böttcher H D and Seifert V 2003 *Medical Physics* **30**(9), 2399–2409.

Mason D 2011 *Medical Physics* **38**(6), 3493.

McCullough E and Holmes T 1985 *Medical Physics* **12**(2), 237–242.

McEwen M, Kawrakow I and Ross C 2011 *Medical Physics* **35**(3), 950–958.

McLaughlin W L, Soares C G, Sayeg J A, McCullough E C, Kline R W, Wu A and Maitz A H 1994 *Medical Physics* **21**(3), 379–388.

Mesbahi A, Fix M, Allahverdi M, Grein E and Garaati H 2005 *Applied Radiation and Isotopes* **62**(3), 469–77.

Mohan R, Chui C and Lidofsky L 1985 *Medical Physics* **12**(5), 592–597.

Mountford J, Porrovecchio G, Smid M and R S 2008 *Applied Optics* **47**(31), 5821–5828.

Naqa I E, Kawrakow I, Fippel M, Siebers J V, Lindsay P E, Wickerhauser M V, Vicic M, Zakarian K and Kauffmann N 2005 *Physics in Medicine and Biology* **50**(5), 909–922.

Nelson W R, Hirayama H and Rogers D W O 1985 'The EGS4 code system Report SLAC–265 Stanford Linear Accelerator Center, Stanford'.

NIST 2011*a* 'Composition of Materials used in STAR Databases'.
URL: *http://physics.nist.gov/cgi-bin/Star/compos.pl?ap*

NIST 2011*b* 'estar: stopping–power and range tables for electrons'.
URL: *http://physics.nist.gov/PhysRefData/Star/Text/ESTAR.html*

NIST 2011*c* 'X–ray Mass Attenuation Coefficients'.
URL: *http://www.nist.gov/pml/data/xraycoef/index.cfm*

Otto K 2008 *Medical Physics* **35**(1), 310–317.

Ottosson R O and Behrens C F 2011 *Physics in Medicine and Biology* **56**(22), N263–N274.

Ottosson R O, Engstrom P E, Sjöström D, Behrens C F, Karlsson A, Knöös T and Ceberg C 2009 *Acta Oncologica (Stockholm, Sweden)* **48**(2), 233–237.

Ottosson R O, Karlsson A and Behrens C F 2010 *Physics in Medicine and Biology* **55**(16), 4521–4533.

Ottosson W, Baker M, Hedman M, Behrens C F and Sjöström D 2010 *Acta Oncologica* **49**(7), 1184–1191.

Paelinck L, Reynaert N, Thierens H, De Neve W and De Wagter C 2005 *Physics in Medicine and Biology* **50**(9), 2055–2069.

Papanikolaou N, Battista J J, Boyer A L, Kappas G, Klein Mallinckrodt E, Rock Mackie T, Sharpe M and Van Dyk J 2004 *Medical Physics Publishing* .

Pawlicki T and Ma C M 2001 *Medical Dosimetry* **26**(2), 157–168.

Pena J, Franco L, Gómez F, Iglesias A, Lobato R, Mosquera J, Pazos A, Pardo J, Pombar M, Rodríguez A and Sendón J 2004 *Physics in Medicine and Biology* **48**(21), 4929–4942.

Pönisch F, Titt U, Kry S F, Vassiliev O N and Mohan R 2006 *Medical Physics* **33**(2), 402–404.

Popescu I A, Shaw C P, Zavgorodni S F and Beckham W A 2005 *Physics in Medicine and Biology* **50**(14), 3375–3392.

Regulla D F and Deffner U 1982 *The International Journal of Applied Radiation and Isotopes* **33**(11), 1101–1114.

Reynaert N, Coghe M, De Smedt B, Paelinck L, Vanderstraeten B, De Gersem W, Van Duyse B, De Wagter C, De Neve W and Thierens H 2005 *Physics in Medicine and Biology* **50**(5), 831–846.

Reynaert N, van der Marck S, Schaart D, Van der Zee W, Van Vliet-Vroegindewiej C, Tomsej M, Jansen J, Heijmen B, Coghe M and De Wagter C 2007 *Radiation Physics and Chemistry* **76**(4), 643–686.

Rogers D W O 2006 *Physics in Medicine and Biology* **51**(13), R287–R301.

Rogers D W O and Cygler J E 2009 *Clinical Dosimetry Measurements in Radiotherapy* Medical Physics Publishing Madison, Wisconsin.

Rogers D W O, Faddegon B A, Ding G A, Ma C M and We J 1995 *Medical Physics* **22**(5), 503–524.

Rogers D W O, Walters B and Kawrakow I 2009 *http://irs.inms.nrc.ca/publications/reports/pdf/PIRS-0509a-2009.pdf* pp. 1–260.

Sanches-Doblado F, Andreo P, Capote R, Leal A, Perucha M, Arrans R, Nunez L, Mainegra E, Lagares J I and Carrasco E 2003 *Physics in Medicine and Biology* **48**(14), 2081–2099.

Saw C B, Loper A, Komanduri K, Combine T, Huq S and Scicutella C 2005 *Medical Dosimetry* **30**(3), 145–148.

Schach von Wittenau A E, Cox L J, Bergstrom P M, Chandler W P, Hartmann Siantar C L and Mohan R 1999 *Medical Physics* **26**(7), 1196–1211.

Schneider U, Pedroni E and Lomax A 1996 *Phys Med Biol* **41**(1), 111–124.

Schneider W, Bortfeld T and Schlegel W 2000 *Phys Med Biol* **45**(2), 459–478.

Scott A J D, Nahum A E and Fenwick J D 2009 *Medical Physics* **36**(7), 3132–3144.

Seco J, Adams E, Bidmead M, Partridge M and Verhaegen F 2005 *Physics in Medicine and Biology* **50**(5), 817–830.

Sempau J, Sánchez-Reyes A, Salvat F, Tahar H O B, Jiang S B and Fernández-Varea J 2001 *Physics in Medicine and Biology* **46**(4), 1163–1186.

Sheikh-Baghei D and Rogers D W O 2002 *Medical Physics* **29**(3), 379–390.

Sheikh-Bagheri D, Rogers D W, Ross C K and Seuntjens J P 2000 *Medical Physics* **27**(10), 2256–2266.

Siebers J, Keall P, Kim J and Mohan R 2002 *Physics in Medicine and Biology* **47**(17), 3225–3249.

Siebers J V, Keall P J, Libby B and Mohan R 1999 *Physics in Medicine and Biology* **44**(12), 3009–3026.

Siebers J V, Keall P J, Nahum A E and R M 2000 *Physics in Medicine and Biology* **45**(4), 983–995.

Sjöström D, Bjelkengren U, Ottosson W and Behrens C F 2009 *Acta Oncologica* **48**(2), 192–200.

Smedt B D, Fippel M, Reynaert N and Thierens H 2006 *Medical Physics* **33**(6), 1678–1687.

Spencer L V and Attix F H 1955 *Radiation Research* **3**(3), 239–254.

Spezi E, Lewis D and Smith C 2002 *Phys Med Biol* **47**(23), 4223–4232.

Steneker M, Lomax A and Schneider U 2006 *Radiotherapy and Oncology* **80**(2), 263–267.

Sterpin E, Salvat F, Olivera G and Vynckier S 2009 *Medical Physics* **36**(5), 1566–1575.

Tanabe E and Hamm R W 1985 *Nuclear Instruments and Methods in Physics Research* **10-11**(2), 871–876.

Tessier F and Kawrakow I 2010 *Medical Physics* **37**(1), 96–107.

Thebaut J and Zavgorodni S 2006 *Physics in Medicine and Biology* **51**(23), N441–N449.

Thieke C, Küfer K H, Monz M, Scherrer A, Alonso F, Oelfke U, Huber P E, Debus J and Bortfeld T 2007 *Radiotherapy and Oncology* **85**(2), 292–298.

Tonkopi E, McEwen M and Walters, BRR adn Kawrakow I 2005 *Medical Physics* **32**(9), 2918–2927.

Torikoshi M, Tsunoo T, Sasaki M, Endo M, Noda Y, Ohno Y, Kohno T, Hyodo K, Uesugi K and Yagi N 2003 *Phys Med Biol* **48**(5), 673–685.

Torikoshi T T M, Ohno Y, Endo M, Natsuhori M, Kakizaki T, Yamada N, Ito N, Yagi N and Uesugi K 2004 *Nuclear Science Symposium Conference Record, IEEE* **6**, 3764–3768.

Tsiakalos M F, Stathakis S, Plataniotis G A, Kappas C and Theodorou K 2006 *Radiotherapy and Oncology* **79**(1), 131–138.

Tyagi N, Moran J M, Litzenberg D W, Bielajew A F, Fraass B a and Chetty I J 2007 *Medical Physics* **34**(2), 651–663.

van Esch A, Tillikainen L, Pyykkonen J, Tenhunen M, Helminen H, Siljamäki S, Alakuijala J, Paiusco M, Iori M and Huyskens D P 2006 *Medical Physics* **33**(11), 4130–4148.

Vanderstraeten B, Chin P, Fix M, Leal A, Mora G, Reynaert N, Seco J, Sokup M, Spezi E, De Neve W and Thierens H 2007 *Physics in Medicine and Biology* **52**(3), 539–562.

Vanderstraeten B, Reynaert N, Paelinck L, Madani I, De Wagter C, De Gersem W, De Neve W and Thierens H 2006 *Medical Physics* **33**(9), 3149–3158.

Varian Medical Systems 1999 *Monte Carlo Project (confidential)*.

Varian Oncology Systems 2008 *Monte Carlo Data Package (confidential)*.

Velkley D E, Manson D J, Purdy J A and Oliver G D J 1975 *Medical Physics* **2**(1), 14–19.

Verhaegen F and Devic S 2005 *Physics in Medicine and Biology* **50**(5), 937–946.

Verhaegen F and Liu H H 2001 *Physics in Medicine and Biology* **46**(2), 287–296.

Verhaegen F and Seuntjens J 2003 *Physics in Medicine and Biology* **48**(21), R107–R164.

Verhaegen F, Symonds-Tayler R, Liu H H and Nahum A E 2000 *Physics in Medicine and Biology* **45**(11), 3159–3170.

Vestad T A, Malinen E, Olsen D R, Hole E O and Sagstuen E 2004 *Phys Med Biol* **49**(20), 4701–4715.

Waldeland E and Malinen E 2011 *Radiation Measurements* **46**(9), 945–951.

Walters B, Kawrakow I and Rogers D W O 2005 *http://www.irs.inms.nrc.ca/BEAM/user_manuals/pirs794/index.html* pp. 1–97.

Walters B R B, Kawrakow I and Rogers D W O 2002 *Medical Physics* **29**(13), 2745–2752.

Walters B R B, Treurniet J, Rogers D W O and Kawrakow I 2012 'QA tests of the EGSnrc system and comparisons with EGS4 (Draft)'. **URL:** *http://irs.inms.nrc.ca/software/egsnrc/documentation/pirs703.pdf*

Wang L, Yorke E and Chui C S 2002 *Medical Physics* **29**(11), 2705–2717.

White D, Woodard H and Hammond S 1987 *The Brittish Journal of Radiology* **60**(717), 907–913.

Wong J W and Purdy J A 1990 *Medical Physics* **17**(5), 807–814.

Woodard H and White D 1982 *The Brittish Journal of Radiology* **55**(652), 277–282.

Woodard H and White D 1986 *The Brittish Journal of Radiology* **59**(708), 1209–1219.

Yin Z, Hugtenburg R P and Beddoe A H 2004 *Physics in Medicine and Biology* **49**(16), 3691–3702.

Zeng G G, McEwen M R, Rogers D W O and Klassen N V 2004 *Physics in Medicine and Biology* **49**(2), 257–270.

Zhu T C 2010 *Journal of Physics: Conference Series* **250**(1).